STUDY OF BEAM DYNAMICS IN 100 MeV, 100 kW RF ELECTRON LINAC

By

RADHAKANTA DASH

Enrolment No: ENGG01201104002

CI Name; Bhabha Atomic Research Centre, Mumbai

A thesis submitted to the

Board of Studies in Engineering Sciences

In partial fulfillment of requirements

for the Degree of

DOCTOR OF PHILOSOPHY

of

HOMI BHABHA NATIONAL INSTITUTE

August, 2016

Homi Bhabha National Institute

Recommendations of the Viva Voce Committee

As members of the Viva Voce Committee, we certify that we have read the dissertation prepared by Radhakanta Dash entitled "Study of Beam Dynamics in 100 MeV, 100 kW RF Electron Linac" and recommend that it may be accepted as fulfilling the thesis requirement for the award of Degree of Doctor of Philosophy.

Chairman - Prof. D.N. Badodkar Date: 4/8/16

Guide / Convener - Dr. Archana Sharma Date: 04-08-2016

Co-guide - Dr. K.C. Mittal Kailash C. Mittal Date: 4-8-16

Examiner - Dr. Dinakar Kanjilal D. Kanjilal Date: 4-8-16

Member 1- Dr. P.K. Pal (Retd wef 31.07.2016) Date:

(Expert Member Coopt) Dr. A.P. Tiwari 04.8.16

Member 2- Dr. Anita Topkar A. Topkar 4/8/16

Member 3- Dr. A.K. Bhattacharjee A.K. Bhattacharjee Date: 04/08/2016

(Invitee) Dr. B. Dikshit B. Dikshit 4-8-16

Final approval and acceptance of this thesis is contingent upon the candidate's submission of the final copies of the thesis to HBNI.

We hereby certify that we have read this thesis prepared under our direction and recommend that it may be accepted as fulfilling the thesis requirement.

Date: 4-8-16

Place: Mumbai

Kailash C. Mittal Archana

Co-guide **Guide**

STATEMENT BY AUTHOR

This dissertation has been submitted in partial fulfillment of requirements for an advanced degree at Homi Bhabha National Institute (HBNI) and is deposited in the Library to be made available to borrowers under rules of the HBNI.

Brief quotations from this dissertation are allowable without special permission, provided that accurate acknowledgement of source is made. Requests for permission for extended quotation from or reproduction of this manuscript in whole or in part may be granted by the Competent Authority of HBNI when in his or her judgment the proposed use of the material is in the interests of scholarship. In all other instances, however, permission must be obtained from the author.

Radhakanta Dash

Radhakanta Dash

DECLARATION

I, hereby declare that the investigation presented in the thesis has been carried out by me. The work is original and has not been submitted earlier as a whole or in part for a degree / diploma at this or any other Institution / University.

Radhakanta Dash

Radhakanta Dash

ABSTRACT

Direct experimental studies of behaviour of the electron beam inside accelerator cavity are very difficult. Numerical simulations are, therefore powerful tools in the analysis of beam dynamics of present linear accelerator facilities as well as the future accelerators. This research work focuses on the beam dynamics of linear accelerator by analytical methods and computer simulations in order to predict the behavior and quality of the electron beam and minimize the beam loss. In this work, we have studied the beam dynamics of a 30 MeV standing wave, biperiodic, coupled cavity rf electron linac with the help of CST Microwave studio and ASTRA code to determine the optimized parameters for a nominal gain of energy of 30 MeV with minimum energy spread and keep the minimal growth of transverse emittance. This facilitates a safety operation of the linac and avoids induced radioactivity with hands on maintenance of the accelerating structure and components. Further we have studied the beam dynamics of a 10 MeV rf electron linac in operation and validate our simulation results with the experimental data within the limit of experimental errors. We present the beam dynamics results of a 100 MeV, 100 kW standing wave rf electron linac with the help of CST MWS, ASTRA and ELEGANT beam dynamics codes along with bunch compression scheme with chicken magnet that comprises four dipoles and compare the results with a 100 MeV traveling wave rf electron linac structure. We have presented analytical expressions for the growth of transverse emittance in an RF gap which includes the coupling between the phase spread of the beam and spherical aberration. Using reduced envelope equation for a laminar beam the shift in frequency of oscillation of the beam envelope in the RF field is calculated. Also, Analytical expression is derived for beam optics in a solenoid field considering terms up to the third order in the radial displacement. Two important phenomena: effect of spherical aberrations in axial -symmetric focusing lens and influence of nonlinear space charge forces on beam emittance growth are discussed for different beam distributions. Chromatic aberration induced growth of emittance and distortion of phase space area is discussed. We have presented a new formulation for the aperture coupling problem in terms of Carlson Symmetric Integrals. The significance of such a method is that it considers the thickness of the aperture in to account to find the coupling coefficients between cavities unlike the earlier works which neglect the thickness of the aperture in aperture coupling problems. We have validated our theoretical model with the earlier works of aperture coupling taking thickness of the aperture tends to zero.

List of Publications arising from the thesis

Journal

1. "Beam dynamics studies and parametric characterization of a standing wave electron linac", **R Dash**, J Mondal, A Sharma and K C Mittal, *Journal of Instrumentation,* **2013**, *8 T07002*, 1-19.
2. "Numerical evaluation of aperture coupling in resonant cavities and frequency perturbation analysis", **R Dash**, B Nayak, A Sharma and K C Mittal, *Journal of Instrumentation*, **2014**, *9 P01012*, 1-14.
3. "Effect of Spherical Aberration on the Emittance Growth and frequency of Oscillation of a Beam Crossing an RF Gap", B Nayak, **R Dash** and K C Mittal, *Nucl. Instr. and Meth. A*, **2014**, *746*, 1-3.
4. "Analysis of Transverse RMS Emittance Growth of a Beam induced by Spherical and Chromatic Aberration in a Solenoidal Field", **R Dash**, B Nayak, A Sharma and K C Mittal, *Nucl. Instr. and Meth. A*, **2016,** *807*, 94-100.

Conferences

1. "Beam Dynamics Studies of a 30 MeV Standing Wave Electron Linac", **R Dash**, J Mondal, A Sharma and K C Mittal, 25th North American Particle Accelerator Conference NA-PAC'13, Pasadena, USA, September 2013, 451-453.
2. "Study of Beam Dynamics of a 30 MeV Standing Wave Electron Linac", **R Dash**, J Mondal, A Sharma and K C Mittal, INPAC-2013, Kolkata, November 2013.
3. **"**Beam dynamics studies of a 10 MeV standing wave electron linac**", R Dash**, A Sharma and K C Mittal, 26th International Symposium on Discharges and Electrical Insulation in Vacuum,ISDEIV-2014,Mumbai, September 2014.
4. "Numerical evaluation of aperture coupling in resonant waveguides and frequency perturbation analysis", **R Dash**, B Nayak, A Sharma and K C Mittal, 26th International Symposium on Discharges and Electrical Insulation in Vacuum 2014,ISDEIV-2014, Mumbai, September 2014.
5. "Study of beam dynamics of a 100 MeV electron linac", **R Dash**, B Nayak, A Sharma

and K C Mittal, 26th International Symposium on Discharges and Electrical Insulation in Vacuum 2014,ISDEIV-2014, Mumbai, September 2014.

6. “Beam dynamics simulation studies of a 30 MeV electron linac”, **R Dash**, B Nayak, A Sharma and K C Mittal, National Symposium on Vacuum Technology & Its Applications to Electron Beams, IVSNS-2015, Mumbai, November 2015.
7. “Beam dynamics study of a 100 MeV RF electron linac”, **R Dash**, B Nayak, A Sharma and K C Mittal, International Conference on Microwave, Optical and Communication Engineering, ICMOCE-2015, Bhubaneswar, December 2015.

Radhakanta Dash

Radhakanta Dash

DEDICATIONS

Dedicated to the Shree Balabhadra, Maa Subhadra, Shree Jagannath and Maa Lakshmee of Puri, Odisha

Dedicated to Shree Lingaraj and Devi Parvati (Maa Bhavani), Bhubaneswar, Odisha

Dedicated to Shree SiddhiVinayaka (Shree Ganesha), Mumbai

Dedicated to Maa Sarala, Jhankad, Odisha

ACKNOWLEDGEMENTS

At this point I express my heartfelt thanks to all who helped me to make this work a success. First of all, I express my sincere gratitude to Prof. Dr. Archana Sharma and Prof. Dr. Kailash C. Mittal to supervise my PhD thesis, and encourage me to work on a very interesting subject. I thank my Doctoral committee members for valuable suggestions. My sincere thank to Dr. Jayanta Mondal for valuable suggestions during my thesis work. I very much appreciate the friendship and enjoyable collaboration with Biswaranjan Nayak, who greatly supported me at various occasions, in particular during the theoretical calculations and analysis explaining beam dynamics related issues that is written in this thesis tome. I thank Susanta Nayak to help me on many occasions and friendliness. I am grateful to Siba P Sahoo to help me as a true friend. I thank Shuvendu Jena for valuable suggestions. Special thanks to Dr. K Flottmann and Dr. M. Dohlus for helping me to learn computer code ASTRA. I am grateful to Dr. M Borland to teach me the Elegant code. I thank Dr Eric Prebys and Dr S Krishnagopal for their valuable lectures. I thank R.I. Bakhtsingh to help me in many occassions. Thanks goes to V.T. Nimje, S. Acharya, Dr. K.V. Nagesh, R.K Rajawat, S.R. Ghodke, D. Bhattacharjee, A. Tilu and R. Tiwari for discussions on accelerator related issues. I thank my fellow students Dr C.S. Reddy, Dr. S.V Tiwari, P. Naresh for generous helps. I thank Mr A Gupte and his wife for their love and affection during my stay in Mumbai. I thank all the staff members of EBC and APPD, BARC, officials of HBNI and BARC for enabling me to do research work at a fascinating facility. My sincere thank to DAE, India to support my research work under DGFS program. My sincere gratitude to Dr B.B Padhy (my M.Tech thesis supervisor), who excited my curiosity about Free Electron Laser (which propelled me to choose my PhD thesis on Beam Dynamics of Linac) and from whom I learnt a lot on presentation skill of the research works. Finally, I would like to thank my parents, my brothers, my wife and other family members and my friends for their moral support.

CONTENTS

LIST OF ABBREVIATIONS

ASTRA	-	A Space Charge Tracking Algorithm
BARC	-	Bhabha Atomic Research Centre
CCL	-	Coupled Cavity Linac
CST MWS	-	CST Microwave Studio
EBC	-	Electron Beam Centre, Kharghar
ELEGANT	-	ELEctron Generation ANd Tracking
LINAC	-	Linear Accelerator
RF	-	Radio Frequency
RMS	-	Root Mean Square
SW	-	Standing Wave
TWS	-	Travelling Wave Structure
TW	-	Travelling Wave

SYNOPSIS

Dynamics of charged particles in accelerators [1] is an important aspect in the design of high energy particle accelerators for the purpose of synchrotron radiation, free electron laser (FEL) and neutron generation. Beam dynamics studies of charged particles [2, 3] explore the behaviour and quality of beam taking into account constraints applied to the particle accelerators for high energy requirements along with manufacturing precision and strength of the steering and accelerating electromagnetic fields. To support the lattice design process, it is essential to study the beam dynamics of accelerator by analytical methods and computer simulations. These predict the beam size and emittance while transporting through accelerator cavities and focusing element and minimize the beam loss.

Accelerator based neutron generation facilities are a promising and challenging technology to generate high quality radiation for various applications. Such neutron generation facilities are driven by bunches of highly relativistic electrons interacting with target materials to generate X- rays and produce neutrons by photo-nuclear or photo-fission process. The high power beam with low emittance is necessary to prevent beam hitting the cavity wall and producing secondary radiations. Direct experimental studies of behaviour of the electron beam inside accelerator cavity are very difficult. Beam diagnostics systems are not feasible to incorporate at all positions along the linac to measure beam characteristics. Lack of information can be supplemented by numerical simulation. It is also required to understand the beam dynamics to find ways of improvement. Numerical simulations are, therefore powerful tools in the analysis of beam dynamics of present linear accelerator facilities as well as the future accelerators.

Beam dynamics studies of a 100 MeV, 100 kW RF Electron Linear Accelerator is the focus of this thesis. Electron bunches accelerating in electric field inside accelerator cavities and bunch compression processes have a significant effect on the beam dynamics and the performance of accelerator for neutron generation. Beam dynamics in 10 MeV, 30 MeV and 100 MeV electron linacs has been studied. Effect of space charge, emittance and aperture thickness in cavity cells has been analysed in depth. Spherical aberration in linacs has been studied analytically and computationally. Results are described in the following chapters. This thesis work has resulted in a no. of journal publications and conference presentations.

The thesis is organized as follows:

Chapter 1 of this thesis introduces the beam dynamics of linear accelerator based on the review of available literature on the beam dynamics study of particle accelerators. It is perceived that both theoretical treatment and numerical simulations are essential to understand the behaviour of beam in linacs for a high quality beam delivery system for the purpose of neutron generation for scientific researches and societal applications. These aspects of beam dynamics studies are presented in the following chapters.

In **Chapter 2** a review of the literature available on the beam dynamics of linear accelerator is presented and the concepts required in the remainder of the thesis are introduced. A special attention is given to the longitudinal and transverse dynamics of the beam in the phase space. The role of space charge and emittance growth in the linacs is discussed. Longitudinal dynamics is provided by an appropriate choice of the phase of the synchronous particle relative to the crest of the RF electric field [2, 3]. A longitudinal restoring force exists when the synchronous phase is chosen corresponding to a field that is rising in time. The early particles experience a smaller field and the late particles a larger field than the synchronous particle. The accelerated particles are formed in stable bunches that are near the synchronous particle. Those particles outside the stable region slip behind in phase and do not experience any net acceleration.

When off-axis particles enter a RF gap and are accelerated by a longitudinal RF electric field, they also experience radial RF electric and magnetic forces and there will be a net radial impulse, which occurs as a result of variation of electric field with time and radial displacement. As the velocity increases while the particle crosses the gap, the particle does not spend equal times in each half of the gap and most particles experience a field in the second half of the gap that is higher than the field in the first half, resulting in a net defocusing force. If the longitudinal forces provide focusing at a given point, the two transverse-force components cannot be focusing at the same point.

The emittance [4, 5, 6] provides a quantitative basis, or a figure of merit, for describing the quality of the beam. It is closely related to two-dimensional projections of the volume occupied by the ensemble of particles in six-dimensional phase space. Nonlinear forces (aberrations) due to the external or space-charge fields and instabilities lead to a deterioration of the beam quality. For beams in particle accelerators, the normalized emittance [7] is a more useful quantity than the unnormalized emittance. Since in an ideal system (linear forces, no coupling) it remains constant. An increase of the normalized emittance is usually an indication that nonlinear effects are present in the system causing a deterioration of beam quality.

The space-charge field [8], which is a result of Coulomb interactions in a multiparticle system reduces the effective focusing strength, causes growth in rms emittances [9]. The growth in rms emittance may lead to beam loss, which results in radioactivation of the accelerating structure

Chapter 3 of this thesis presents the results of the optimization of 30 MeV, 6 kW bi-periodic coupled cavity standing wave accelerator beam parameters and the limits of the possible beam quality. This electron accelerator is a general purpose facility for generation of bremsstrahlung X-rays and neutrons for different physics experiments. This electron accelerator-based experimental neutron facility will be used for measurement of neutron cross-section (n,γ), (n, xn) and (n, f) reactions at different energies for various materials and material irradiation studies. For the pulsed mode operation of this linac, preferential operation parameters have been determined from the results of beam dynamics studies with the help of mutiphysics simulation code CST Studio [10] and beam dynamics code ASTRA [11]. The optimization approach is to keep the growth of transverse emittance and self field effects a minimum as well as to limit the radioactivity and the cost of the linac itself.

Chapter 4 of this thesis presents the beam dynamics study and comparison of the results with experimental data for a 10 MeV, 10 kW standing wave electron linac that is operational at Electron Beam Centre, Kharghar, Navi Mumbai for industrial applications. The optimized output beam dynamics parameters are consistent with the output parameters of the 10 MeV lattice design [12] and experimental results [13, 14]. The effects of space charge, input beam size, beam divergence, emittance growth, energy spread, behavior of bunch and their effect on the beam quality have been studied.

Chapter 5 of this thesis presents the lattice design and beam dynamics simulation of the 100 MeV linac. Beam dynamics of a coupled cavity standing wave 100 MeV linac is studied and the behaviour of beam in the longitudinal and transverse phase space is presented. The electron beam is tracked in the injector section with the help of ASTRA [11] beam dynamics code and after injector section the electron bunches are tracked with ELEGANT [15] beam dynamics code up to the end. A four dipole based chicane magnet is used to compress the beam for a shorter pulse at the output. Further the beam dynamics studies of a travelling wave cavity [7] have been done in the longitudinal and transverse phase space along with bunch compression.

Chapter 6 of this thesis presents the effect of spherical aberration on the transverse emittance growth and frequency of oscillation of a beam envelope inside an RF Cavity. The coefficient of spherical aberration that arises due to third order terms of on-axis electric field component is discussed. An expression is derived for the growth of transverse emittance in an RF gap [16] which includes the coupling between the phase spread of the beam and spherical aberration. Further, using reduced envelope equation for a laminar beam, effect of aberration on the invariant envelope solution is discussed [17, 18]. An expression is found using Lindstedt-Poincare theory [19] for solution of the envelope equation. The shift in frequency of oscillation of the beam envelope in the RF field is calculated.

Also in a medium energy beam transport line of a 6 MeV linac transverse emittance growth associated with spherical aberration [20] is analyzed. An analytical expression is derived for beam optics in a solenoid field considering terms up to the third order in the radial displacement. Two important phenomena: effect of spherical aberrations in axial -symmetric focusing lens and influence of nonlinear space charge forces [3] on beam emittance growth are discussed for different beam distributions. Further the nonlinear effect associated with chromatic aberration [21] that describes the growth of emittance and distortion of phase space area is discussed.

Chapter 7 of this thesis presents a general formulation for numerical evaluation of the coupling between two identical resonant cavities by a small elliptical aperture in a plane common wall of arbitrary thickness. The aperture coupling is expressed in terms of electric and magnetic dipole moments and polarizabilities using Carlson symmetric elliptical integrals [22]. Carlson integrals have been numerically evaluated and under zero thickness approximation, the results are compared with the complete elliptical integrals of first and second kind [23]. Further, Slater's perturbation method [24] is applied to electrically and magnetically coupled cavities in order to find the frequency changes due to apertures of finite thickness on the cavity wall.

Chapter 8 of this thesis presents the summary and conclusions. Based on the above studies the following conclusions have been made.

a) It is found that space charge effect plays a pivotal role in the injector section and 1st cavity of the 30 MeV linac. A solenoid of length 15 cm and 15000 ampere turns over the injector section is necessary to compensate the space charge effect. With an output beam of size ~ 4.5 mm in the bore of aperture diameter 10 mm, and an energy spread of ~ 2.5% the beam loss on the cavity wall is minimized and the heavy irradiation of accelerator components is prevented.
b) For a 10 MeV linac, space charge effect is minimized with a solenoid of 15000 ampere turns and the beam satisfies the industrial norms to generate X rays.
c) The 100 MeV linac beam dynamics study explores that although both standing wave linac and travelling wave linac are highly efficient for high energy beam, the travelling wave linac may be preferred because of its large aperture and versatility to deal with high current and high power beam.
d) Spherical aberration that is induced due to third order term in the radial co-ordinate of the electric field of a RF cavity results in a growth of transverse emittance for a uniform beam distribution and shifts the invariant envelope solution from its original value. Change in frequency of oscillation of the beam is found using Lindstedt –Poincare expansion method.
e) Spherical aberration induced due to third order term in the radial co-ordinate of the magnetic field and space charge non-uniformity results in growth of transverse rms

emittance for uniform, Gaussian, parabolic and waterbag beam distributions. Also, distortion in phase space due to the energy spread of the beam gives rise to growth of rms emittance.

f) It is found that numerical evaluation of elliptic integrals for electromagnetic coupling through small elliptic aperture gives a faster and efficient method for aperture coupling problems. Further, this method extends the concept of aperture polarizability to include apertures in walls of finite thickness and explains the well-established zero wall thickness case.

Finally some future scope of work has been outlined.

a) Study of photo neutron generation using various target materials is to be carried out.
b) Thermodynamical studies are to be carried out for heating of the accelerator components during high power beam generation and transport.

REFERENCES

[1] E.D. Courant, H.D. Snyder,"Theory of the alternating gradient synchrotons", Ann. Phys. 3, (1958) 1.

[2] T. P. Wangler, "RF Linear Accelerator", 2nd ed., Weinheim, Wiley-VCH, 2008.

[3] M. Reiser, "Theory and Design of Charged Particle Beams", 2nd ed., Willey, New York 2008.

[4] J. Buon, "Beam Phase Space and Emittance", Proc. CERN Accelerator School, University of Jyv¨askyl¨a, Finland, (1992) p. 89.

[5] J.D. Lawson, "The Physics of Charged Particle Beams", 2nd ed., Oxford Univ. Press, 1988.

[6] K. Floettmann, "Some basic features of the beam emittance", Phys. Rev. ST Accel. Beams. 6 (2003) 034202.

[7] P.M. Lapostolle, A.L. Septier,“Linear Acceleartors“, North-Holland, Amsterdam, 1970.

[8] T. P. Wangler, “Space-Charge Limits in Linear Accelerator”, Los Alamos Report LA-8388, Los Alamos, 1980.

[9] T. P. Wangler, K.R. Crandall, R. S. Mills, M. Reiser, “Relation between field energy and rmsemittance in intense particle beams”,IEEE Trans. Nucl. Sci. 32 (1985) 2196

[10] CST Microwave Studio 2008, < http://www.cst.com >.

[11] K. Floettmann, ASTRA, “A Space charge Tracking Algorithm”, <http://www.desy.de/~mpyflo>.

[12] R.C. Sethi etal, “Design and Development of 10 MeV RF Electron Linac for Applied Research and Industrial Applications” Proceedings of the Ist Asian Particle Acc. Conf. KEK, Japan, Oct. 1998.

[13] V.T. Nimje etal, “Beam Energy Measurement of 10 MeV, 10kW Industrial RF Electron Linac”, Proceedings of the Indian Particle Acc. Conf., India, 2006.

[14] K.C. Mittal etal, “Operating Experience of 10 MeV industrial Linac”, Proceedings of the Indian Particle Acc. Conf, India, 2011.

[15] M. Borland, “elegant: A Flexible SDDS-Compliant Code for Accelerator Simulation, ” Advanced Photon Source LS-287, September 2000

[16] K. R. Crandall and D. P. Rusthoi, “TRACE 3-D Documentation,” 3rd Edition, (Los Alamos National Laboratory, 1997).

[17] Chun-xi Wang, “Hamiltonian analysis of transverse beam dynamics in high-brightness photoinjectors”,Phy. Rev. E 74 (2006) 046502.

[18] S.G. Anderson, J,B Rosenzweig, “Nonequilibrium transverse motion and emittance growth in ultrarelativistic space-charge dominated beams”,Phys. Rev. ST Accel. Beams. 3 (2000) 094201.

[19] A.H. Nayfeh,“Perturbation Methods“, Wiley-VCH Weinheim, 2004.

[20] P. R. Sarma etal, “Improvement of field quality of Glaser magnets used for focusing ion beams ”Nucl. Instr. and Meth. A 426 (1999) 243

[21] Z. Liu, and J.Y. Ximen, "Numerical computation of higher-order chromatic aberrations for rotationally symmetric electrostatic lenses",J. Appl. Phys., 72(1), (1992), 28.

[22] B. C. Carlson, "A table of elliptic integrals of the second kind", Math. Comp. 49 (1987) 595.

[23] J. Gao, "Analytical formulas for the resonant frequency changes due to opening apertures on cavity walls",Nucl. Instr. and Meth. A 311 (1992) 437.

[24] J.C. Slater, "Microwave electronics", Rev. of Mod. Phys. 18(4), (1946), 441.

LIST OF FIGURES

LIST OF TABLES

CHAPTER 1

INTRODUCTION

In pursuit of high energy and high intensity beam that serves as the platform for frontier science research, accelerators have been built with cutting edge technology and find applications in the field of academic research as well as industry [1]. Accelerator based radiation sources allow researchers to probe the structure of a wide range of samples with a resolution down to the level of atoms and molecules. The growing interest in accelerator beam can be credited to their potential to become standard diagnostic tool in a variety of fields of research, both basic and applied research in the chemical, materials, biotechnology and pharmaceutical sciences [2]. It is always challenging task to build accelerator facilities that require a critical design parameters of the accelerator components along with manufacturing precision for high energy requirements. To support the lattice design process in particle accelerators, it is essential to study the beam dynamics of charged particles [3] to predict the behaviour and quality of beam [4-6] while transporting through accelerator cavities and focusing element and minimize the beam loss. The motivation behind our research work on the beam dynamics studies of electron linear accelerator is the development of indigenous particle accelerator technology to deliver high quality beam for societal applications.

Owing to their functionality, efficiency and long-term reliability; electron accelerators have become more affordable to deliver beams with varying power and energy and are extensively used for various scientific and industrial applications [2, 7]. Electron Beams in the energy range of 0.1 MeV to 10 MeV find applications for industrial radiation processing like plastic modifications, food irradiation, pollution control and medical products sterilizations [2, 7, 8].

Electrons beams in the energy range of 30 to 100 MeV are employed for neutron production [2, 9]. Electron linear accelerator based neutron generation facilities are driven by bunches of highly relativistic electrons interacting with target materials to generate X- rays and produce neutrons by photo-nuclear or photo-fission process. These neutron sources are inherently compact, economical, reliable, easy to handle, less hazardous in nature and most suitable for applications such as neutron capture and fission cross-section studies, radio-isotope production and basic neutron scattering experiments for material science studies [2, 7, 9]. Since secondary radiations must be kept to a minimum for safe operation and hands on maintenance of the hardware of accelerator, a major concern for these accelerator facilities is to prevent the beam hitting the cavity wall of linac for high power beam delivery with low emittance value. Further the operation of a high energy electron linac puts stringent demands on the peak current, transverse emittance and energy spread of the electron beam.

Direct experimental studies of the behaviour of the electron beam inside accelerator cavity are very difficult. Further, beam diagnostics elements cannot be put at all positions along the linac to measure beam characteristics. On the other hand, analytical methods and computer simulations provide powerful tools in the beam dynamics studies [5, 10, 11] of linear accelerator facilities to understand the behaviour of beam in linacs and predict the beam energy, energy spread, beam size and emittance for high quality beam delivery systems for the purpose of scientific researches and societal applications.

Realizing the tremendous potential of electron beam in tune with the present and future scenario [2, 7, 8], Accelerator and Pulse Power Division (APPD), BARC has initiated the design and development of various types of industrial electron accelerators. A 10 MeV, 10 kW standing wave electron linac, a 3 MeV DC linac and a 6 MeV linac for cargo scanning are operational at Electron Beam Center, Kharghar, Navi Mumbai for industrial applications. Based on the experience gained from available 10 MeV RF linac technology, a programme to set up an experimental Neutron Facility using a 100 MeV, 100 kW pulsed normal conducting electron linac (S band) producing a pulsed neutron flux ~ 10^{14} n/cm^2/s has been taken up. This facility consists of an electron Gun, linac cavities, RF power sources, beam diagnostics, X ray and neutron target, neutron diagnostics and many other sub systems. This accelerator will be used for nuclear physics studies, generation of neutrons and neutron rich radioactive nuclei. In this thesis the lattice design and beam dynamics simulation of a coupled cavity standing wave 100 MeV linac [12] and a travelling wave cavity 100 MeV linac [13] have been studied and the behaviour of beam in the longitudinal and transverse phase space are investigated. The electron beam is tracked in the injector section with the help of ASTRA [14] beam dynamics code and after injector section the electron bunches are tracked with ELEGANT [15] beam dynamics code up to the end. A four dipole based chicane magnet is used to compress the beam for a shorter pulse at the output.

Further, the beam dynamics of a 30 MeV, 6 kW bi-periodic coupled cavity standing wave electron linac under development for the purpose of neutron generation has been studied [16-18]. To use this linac as an experimental tool as well as to limit the radioactivity and the cost of the linac itself, it is highly important for the linac to keep the growth of transverse emittance and self field effects a minimum. In order to predict the quality of electron beam [6], the electron-tracking code ASTRA [14] that takes the space charge of the beam in to account has been used to study the emittance evolution. This study has found the optimized beam parameters and the limits of the possible beam quality for different bunched beam.

The existing 10 MeV electron linac facility [19] is being used for food preservation, medical sterilization, semiconductor irradiation, radiography, radiation therapy, etc. In addition, bremsstrahlung radiation generated from the electron beam can be employed for studying the radiation damage and chemistry of special materials like zirconium and its alloys. Beam dynamics studies of the 10 MeV, 10 kW bi-periodic coupled cavity standing wave electron linac have been done [20] and the optimized output parameters are consistent with the simulation results of the 10 MeV lattice design [21] and experimental results [22, 23]. This study has explored the effects of space charge, input beam size, beam divergence, emittance growth, energy spread, behavior of bunch and their effect on the beam quality.

The coefficient of third order terms of on-axis electric field component gives rise to spherical aberration [24]. An expression has been derived for the growth of transverse emittance in an RF gap [25] which includes the coupling between the phase spread of the beam and spherical aberration and leads to an increase in the beam size. The effect of spherical aberration on the solution of beam envelope equation using Lindstedt-Poincare theory [26] has been found and the shift in frequency of oscillation of the beam envelope in the RF field is calculated. Also coefficient of third order terms in the radial displacement of solenoidal magnetic field component gives rise to spherical aberration [27]. In a medium energy beam transport line of a 6 MeV linac, effect of spherical aberrations in axial -symmetric focusing lens and influence of nonlinear space charge forces [28] on beam emittance growth have been calculated for different beam distributions. Further the nonlinear effect associated with chromatic aberration [29, 30] that describes the growth of emittance and distortion of phase space area has been investigated.

Earlier formulations [31, 32] for coupling of electromagnetic energy through a small aperture in a common wall between two regions are restricted in its application to conducting walls of zero thickness. In this thesis, the coupling between two identical resonant cavities by a small elliptical aperture in a plane common wall of finite thickness has been expressed in terms of electric and magnetic dipole moments and polarizabilities using Carlson symmetric elliptical integrals [33]. Carlson integrals [34] have been numerically evaluated and under zero thickness approximation, the results match with earlier formulation that involves the complete elliptical integrals of first and second kind [35]. Further, Slater's perturbation method [36] is applied to electrically and magnetically coupled cavities in order to find the frequency changes due to apertures of finite thickness on the cavity wall.

The analytical and computational results of beam dynamics studies for electron linacs in this thesis are organized in the following chapters. In chapter 2, an overview of the linac structures and the dynamics of electron bunches in linear accelerators are presented and the concepts required in the remainder of the thesis are introduced. Chapter 3 deals with beam dynamics study and parametric characterization of a 30 MeV standing wave linac. Chapter 4 gives the beam dynamics studies of a 10 MeV industrial electron linac and the comparison of the experimental results with those of numerical simulations within the limits of experimental error. The beam dynamics studies of 100 MeV linac structures are investigated in chapter 5. A comparison is made between standing wave linac and travelling wave linac options for high quality beam delivery. The following two chapters are dedicated to analytical studies for beam dynamics and linac cavity. Chapter 6 presents the analytical calculation for transverse emittance growth due to spherical aberration that is result of the third order terms in the electric and magnetic field expansion respectively. Numerical investigation of the aperture coupling in resonant cavities and the frequency perturbation analysis is presented in chapter 7. The last chapter gives summary and conclusions of the studies presented in this thesis and future scope of works.

CHAPTER 2

LITERATURE SURVEY

In this chapter we present a brief review of the literature available on beam dynamics of electron Linac. Section 2.1 gives a brief introduction to periodic accelerating structures. Section 2.2 discusses the bi-periodic coupled cavity linac. Section 2.3 studies the various figures of merits for beam injection and acceleration. Section 2.4 gives a brief introduction to co-ordinate system and the design trajectory of a linac. Section 2.5 discusses the equation of motion of the particles in the beam. Section 2.6 gives a brief discussion on emittance. Section 2.7 discusses the effect of space charge on the accelerator beam. Section 2.8 discusses the longitudinal particle dynamics in an rf linac. Section 2.9 gives a discussion on transverse particle dynamics in an rf linac. Section 2.10 discusses the Courant Snyder parameters and Hill's equation. Section 2.11 discusses a brief overview of the concept of aberration in charged particle optics.

2.1. PERIODIC ACCELERATING STRUCTURES

The Linac technology requires the propagation of electromagnetic waves in transmission lines, waveguides, and cavities. There are no truly monochromatic waves in nature. A real wave exists in the form of a wave group, which consists of a superposition of waves of different frequencies and wave numbers. If the spread in the phase velocities of the individual waves is small, the envelope of the wave pattern will tend to maintain its shape as it moves with a velocity that is called the group velocity.

Suppose the phase velocities of component waves are ω_1/k_1 and ω_2/k_2, where $\omega_1$and ω_2 are frequencies and k_1 and k_2 are wave numbers, then the mean phase velocity is defined as

$$v_p = \frac{\omega_1+\omega_2}{k_1+k_2} \tag{2.1}$$

The group velocity is defined as the velocity of the amplitude-modulation envelope, which is

$$v_g = \frac{\omega_1-\omega_2}{k_1-k_2} \tag{2.2}$$

The phase velocity at any point on the curve is the slope of the line from the origin to that point, and the group velocity is the slope of the dispersion curve, or tangent at that point.

For an electromagnetic wave to deliver a continuous energy gain to a moving charged particle, two conditions must be satisfied [10] :

(1) the wave must have an electric field component along the direction of particle motion and

(2) the particle and wave must have the same velocity to maintain synchronism.

The first condition is not satisfied by electromagnetic waves in free space, but can be satisfied by a transverse magnetic wave propagating in a uniform waveguide. However, the second condition is not satisfied for a uniform waveguide, because the phase velocity $v_p > c$. The most widely used solution for obtaining phase velocity $v_p < c$ in linacs has been the use of accelerating structures with periodic geometries. A periodic structure has the property that its modes are composed of a Fourier sum of waves, some of which are suitable for synchronous-particle acceleration.

In a lossless uniform waveguide with azimuthal symmetry, the axial electric field for the lowest transverse-magnetic mode, the TM_{01} mode, is

$$E_z(r,z,t) = EJ_0(kr)e^{j(\omega t - k_0 z)} \tag{2.3}$$

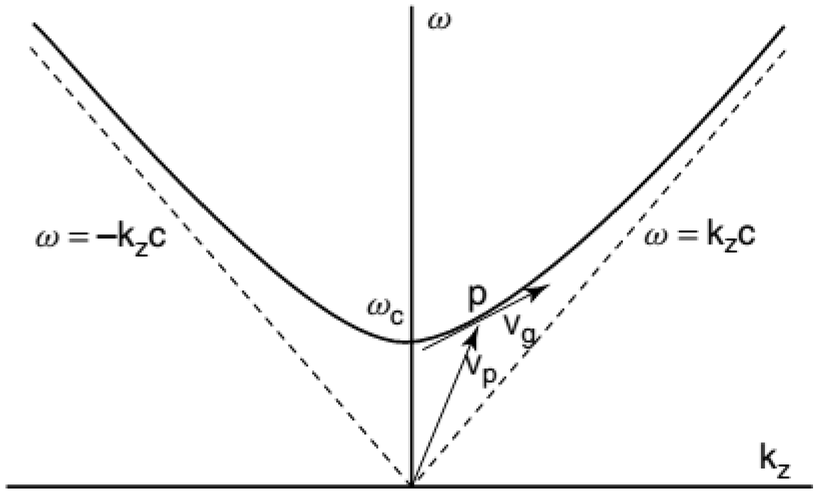

Fig. 2.1 Dispersion curve for a uniform waveguide [10].

This describes a wave propagating in the +*z* direction, with wavenumber $k_0 = 2\pi/\lambda_g$, where λ_g is the guide wavelength.

The uniform waveguide has a dispersion relation $\omega^2 = (Kc)^2 + (k_0 c)^2$,where K is the cutoff wavenumber for the TM_{01} mode, related to the cutoff angular frequency by $\omega_c = Kc$. Then the phase velocity is $v_p = \frac{\omega}{k_0} = \frac{c}{\sqrt{1-(Kc)^2/\omega^2}}$.

Because the phase velocity is always larger than c, the uniform guide is unsuitable for synchronous-particle acceleration, and the uniform waveguide is modified to obtain a lower phase velocity. Converting the uniform guide to a periodic structure perturb the field distribution by introducing a z-periodic modulation of the amplitude of the wave, giving a TM_{01} propagating-wave solution of the form $\boldsymbol{E}(r,z,t) = \boldsymbol{E}_d(r,z)e^{j(\omega t - k_0 z)}$, where $\boldsymbol{E}_d(r,z)$ is a periodic function with the same period d as the structure.

There are two basic types of periodic accelerating structures.

(i) Travelling wave structure

(ii) Standing Wave Structure

A comparative study of both the type of accelerator is given below [37].

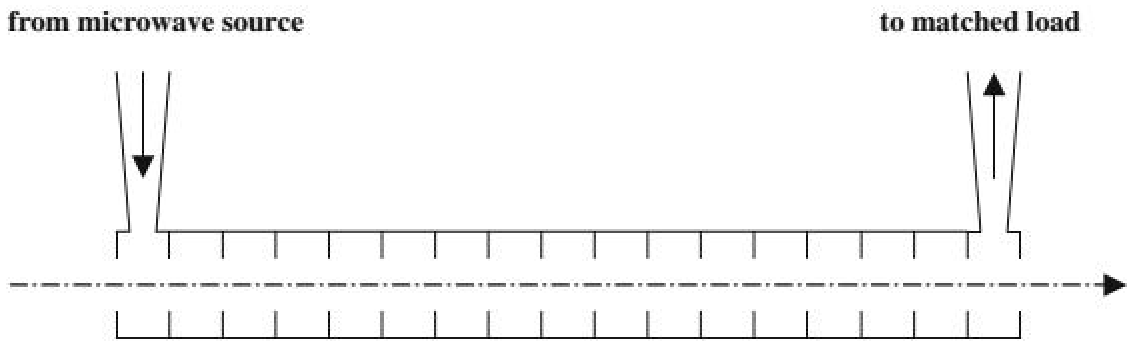

Fig. 2.2 Travelling wave structure [37].

The TW structure consists of a cylindrical waveguide that is periodically loaded with conducting disks, as schematically shown in Figure 2.2. The microwave power travels in one direction, from input to output. Internal reflections from the periodic disks reduce the wave phase velocity below the speed of light, enabling particle acceleration as the waves and particle bunches travel synchronously down the structure. The unused microwave power at the high-energy end is usually coupled into a matched resistive load. TW linacs can be designed to operate in either constant impedance or constant gradient modes. If the accelerating cavities defined by the disks are identical, then the impedance per unit length is constant, and the accelerating gradient decreases as the transmitted power droops. If a constant gradient is desired, the diameter of the disk apertures is gradually decreased down the structure. For modern TW linacs, the phase advance per cavity is chosen to be $2\pi/3$ (i.e., three cavities per wavelength).

In a SW linac both ends of the structure are effectively shorted, so that electromagnetic waves are reflected back and forth resulting in a standing wave pattern (as in a single resonant cavity). Both TW and SW structures can be thought of as series of individual resonators that are electromagnetically coupled. A TW linac is capacitively coupled through the disk apertures, which must be large and thin to obtain adequate coupling. In contrast, the SW linac uses inductive coupling through peripheral slots from one cavity to its neighbors. The spatial concentration of the electric field at the electron bunch is therefore better in the SW structure, and the transit time characteristics are usually somewhat more favorable. As a result, the rf efficiency is significantly higher for a SW waveguide for the same accelerating gradient, although the SW cavity surfaces must be machined with greater precision.

The TW structure is somewhat less complex, and usually less expensive per unit length to fabricate. It does not require an isolator or circulator, since it is a matched device, but it does require both input and output couplers. The larger radius apertures permit a somewhat higher beam current. On the other hand, since the cavities are much more tightly coupled, the SW accelerator is much more stable in phase with respect to temperature variations, and has much less tuning sensitivity. For applications in which physical space and rf power efficiency are important, and beam stability is essential, the SW accelerator offers a number of advantages, and it has become the linac structure of choice for most irradiation applications.

2.2. COUPLED CAVITY LINACS AND BIPERIODIC STRUCTURE

The coupled-cavity linac or CCL (Fig. 2.3) consists of a linear array of resonant cavities, coupled together to form a multicavity accelerating structure. The CCL is used for acceleration of higher velocity beams of electrons and protons in the typical velocity range $0.4<\beta<1.0$. The individual cavities are sometimes called cells, and each cell usually operates in a TM_{010}-like standing-wave mode. CCL structures provide two accelerating gaps per $\beta\lambda$. Most of the properties of the CCL can be understood from a model of N+1 coupled electrical oscillators [38]. There will be N+1 normal modes of the system, each with a characteristic resonant frequency and a characteristic pattern of the relative amplitudes and phases for the different oscillators. The properties of these N+1 normal modes can be determined by solving an eigenvalue problem. This is done in the following way. Kirchoff's law is applied to the N+1 circuits, and the sum of the voltages around each loop is set to zero. The resulting N+1 simultaneous equations are solved for the eigenfrequencies and the corresponding eigenvectors. The eigenvector components give the currents in the individual oscillators for each normal mode.

The $\pi/2$ normal mode of a chain of coupled oscillators has unique properties that would be especially important when the number of cells is large. It would be attractive to use this mode for a linac if we could devise a suitable geometry satisfying a synchronous condition for the particles, and resulting in high shunt impedance. To ensure synchronism in the $\pi/2$ normal mode in a periodic array of cavities, one can choose the cavity lengths so that the spacing between sequential excited cavities is $\beta\lambda/2$ corresponding to half an RF period. This gives the configuration shown in Fig. 2.4.

2.3. FIGURES OF MERITS FOR LINACS

There are several figures of merit that are commonly used to characterize accelerating cavities, and we will define them in this section. Some of these depend on the power, which is dissipated because of electrical resistance in the walls of the cavities.

The well-known quality factor of a resonator is defined in terms of the average power loss P as $Q_0 = \frac{\omega_0 U}{P_c}$ (2.4)

The shunt impedance is a figure of merit that is independent of the excitation level of the cavity and measures the effectiveness of producing an axial voltage V_0 for a given power dissipated. The shunt impedance r_s of a cavity is usually expressed in megohms, and is defined by [10]

$$r_s = \frac{V_0^2}{P} \quad (2.5)$$

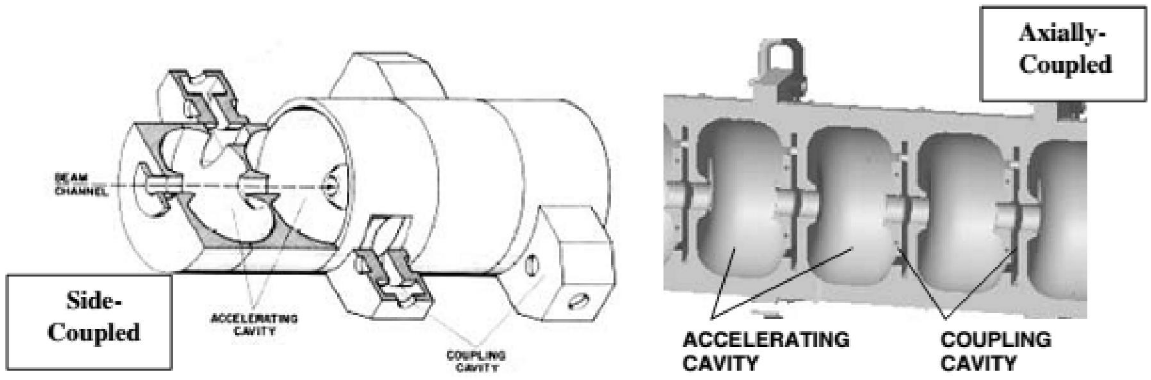

Fig. 2.3 Coupled Cavity Linacs [37].

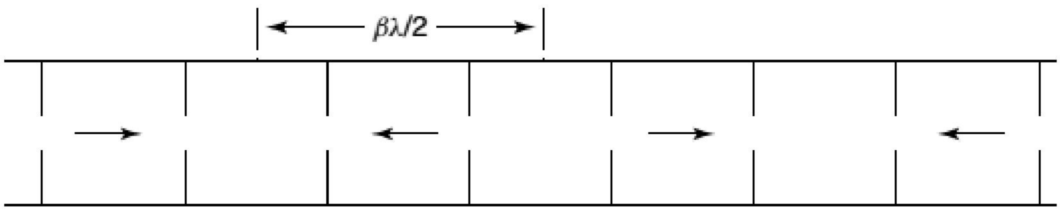

(a) π/2 mode of periodic structure

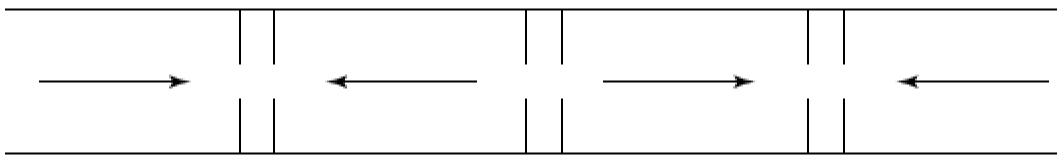

(b) Biperiodic on-axis-coupled structure

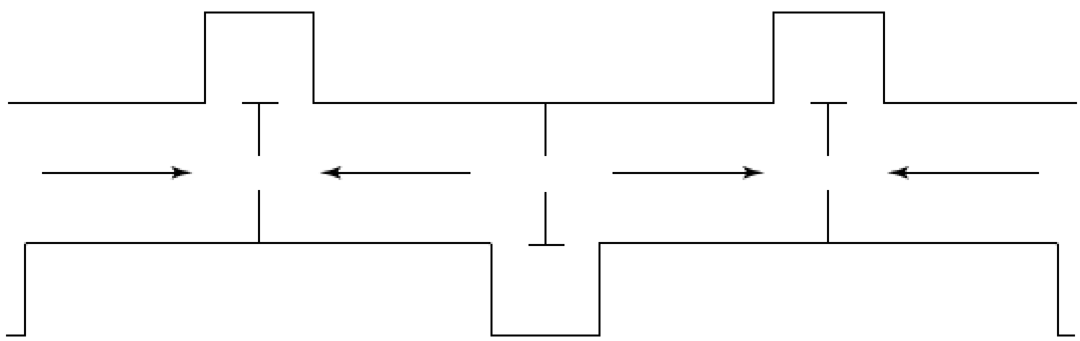

(c) Biperiodic side-coupled structure

Fig. 2.4 π/2 mode like operation of a cavity resonator chain [10].

In an accelerating cavity we are really more interested in maximizing the particle energy gain per unit power dissipation. Consequently,we define an effective shunt impedanceof a cavity as

$$r = \frac{(V_0 T)^2}{P} = r_s T^2 \tag{2.6}$$

This parameter in megohms measures the effectiveness per unit power loss for delivering energy to a particle. For a given field both $V_0 = E_0 L$ and P increase linearly with cavity length, as do both r and r_s . For long cavities we use a figure of merit called shunt impedances per unit length, that is independent of both the field level and the cavity length., Z, is

$$Z \equiv \frac{r_s}{L} = \frac{E_0^2}{P/L} \tag{2.7}$$

The effective shunt impedance per unit length is

$$ZT^2 = \frac{r}{L} = \frac{(E_0 T)^2}{P/L} \tag{2.8}$$

Another useful parameter is the ratio of effective shunt impedance to *Q*, often called *r* over *Q,*

$$\frac{r}{Q} = \frac{(V_0 T)^2}{\omega U} \tag{2.9}$$

At sufficiently high fields, room-temperature copper cavities will suffer electric breakdown or sparking. The mechanism may be initiated by electron field emission and it has been suggested that protons, originating on the surfaces or perhaps from hydrogen in the residual gas, are involved in the discharge. Kilpatrick [39] analyzed the data on RF breakdown, and defined the conditions that would result in breakdown-free operation. The Kilpatrick results were expressed in a convenient formula by T. J. Boyd [40] given as

$$f(MHz) = 1.64 E_k^2 e^{-8.5/E_k} \tag{2.10}$$

Where f is the frequency, and E_k in megavolts per meter is known as the Kilpatrick limit.

2.4. CO-ORDINATE SYSTEM AND PHASE SPACE OF A PARTICLE

A beam transport of accelerator system has a specified design trajectory [41]. This configuration is shown in Figure 2.5. The distance along this design trajectory is given by the independent variable *s*. There also exists the synchronous particle, which has a specified design velocity $v(s)$ at each point *s* on the design trajectory. The relative velocity $\beta=v/c$ and relativistic parameter $\gamma=1/(1-\beta^2)^{1/2}$ are always given with respect to this design velocity, unless otherwise noted. With respect to the synchronous particle, we construct a system of coordinates (x,y,z), that is, the synchronous particle is at the origin. The coordinates x,y,z represent displacements from the synchronous particle in the x, y, z directions, respectively. Locally, the *z*-coordinate is always aligned with the design trajectory. Specifically, the tangent vector of the design trajectory always points in the *z*-direction. Thus, the *xy*-plane represents the transverse plane while the *z*-direction is the longitudinal direction of beam propagation (in a local sense). Note that the coordinates (x,y,z) are not the inertial frame of the beam, they are laboratory coordinates that follow the beam.

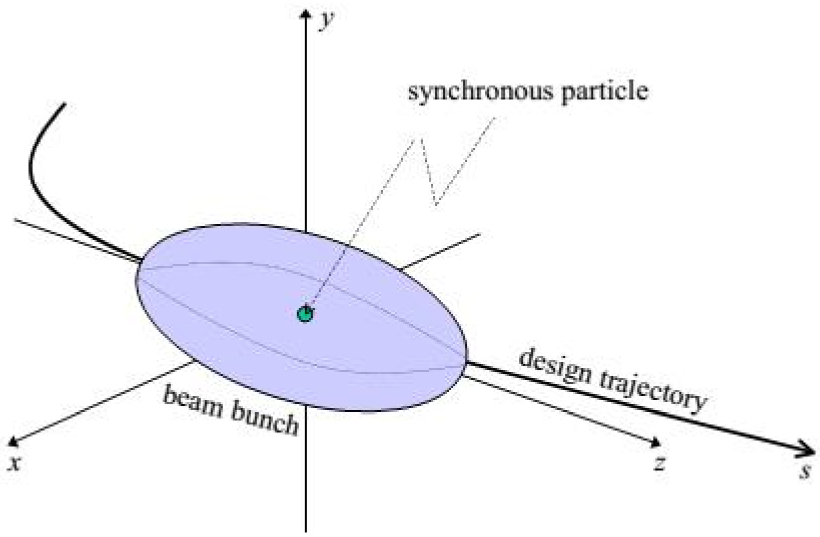

Fig. 2.5 Design trajectory and co-ordinate system [41].

The phase space (or state space) of the particle is defined by considering the momenta (x',y',z') normalized with respect to the synchronous particle. Let $p(s)=\gamma mv(s)$ represent the mechanical momentum magnitude of the synchronous particle. Then the x and y plane relative momentum x' and y' are given by

$$x' \equiv \frac{dx}{ds} = \frac{p_x}{p} = \frac{\gamma m\dot{x}}{\gamma m\dot{s}} \tag{2.11}$$

$$y' \equiv \frac{dy}{ds} = \frac{p_y}{p} = \frac{\gamma m\dot{y}}{\gamma m\dot{s}} \tag{2.22}$$

For the z plane the situation is different since the coordinate z is defined to be the difference in longitudinal position from the synchronous particle, which is travelling at velocity v. Therefore,

$$z' \equiv \frac{dz}{ds} = \lim_{\Delta t\to 0}\frac{\Delta z}{\Delta s} = \lim_{\Delta t\to 0}\frac{\Delta t\Delta v}{\Delta t v} = \frac{\Delta v}{v} \tag{2.23}$$

Where Δv is the difference in velocity v of the synchronous particle, $\Delta\beta$ is the difference in normalized velocity, Δp is the difference in longitudinal momentum p of the synchronous particle, and the last equality comes from relativistic mechanics.

The complete set of phase space coordinates for a particle, including both position and normalized momentum, at location sis given by ($x,x',y,y',z,z';s$). This coordinate space, specifically with the normalized momenta x', y', and z', is also commonly called trace space.

2.5. EQUATION OF MOTION

The force on a point charge q in an electromagnetic field, called the Lorentz force is given by

$$\boldsymbol{F} = q(\boldsymbol{E} + (\boldsymbol{v} \times \boldsymbol{B})) \tag{2.24}$$

This equation is valid for static as well as time-dependent fields. The field vectors **E** and **B** obey Maxwell's equations, which can be written for charged particle motion in vacuum as

$$\nabla.\boldsymbol{E} = \frac{\rho}{\epsilon_0}, .\boldsymbol{B} = 0, \nabla \times \boldsymbol{E} = -\frac{\partial \boldsymbol{B}}{\partial t}, \nabla \times \boldsymbol{B} = \mu_0 \boldsymbol{J} + \frac{1}{c^2}\frac{\partial \boldsymbol{E}}{\partial t} \tag{2.25}$$

Where c is the speed of light. $\in_0$ and μ_0 are the permittivity and permeability of free space respectively.

The current density **J** and the space charge density ρ satisfy the continuity equation

$$\nabla.\boldsymbol{J} + \frac{\partial \rho}{\partial t} = 0 \tag{2.26}$$

The motion of a particle due to the Lorentz force of Equation (2.24) is determined by Newton's equation

$$\frac{d\boldsymbol{P}}{dt} = \boldsymbol{F} = q(\boldsymbol{E} + (\boldsymbol{v} \times \boldsymbol{B})) \tag{2.27}$$

Where **P** is the mechanical momentum and for relativistic mechanics $= \frac{mv}{\sqrt{1-\frac{v^2}{c^2}}}$.

We can write $= \gamma m\boldsymbol{v}$, where $\gamma = \frac{1}{\sqrt{1-\beta^2}}$ is the Lorentz factor and $\beta = v/c$ is the ratio of the particle velocity v to speed of light in vacuum c.

Substitution of the expression in equation of motion gives the relativistic equation of motion as [28]

$$\gamma m\frac{dv}{dt} + m\boldsymbol{v}\frac{d\gamma}{dt} = \boldsymbol{F} = q(\boldsymbol{E} + (\boldsymbol{v} \times \boldsymbol{B})) \tag{2.28}$$

Solving for the acceleration $= d\boldsymbol{v}/dt$, we can equation (2.28) in the form

$$\boldsymbol{a} = \frac{\boldsymbol{F} - (\boldsymbol{F}.\boldsymbol{\beta})\boldsymbol{\beta}}{m} \tag{2.29}$$

The main task of charged particle dynamics is to determine the particle motion by solving Newton's equation for a given configuration of fields **E** and **B**. A special difficulty arises in high-intensity beams, where the fields depend also on the particles' electric and magnetic self fields, which in turn depend on the particles' motion.

Equation (2.28) is a vector equation that consists of a set of three second-order coupled differential equations. In cartesian coordinates these equations are of the form

$$\frac{d}{dt}(\gamma m\dot{x}) = \dot{\gamma}\, m\dot{x} + \gamma m\ddot{x} = q\left(E_x + \dot{y}B_z - \dot{z}B_y\right)$$

$$\frac{d}{dt}(\gamma m\dot{y}) = \dot{\gamma}\, m\dot{y} + \gamma m\ddot{y} = q\left(E_y + \dot{z}B_x - \dot{x}B_z\right) \tag{2.30}$$

$$\frac{d}{dt}(\gamma m\dot{z}) = \dot{\gamma}\, m\dot{z} + \gamma m\ddot{z} = q\left(E_z + \dot{x}B_y - \dot{y}B_x\right)$$

In cylindrical coordinates$(r, \theta\ , z)$, the velocity vector is given by $= \left(\dot{r}, r\dot{\theta}, \dot{z}\right)$, and the equations of motion take the form

$$\frac{d}{dt}(\gamma m\dot{r}) - \gamma m r\dot{\theta}^2 = q\left(E_r + r\dot{\theta}B_z - \dot{z}B_\theta\right)$$

$$\frac{1}{r}\frac{d}{dt}\left(\gamma m r^2\dot{\theta}\right) = q(E_\theta + \dot{z}B_r - \dot{r}B_z) \tag{2.31}$$

$$\frac{d}{dt}(\gamma m\dot{z}) = q\left(E_z + \dot{r}B_\theta - r\dot{\theta}B_r\right)$$

2.6. BEAM EMITTANCE

In practice, the velocity spread of the beam from a given source may be considerably greater than the ideal thermal limit since many factors, such as temperature fluctuations in a plasma source, nonlinear forces (aberrations) due to the external or space-charge fields, and instabilities lead to a deterioration of the beam quality. The emittance provides a quantitative basis, or a figure of merit, for describing the quality of the beam [42]. It is closely related to two-dimensional projections of the volume occupied by the ensemble of particles in six-dimensional phase space as defined by the set of canonical coordinates (q_i, p_i).

Most beams of practical interest have two planes of symmetry or are circularly symmetric. For the following discussion, assume that the beam propagates in the z-direction and has two planes of symmetry (x–z and y–z). The motion of each individual particle is defined by the three space coordinates(x, y, z) and the three mechanical momentum coordinates (Px,Py,Pz) at any given instant of time. An ensemble of particles forms a beam if their momentum component in the longitudinal direction is much larger than the momentum component in the transverse directions (i.e., in our case of cartesian coordinates if $P_x << P_z$, $P_y << P_z$). If the length of the beam is much greater than the diameter, we can treat the distribution as a continuous beam. On the other hand, if the length is comparable to the diameter, we deal with bunched beams.

We consider a particle in the *x–z* plane with total momentum $P = \left(P_x{}^2 + P_z{}^2\right)^{1/2}$, where $P_x \leq P_z \approx P$. The slope of the trajectory is by definition $x' \ = dx/dz = \dot{x}/\dot{z} \approx P_x/P$. At any given distance z along the direction of beam propagation, every particle represents a point in *x–x'* space, known as trace space. The area occupied by the points that represent all particles in the beam $A_x = \int dxdx'$ is related to the emittance of the beam. However, the definition that the trace space area as emittance does not distinguish between a well-behaved beam in a linear focusing system and a beam with the same trace-space area but a distorted shape due to nonlinear forces [28].

We prefer, therefore, a definition of emittance that measures the beam quality rather than the trace-space area. A measure of the beam quality is the product of the beam's width and divergence, where the divergence relates to the random (or thermal) velocity spread. To be mathematically more precise, we will use the moments of the particle distribution in *x–x'* trace space, $\overline{x^2}, \overline{x'^2}, \overline{xx'}^2$ to define an rms emittance $\widetilde{\epsilon_x}$ by

$$\widetilde{\epsilon_x} = \left(\overline{x^2}\,\overline{x'^2} - \overline{xx'}^2\right)^{1/2} \tag{2.32}$$

The term $\overline{xx'}^2$ reflects a correlation between *x* and *x'* which occurs, for instance, when the beam is either converging (e.g., after passing through a lens) or diverging (e.g., after passing through a waist); it is zero at the waist of an ideal uniform beam. The rms emittance provides the desired quantitative information on the quality of the beam. For the ideal uniform beams with linear focusing forces we call x the width, x' the divergence, and $\widetilde{\epsilon_x}$ the emittance of the beam. The units of measurement for emittance are m-rad. However, since the typical widths and divergence angles of beams are in the range of mm (or cm) and milli radians, respectively, it is customary to use units of mm-mrad or cm-mrad. Also, the normalized longitudinal emittance is often given in units of "electronvolt-seconds".

Moreover, if there is no acceleration or deceleration ($\beta\gamma$=const), the area A_x in x–x' trace space is also conserved. However, if there is an energy change (i.e. $\beta\gamma \neq$ const), A_x and, the emittance $\widetilde{\epsilon_x}$, do not remain constant, the change being inversely proportional to $\beta\gamma$ according to Liouville's theorem . For this reason, we introduce the normalized rms emittance

$$\widetilde{\epsilon_n} = \beta\gamma\tilde{\epsilon} \tag{2.33}$$

For beams in particle accelerators, the normalized emittance is a more useful quantity than the unnormalized emittance since in an ideal system (linear forces, no coupling) it remains constant. An increase of the normalized emittance is usually an indication that nonlinear effects causing a deterioration of beam quality are present in the system.

2.7. SPACE CHARGE EFFECT ON BEAM

The Coulomb effects in linacs are usually most important in non-relativistic beams at low velocities, because at low velocities the beam density is larger, and for relativistic beams the self-magnetic forces increase and produce a partial cancellation of the electric Coulomb forces. The net effect of the Coulomb interactions in a multiparticle system can be separated into two contributions. First is the space-charge field, the result of combining the fields from all the particles to produce a smoothed field distribution, which varies appreciably only over distances that are large compared with the average separation of the particles. Second are the contributions arising from the particulate nature of the beam, which includes the short-range fields describing binary, small impact-parameter Coulomb collisions. Typically, the number of particles in a linac bunch exceeds 10^8, and the effects of the collisions are very small compared with the effects of the averaged space-charge field [43].

The disadvantage of the space-charge fields is not only that they reduce the effective focusing strength, but also the nonlinear terms, a consequence of the deviations from charge-density uniformity, cause growth of the rms emittances, which degrades the intrinsic beam quality. One consequence of space-charge-induced emittance growth is the formation of a low-density beam halo surrounding the core of the beam, which can be the cause of beam loss, resulting in radioactivation of the accelerating structure

To describe the space-charge field, we need to understand the properties of an evolving particle distribution, which requires a self-consistent solution for the particles and the associated fields. This is a problem, which has been formulated in terms of the coupled Vlasov–Maxwell equations, for which there are no generally successful analytic solutions in a linac, and computer simulation is the most reliable tool. Even the most advanced computer codes can use only a relatively small number of macroparticles to represent the actual particle distribution in a beam and to thereby “simulate” the effects of the mutual interaction between the particles. Such codes, tracing thousands of macroparticles, have become indispensable tools for the study of beam physics and for the design of charged-particle beam devices in which self-field effects are important.

In most practical beams, however, the collisional force is a relatively small effect, and the mutual interaction between particles can be described largely by a smoothed force in which the "graininess" of the distribution of discrete particles is washed out. The space-charge potential function in this case obeys Poisson's equation, and the resulting force can be treated in the same way as the applied focusing or acceleration forces acting on the beam. A measure for the relative importance of collisional versus smoothed interaction, or single-particle versus collective effects, is the Debye length, λ_D, a fundamental parameter in plasma physics that can also be applied to charged particle beams. Debye length in a relativistic beam is

$$\lambda_D = \frac{\widetilde{v_x}}{\omega_p} = \left(\frac{\epsilon_0 m \gamma^3 \widetilde{v_x}^2}{q^2 n}\right)^{1/2} \tag{2.34}$$

Where $\widetilde{v_x}$ is the rms random velocity and ω_p is the plasma frequency.

If the Debye length is large compared with the beam radius (λ_D>>a), the screening will be ineffective and single-particle behaviour will dominate. On the other hand, if the Debye length is small compared to the beam radius (λ_D<<a), collective effects due to the self fields of the beam will play an important role.

When self-field effects dominate the beam physics (i.e., when λ_D<<a), it is convenient for the mathematical analysis to neglect the thermal velocity spread altogether and use a laminar-flow model for the beam. In laminar flow, all particles at a given point are assumed to have the same velocity, so that particle trajectories do not cross. With collisions neglected, Liouville's theorem that expresses continuity of particles in phase space, is

$$\frac{df}{dt} = \frac{\partial f}{\partial t} + \dot{x}.\frac{\partial f}{\partial x} + \dot{\boldsymbol{p}}.\frac{\partial f}{\partial \boldsymbol{p}} = 0 \tag{2.35}$$

Where $f(\boldsymbol{x}, \boldsymbol{p}, t)$ is the particle density in phase space.

Expressing $\dot{\boldsymbol{p}}$ in terms of the sum of the external fields plus the smoothed self fields yields the Vlasov equation, [43] also known as the kinetic equation, or the collisionless Boltzmann equation

$$\frac{\partial f}{\partial t} + \frac{\boldsymbol{p}}{\gamma m}.\frac{\partial f}{\partial \boldsymbol{x}} + q\left(\boldsymbol{E} + \frac{(\boldsymbol{p}\times\boldsymbol{B})}{\gamma m}\right).\frac{\partial f}{\partial \boldsymbol{p}} = 0 \tag{2.36}$$

The Vlasov equation and Maxwell's equations form a set of closed equations, which determine the self-consistent dynamics of a distribution of charges satisfying Liouville's theorem.

2.8. NUMERICAL SPACE CHARGE CALCULATION

Beam-dynamics codes used for simulation of intense linac beams normally include a subroutine for calculating the space-charge forces. In principle the effects of space-charge can be calculated by adding the Coulomb forces between all the particles. However, to represent bunches with a typical number of particles near 10^8 or more, this approach is impractical. Several methods for calculating space-charge forces have been developed [44]. The first method is based on the assumption of linear space charge forces. Linear space-charge forces allow the use of analytical and matrix methods resulting in a significant simplification, but imply a uniform density distribution, which is rarely the case for a real beam. However, it has been discovered by [45, 46] that for ellipsoidal bunches, where the rms emittance is either constant or specified in advance, the evolution of the rms beam projections is nearly independent of the density profile. This means that for calculation of the rms dynamics, the actual distribution can be replaced by an equivalent uniform beam, which has the same rms values.

2.8.1 RMS ENVELOPE EQUATION WITH SPACE CHARGE

Following the early work of [45, 46], the rms envelope equation that expresses the equation of motion of the rms beam size is given by

$$R'' + k_0^2 R - \frac{\varepsilon_r^2}{R^3} - \frac{K}{R} = 0 \tag{2.37}$$

The second term is the focusing term, and the third term is the emittance term. The emittance term is negative and is analogous to a repulsive pressure force acting on the rms beam size. The last term in the above equation is the repulsive space-charge term.

For a three-dimensional uniform ellipsoid describing a typical linac bunch, the rms envelope equations are

$$\begin{gathered} a_x'' + k_{0,x}^2 a_x - \frac{\varepsilon_{r,x}^2}{a_x^3} - \frac{3K_3(1-f)}{(a_x+a_y)a_z} = 0 \\ a_y'' + k_{0,y}^2 a_y - \frac{\varepsilon_{r,y}^2}{a_y^3} - \frac{3K_3(1-f)}{(a_x+a_y)a_z} = 0 \\ a_z'' + k_{0,z}^2 a_z - \frac{\varepsilon_{r,z}^2}{a_z^3} - \frac{3K_3 f}{a_x a_y} = 0 \end{gathered} \tag{2.38}$$

Where we have defined a three-dimensional space-charge parameter $K_3 = \frac{qI\lambda}{20\sqrt{5}\pi\varepsilon_0 mc^3\gamma^3\beta^2}$, $I = qNc/\lambda$ is the average current over an rf period, N is the number of particles per bunch, λ is the RF wavelength. The quantity f is an ellipsoid form factor and is a function of the parameter $= \gamma r_z/\sqrt{r_x r_y}$. The semi axes r_i are related to the rms beam sizes a_i by

$$r_i = \sqrt{5} a_i\,, \; i = x, y, z \tag{2.39}$$

2.8.2 EMITTANCE GROWTH FROM SPACE CHARGE

Beams that are in equilibrium in the focusing channel of a linac experience no emittance growth. Unfortunately, beams observed in linac numerical simulations are rarely in equilibrium, and when they appear to be near equilibrium, any changes that occur in the focusing system produce changes in the beam, usually accompanied by emittance growth. Nonlinear forces that act on a nonequilibrium beam will cause the rms emittance to increase. Four different space-charge mechanisms [47] are responsible for emittance growth. First, when a high current, rms-matched beam is injected into the accelerator, the emittance can grow very rapidly as the charges redistribute to provide shielding of the external focusing field. This mechanism, called charge redistribution, is the fastest known emittance-growth mechanism, producing growth in only one quarter plasma period. Second, if the injected beam is not rms matched, additional energy from the mismatch oscillations of the beam is available for emittance growth. Even for relatively small mismatches, this mechanism can become the largest contributor to emittance growth. Third, for non-symmetric or anisotropic beams, there can be emittance transfer as a result of space-charge resonances that couple longitudinal and transverse oscillations, where in some cases the kinetic energies in the three planes may approach an approximate equalization, sometimes referred to as equipartitioning. In such cases, the emittance grows in a plane that receives energy, and decreases in a plane that looses energy. Finally, the periodic focusing structure can resonantly excite density oscillations in the beam, the most serious of which is the envelope instability.

2.9. LONGITUDINAL PARTICLE DYNAMICS IN RF LINAC

The Longitudinal dynamics is provided by an appropriate choice of the phase of the synchronous particle relative to the crest of the accelerating wave. A longitudinal restoring force exists when the synchronous phase is chosen corresponding to a field that is rising in time, as shown in Fig. 2.6. The early particles experience a smaller field and the late particles a larger field than the synchronous particle. The accelerated particles are formed in stable bunches that are near the synchronous particle. Those particles outside the stable region slip behind in phase and do not experience any net acceleration.

We consider an array of accelerating cells (Fig. 2.7), containing drift tubes and accelerating gaps, designed at the *n*th cell for a particle with synchronous phase ϕ_{sn} , synchronous energy W_{sn}, and synchronous velocity β_{sn}.We express the phase, energy, and velocity of an arbitrary particle in the nth cell as ϕ_n, W_n and β_n. The particle phase in the nth cell is defined as the phase of the field when the particle is at the centre of the nth gap, and the particle energy for the nth cell is the value at the end of the nth cell at the centre of the drift tube.

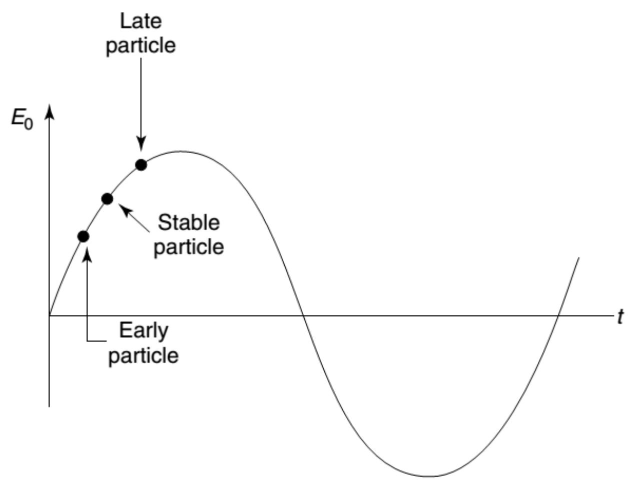

Fig. 2.6 Stable Phase Oscillation [10].

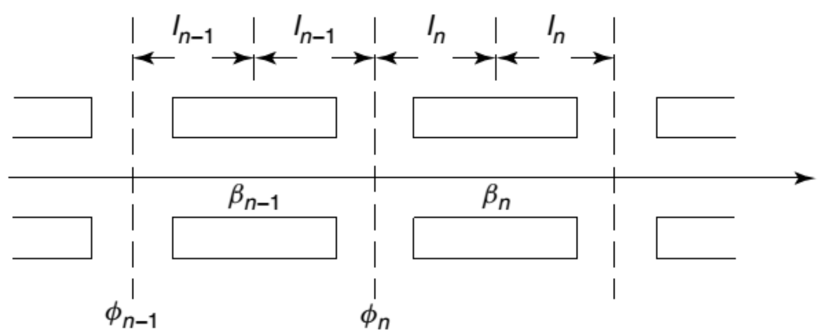

Fig. 2.7 The Longitudinal Motion in Accelerating cells [10].

We assume that the synchronous particle always arrives at each succeeding gap at the correct phase, and we consider particles with velocities that are close enough to the synchronous velocity that all particles have about the same transit-time factor. We now investigate the motion of particles with phases and energies that deviate from the synchronous values.

The RF phase changes as the particle advances from gap n−1 to gap n according to the expression [10]

$$\phi_n = \phi_{n-1} + \omega \frac{2l_{n-1}}{\beta_{n-1}c} + \begin{cases} \pi \ for \ \pi \ mode \\ 0 \ for \ 0 \ mode \end{cases} \tag{2.40}$$

where the half-cell length is $l_{n-1} = N\beta_{s,n-1} {}^{\lambda}/_{2}$ with $N = \begin{cases} \frac{1}{2} \ for \ \pi \ mode \\ 1 \ for \ 0 \ mode \end{cases}$

The phase change during the time an arbitrary particle travels from gap n–1 to gap n relative to that of the synchronous particle is

$$\Delta(\phi - \phi_s)_n = -2\pi N \frac{(W_{n-1} - W_{s,n-1})}{mc^2\gamma_{s,n-1}^3\beta_{s,n-1}^2} \tag{2.41}$$

The difference equation for the energy change of a particle relative to that of the synchronous particle is

$$\Delta(W - W_s)_n = qE_0T\left(\cos\phi_n - \cos\phi_{s,n}\right) \tag{2.42}$$

Equations (2.41) and (2.42) form two coupled difference equations for relative phase and energy change of a standing wave linac that can be solved numerically for the motion of any particle.

To study the stability of the motion, we convert the difference equations to differential equations and replace the discrete standing-wave fields by a continuous field. Then the coupled difference equations, Equations (2.41) and (2.42) become the coupled differential equations

$$\gamma_s^3\beta_s^3\frac{d(\phi-\phi_s)}{ds} = -2\pi\frac{(W-W_s)}{mc^2\lambda} \tag{2.43}$$

$$\frac{d(W-W_s)}{ds} = qE_0T(\cos\phi - \cos\phi_s) \tag{2.44}$$

Combining these two equations, we get a nonlinear second-order differential equation for the phase motion as

$$\gamma_s^3\beta_s^3\frac{d^2(\phi-\phi_s)}{ds^2} + 3\gamma_s^2\beta_s^2\left[\frac{d\beta_s\gamma_s}{ds}\right]\left[\frac{d(\phi-\phi_s)}{ds}\right] + 2\pi\frac{qE_0T}{mc^2\lambda}(\cos\phi - \cos\phi_s) = 0 \tag{2.45}$$

Because phase is proportional to time, the more negative the phase, the earlier the particle arrival time relative to the crest of the wave. The phase difference $(\phi - \phi_s)$ between a particle and the synchronous particle is proportional to a spatial separation

$$z - z_s = -\frac{\beta_s}{2\lambda}(\phi - \phi_s) \tag{2.46}$$

We assume that the acceleration rate is small, and that E_0T, ϕ_s and β_s are constant

In case of an electron linac, after beam injection into electron linacs, the velocities approach the speed of light so rapidly that hardly any phase oscillations take place. The electrons initially slip relative to the wave and rapidly approach a final phase that is maintained all the way to high energy. The final energy of each electron with a fixed phase depends on the accelerating field and on the value of the phase.

We introduce the following notation $w \equiv \delta\gamma = \frac{W-W_s}{mc^2}$, $A \equiv \frac{2\pi}{\gamma_s^3\beta_s^3\lambda}$, $B \equiv \frac{qE_0T}{mc^2}$, such that

$$w' \equiv \frac{dw}{ds} = B(\cos\phi - \cos\phi_s) \tag{2.47}$$

$$\phi' \equiv \frac{d\phi}{ds} = -Aw \tag{2.48}$$

$$\phi'' \equiv \frac{d^2\phi}{ds^2} = -AB(\cos\phi - \cos\phi_s) \tag{2.49}$$

Integrating the equation (2.49), we get

$$d\phi' = -AB(\cos\phi - \cos\phi_s)ds \tag{2.50}$$

With $= d\phi/\phi'$, and multiplying the equation (2.50) by ϕ' , and integrating we get

$$\frac{Aw^2}{2} + B(\sin\phi - \phi\cos\phi_s) = H_\phi \tag{2.51}$$

Where H_ϕ is the Hamiltonian. The first term of Eq. (2.51) is a kinetic energy term, and the second is the potential energy. The potential energy is

$$V_\phi = B(\sin\phi - \phi\cos\phi_s) \tag{2.52}$$

The constant H_ϕ depends on the initial conditions $(\Delta w_i, \phi_i)$ and is readily evaluated for any given set of the parameters β_s , γ_s , λ, E_0, ϕ_s , and q/m.

For each value of H_ϕ , Equation (2.52) gives a possible trajectory in the $\Delta W - \phi$ phase plane [28]. Several such trajectories are shown in Fig. 2.8.

With the choice of the synchronous phase $\phi_s < 0$ in the figure we see that the particle motion is stable provided that the initial conditions are within the so-called separatrix. Separatrix is the limiting stable trajectory that passes through the unstable fixed point at $\Delta W = 0$ and $\phi = -\phi_s$. Inside the separatrix, particles move on closed curves in a counter-clockwise direction, as illustrated in the Fig. 2.8.

Particles whose initial phase and/or energy values are outside the separatrix will not be trapped and accelerated by the wave. They move on unstable trajectories similar to the one shown in Fig. 2.8. Thus the separatrix, also known in the literature as the rf bucket, separates the stable from the unstable trajectories. As shown in Fig. 2.8, the separatrix intersects the positive side of the ϕ-axis at the point $\phi_{max} = -\phi_s$, where $\phi_s < 0$ represents the synchronous phase.

Setting $= -\phi_s$, $\Delta W = 0$ in Equation (2.51) yields the value

$$H_\phi = B(\sin(-\phi_s) - (-\phi_s)\cos(-\phi_s))$$

Or

$$H_\phi = -B(\sin\phi_s - \phi_s\cos\phi_s) \tag{2.53}$$

that defines the trajectory for the separatrix.

We find that points on the separatrix must satisfy

$$\frac{Aw^2}{2} + B(\sin\phi - \phi\cos\phi_s) = -B(\sin\phi_s - \phi_s\cos\phi_s) \tag{2.54}$$

The separatrix defines the area within which the trajectories are stable, and it can be plotted if the constants A and B are given. In common accelerator jargon, the separatrix is also called the fish, and the stable area within is called the bucket. There are two separatrix solutions for w=0, which determine the maximum phase width of the separatrix. One solution is $\phi_1 = -\phi_s$ which is a positive number for stable motion because ϕ_s is negative, and this point gives the maximum phase for stable motion.

The point at $\phi = \phi_2$ and $w = 0$ is the other solution that gives the minimum phase for stable motion. The equation for the separatrix for this case becomes

$$(\sin\phi_2 - \phi_2\cos\phi_s) = (\phi_s\cos\phi_s - \sin\phi_s) \tag{2.55}$$

and this can be solved numerically for $\phi_2(\phi_s)$.

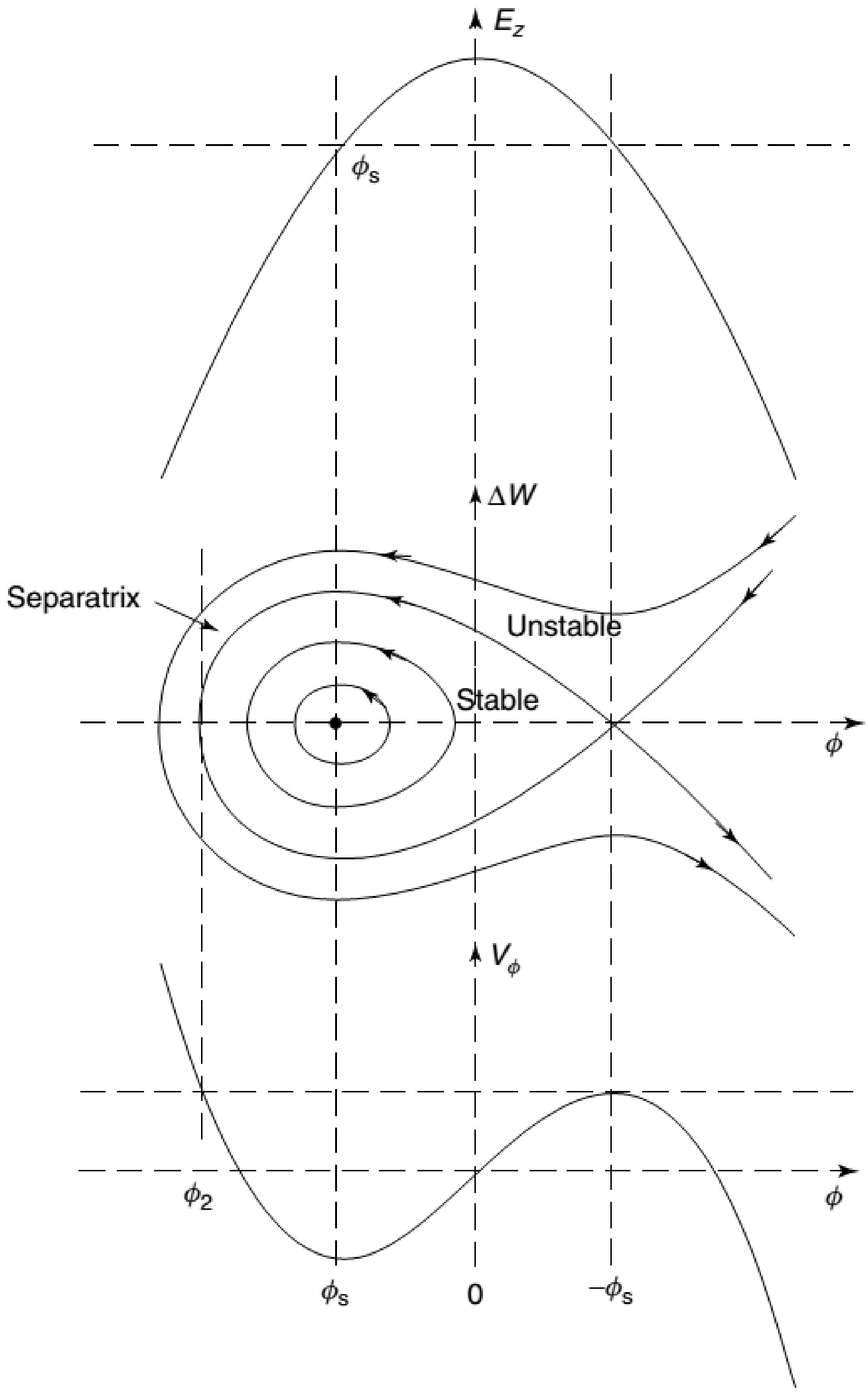

Fig. 2.8 At the top, the accelerating field is shown as a cosine function of the phase. The middle plot shows longitudinal phase-space trajectories, including the separatrix. The longitudinal potential well has its minimum as shown in the bottom plot [10].

The total phase width of the separatrix is

$$\Psi = |\phi_s| + |\phi_2| = -\phi_s - \phi_2 \tag{2.56}$$

Then $\sin\phi_2 = -\sin(\phi_s + \Psi) = -(sin\phi_s cos\Psi + sin\Psi cos\phi_s)$ (2.57)

Substituting equation (2.57) into equation (2.55), we get

$$tan\phi_s = \frac{sin\Psi - \Psi}{1 - cos\Psi} \tag{2.58}$$

When $\Psi \ll 1$ and $\phi_s \ll 1$, $sin\Psi = \Psi - \Psi^3/6 + \cdots$, $\cos\Psi = 1 - \Psi^2/2 + \cdots$, we get

$tan\phi_s \cong -\frac{\Psi}{3}$, which is a good approximation even up to $\phi_s \approx 1$.

With $\phi_s = \phi_s$, we have $\Psi = 3|\phi_s|$, $\phi_2 = 2\phi_s$. At $\phi_s = -90°$, the phase acceptance is maximum, extending over the full 360° and there is no acceleration as shown in Fig. 2.9.

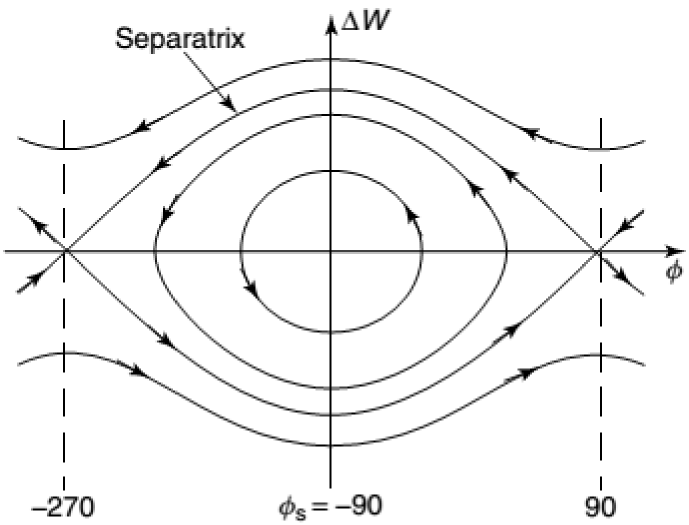

Fig. 2.9 Separatrix for $\phi_s = -90°$ [10].

2.10. TRANSVERSE PARTICLE DYNAMICS

2.10.1 TRANSVERSE RF FOCUSSING AND DEFOCUSSING

As can be seen from the electric-field lines in Fig. 2.10, when off-axis particles enter a gap and are accelerated by a longitudinal RF electric field, they also experience radial RF electric and magnetic forces. At first it might be thought that the oppositely directed radial electric forces in the two halves of the gap will produce a cancellation in the total radial momentum impulse. On closer examination, it is found that generally there will be a net radial impulse, which occurs as a result of three possible mechanisms:

(1) the fields vary in time as the particle cross the gap;

(2) the fields also depend on the radial particle displacement, which varies across the gap;

(3) the particle velocity increases, while the particle crosses the gap, so that the particle does not spend equal times in each half of the gap.

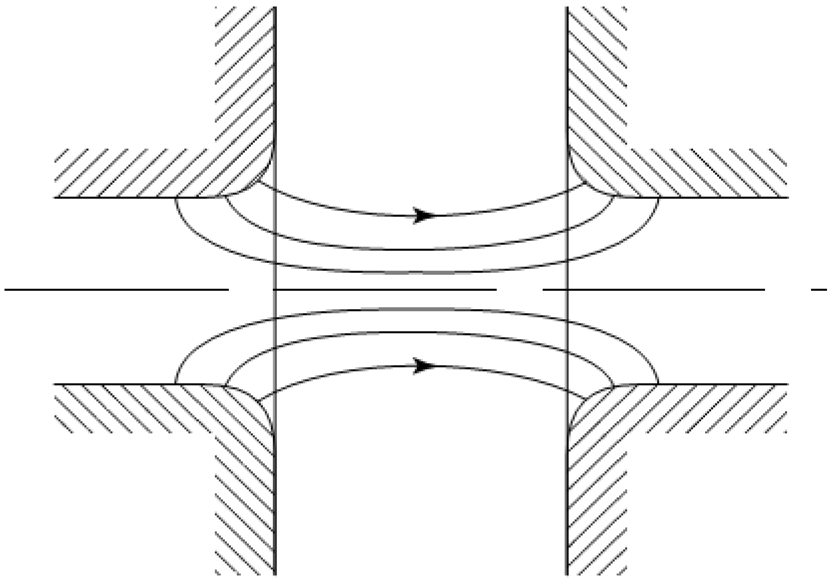

Fig. 2.10 Electric Field Lines in an RF Gap [10].

For longitudinal stability we have seen that ϕ_s must be negative; which means the field is rising when the synchronous particle is injected. This means that most particles experience a field in the second half of the gap that is higher than the field in the first half, resulting in a net defocusing force. This corresponds to mechanism (1), and for ion linacs this is the dominant effect, known as the RF-defocusing force. Mechanisms (2) and (3) are relatively more important in electron linacs than in most proton linacs.

As a consequence of Earnshaw's theorem and Laplace equation, if the longitudinal forces provide focusing at a given point, the two transverse-force components cannot both be focusing at the same point.

2.10.2 RADIAL IMPULSE NEAR THE AXIS IN AN ACCELERATING GAP

Assuming that for the mode of interest E_z, E_r, B_θ are the only nonzero field components, the nonzero components of Maxwell's equations are

$$\begin{aligned}
&\frac{1}{r}\frac{\partial(rE_r)}{\partial r}+\frac{\partial E_z}{\partial z}=0 && \text{from}\quad (\nabla.\boldsymbol{E}=0)\\
&\frac{\partial E_r}{\partial z}-\frac{\partial E_z}{\partial r}=-\frac{\partial B_\theta}{\partial t} && \text{from}\ \ (\nabla\times\boldsymbol{E})_\theta=-\frac{\partial B_\theta}{\partial t}\\
&-\frac{\partial B_\theta}{\partial z}=\frac{1}{c^2}\frac{\partial E_r}{\partial t} && \text{from}\ \ (\nabla\times\boldsymbol{B})_r=\frac{1}{c^2}\frac{\partial E_r}{\partial t}\\
&\frac{1}{r}\frac{\partial(rB_\theta)}{\partial r}=\frac{1}{c^2}\frac{\partial E_z}{\partial t} && \text{from}\ \ (\nabla\times\boldsymbol{B})_z=\frac{1}{c^2}\frac{\partial E_z}{\partial t}
\end{aligned}\tag{2.59}$$

We assume that near the axis, E_z is approximately independent of r, then

$$E_r=-\frac{r}{2}E_z \tag{2.60}$$

$$B_\theta=\frac{r}{2c^2}\frac{\partial E_z}{\partial t} \tag{2.61}$$

We assume that the standing-wave electric-field solution for E_z near the axis looks like

$$E_z(r,z,t)=E_a(z)\cos(\omega t+\phi) \tag{2.62}$$

If we look at the shape of the amplitude $E_a(z)$ in a typical accelerating gap, shown in Fig. 2.11, we see that when E_a is increasing with respect to *z* at the beginning of the gap, E_r is negative, which implies radial focusing. When E_a is decreasing with respect to *z* at the end of the gap, E_r is positive, which implies radial defocusing. These results are in accordance with Eq. (2.60).

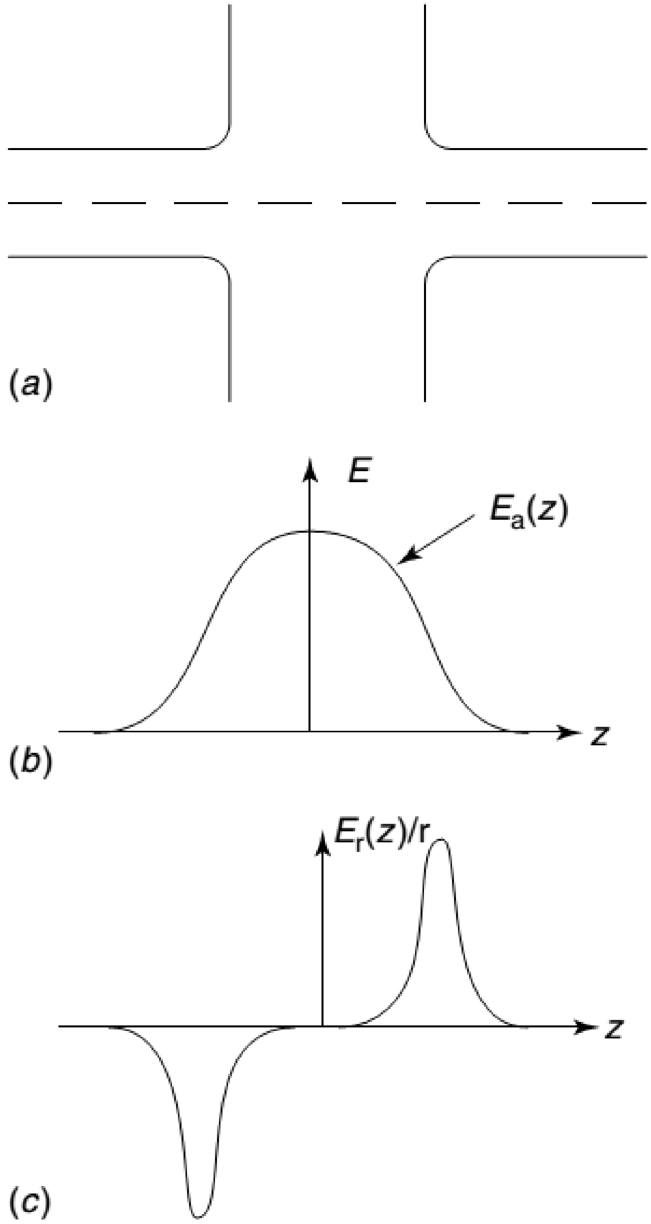

Fig. 2.11 Longitudinal and radial electric fields in an RF gap [10].

If the field is rising in time, as is necessary for longitudinal focusing, the defocusing field experienced by a particle at the exit will be larger than the focusing field at the entrance. But, especially for very low velocities when there are large velocity changes in the gap, the particle spends less time in the exit half of the gap than in the entrance half. This can give rise to a net focusing impulse, which is called electrostatic focusing, because it is the same focusing mechanism that is the basis for electrostatic lenses.

2.10.3 COURANT SNYDER PARAMETERS AND HILL'S EQUATION

The motion of a charged particle in the transverse planes, *x(s)* and *y(s)*, can to a good approximation be considered as decoupled, so that one can write separate equations for each plane. The motion in the horizontal plane is described by the equation [48, 49]

$$\frac{1}{\gamma(s)}\frac{d}{ds}\left(\gamma(s)\frac{dx}{ds}\right) + K_x(s)x(s) = \frac{1}{\rho(s)}\frac{\Delta p(s)}{p(s)} \tag{2.63}$$

where x is the horizontal offset of the particle from the design trajectory at the longitudinal position s, $\gamma = {E}/{m_0c^2}$ is the relativistic factor , $\rho(s)$ the bending radius at the location s. p is the particle design momentum and Δp is the momentum deviation. $K_x(s)$ is a function describing the focusing strength of the magnets at the position s.

A similar equation can be written for the vertical offset, y. In the following we will denote by x the transverse particle offset, which can be either horizontal or vertical, unless otherwise specified. In the absence of acceleration, the γ factors cancel. In a linear accelerator, when not taking into account alignment errors and steering magnets, $\rho = \infty$ and the right-hand part of the equation vanishes.

From equation (2.63) the particle position and slope, x and x', can be obtained as a linear transformation from the initial values, x_0 and x_0' . Transfer matrices can be used to track the motion through various sections of the accelerator:

$$\begin{pmatrix} x \\ x' \end{pmatrix}_{s_2} = \boldsymbol{M}_{12}\begin{pmatrix} x \\ x' \end{pmatrix}_{s_1} \tag{2.64}$$

where $\boldsymbol{M}_{12}$ is the transfer matrix in the x plane from position s_1 to position s_2 in the accelerator . A matrix can be written for each component of the accelerator, so that $\boldsymbol{M}_{12}$ is itself a product of matrices. The transfer matrices for common accelerator components can be found, for example, in [49].

The solution of the equation of motion (2.63) can be written in terms of the Twiss parameters, $\tilde{\alpha}$, $\tilde{\beta}$ and a phase function μ:

$$x(s) = \sqrt{\in \tilde{\beta}(s)} \cos(\mu(s) - \mu_0) \quad (2.65)$$

$$x'(s) = -\sqrt{\frac{\in}{\tilde{\beta}(s)}} [\tilde{\alpha}(s) \cos(\mu(s) - \mu_0) + \sin(\mu(s) - \mu_0)] \quad (2.66)$$

$\tilde{\beta}(s)$ is called the beta function and the other Twiss parameters can be derived from it. $\tilde{\alpha}(s) = -\frac{1}{2} {d\tilde{\beta}(s)}/{ds}$ describes the convergence or divergence of the trajectory at the position s. $\mu(s) = \int_0^s {ds}/{\tilde{\beta}(s)}$ is the betatron phase advance and $\mu_0 = \mu(0)$. $\in$ is a constant describing the amplitude of the particle oscillations. From these equations it can be seen that particles execute betatron oscillations around the ideal trajectory. From the trigonometric relation $sin^2(\xi) + cos^2(\xi) = 1$ for any argument ξ, one finds from equations (2.65) and (2.66), an invariant of motion, the so-called Courant-Snyder invariant:

$$\tilde{\gamma}(s)x^2(s) + 2\tilde{\alpha}(s)x(s)x'(s) + \tilde{\beta}(s)x'^2(s) = \epsilon = a\ constant \quad (2.67)$$

This equation defines the trajectory of one particle in the phase space *(x, x')* as being an ellipse. The area of this ellipse is $\pi \in$.

For a bunch having many particles one can define an emittance with the help of the second-order moments of the particle distribution [4]

$$\overline{x^2} = \frac{1}{q}\sum_i q_i(x_i - \bar{x})^2 , \overline{x'^2} = \frac{1}{q}\sum_i q_i\left(x'_i - \overline{x'}\right)^2 , \overline{xx'} = \frac{1}{q}\sum_i q_i(x_i - \bar{x})\left(x'_i - \overline{x'}\right) \quad (2.68)$$

In equation (2.68) $\bar{x}$, $\overline{x'}$ are the average position and angle of the bunch, q_i is the charge of the particle i and $q = \sum_i q_i$.

Of course, a bunch is normally made of identical particles. But to calculate the position and trajectory slopes of, for example, 10^{10} particles along a long accelerator would be impossible. Therefore it is practical to group many particles together in macro-particles or slices, often with different charges.

RMS emittance $\widetilde{\epsilon_x}$ is defined as $\widetilde{\epsilon_x} = \left(\overline{x^2}\,\overline{x'^2} - \overline{xx'}^2\right)^{1/2}$ (2.69)

The position and angles of the particles of a bunch can be represented in the transverse phase space $(x\,, x')$. The ellipse defining the emittance can be seen. The beam transverse dimension and divergence can then be derived from the parameters of the ellipse, using the emittance and beta function.

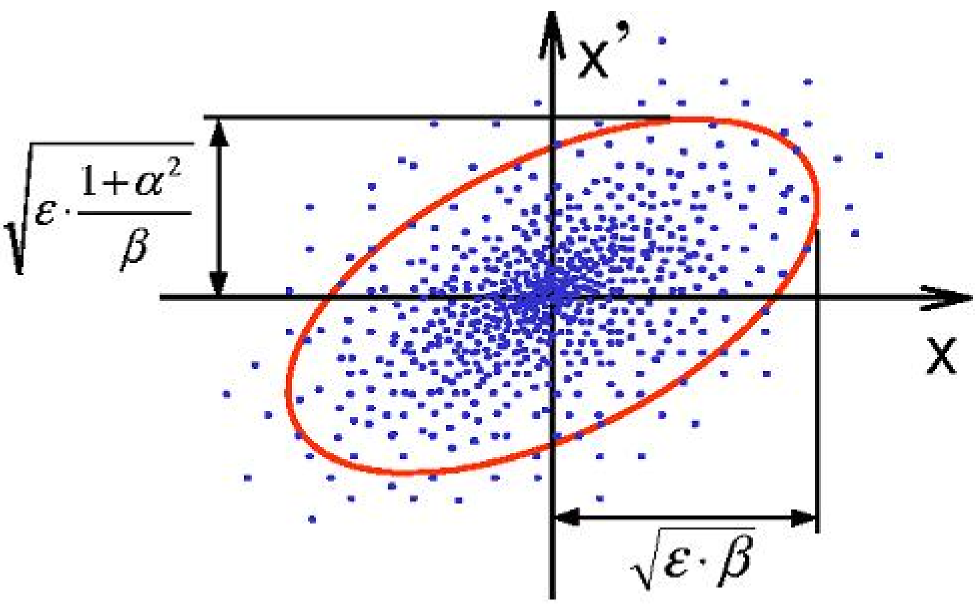

Fig. 2.12 Transverse phase space of a bunch.

The beta function at a certain point depends on the initial Twiss parameters and emittance. A lattice often used in high energy accelerators is the FODO cell. This consists of a focusing quadrupole (F), a drift space (O), a defocusing quadrupole (D) and another drift space (O).

2.11. ABERRATION IN LENSES

In practice, perfect lenses do not exist as nonlinearities in the focusing fields, and other effects cause imperfections or aberrations. These aberrations can be classified according to the source by which they are caused, as follows: (1) geometrical aberrations (spherical aberration, coma, curvatures of field, astigmatism, and distortion of the barrel, pin cushion, or rotational type); (2) chromatic aberrations(due to energy spread in the beam); (3) space-charge effects; (4) diffraction(limits resolutions of electron microscopes); and (5) imperfection[such as mechanical misalignments, fluctuations (ripple) in the voltages and currents supplying the electric and magnetic lens elements, etc.].

In an ideal lens, all particles leaving a point r_0 , θ_0 in the object plane will arrive at the same point r_i , θ_i in the image plane. When aberrations are present, this is no longer the case, and particles emerging from an object point r_0 , θ_0 with different initial angles will arrive at different points $r_i + \Delta r_i , \theta_i + \Delta\theta_i$ in the image plane. We will briefly discuss two types of aberrations that are of particular importance: the spherical aberration and the chromatic aberration.

2.11.1 SPHERICAL ABERRATION

The spherical aberration is a geometrical aberration that arises from third-order terms ($r^3, r^2 r'$, - etc) that are neglected in the paraxial ray equation. We note that r^2 terms are excluded by symmetry since the radial forces on a particle must change direction when the sign of r is changed. As an example, if one includes all terms up to third order in r and r' in the equations for solenoidal magnetic lenses, we obtain in place of the paraxial ray equation the nonlinear equation [28]

$$r'' + \kappa r + \kappa r'^2 r - \kappa\left(\frac{B'}{B}\right) r' r^2 + \left[\kappa^2 - \frac{1}{2}\kappa(B'')\right] r^3 = 0 \tag{2.70}$$

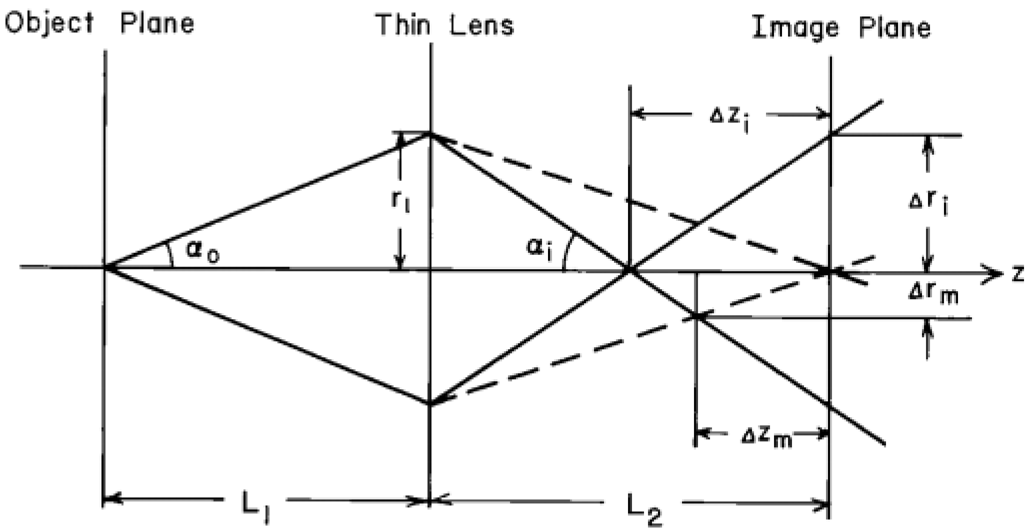

Fig. 2.13 Effect of Spherical Aberration [28].

To illustrate the effect of spherical aberrations, consider the case of a thin lens shown in Fig. 2.13. Two particle trajectories emerge from an object point on the axis with angles α_0 and $-\alpha_0$and pass through the midplane of the lens at radial distance r_1 and $-r_1$. Due to the r_1^3 term, they will experience a stronger force than in the perfect lens and as a result, they will cross the axis at angles α_i and $-\alpha_i$ before reaching the image plane of the perfect lens. For small angles α_i, the displacement Δr_i at the image plane can be defined to good approximation by the relation $\Delta r_i = C_s \alpha_i^3$

Where C_s is the spherical aberration coefficient, which depends on the initial conditions and the lens geometry. The crossing angle α_i depends on the initial angle α_0 , or the object distance L_1 . The crossover point is at a distance Δz_i upstream from the perfect image plane. If we consider the entire ensemble of trajectories within a beam, we find that the minimum radius (waist of the beam envelope), which defines what is known in the literature as the disk of least confusion, is located at a distance of $\Delta z_i < \Delta z_m$ upstream from the perfect image plane, as indicated in Fig. 2.13. If the object is at a large distance ($L_1 \gg L_2$, L_2 , $L_2 \approx f_2$), the incident rays are practically parallel to the axis. In this case, defining the spherical aberration coefficient as $C_s(\infty)$, we can show that the radius Δr_m of least confusion and the associated distance Δz_m are given by

$$\Delta r_m \approx \frac{1}{4} C_s(\infty)\alpha_i^3 \text{ , } \Delta z_m \approx \frac{3}{4} \Delta z_i = \frac{3}{4} C_s(\infty)\alpha_i^2 \tag{2.71}$$

For a unipotential or magnetic lens ($f_1 = f_2 = f$), the relation between the spherical aberration coefficient for infinite and finite object distance is found to be

$$C_s(\infty) = \frac{f}{L_2} C_s(L) \tag{2.72}$$

Where L_2 defines the location of the ideal image plane, L_1 the object distance, and f the focal length of the lens. Spherical aberrations constitute a fundamental form of lens defects that, unlike the situation in light optics, cannot be eliminated completely. This is due to the constraints imposed on the field shapes by the conditions $\nabla \times B = 0$, $\nabla \cdot E = 0$ when space charge is neglected. (Unfortunately, space-charge effects tend to make things worse rather than better.) The ratio of the spherical aberration coefficient to the focal length, C_s/f, is used as a figure of merit defining the quality of a lens.

2.11.2 CHROMATIC ABERRATIONS

Chromatic aberrations [28, 50] are due to the spread in kinetic energy that is inherent to some degree in any beam. They are different from geometrical aberrations in that they do not imply any nonlinear terms in the trajectory equations. Since the focal length f(or f_1 and f_2 for bipotential lenses) depends on the momentum, particles with different momentum or energy produce images at different distances from the lens. These images are perfect in the paraxial approximation, and the spread in the image locations, Δz_i, depends on the momentum spread ΔP in the beam. The variation of the focal length f with particle momentum responsible for this effect also produces a circle of least confusion of radius r_c. We can calculate this radius by considering a parallel beam consisting of trajectories that enter the lens with zero initial slope (i.e., $r' = 0$). Particles of momentum P will cross the axis downstream from the lens at the focal distance z_f . Those with a different momentum, say $P + \Delta P$, will be focused at a point $z_f + \Delta z_f$, where $\Delta z_f = (\partial f/\partial P)\Delta P$. If the angle of convergence for the particle with momentum P is α, then the radius of the circle of least confusion is

$$r_c = \alpha\left(\frac{\partial f}{\partial P}\right)\Delta P = \alpha f\left(\frac{P}{f}\frac{\partial f}{\partial P}\right) \tag{2.73}$$

We now define a chromatic aberration coefficient C_c for a lens by

$$\frac{C_c}{f} = \frac{1}{2}\left(\frac{P}{f}\frac{\partial f}{\partial P}\right) \tag{2.74}$$

and writes $r_c = 2\alpha C_c\frac{\Delta P}{P} = 2C_c\alpha\frac{\Delta\gamma}{\beta^2\gamma}$ (2.75)

In the nonrelativistic limit one gets $r_c = C_c\alpha\frac{\Delta V}{V}$, where V is the voltage equivalent of the kinetic energy and ΔV represents half the total energy spread in the beam. For a thin, solenoidal magnetic lens we found that the focal length fis proportional to P^2 and hence we get for the chromatic aberration coefficient the value $C_c/f = 1$.

CHAPTER 3

BEAM DYNAMICS STUDIES AND PARAMETRIC CHARACTERIZATION OF STANDING WAVE ELECTRON LINAC

The design of high energy range electron linac is subjected to a number of challenges for a The design of high energy range electron linac is subjected to a number of challenges for a high quality beam delivery to the users in application areas like material science and neutron spectroscopy. To use the linac as an experimental tool as well as to limit the radioactivity and the cost of the linac itself, it is highly important for the linac to keep the growth of transverse emittance and self field effects a minimum. A large emittance growth may result in beam losses. Possible counter measures include a machine design with a generous ratio between the bore aperture and the beam size and a shielding adapted to heavy beam losses. This approach however leads to high costs and to heavy irradiation of the accelerator components which in turn prevents hands-on maintenance. In this chapter we have studied the beam dynamics of a 30 MeV, 6 kW bi-periodic coupled cavity standing wave electron linac under development at Electron Beam Centre (EBC) Kharghar, Navi Mumbai, India. This study has been carried out to find the optimized beam parameters and the limits of the possible beam quality for different bunched beams. In order to predict the quality of electron beam [6] the electron-tracking algorithm ASTRA [14] has been used. Although there are a few self-consistent space-charge codes that can be used to study the emittance evolution, we choose the ASTRA model [5] in order to provide a fast parametric study.

3.1. MULTIPARTICLE SIMULATION WITH SPACE CHARGE

The general equation of motion for a charged particle in an electromagnetic field [28] is

$$\frac{d\vec{r}}{dt} = \frac{\vec{p}}{m_0\gamma} \tag{3.1}$$

$$\frac{d\vec{p}}{dt} = q(\vec{E} + \frac{\vec{p}}{m_0\gamma}\ x\,\vec{\mathrm{B}}) \tag{3.2}$$

We can write the general expression for steady state TM_{010} electric field components in a biperiodic standing wave linac in π/2 mode as

$$E_z = E_0 \sum_{n=1,odd}^{\infty} a_n \cos(nkz)\sin(\omega t + \phi_0) \tag{3.3}$$

$$E_r = \frac{kr}{2} E_0 \sum_{n=1,odd}^{\infty} n a_n \sin(nkz)\sin(\omega t + \phi_0) \tag{3.4}$$

$$B_\theta = c\frac{kr}{2} E_0 \sum_{n=1,odd}^{\infty} a_n \cos(nkz)\cos(\omega t + \phi_0) \tag{3.5}$$

with $k=2\pi/\lambda = \omega/c$ and a_n are the spatial harmonics that depend on the geometry of the cavity and can be computed using computer codes and measured using bead pull arrangements [51]. Due to symmetry even a_n's vanish, $a_1=1$. E_0 is the amplitude of the fundamental harmonic component of rf wave. All higher harmonic amplitudes are normalized to the fundamental amplitude [52].

For ASTRA code, the space-charge fields are calculated in the beam rest frame via Poisson's equation in free space

$$\nabla^2 V(r,\theta,z) = -\frac{\rho(r,\theta,z)}{\epsilon_0} \tag{3.6}$$

and Lorentz's transformed back into the laboratory frame. Where V the electrostatic potential, ρ the charge density, ϵ_0 the dielectric constant. ASTRA is based on Runge-Kutta integration of 4th order with fixed time step through the user defined external electric and magnetic fields, taking into account the space charge field of the particle cloud. A cylindrical grid, consisting of rings and slices, is set up over the bunch extension for the space charge calculations. The code automatically updates the mesh size as the simulation progresses. The space charge effect is a principal cause of emittance growth when the beam energy is low.

The particles are distributed quasi-randomly following the Hammersley sequence, a quasi-Monte Carlo deterministic method. In this way, statistical fluctuations are reduced and artificial correlations are avoided [14].

A uniform beam of radius R and density ρ can be represented by

$$\rho(r) = \begin{cases} \rho & if\ r \leq R \\ 0 & if\ \ r > R \end{cases} \tag{3.7}$$

For a uniformly charged cylindrical bunch of finite length L with a circular cross section of radius r, the longitudinal and the radial space charge electric field of the bunch are given by [53]

$$E_z(z, r = 0) = \frac{\rho}{2\epsilon_0\gamma}[\sqrt{R^2 + \gamma^2(L - z)^2} - \sqrt{R^2 + \gamma^2 z^2} + \gamma|z| - \gamma|z - L|] \tag{3.8}$$

$$E_r(r, z) = \frac{\beta\gamma}{4\epsilon_0} r[\frac{L-z}{\sqrt{r^2+\gamma^2(L-z)^2}} + \frac{z}{\sqrt{r^2+\gamma^2 z^2}}] \tag{3.9}$$

The outward force on the electrons in a uniform, cylindrical beam can be shown, by summing the induced magnetic force caused by the moving beam and the electrostatic force to be

$$F_{beam} = \frac{\rho e}{2\epsilon_0}\frac{r\hat{r}}{\gamma^2} \tag{3.10}$$

In all simulations presented, thermal emittance is taken into account, where thermal emittance is given by the relation

$$\epsilon_{th} = \gamma\frac{r_c}{2}\sqrt{\frac{k_B T}{m_0 c^2}} \tag{3.11}$$

For a cathode of radius 5 mm, temperature 1300 ^{0}C and 85 keV injection energy the thermal emittance has been calculated to be 0.48 π mm-mrad. This value of thermal emittance has been included in the input distribution of the macroparticles.

3.2. BEAM DYNAMICS STUDIES OF A 30 MeV LINAC

Schematic of the accelerating module is shown in Fig. 3.1. A 85 keV thermionic Triode electron gun with Pierce Focusing electrode of ID 23 mm and angle ~ 67.5^{0}, serves as the source of electron beam. The cathode of the electron gun is a LaB_6 Pellet of diameter 10 mm and thickness 1 mm. A filament power of approximately 260 W raises the temperature of the LaB_6 pellet to about 1300 ^{0}C to emit a dc current of 500 mA. The emitted electron beam from Pierce focusing gun has a size of 3.6 mm such that entrance of injector is placed at the waist of the beam envelope. The accelerating module of the accelerator contain an injection section and two accelerating sections of 22 cell and 23 cell respectively operating in π/2 mode at a frequency of 2856 MHz .The injection section consists of three bunching cells and a power feed cell. The length of each accelerating cell is 52 mm, whereas the buncher cells are 45, 48 and 50 mm respectively. The bore radius is 5mm for all the buncher cells and accelerating cell. The effective shunt impedance for the buncher cells is ~ 80 MΩ/m, while for the accelerating cells, it is ~ 90 MΩ /m. The bunching cells have been optimized for 85 keV injection. The separation gap between injection and first accelerating cavity as well as the first accelerating cavity and the second cavity is 52 mm each..

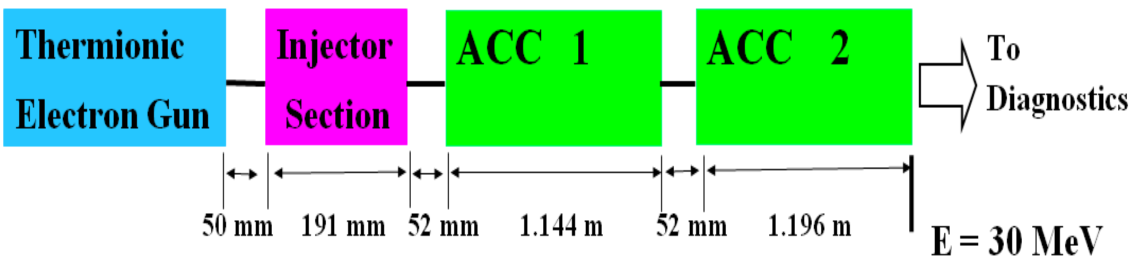

Fig. 3.1 Schematic Layout of the 30 MeV Linac Test Facility

For all the simulations presented in the following, we have used 2.5 x 10^4 macro particles in uniform distribution with input parameters corresponding to a real rms width $\sigma_{x,y}$ of 1.80 mm of the real beam and a micro bunch charge of -0.175 nC. The initial energy of the particles injected in the guide is 85 keV.

For the present work the longitudinal electric field components on the symmetry axis (r=0) have been computed using CST MWS [54] as shown in Fig. 3.2.

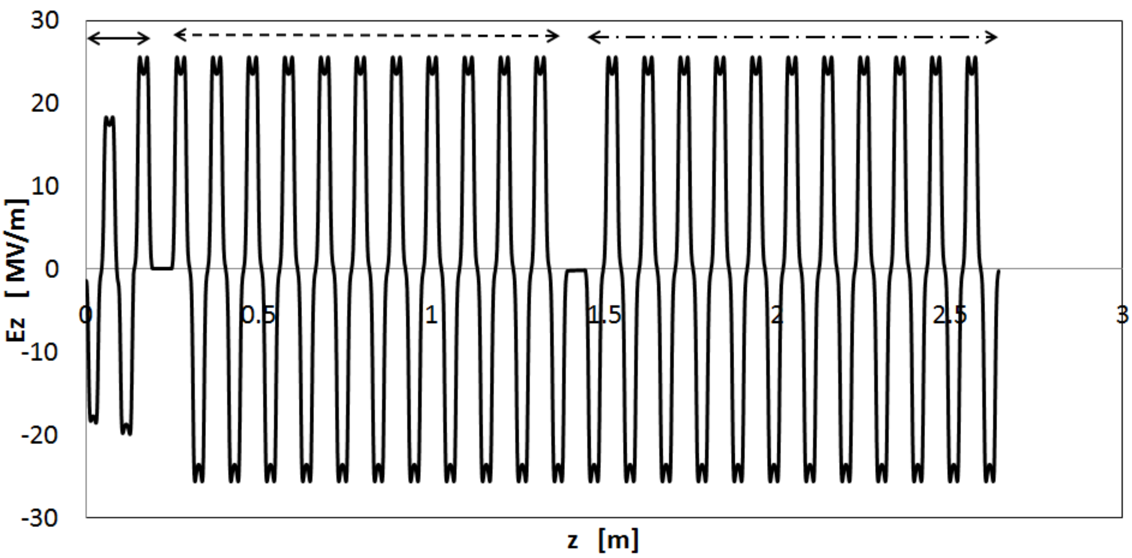

Fig. 3.2 CST Microwave studio result of Longitudinal Electric field profile for the entire accelerating structure of 30 MeV. Injector section (solid arrow), 1st cavity (Dashed arrow), 2nd cavity (Dash-dot-Dash arrow)

3.2.1 STUDY OF SELF FIELD EFFECTS ON ELECTRON BEAM

3.2.1.1 EFFECT OF SPACE CHARGE ON BEAM DYNAMICS

The electron beam through the accelerating structure, starting from the injector section, has been tracked with ASTRA both with and without space charge over the desired final energy of 30 MeV. The input distribution is same for both the simulations.

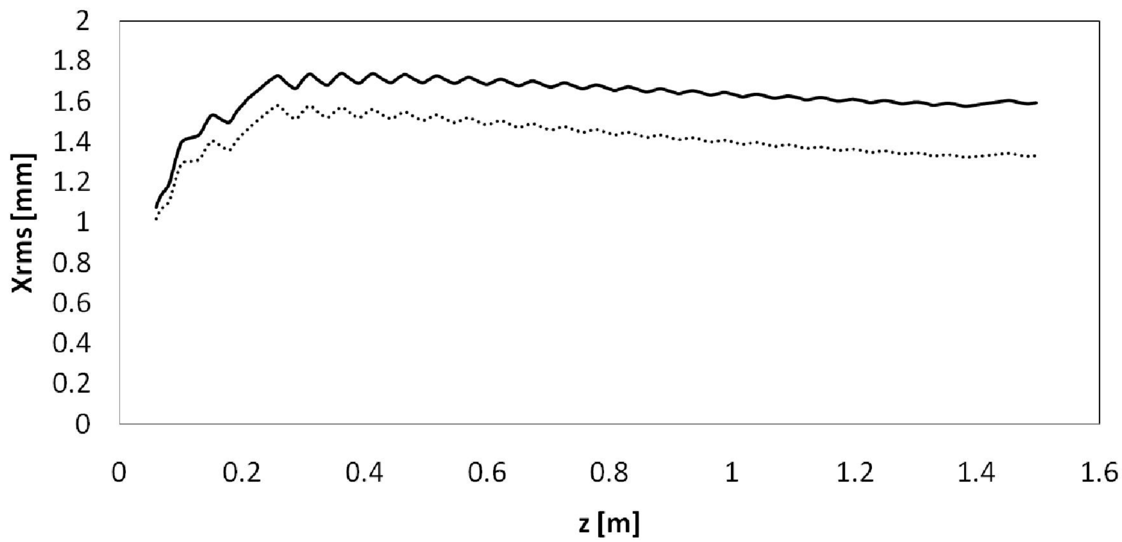

Fig. 3.3 ASTRA simulations for rms beam size without space charge effect (Dotted line) and with space charge effect (solid line) for a bunch of charge 0.175 nC

Fig. 3.3 gives the evolution of rms beam size for the nominal energy of 30 MeV. We have used a uniform distribution of particles having energy 85 ± 2 keV for the longitudinal direction with rms bunch length of 15.61 mm and Gaussian distribution in all transverse dimensions with rms beam sizes of 0.8 mm each. The results show that space charge gives rise to a transverse spread of the beam in the injection section and 1st cavity at low energies. To further study the effect of space charge on the beam we have varied the input bunch charge from 0.15 nC to 3 nC and the summary of the results are given in the Fig. 3.4. It is clear that the rms beam size increases (together with the beam emittance) for larger bunch charges, which can lead to loss of beam through aperture. Therefore the initial bunch charge should be small enough to ensure no loss of beam through the aperture.

As linear space charge effects strongly influence bunch behaviour [46, 55-57] it is important to understand how bunch characteristics change with total charge per bunch. Table 3.1 shows the values of several bunch attributes at the end of the linac as a function of the total charge per bunch.

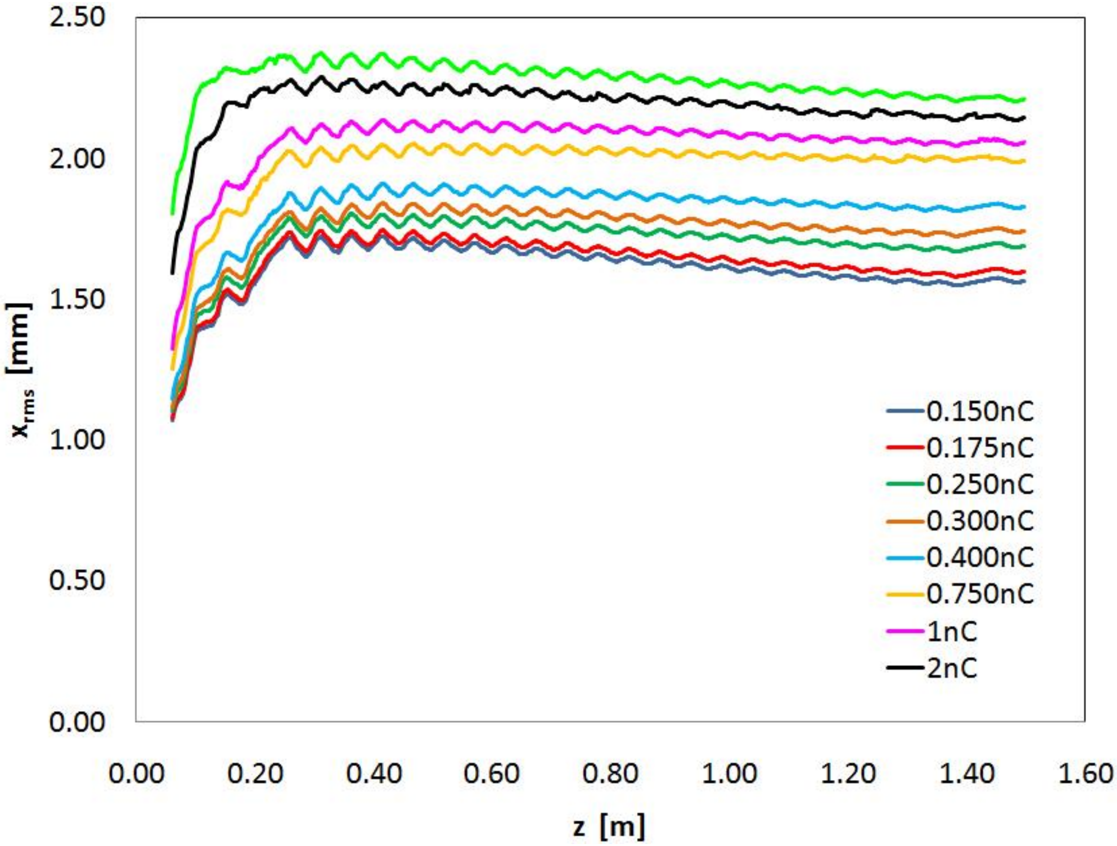

Fig. 3.4 ASTRA simulations for rms beam size as a function of space charge effect for bunch charges of 0.15 nC, 0.175 nC, 0.25 nC, 0.3 nC, 0.4 nC, 0.75 nC, 1 nC, 2 nC, 3 nC

The % transmission of the beam refers to the ratio of the no of active macroparticles having an average gain in energy of 30 MeV to the no of macroparticles injected from the gun having energy 85 ± 2 keV.

The general increasing nature of transverse emittance in Fig. 3.5 shows what we would expect: the beam has more of a tendency to diverge and % transmission decreases as we increase the bunch charge. If the bunch length is too long, then different regions of the bunch will be accelerated differently, resulting in a spread of the bunch energy in the longitudinal direction. While a decrease in the longitudinal emittance may reduce the bunch length, i.e. bunch will squeeze and the longitudinal energy spread decreases, but this results in increase of the charge density of the bunch. Consequently, a higher magnitude of self fields leads to increase in transverse emittance which causes overall transmission loss. So the charge per bunch should be an optimum value for efficient operation of linac.

However, as the bunch charge is increased to a higher value nonlinear space charge effects come into picture due to intense space charge effect [58, 59]. This leads to the abrupt change in the curves as shown in Fig. 3.5.The shapes of these curves are all likely to change significantly as we vary other parameters such as initial spot size, field strengths, cavity phases, etc-. For example, if we decrease the input rms beam size from 0.8 mm to 0.1 mm, the space charge effects becomes quite prominent and leads to growth of curve at a faster rate as shown in Fig. 3.5.

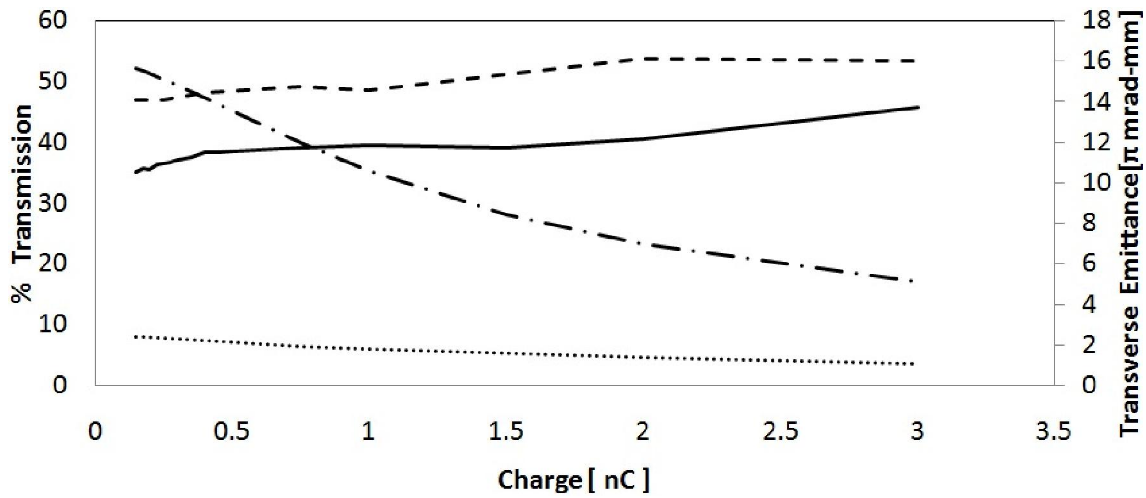

Fig. 3.5 ASTRA simulations showing the effect of space charge on transverse emittance (solid line) and % transmission (Dash-dot-Dash) for rms beam size of 0.8mm .Transverse emittance (Dashed line) and % transmission (Dotted line) for rms beam size of 0.1 mm.

Table 3.1. Study of beam parameters as a function of space charge

Charge per Bunch (Q in nC)	Output rms Beam size (x_{rms} in mm)	Transverse Emittance (ϵ_x in π mrad mm)	Longitudinal Emittance (ϵ_z in π keV-mm)	Bunch Length (in mm)	% transmission	
0.15	1.39	10.49	2217	3.3	52	
0.175	1.43	10.65	2198	3.3	52	
0.2	1.46	10.63	2176	3.3	51	Linear
0.225	1.50	10.84	2159	3.3	51	Space
0.25	1.53	10.92	2141	3.2	50	Charge
0.275	1.56	10.96	2121	3.2	50	Effect
0.3	1.59	11.08	2115	3.2	49	Regime
0.35	1.63	11.24	2101	3.2	48	
0.4	1.68	11.44	2082	3.2	47	
0.45	1.71	11.46	2070	3.2	46	
0.5	1.74	11.5	2055	3.2	45	
0.75	1.87	11.7	1996	3.2	40	
1	1.93	11.79	1988	3.2	35	
1.5	1.98	11.68	2009	3.2	28	
2	2.00	12.12	2096	3.3	23	
3	2.04	13.68	2316	3.5	17	

3.2.1.2 BEHAVIOUR OF BUNCH WITH SELF FIELD EFFECT

Assuming a uniform bunch we have studied the effect of space charge on two different values of charges per bunch 0.175nC, 0.75nC at the injector output, at the output of 1st cavity and at the end of the linac.

As shown in the Fig. 3.6 (a[(i), (ii), (iii)]) and (b[(i), (ii), (iii)]), the variation of the effective space charge field field on the bunch in radial direction takes place according to equation (3.9) and Lorentz force law. The magnitude of the space charge field is higher near the injector section and it becomes very small after accelerating sections. The green hatched area in the lower part of the plot indicates the extension of the bunch. Each line in the plot represents the field component at a different offset in the orthogonal direction. The offsets are equally distributed between plus/minus two times the rms-width. $z = 0$ correspond to the centre of the bunch at the entrance of the injector section.

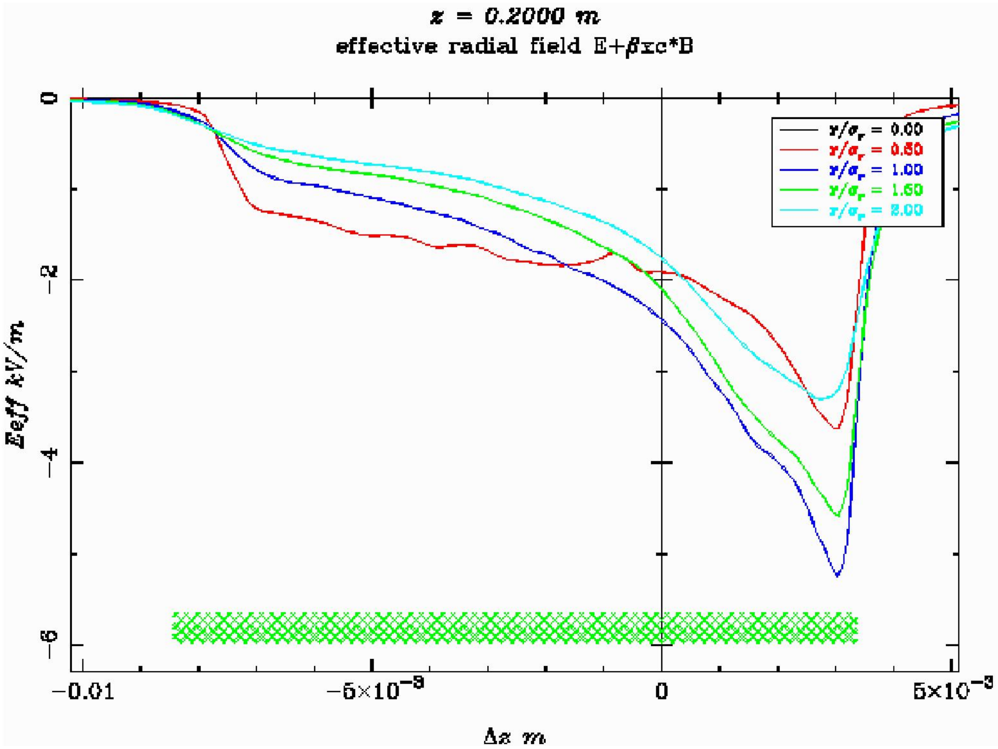
z = 0.2000 m
effective radial field E+βxc*B
Eeff kV/m
0
−2
−4
−6
−0.01
−5×10−3
0
5×10−3
Δz m
r/σr = 0.00
r/σr = 0.50
r/σr = 1.00
r/σr = 1.50
r/σr = 2.00

(i)

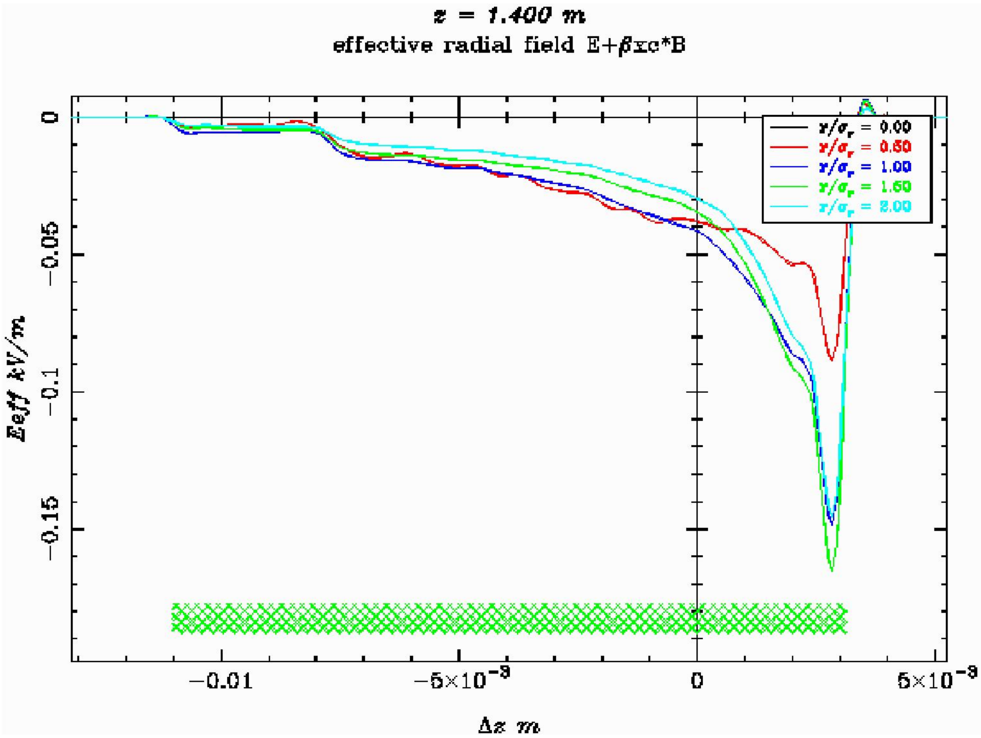
z = 1.400 m
effective radial field E+βxc*B
Eeff kV/m
0
−0.05
−0.1
−0.15
−0.01
−5×10−3
0
5×10−3
Δz m
r/σr = 0.00
r/σr = 0.50
r/σr = 1.00
r/σr = 1.50
r/σr = 2.00

(ii)

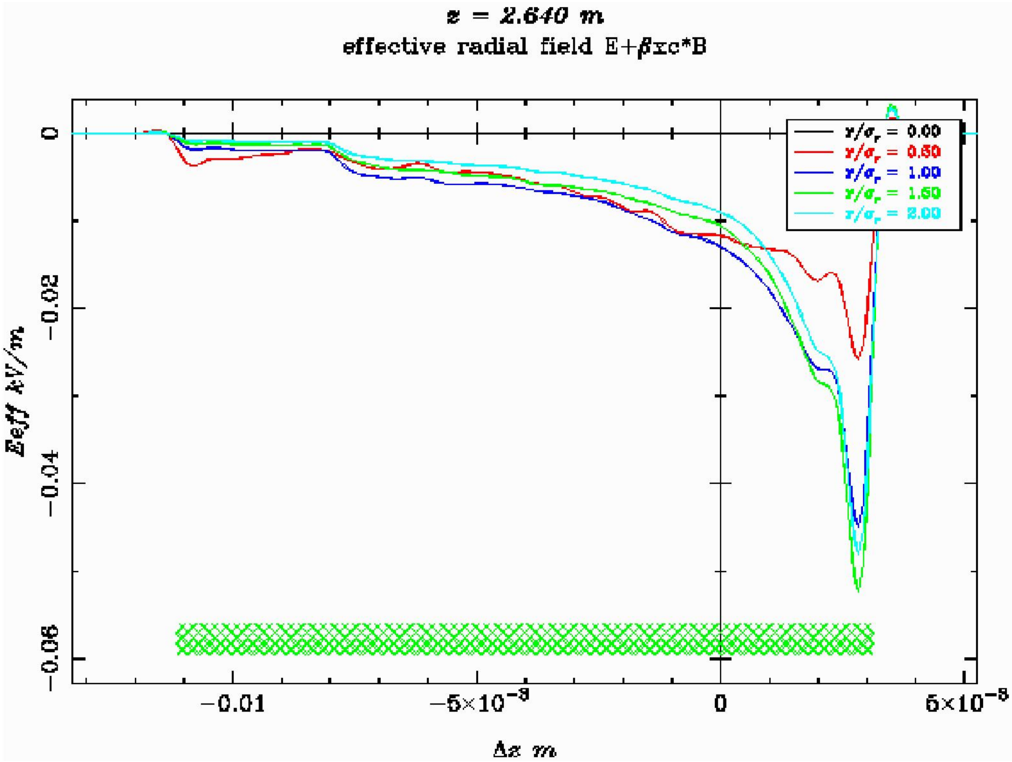
z = 2.640 m
effective radial field E+βxc*B
r/σr = 0.00
r/σr = 0.50
r/σr = 1.00
r/σr = 1.50
r/σr = 2.00
Eeff kV/m
0
−0.02
−0.04
−0.06
−0.01
−5×10−3
0
5×10−3
Δz m

(iii)

(a)

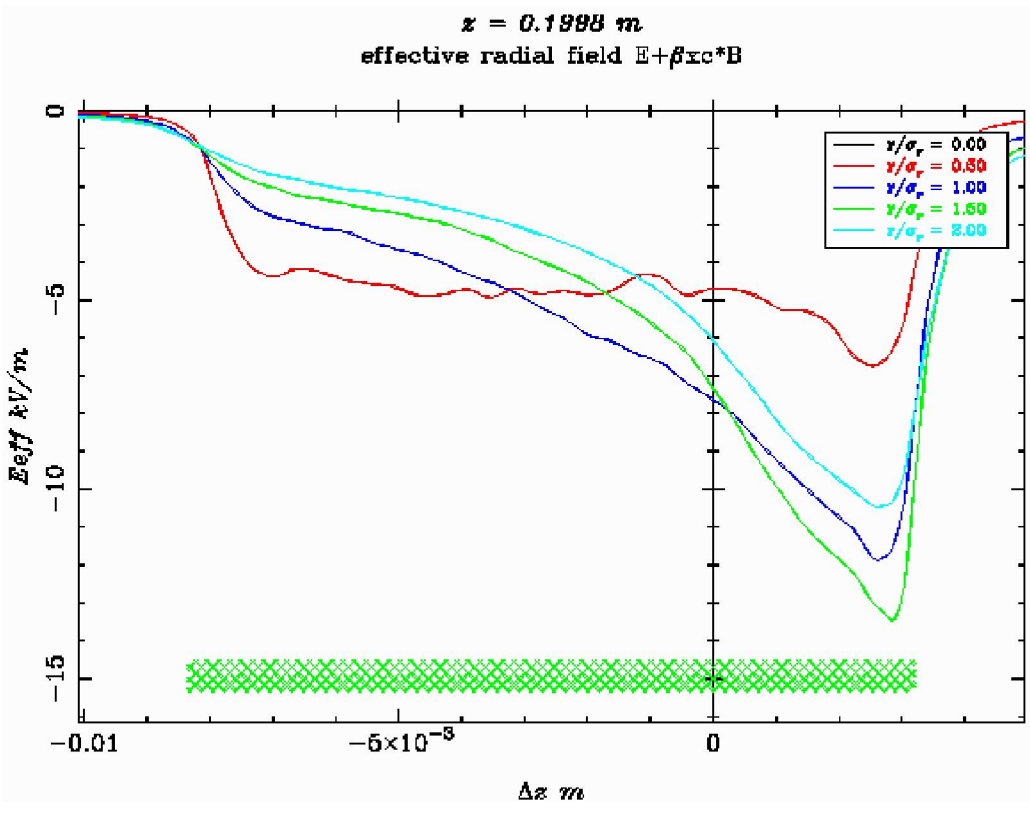
z = 0.1998 m
effective radial field E+βxc*B
r/σr = 0.00
r/σr = 0.50
r/σr = 1.00
r/σr = 1.50
r/σr = 2.00
Eeff kV/m
0
−5
−10
−15
−0.01
−5×10−3
0
Δz m

(i)

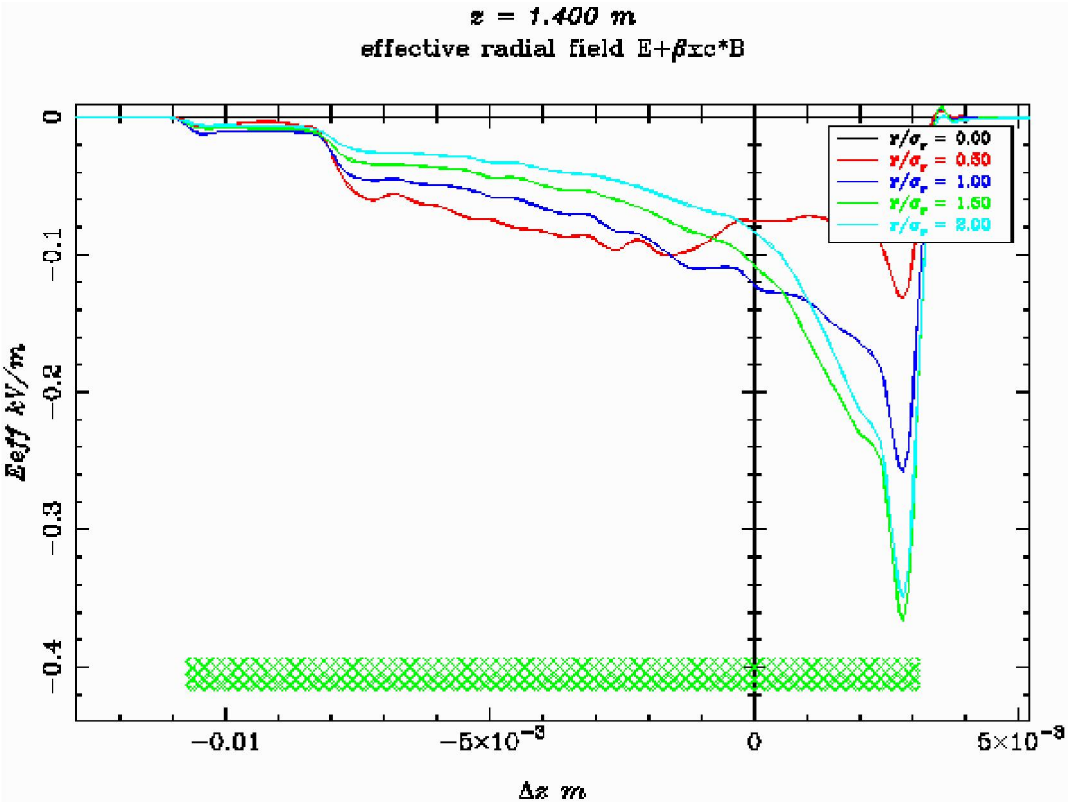

(ii)

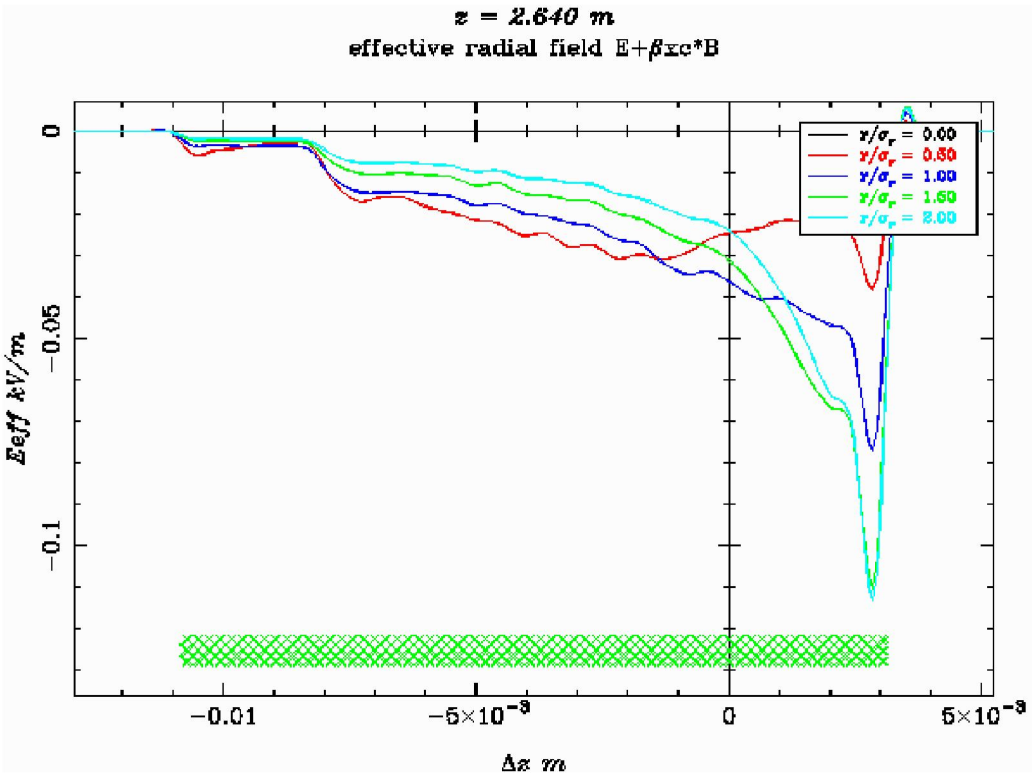

(iii)

(b)

Fig. 3.6 ASTRA Plot of radial space charge field acting on a bunch of charge (a) 0.175 nC (b) 0.75nC

From Fig. 3.7 (a[(i), (ii), (iii)]) and (b[(i), (ii), (iii)]), we can find that the radial electric field variation inside the bunch and outside the bunch is in accordance with equation (3.9). As shown in the Fig. 3.7(a[(i)]), initially particles in the head of the bunch of 0.175 nC at z/σ_z =1.0 experience more radial electric field and the particles in the tail at z/σ_z = -1.0 less field. But as the bunch is accelerated the particle in the tail of the bunch moves towards the centre of the bunch and both the particles experience nearly same radial field. A large amount of charge per bunch implies larger space charge force. Due to the larger space charge repulsion in 0.750 nC bunch in Fig. 3.7(b), the movement of the particle in the bunch tail at z/σ_z = -1.0 and that in the head of the bunch at at z/σ_z = +1.0 towards the centre is reduced leading to the increase in beam size.

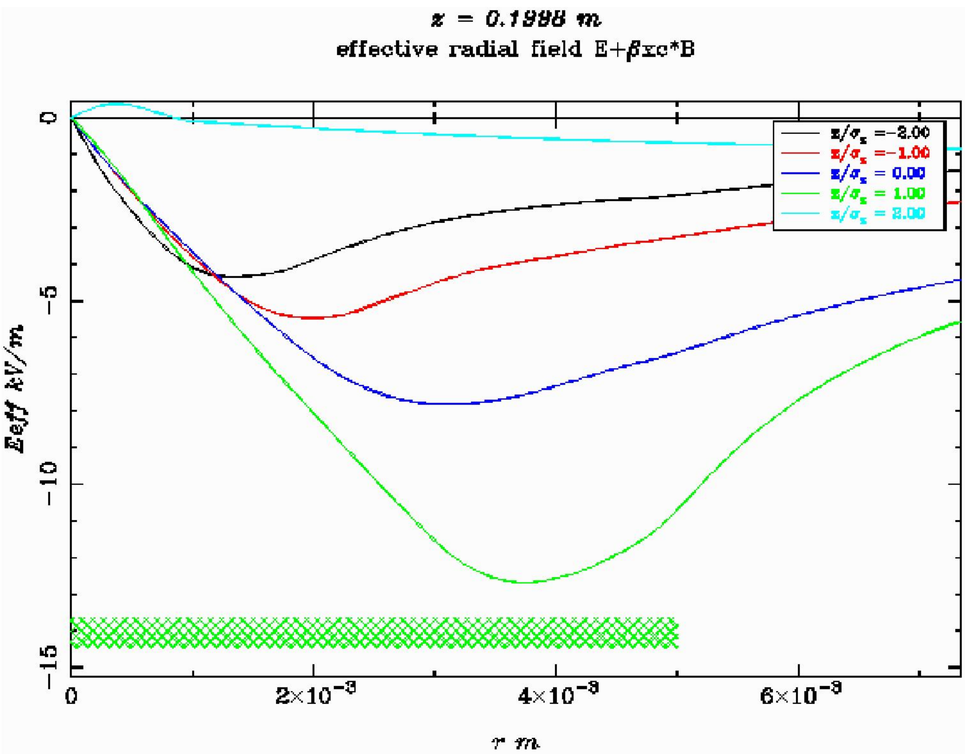

(i)

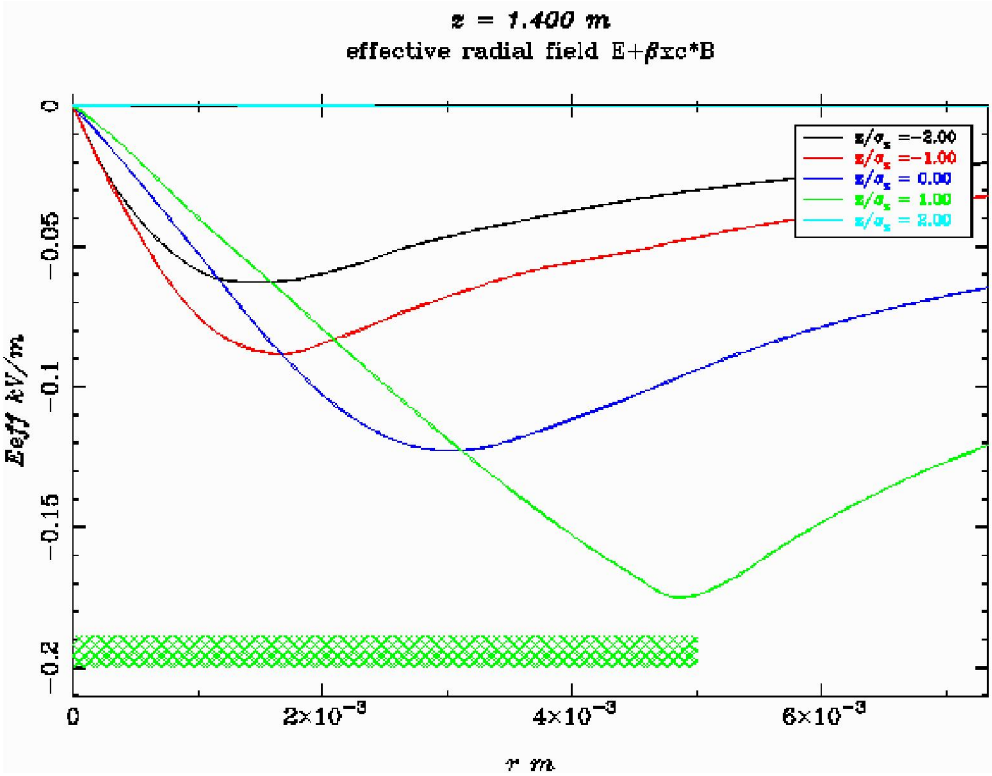
z = 1.400 m
effective radial field E+βxc*B
z/σz =-2.00
z/σz =-1.00
z/σz = 0.00
z/σz = 1.00
z/σz = 2.00
Eeff kV/m
0
-0.05
-0.1
-0.15
-0.2
0
2×10⁻³
4×10⁻³
6×10⁻³
r m
(ii)

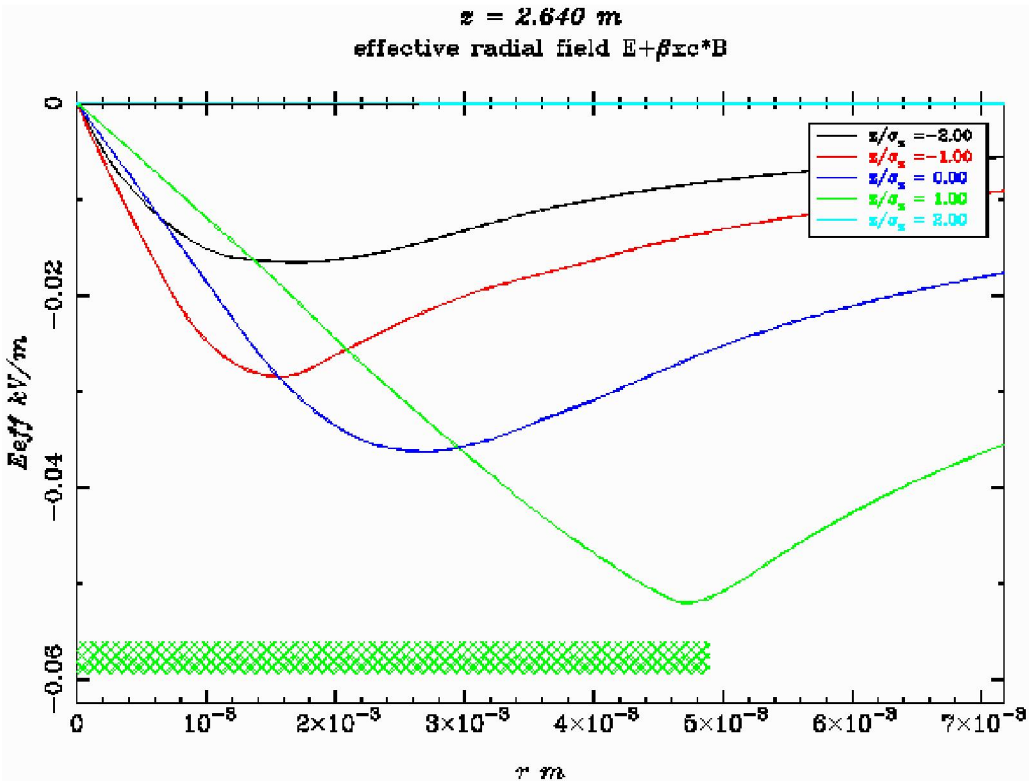
z = 2.640 m
effective radial field E+βxc*B
z/σz =-2.00
z/σz =-1.00
z/σz = 0.00
z/σz = 1.00
z/σz = 2.00
Eeff kV/m
0
-0.02
-0.04
-0.06
0
10⁻³
2×10⁻³
3×10⁻³
4×10⁻³
5×10⁻³
6×10⁻³
7×10⁻³
r m
(iii)

(a)

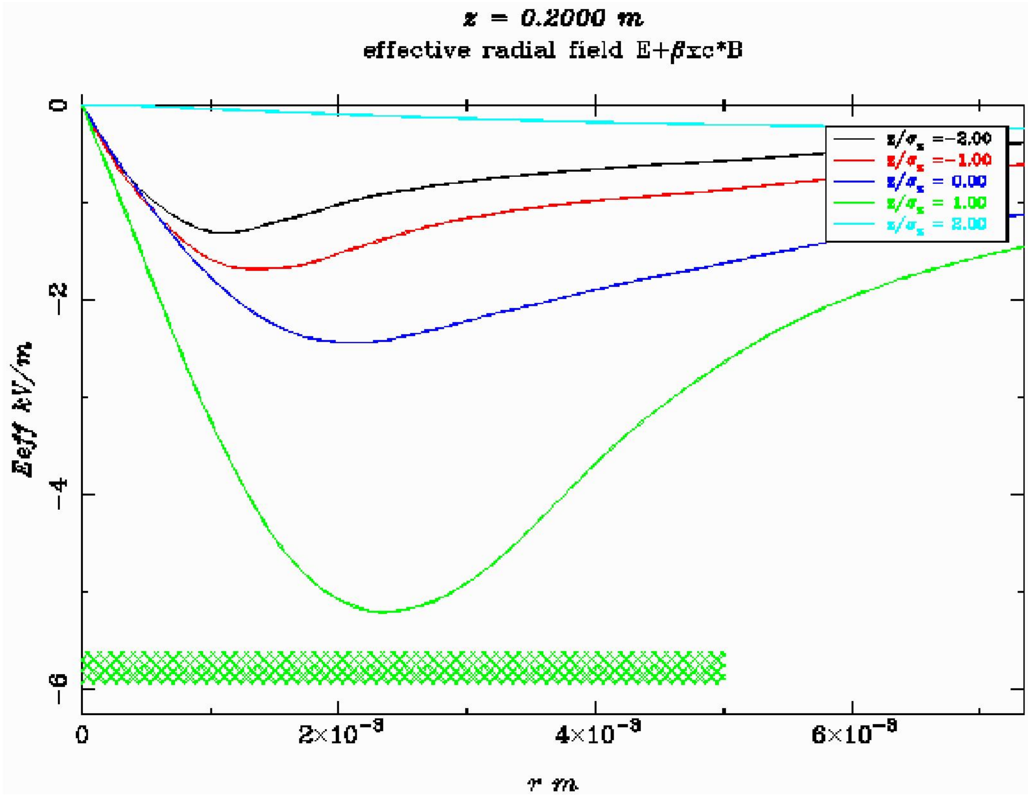
z = 0.2000 m
effective radial field E+βxc*B
Eeff kV/m
r m
0
-2
-4
-6
0
2×10⁻³
4×10⁻³
6×10⁻³
z/σz =-2.00
z/σz =-1.00
z/σz = 0.00
z/σz = 1.00
z/σz = 2.00
(i)

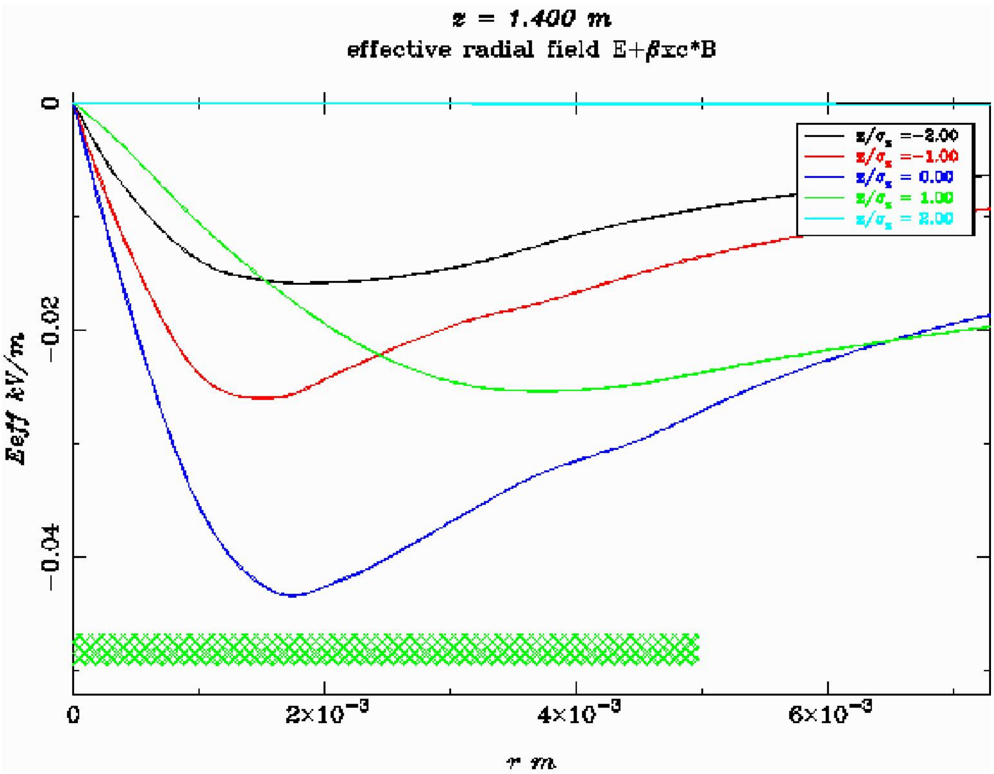
z = 1.400 m
effective radial field E+βxc*B
Eeff kV/m
r m
0
-0.02
-0.04
0
2×10⁻³
4×10⁻³
6×10⁻³
z/σz =-2.00
z/σz =-1.00
z/σz = 0.00
z/σz = 1.00
z/σz = 2.00
(ii)

(iii)

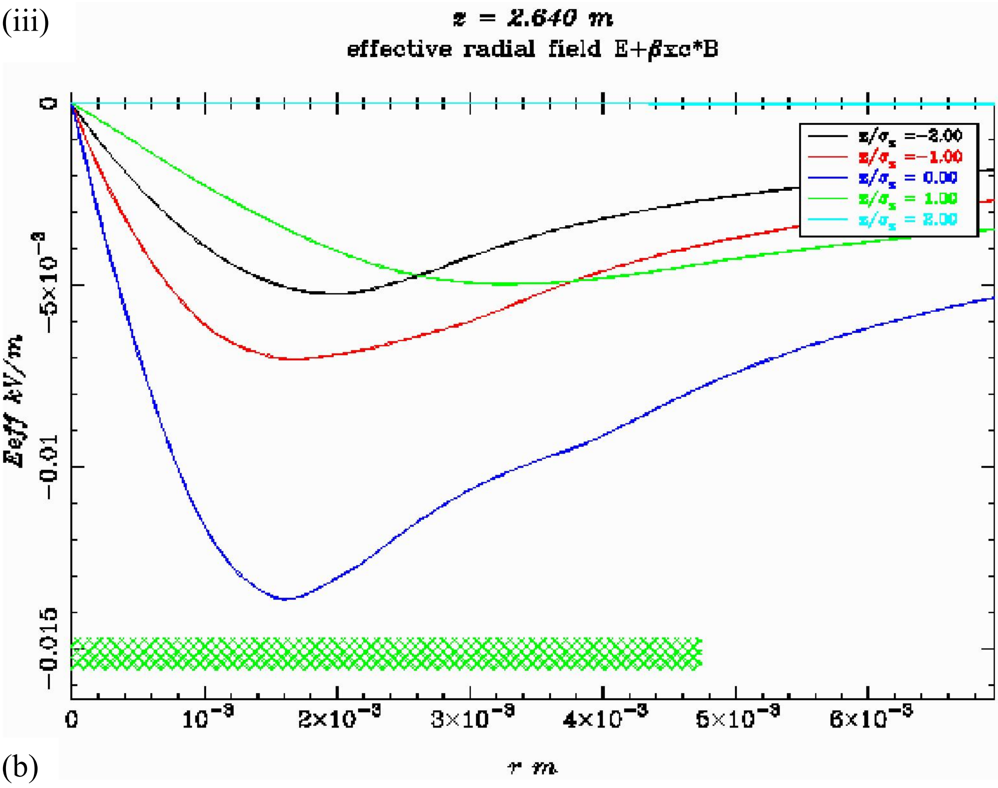

(b)

Fig. 3.7 Radial space charge field acting on the bunch at different z/σz positions of the bunch (a) 0.175 nC charge (b) 0.75 nC charge

3.2.2 PARAMETRIC CHARACTERIZATION OF INPUT BEAM

Emittance of a beam is a suitable parameter to define the qualities of a beam in terms of size and divergence of the beam. Beam emittance is given approximately by the product of spot size and divergence, and is proportional to the volume of the bounding region that each bunch occupies in its region of six-dimensional phase space. We define each point in this phase space by a phase space vector, $r = (x, y, z, p_x, p_y, p_z)$.

The normalized RMS emittance is defined by [45]

$$\epsilon_{n,rms} = \beta\gamma\sqrt{\langle u^2\rangle\langle (u')^2\rangle - \langle uu'\rangle^2} \tag{3.12}$$

Where βc is the velocity of the beam, γ is the Lorentz factor, u and u′ are the transverse coordinate and divergence of x or y, and < > denotes an RMS value. Equation (3.12) defines the normalized trace-space emittance, which is equivalent to the normalized RMS emittance for beams with small energy spread [5].

The thermal emittance as stated in equation (3.11) is defined as

$$\epsilon_{th} = \frac{1}{m_0 c}\sqrt{\langle x^2\rangle\langle\langle {p_x}^2\rangle - \langle x p_x\rangle^2} \;= \frac{\gamma r_c}{2}\sqrt{\frac{k_B T}{m_0 c^2}} \tag{3.13}$$

All the simulations data presented in this section have been noted at z = 2.64 m, that is at the end of the linac. Except section 3.2.1, All the ASTRA simulations have been carried out for different input beam parameters with phases equal to 137.84 degrees in the injector section, 126.72 degrees in the 1st cavity, and 166.3 degrees 2nd cavity respectively, and for an electric field gradient E_0 = 24 MV/m. These absolute phase values give the maximum energy gain with minimum energy spread for a given input. In section 3.2.2, we have studied the evolution of emittance with different bunch charges, So the absolute phases have been chosen in accordance with the nominal value of energy gain and energy spread. The gradient is chosen in accordance with the Kilpatrick limit.

3.2.2.1 EVOLUTION OF EMITTANCE WITH SPACE CHARGE

ASTRA simulations have been carried out for charge per bunch Q = 0.175 nC, 0.2 nC, 0.3 nC,..., 3 nC and the results are summarized in Table 3.1

3.2.2.2 EVOLUTION OF EMITTANCE WITH BEAM SIZE

In rf cavities the radial component of the electric field grows quadratically with radius up to half of maximum radius of the rf cavity, whereas the longitudinal electric field increases linearly toward higher radii. As a result, the variation of the beam size (due to RF focussing) depends nonlinearly on the value of the beam size itself, therefore an increase of the emittance, proportional to the fourth power of the beam radius, is to be expected when a beam crosses a rf cavity .In order to numerically test this effect, we have tracked beams of charge 0.175 nC and of different transverse sizes through the rf cavity excited at the average field of 10.81 MV/m. The simulation results of variation of transverse beam sizes for a fixed input value of rms emittance are summarized in Table 3.2.

From Table 3.2 we can clearly find two different regimes in the output beam, a space charge dominated region where the emittance growth is a function of space charge, and an emittance dominated region where the emittance growth is due to increase in the input beam size. Fig. 3.8 describes the transverse emittance as a function of input rms beam size.

Table 3.2. Study of emittance growth as a function of input beam size keeping a fixed emittance of the input beam

Input Rms Beam size (x_{rms} in mm)	Input Rms Beam size (y_{rms} in mm)	Transverse Emittance (ϵ_x in π mrad mm)	Transverse Emittance (ϵ_y in π mrad mm)	% transmission	
0.2	0.2	11.96	11.86	33	Space charge dominated regime
0.3	0.3	10.74	10.82	45	
0.4	0.4	10.44	10.59	50	
0.5	0.5	9.93	10.02	53	
0.6	0.6	9.61	9.66	54	
0.7	0.7	9.49	9.23	54	
0.8	0.8	9.44	9.01	54	
0.9	0.9	9.57	9.39	53	Emittance dominated regime
1	1	9.84	9.70	52	
1.1	1.1	10.18	9.96	51	
1.2	1.2	10.67	10.67	50	
1.3	1.3	11.22	11.33	49	
1.4	1.4	11.98	12.01	48	
1.5	1.5	12.64	12.69	47	
2	2	16.14	15.91	41	
2.5	2.5	18.74	18.25	35	

So we may observe that there exists an optimal initial beam size that minimizes the sum of the rf and space-charge induced emittance growth.

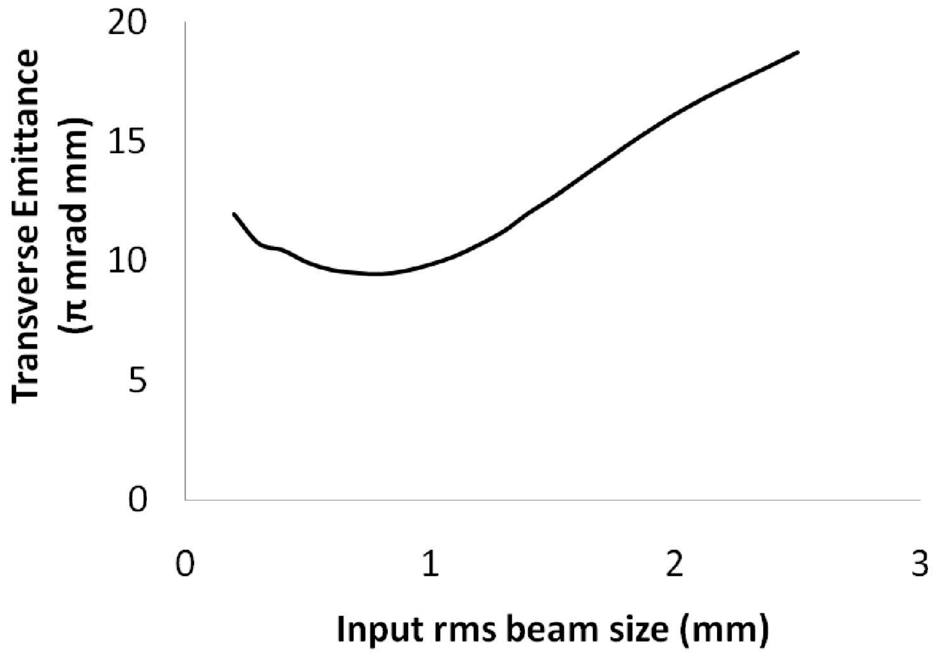

Fig. 3.8 Evolution of transverse emittance with input beam size

3.2.2.3 EVOLUTION OF EMITTANCE WITH DIVERGENCE

In rf cavities the beam divergence strongly affects the beam behaviour. In order to study the emittance growth due to beam divergence we have taken an input beam of rms size 0.8 mm and varied the beam divergence as given in Table 3.3. We find that the transverse emittance shows a linear growth with increase in beam divergence. To verify this we observe that bunch length gradually decreases. Thus while traversing a rf cavity the initial divergence is the effective factor in inducing more emittance growth in transverse directions, which leads to loss of electrons through the beam tube.

3.2.2.4 EVOLUTION OF EMITTANCE WITH BEAM ASPECT RATIO

We have studied the effect of the aspect ratio of the rms beam sizes in transverse direction and their effects on emittance growth. The summary of the results are given in Table 3.4. We observe that for any beam, the emittance growth in one transverse plane of the beam as compared to the other plane is within space-charge statistical error. Thus we treat each plane irrespective of the other plane, i.e. the two transverse planes behave independently of each other.

Table 3.3. Study of emittance growth as a function of divergence of the input beam

Input Beam divergence (x'_{rms} in mrad)	Input Beam divergence (y'_{rms} in mrad)	Transverse Emittance (ϵ_x in π mrad mm)	Transverse Emittance (ϵ_y in π mrad mm)	Bunch Length (in mm)	% transmission
2.1	2.1	7.71	7.71	3.4	55
3.1	3.1	7.81	7.85	3.3	55
4.2	4.2	8.02	8.06	3.3	55
5.2	5.2	8.26	8.30	3.3	54
6.2	6.2	8.53	8.59	3.3	54
7.3	7.3	8.97	8.89	3.3	54
8.3	8.3	9.33	9.18	3.3	54
9.4	9.4	9.67	9.52	3.3	53
10.4	10.4	9.97	9.88	3.3	53
11.5	11.5	10.34	10.24	3.3	52
12.5	12.5	10.65	10.56	3.3	52
13.5	13.5	10.92	10.95	3.3	51
14.6	14.6	11.26	11.21	3.3	50
15.6	15.6	11.48	11.45	3.3	50
16.7	16.7	11.76	11.76	3.2	49
17.7	17.7	12.11	12.05	3.2	48
18.7	18.8	12.32	12.31	3.2	47

Table 3.4. Study of emittance growth as a function of beam aspect ratio of the input beam

Rms Beam size (x_{rms} in mm)	Rms Beam size (y_{rms} in mm)	Transverse Emittance (ϵ_x in π mrad mm)	Transverse Emittance (ϵ_y in π mrad mm)	Bunch Length (in mm)	% transmission
	0.56	10.12	12.09	3.3	47
	1.50	11.65	12.67	3.2	49
0.82	2.00	9.24	17.83	3.1	46
	2.50	8.94	21.02	3.1	43
	3.00	8.69	23.56	3.1	39
0.59		11.31	10.49	3.3	50
1.50		13.65	10.33	3.2	49
2.00	0.82	18.18	8.91	3.1	46
2.50		21.18	8.58	3.1	43
3.00		23.58	8.35	3.1	39

3.2.2.5 EFFECT OF VARIATION OF FIELD GRADIENT ON BEAM QUALITY

As the output of the accelerator beam is a function of the input beam parameters like beam size and accelerator cavity parameter like field gradient etc-, we have studied the evolution of the beam subject to variation in field gradient. The results are given in Table 3.5 and from this we can estimate the changes in the output due to errors in the field gradient. An error of ± 4% in the field gradient changes the output energy gain ≈ ± 4% and error in gradient of ± 8% changes the output energy gain ≈ ± 8%. But the energy spread becomes significant once the field gradient is changed by -8% of its optimum value, which is undesirable.

Table 3.5. Study of output beam parameters as a function of variation of field gradient

Electric Field Gradient (in MV/ m)	Beam size (x_{rms} in mm)	Bunch Length (in mm)	Output Energy (in MeV)	Energy spread (in keV)	Transverse Emittance (π mrad mm)
22	1.46	3.6	27.5	1230	11.78
23	1.45	3.4	28.8	908	11.21
24	1.43	3.3	30.0	719	10.65
25	1.41	3.2	31.2	648	10.03
26	1.39	3.3	32.4	678	9.58

3.2.2.6 EFFECT OF SOLENOID FOCUSSING ON BEAM QUALITY

As the magnetic field plays an important role in focusing of the beam and prevents the loss beam through the cavity, we have studied the quality of beam subjected to solenoid focusing. An air core solenoid of length 15 cm and 15000 ampere-turns is applied over the injection section as shown in the Fig. 3.9. The longitudinal magnetic field of solenoid is plotted in Fig. 3.10.The solenoid field reduce the beam diameter from ~ 8 mm to ~ 4.5 mm and improve the overall transmission ≈ 9% . Fig. 3.11 describes the computed beam envelope over the entire length of the linac without solenoid and with solenoid.

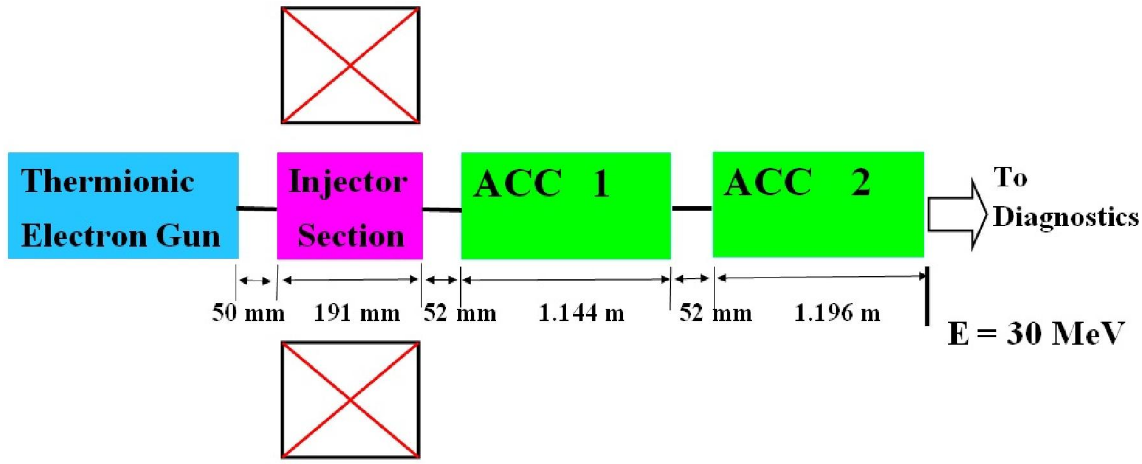

Fig. 3.9 Schematic Layout of the 30 MeV Linac Test Facility with solenoid over the injector section

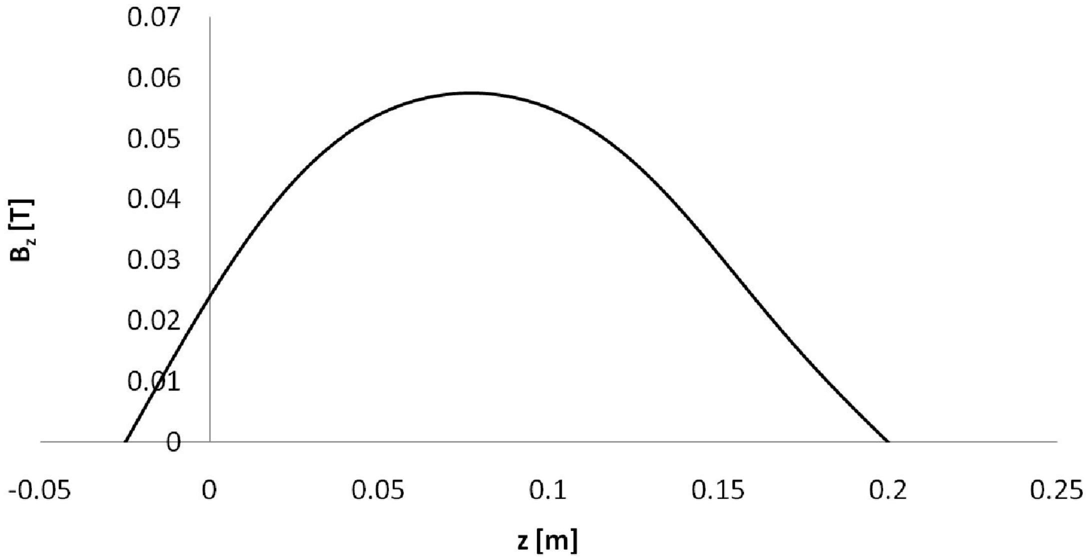

Fig. 3.10 CST Particle Studio result of Solenoid magnetic field profile over the injector section

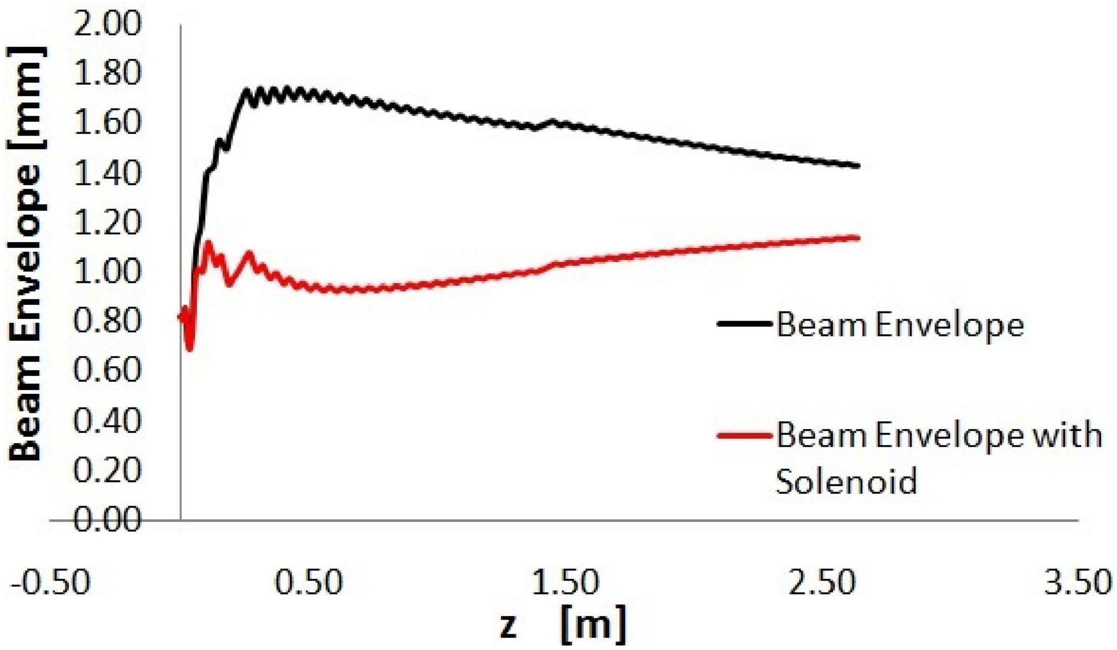

Fig. 3.11 Computed beam envelope over the entire length of linac

3.3. CONCLUSION

For a 30 MeV linac, the effects of the space charge and input beam parameters like variation of beam size, divergence, variation of field gradient have been studied theoretically [16, 18]. We have investigated the effect of horizontal plane and vertical plane on beam dynamics and found that both the planes can be treated separately excluding space charge effect. We conclude from these beam dynamics studies that space charge effect plays a pivotal role in the injector section and 1st cavity of the 30 MeV linac. We have applied a solenoid of length 15 cm and 15000 ampere turns over the injector section to compensate the space charge effect. An energy spread of ~ 2.5% improves the quality of the output beam. With a beam size of ~ 4.5 mm in the bore of aperture diameter 10 mm, the beam loss on the cavity wall is minimized and the heavy irradiation of accelerator components is prevented.

CHAPTER 4

STUDY OF BEAM DYNAMICS FOR A 10 MeV INDUSTRIAL RF ELECTRON LINAC AND ITS VALIDATION WITH EXPERIMENTAL DATA

Electron beam accelerator based industrial applications have boosted in the recent years contributing in many aspects of national economies. The distinct advantage of electron beam for radiation processing is used in diverse industries to enhance the physical and chemical properties of materials and to reduce undesirable contaminants such as pathogens or toxic by-products. Utilization of electron beam for sterilization of medical devices, commercial processing of polymers, non-destructive testing, cargo scanning applications and food processing offers low cost techniques for irradiation of products in larger capacities [2, 7, 37]. A linear electron accelerator is usually considered to be a highly efficient source of electron beam for x-ray generation due to its flexible size depending upon beam power [2, 7, 37].

As a part of indigenous accelerator development programme for societal applications, a 10 MeV electron linac is designed and developed by Accelerator and Pulse Power Division, BARC, India, and it is operational at Electron Beam Centre, Kharghar, Navi Mumbai for industrial applications [19, 21, 23, 60, 61]. In this chapter we investigate the beam dynamics of this 10 MeV, 10 kW bi-periodic coupled cavity standing wave electron linac using the beam dynamics code ASTRA [14]. This beam dynamics study finds the optimized beam parameters and explores the quality of electron beam [5, 45]. The effects of space charge, input beam size, beam divergence, emittance growth, energy spread, behavior of bunch and their effect on the beam quality have been studied. To validate the beam dynamics results, the simulation data is compared with the experimental observations.

4.1. BEAM DYNAMICS STUDIES OF A 10 MeV LINAC

The picture of the 10 MeV linac along with a schematic layout is shown in Fig. 4.1. The linac consists of a DC thermoionic gun, followed by a bunching and accelerating section. An electron gun having LaB_6 cathode injects the beam of 50-70 keV in to the linac.

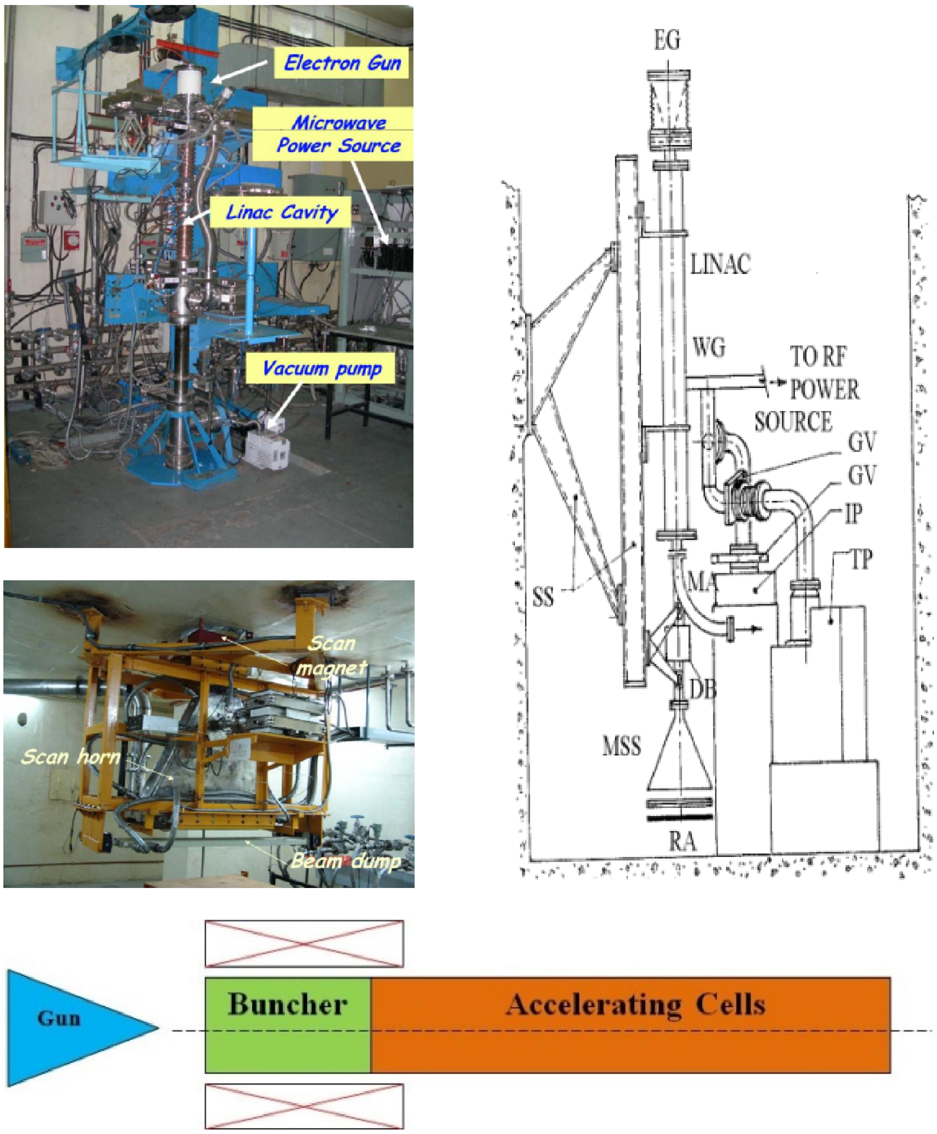

Fig. 4.1 10 MeV Linac (Courtsey: [21, 60]) and its Schematic

The accelerating cavity consists of 3 bunching cells and 14 accelerating cells operating in π/2 mode at a frequency of 2856 MHz. The length of each accelerating cell is 52 mm, whereas the buncher cells are 45, 48 and 50 mm respectively. The bore radius is 5 mm for all the buncher cells and accelerating cells. The effective shunt impedance for the buncher cells is ~80 MΩ/m, while for the accelerating cells; it is ~ 90 MΩ /m. Beam focusing is ensured by solenoids up to the bunching system exit. A klystron feeds RF power into the linac cavity at 2856 MHz. A vacuum level of 10^{-7} is maintained in the linac structure using a distributed turbo-cum-sputter-ion pumping system [62]. The output electron beam is scanned using C-shaped scan magnet. At the linac end the electron beam hits a tantalum foil and produces X-rays.

For the present work the longitudinal electric field components on the symmetry axis (r=0) have been computed using CST MWS [54] as shown in Fig. 4.2. Fig. 4.3 shows the solenoid field profile over the buncher section. For all the simulations presented in the following, we have used the following input beam parameters that are given in Table 4.1. A typical simulation result at the end of the linac is presented in Table 4.2.

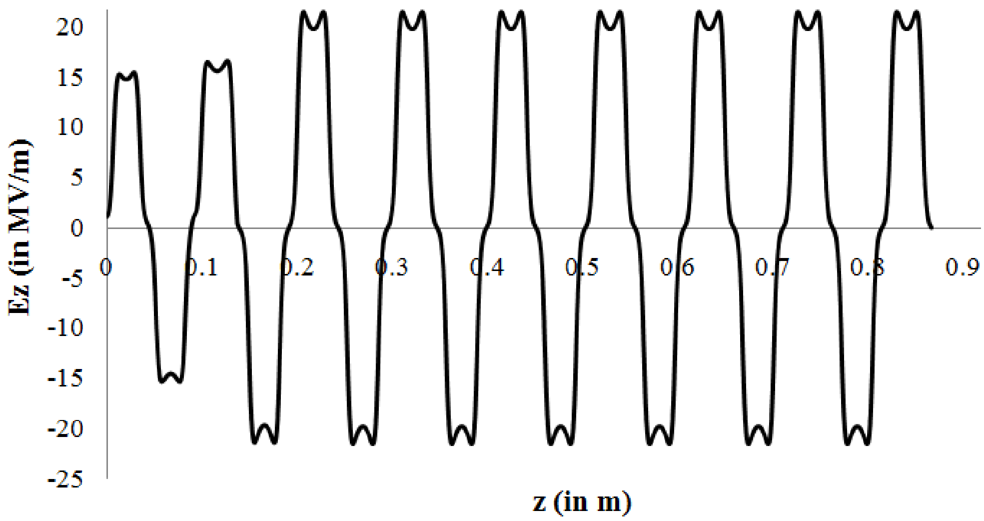

Fig. 4.2 Accelerating Field Profile along the 10 MeV Cavity (from CST Microwave Studio)

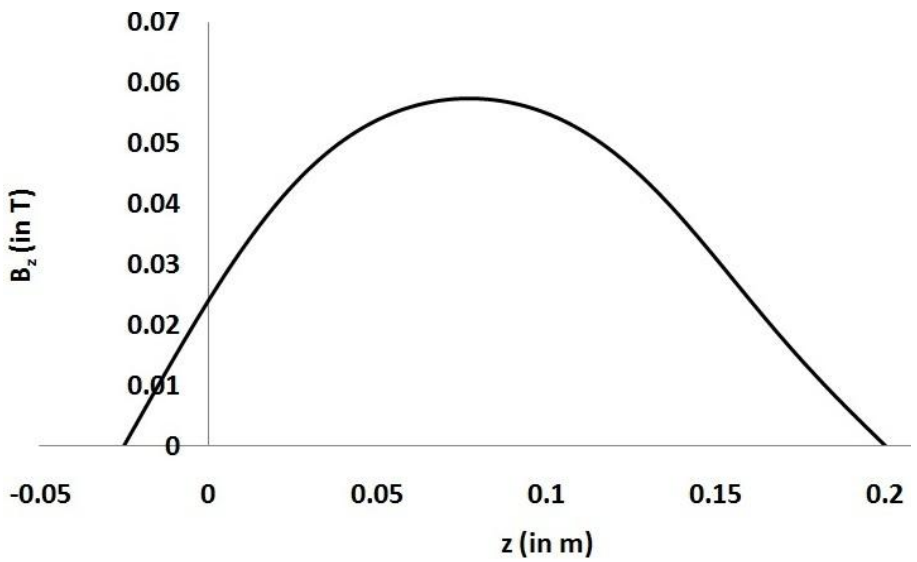

Fig. 4.3 Solenoid Field profile over the bunching section (from CST Particle Studio)

Table 4.1. Input beam parameter at injection

Input Beam Parameter	
No. of macro particles	25000
Distribution	Gaussian
Beam current	500 mA
Energy	50 keV
Energy Spread	2 keV
Beam size	3.0 mm
Transverse Emittance	6 π mm-mrad

Table 4.2. Simulation Result at the Linac end

Output Beam Parameter	
Energy	10.2 MeV
Energy Spread	505 keV
Bunch Length	4.237 mm
beam size	8 mm
Transverse Emittance	40.47 π mm-mrad
% of Transmission	47.96 %

4.1.1 LONGITUDINAL BEAM DYNAMICS

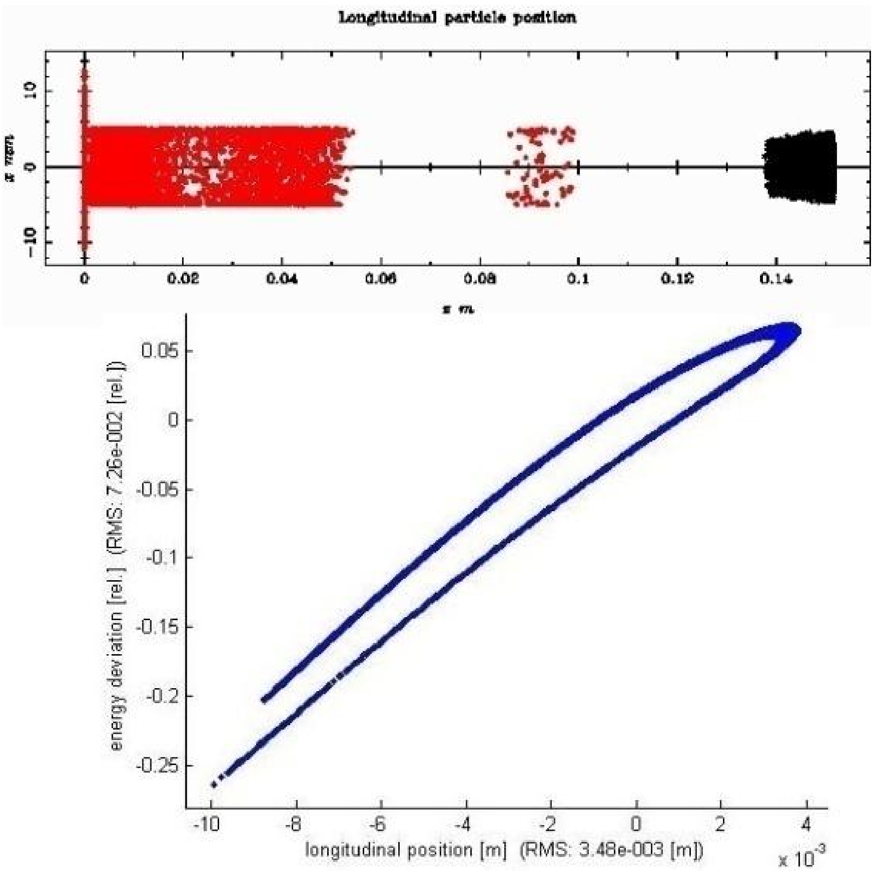

Fig. 4.4 Bunching process in the buncher section (upper part) and the shape of the bunch (lower part)

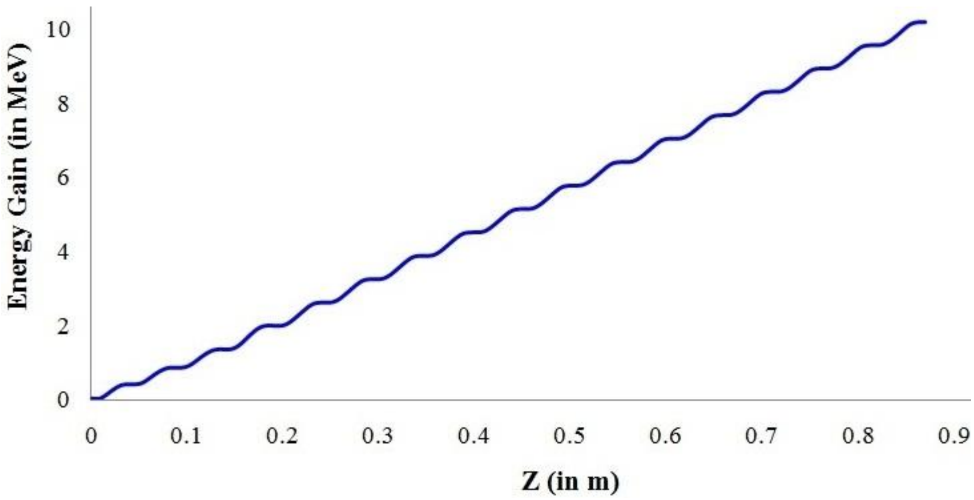

Fig. 4.5 Energy gain along the 10 MeV linac.

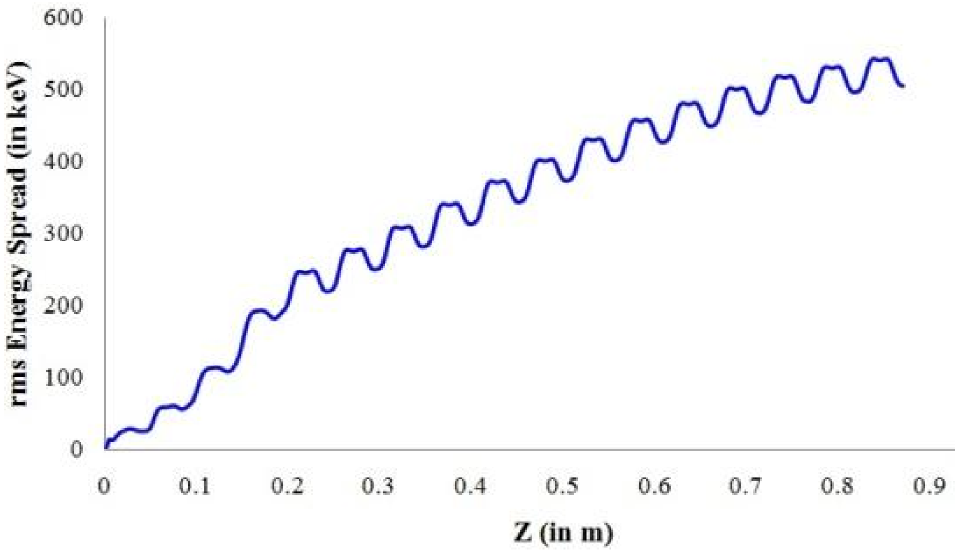

Fig. 4.6 Energy spread along the 10 MeV linac

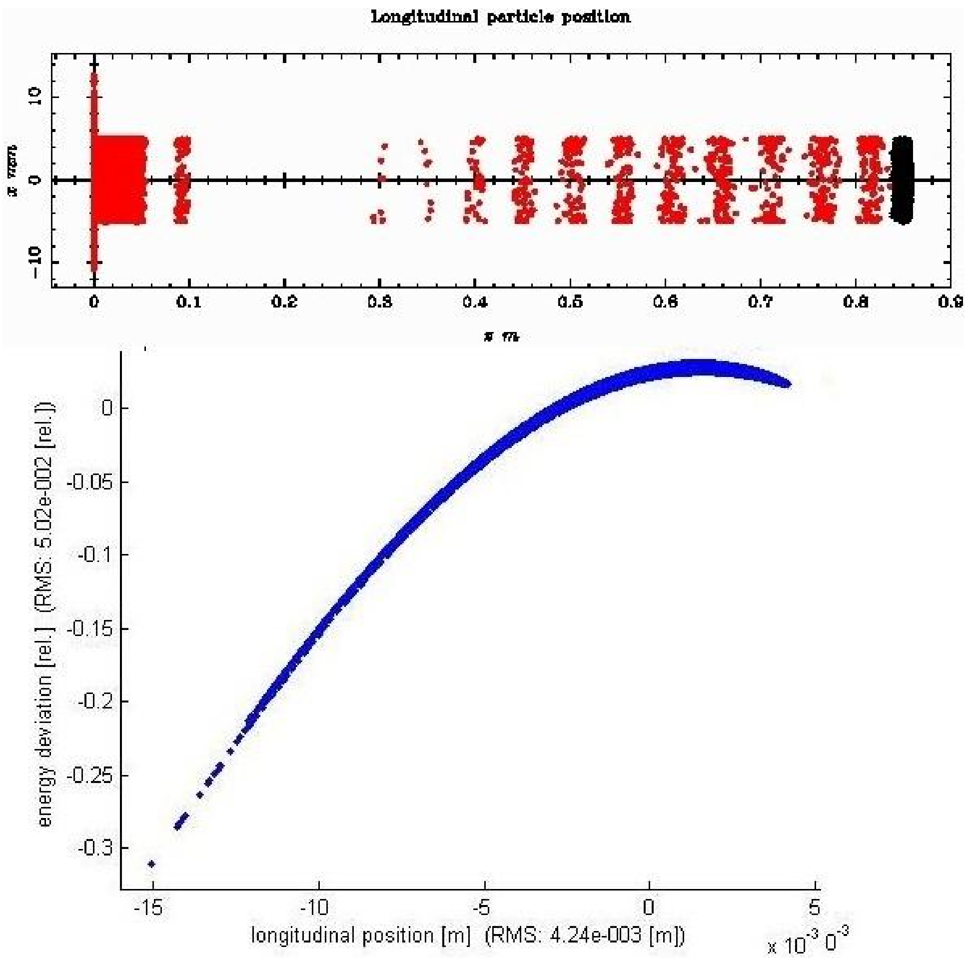

Fig. 4.7 Longitudinal position of particle (upper part) and the shape of the bunch (lower part)

Fig. 4.4 describes the particle tracking and formation of bunched beam in the buncher cells and the corresponding plot of the bunch. The red colour dots indicate the lost particles. The black colour dots indicate the standard particles that are tracked. The energy gain in each cell of the cavity of 10 MeV linac is shown in Fig. 4.5. The energy spread along the entire length is shown in Fig. 4.6. From these two pictures it is clear that the energy gain of 10 MeV is achieved with 5 % energy spread. This result shows that the 10 MeV linac can deliver good quality beam for industrial applications. Fig.4.7 describes the start-to-end longitudinal particle position and the shape of the bunch at the linac end.

4.1.2 TRANSVERSE BEAM DYNAMICS

4.1.2.1 EFFECT OF SPACE CHARGE ON BEAM DYNAMICS

The electron beam through the accelerating structure has been tracked with ASTRA with space charge. Six probe particles are specified at $\pm0.5\sigma$, $\pm1.0\sigma$, $\pm1.5\sigma$ over the extension of the bunch. The radial space charge field acting on the probe particles is shown in Fig. 4.8. The space charge [28, 46, 63, 64] may lead to growth of beam size and the beam may hit the cavity wall. The effect of space charge on the probe particle trajectories is shown in Fig. 4.9. The hitting of the electron beam with the cavity wall may induce radioactivity in the linac structure.

To compensate the space charge effect a solenoid is applied over the buncher section as shown in Fig. 4.1. The trajectories of the probe particles with a solenoid over the buncher section is plotted in Fig. 4.10. This leads to higher transmission efficiency.

The beam envelopes with and without application of solenoid is shown in Fig. 4.11. It is clear that the solenoid focuses the beam in the buncher section and compensates the space charge field of the beam.

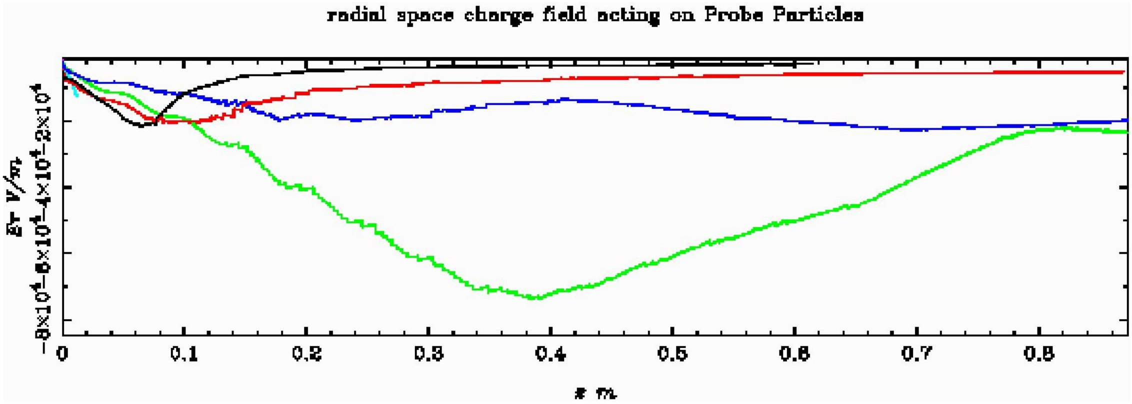

Fig. 4.8 Radial space charge field profile along the linac

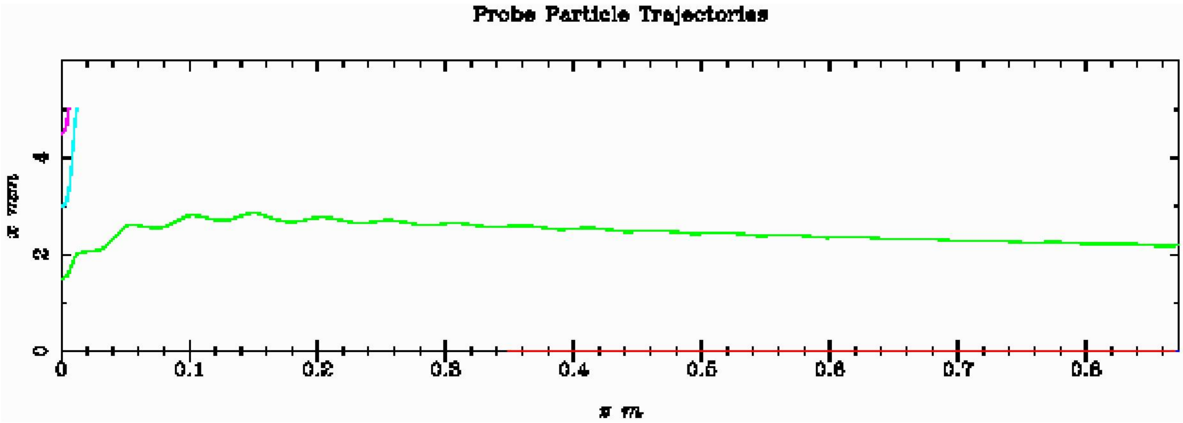

Fig. 4.9 Probe particle trajectory along the linac under space charge effect

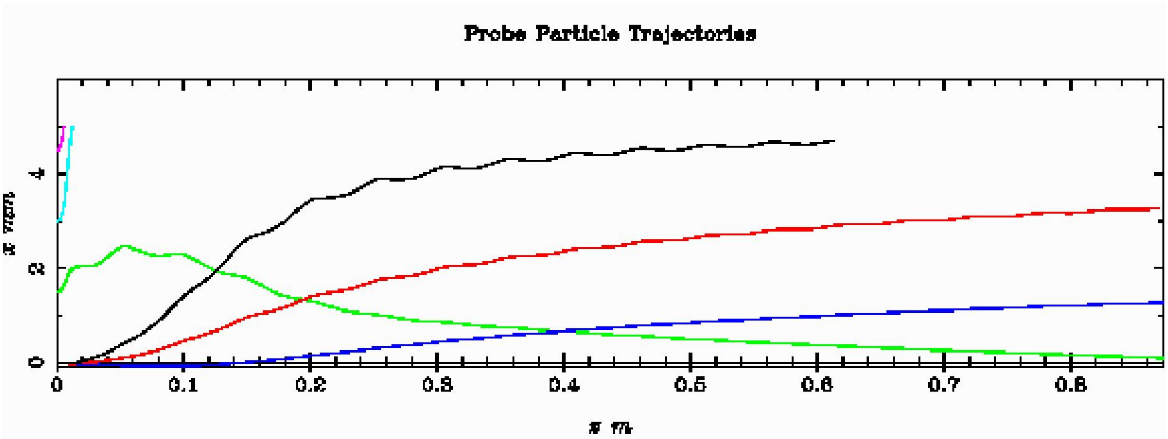

Fig. 4.10 Probe particle trajectory along the linac with a solenoid over the buncher section

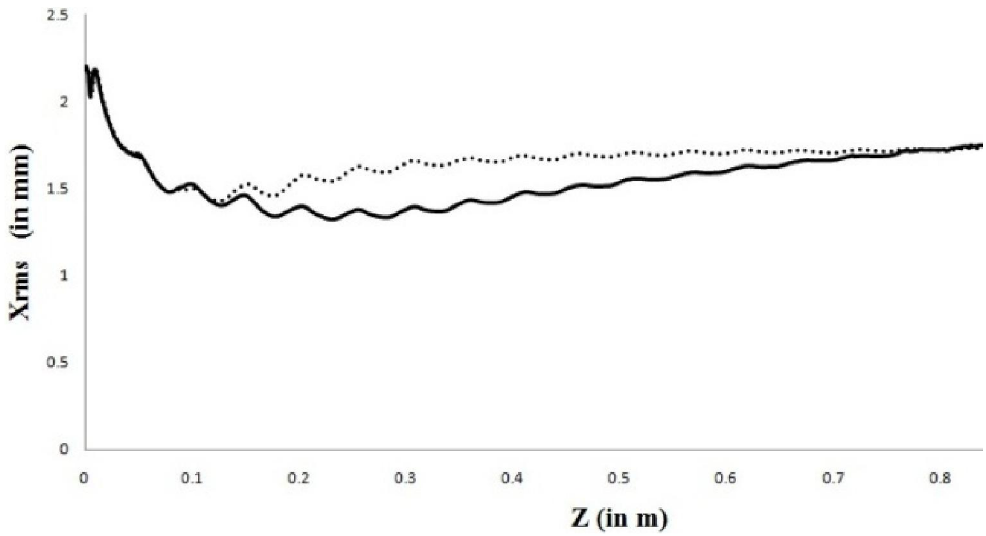

Fig. 4.11 Beam envelope with space charge (dotted line) and with application of solenoid (solid line)

4.1.2.2 GROWTH OF TRANSVERSE EMITTANCE

Fig. 4.12 describes the transverse emittance growth along the linac. The plot shows that application of solenoid over the buncher cells reduces the emittance growth along the linac structure.

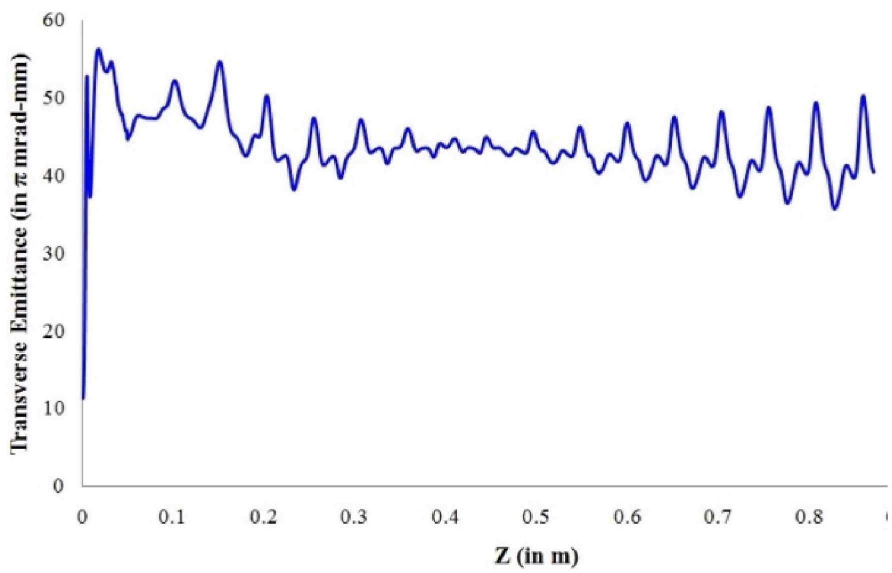

Fig. 4.12 Transverse emittance along the linac structure

To study the effect of variation of beam size on emittance growth, the input rms beam size is varied and the corresponding result is plotted in Fig. 4.13. Further the % transmission of the beam with variation of input beam size is plotted in Fig. 4.14. The decrease in beam transmission for small beam size can be attributed to intense space charge effect [19]-[22]. This shows that an optimum value of the input rms beam size should be chosen in order to prevent emittance growth and higher transmission efficiency.

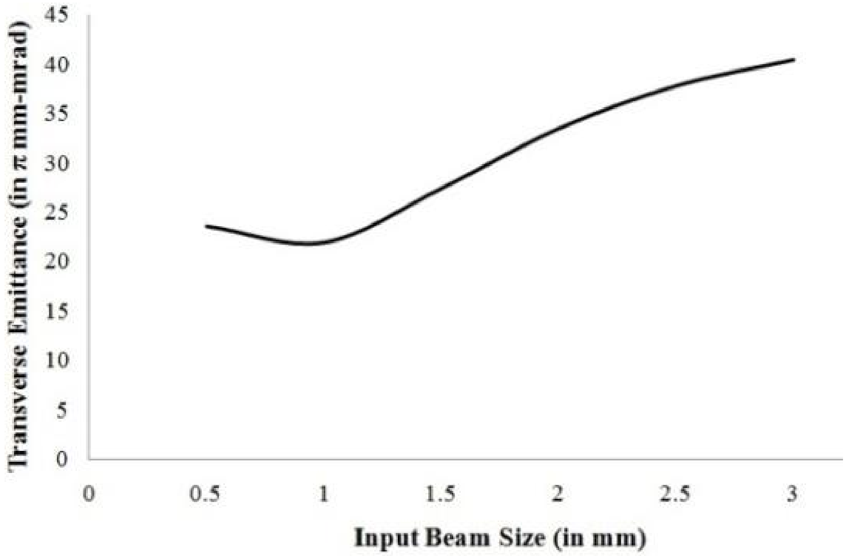

Fig. 4.13 Growth of transverse emittance with input beam size

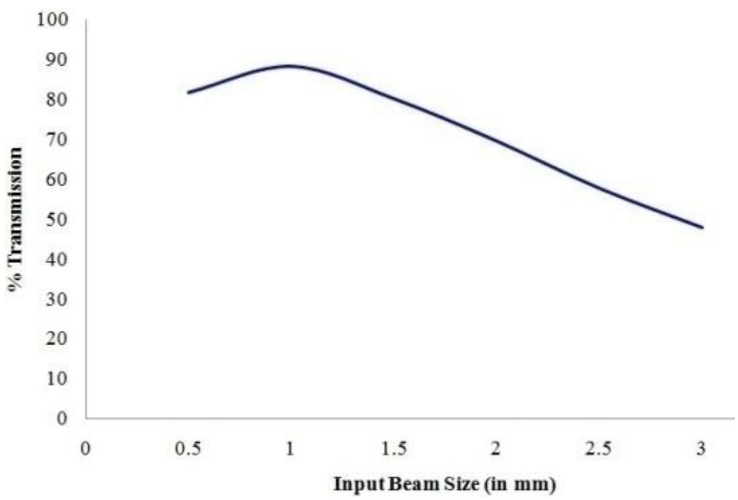

Fig. 4.14 % Transmission with variation of input beam size

4.1.2.3 STUDY OF DIVERGENCE OF THE BEAM

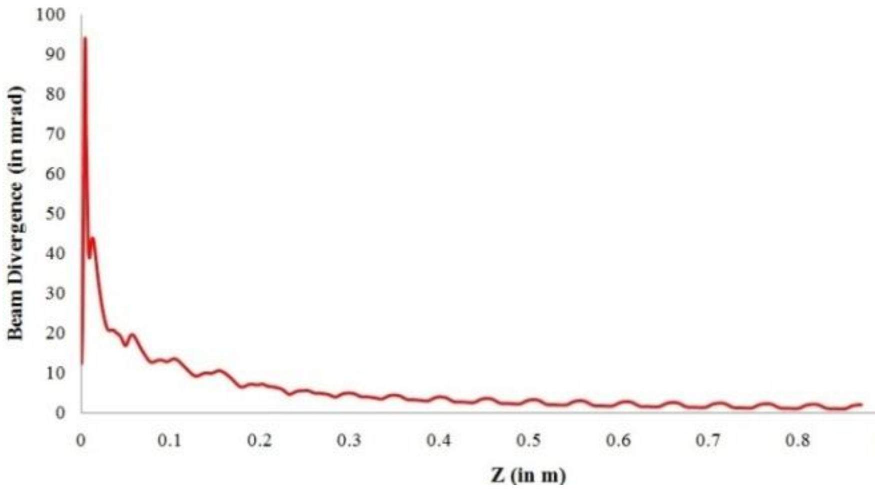

Fig. 4.15 Beam divergence along the linac

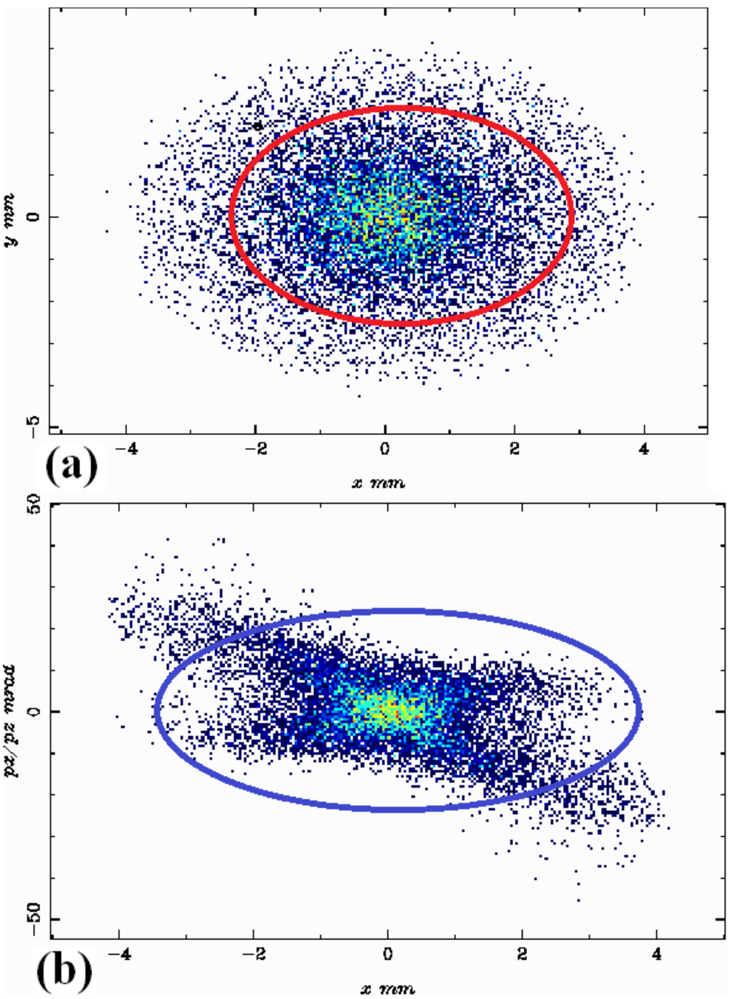

Fig. 4.16 (a) Beam size (red oval) (b) Beam divergence (blue oval) after buncher section

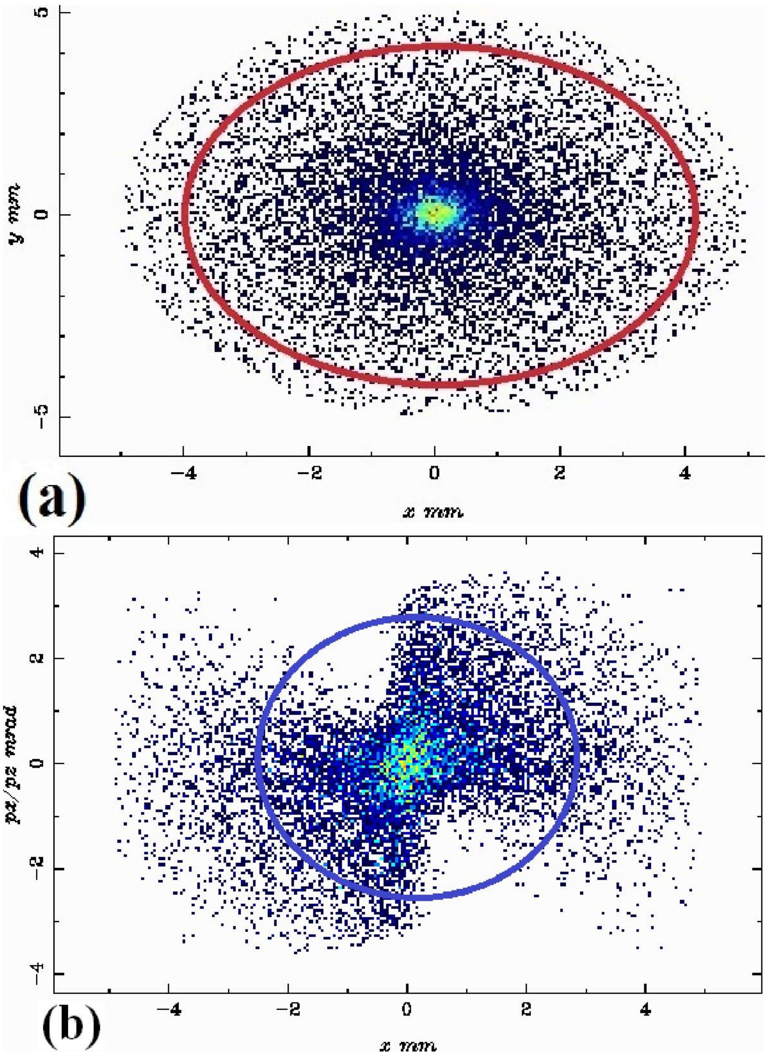

Fig. 4.17 (a) Beam size (red oval), and (b) Beam divergence (blue oval) at the end of the linac

The divergence of the beam is plotted along the linac structure, as shown in Fig. 4.15. It is clear that the divergence decreases along the linac and beam converges to a smaller spot size. This conclusion can be drawn from the phase plots of the beam size and divergence after the buncher section and at the end of the linac.

In Fig. 4.16, the beam divergence after the buncher section is very high which is 20 mrad. At the end of the linac the divergence of the beam is 3.5 mrad as shown in Fig. 4.17.

4.2. COMPARISON OF EXPERIMENTAL DATA AND THEORETICAL BEAM DYNAMICS SIMULATION

It has been found that the optimized output beam dynamics parameters of 10 MeV linac are consistent with the output parameters of the 10 MeV lattice design [21] and experimental observations [22, 23, 65, 66]. A comparison between beam dynamics simulation results and experimental observations are presented in the Table 4.3.

Table 4.3. Comparison of simulation data with experimental observation

Beam Parameters	ASTRA Simulation Results	Experimental Observation
Beam Energy	10 MeV	10 MeV
Beam Energy Spread	5 % of energy gain	10 % of energy gain
Beam Current	120 mA	100 mA
Beam Size	8 mm	5-10 mm
Beam Divergence	3 mrad	3-5 mrad
% Transmission	24 %	20-25 %

From the experimental results, the energy gain of the linac is observed to be 10 MeV [22, 65] which matches with our simulation result and validates the beam dynamics simulation results.

The energy spread of the beam is found to be 10 % of the energy gain that is ≈ 1 MeV. But from simulation we find the energy spread of the beam is 5% of the maximum energy gain which corresponds to ≈ 0.5 MeV. This mismatch is due to the fact that we have presented our result for a single bunch formed from an initial beam phase width of 180^0 and tracked along the linac. But in actual experimental case there are 28560 numbers of full RF cycles in a macro pulse. So it is believed that the energy spread of 10% is due the electrons which are in decelerating phase. These electrons in the decelerating phase increase the longitudinal bunch length of the trailing bunch. An increase in longitudinal phase width proportionally increases the final energy spread in the output beam from the linac.

The beam spot size has been measured to be 50 mm [22] on a glass plate which is being irradiated with 10 MeV beam and placed at a distance of 200 mm below the scan horn. The measured divergence angle 5 mrad [22], while the expected value of beam divergence is 3-4 mrad [21]. So the beam spot size is ~ 10 mm. Further the beam spot size has been measured [66] and it is of the order of 5-10 mm with a divergence ~ 3-4 mrad. From beam dynamics simulation we find the beam size to be 8 mm with a divergence ~ 3.5 mrad and the simulation data is consistent with experimental observations.

We have taken 180^0 phase injection of the electron beam into the linac and we get 48 % transmission. This result matches with the the simulation using PARMELA beam dynamics code [21]. But in the experimental case the injected electron beam is of 10 μs pulse and the resonant frequency of linac cavity is 2856 MHz and one rf cycle is 0.35 ns. Thus the injected beam acts like a dc beam for the linac cavity and 360^0 injection phase is considered. So for 360^0 injection phase the simulated value of transmission efficiency is 24 %. Experimental observations give a transmission efficiency of 20-25 % [23]. Thus the simulated value of transmission of electron beam is consistent with experimental observation.

The accelerator is operational at 10 MeV, 3 kW with a peak current of 100 mA [23]. With a transmission efficiency of 24% we get a beam current of 120 mA from beam dynamics simulation for an input beam current of 500 mA from electron gun. The simulation data matches with the experimental observation within experimental error.

4.3. CONCLUSION

For a 10 MeV linac, the effects of the space charge and typical beam parameters like variation of beam size, divergence, emittance growth have been studied theoretically. We conclude from these beam dynamics studies that space charge effect plays a pivotal role in the buncher and first few accelerating cells of the cavity of the 10 MeV linac. So a solenoid of strength 15000 Ampere-Turns is to be applied over the buncher section to compensate the space charge effect. Further the simulation results are consistent with the experimental results within the limit of experimental errors.

CHAPTER 5

STUDY OF BEAM DYNAMICS IN 100MeV, 100 kW ELECTRON LINAC

Neutron sources have played an important role in various nuclear physics and material science experiments. Among the various types of neutron sources namely, nuclear reactor, radio-isotope and accelerator based neutron sources, reactor based neutron sources offer high neutron flux density but with poor resolution of the energy spectrum. Although the radio-isotope based neutron sources offer low cost, quite accurately calculable neutron flux intensity, but they are not well suited for high- resolution measurements because of poor resolution of neutron energies. On the other hand, Accelerator based neutron sources [2, 7] are highly efficient to produce short burst of neutrons by photo-nuclear and photo-fission reaction mechanisms [9] over a broad continuous energy spectrum that extends from thermal energies to several MeVs. They have distinct advantages over reactor and radio-isotope based neutron sources and are used for neutron cross-section experiments with high resolution.

A growing interest in electron beam based pulsed neutron generators have increased in the recent years because of their ergonomics. For neutron beam irradiation application areas like material science studies and measurement of neutron cross-section, scattering cross-section, capture cross section, fission cross section via (n,γ), (n, xn) and (n, f) reactions at different energies for various materials linacs require 30-100 MeV pulsed electron beams of several kilowatts. A 100 MeV and 100 kW accelerator facility for neutron generation is under development at Accelerator and Pulse Power Division, BARC, Mumbai.

The important components of the facility are an S-band electron linac, beam transport system to the target complex, the neutron producing target. Considerable high beam power obviously demands minimizing the high-energy particles loss during their acceleration and transport. In this chapter, we present ASTRA [14] and ELEGANT [15] simulation results and beam dynamics study [5, 11, 28, 45] in the 100 MeV linac structure

5.1. BEAM DYNAMICS OF A 100 MEV STANDING WAVE STRUCTURE

5.1.1 GENERAL LAYOUT OF THE LINAC

A schematic of the 100 MeV standing wave structure is given in Fig. 5.1 and the main design parameters are specified in Table 5.1. It consists of an injector section, two accelerating sections and a bunch compressor chicane in between two accelerating sections. The injector section consists of a DC thermionic gun, followed by a pre buncher and buncher section. An electron gun having LaB_6 cathode injects the beam of 85 keV into the linac. The prebuncher is a 2856 MHz cell with a length 65 mm, gap of 5 mm and diameter of 48.95. The buncher section consists of 4 coupled cavity biperiodic accelerating cells operating in π/2 mode at a frequency of 2856 MHz and each of length 45, 48, 50 and 52 mm respectively. The electron beam is being injected into the buncher cavitiy at an offcrest angle of 40^0. The accelerating sections consist of 10 S-band linacs SW1, SW2, …, SW10, each of which is composed of one standing wave cavity of length 0.884 m operating at a frequency of 2856 MHz. Each of these linacs requires proper lattice design in order to minimize the transverse emittance. The Linac SW1 and SW2 include horizontal corrector and a vertical corrector, beam position monitor and quadrupoles.

The accelerating cavity of 10 S-band linacs consists of 17 accelerating cells operating in π/2 mode at a frequency of 2856 MHz. The length of each accelerating cell is 52 mm. The bore radius is 5mm for all the buncher cells and the accelerating cells. The effective shunt impedance for the buncher cells is ~80 MΩ/m, while for the accelerating cells the effective shunt impedance is ~ 90 MΩ /m. The prebuncher and a buncher at 2856 MHz initiate the bunching of the 85 keV electrons injected from the electron gun and the final energy of the electron from the injector is 2.5 MeV. At this energy the effect of space charge is important. The effect of space charge on the beam envelope and corresponding emittance growth may lead to the loss of beam. So we ensure beam focusing by solenoids up to the bunching system exit to compensate space charge. The magnetic field strength of solenoid over the buncher cavity is 0.06.

The SW1,…, SW5 linacs exist after the injector section and accelerate the bunched electron from the injector section from an energy of 2.5 MeV to an energy of 54 MeV with an off-crest angle 3^0 and thus provides the necessary energy-time correlation that is required by the bunch compressor to compress the bunch. The bunch compressor is a 4 dipole chicane magnet and it compresses the beam from the SW5 linac from 50 ps to 20 ps. The SW6,…, SW10 linac exists between the bunch compressor and the beam transport line and these linacs accelerate the beam from 54 MeV to 100 MeV. The rms energy spread becomes 7% from 10%.

Quadrupole doublets are placed in between each cavity sections along with drift spaces to focus the beam during acceleration. The length of quadrupole doublets are of 0.250 m each. The focusing strengths of doublets are 5.50 each. Further upstream the bunch compressor quadrupole triplet of length 0.05, 0.1 and 0.05 each having strength 6.5, -15, 25.0 respectively along with steering magnets are used to focus the beam before it enters the chicane magnet. Downstream the bunch compressor quadrupoles of length 0.25 and strength 4.0, -6.1, 10.6, -7.9, 4.8 are used to focus the beam before it enters the linac SW6.

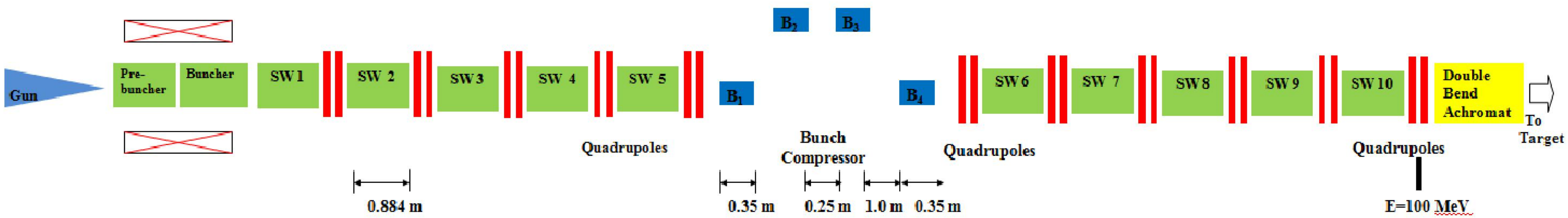

Fig. 5.1 Schematic diagram of 100 MeV standing wave Linac

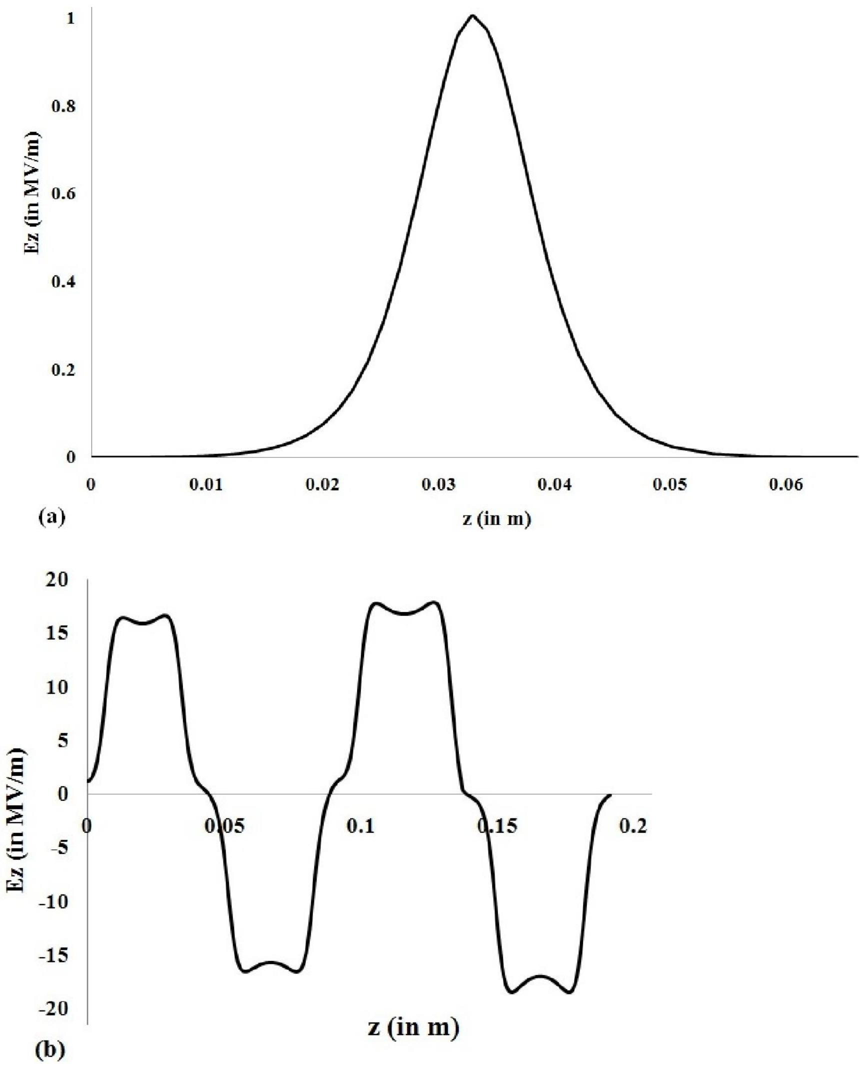

Fig. 5.2 Longitudinal electric field profile (from CST Microwave Studio)

(a) Pre Buncher, (b) Buncher

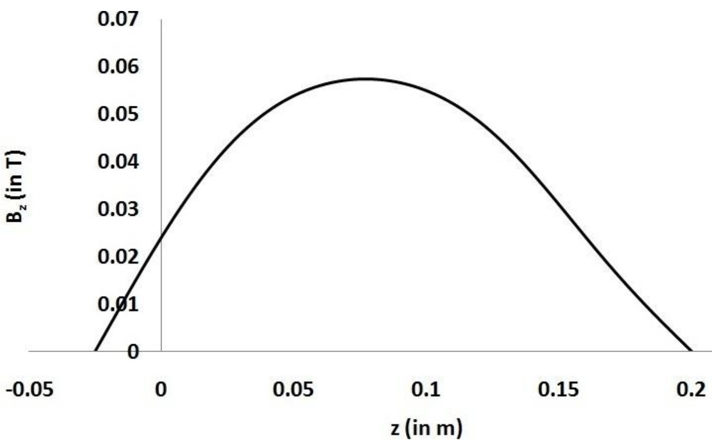

Fig. 5.3 Solenoid field profile (from CST Particle Studio)

To study the beam dynamics the longitudinal electric field components on the symmetry axis (r=0) of the prebuncher and buncher section have been computed using CST Microwave Studio [54]. The electric field profiles are shown in Fig. 5.2. The solenoid field profile is computed with CST Particle studio [54] and is shown in Fig. 5.3. The beam dynamics simulation of injector section is carried out with ASTRA [14] and that of linacs including bunch compressor is carried out with ELEGANT [15].

Table 5.1. Main specification of the 100 MeV standing wave electron Linac

Parameters	Values Unit
RF Frequency	2856 MHz
Beam Energy	100 MeV
Beam Current (Max.)	250 mA
Energy Spread (1σ)	7 %
Emittance (1σ)	4×10^{-7} m-rad
Beam Pulse Width	8 μs
Accelerating Structure	10 units/ 0.884 m
Klystron	15 MW
RF Pulse Width	10 μs
RF Pulse Repetition rate (max.)	400 Hz

Bunch Compressor

In order to control the beam size at the bending section achromat, the energy spread of the beam at the end of the linac should be small. So we adopted a 4 dipole chicane system [67] which seems to be an economical and convenient approach for a relatively small-scale linac of 100 MeV [68]. The 4 dipole chicane magnet is designed to compress the bunch to have shorter pulses at the output for high quality beam. From the results of longitudinal beam dynamics simulations the parameters of the bunch compressor is chosen to reduce the bunch length to 20 ps. The bunch length can be controlled by optimal choice of the momentum compaction factor R_{56} that is a function of the desired bunch compression ratio, energy spread and the rf phase angle of the linacs before the chicane magnet. R_{56} value is not unique and it depends on the bunch charge. R_{56} is determined from the design parameter of the chicane such as bending angles, bend lengths and drift lengths [67, 69]. For relativistic electrons and small bending angles the R_{56} value of the bunch compressor is given by

$$R_{56} \approx -2\theta_B^2 \left(\Delta L + \frac{2}{3} L_B\right)$$

Where θ_B is the bending angle of the dipole, ΔL is the drift length between the first two and the last two dipoles. L_B is the length of each dipole magnet.

The bunch compressor of this accelerator facility provides a bunch compression in a factor of 3. The design parameters for bunch compressor are given in Table-5.2.

Table 5.2. Parameters of the bunch compressor for 100 MeV standing wave Linac

Beam Energy	54 MeV
Initial bunch length	50 ps
Final bunch length	20 ps
Magnetic Field	0.080743 T or 807.43 gauss
R_{56}	-60.8 mm
Bending Angle	0.157 rad
Maximum Dispersion	220 mm
Length of Bending Magnet	35 cm

5.1.2 LONGITUDINAL BEAM DYNAMICS

The phase space plot of the electron bunch after the injector section is shown in Fig. 5.4. Fig. 5.13 describes the longitudinal dynamics of the electron bunch during acceleration and compression processs. The bunched beam after the SW5 linac is shown in Fig. 5.5 (a). The 4-dipole chicane compress the bunch from 50 ps to 20 ps as shown in Fig. 5.5 (b). The final bunch at the linac SW10 output as shown in Fig. 5.5 (c) indicates that that the energy gain of 100 MeV is achieved with ≈ 7 % energy spread. Table 5.3 shows the typical beam parameters at injection and at the output.

Table 5.3. Beam parameters at injection and at the output of 100 MeV standing wave Linac

Beam Parameter	Input Value	Output Value
Energy	2.5 MeV	104.0 MeV
Energy Spread	3 %	7 %
Bunch Length	60 ps	20 ps
Beam size	4.0 mm	8.0 mm
Beam divergence	1.5 mrad	2.0 mrad

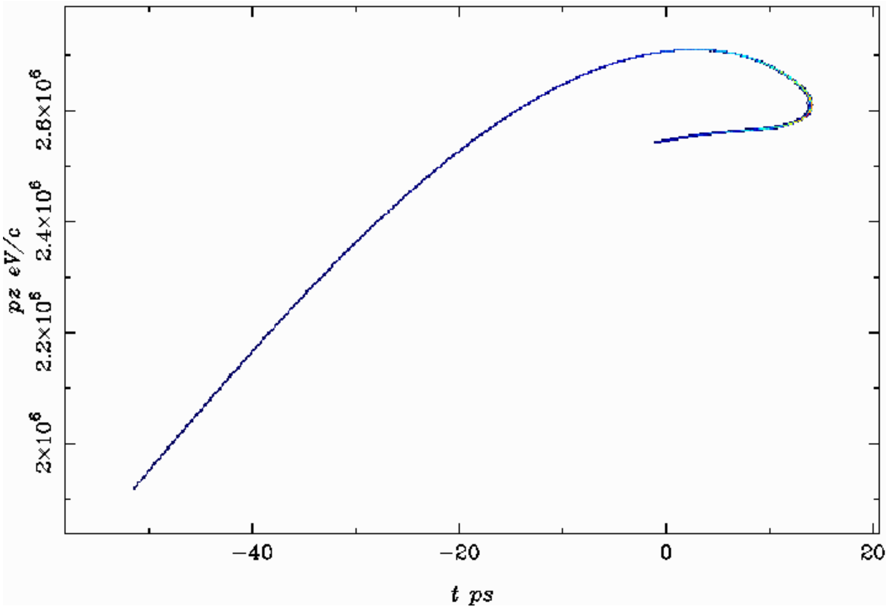

(a)

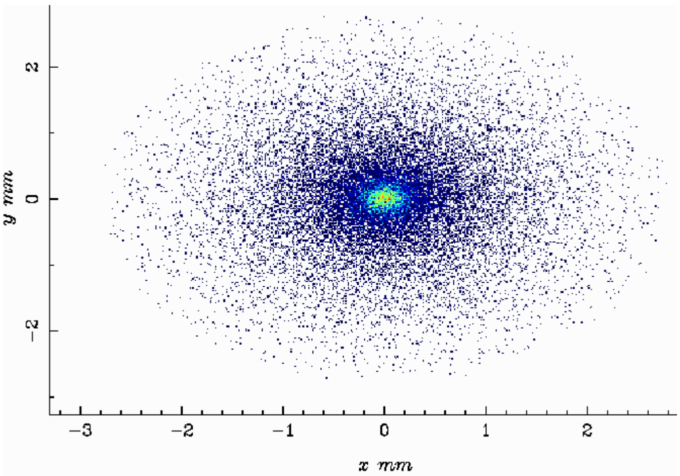

(b)

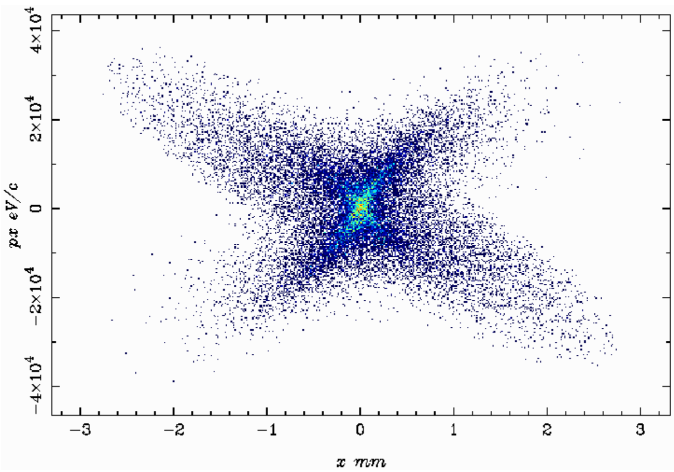

(c)

Fig. 5.4 Longitudinal dynamics of the bunch after injector section (a) bunch shape (b) beam size (c) divergence

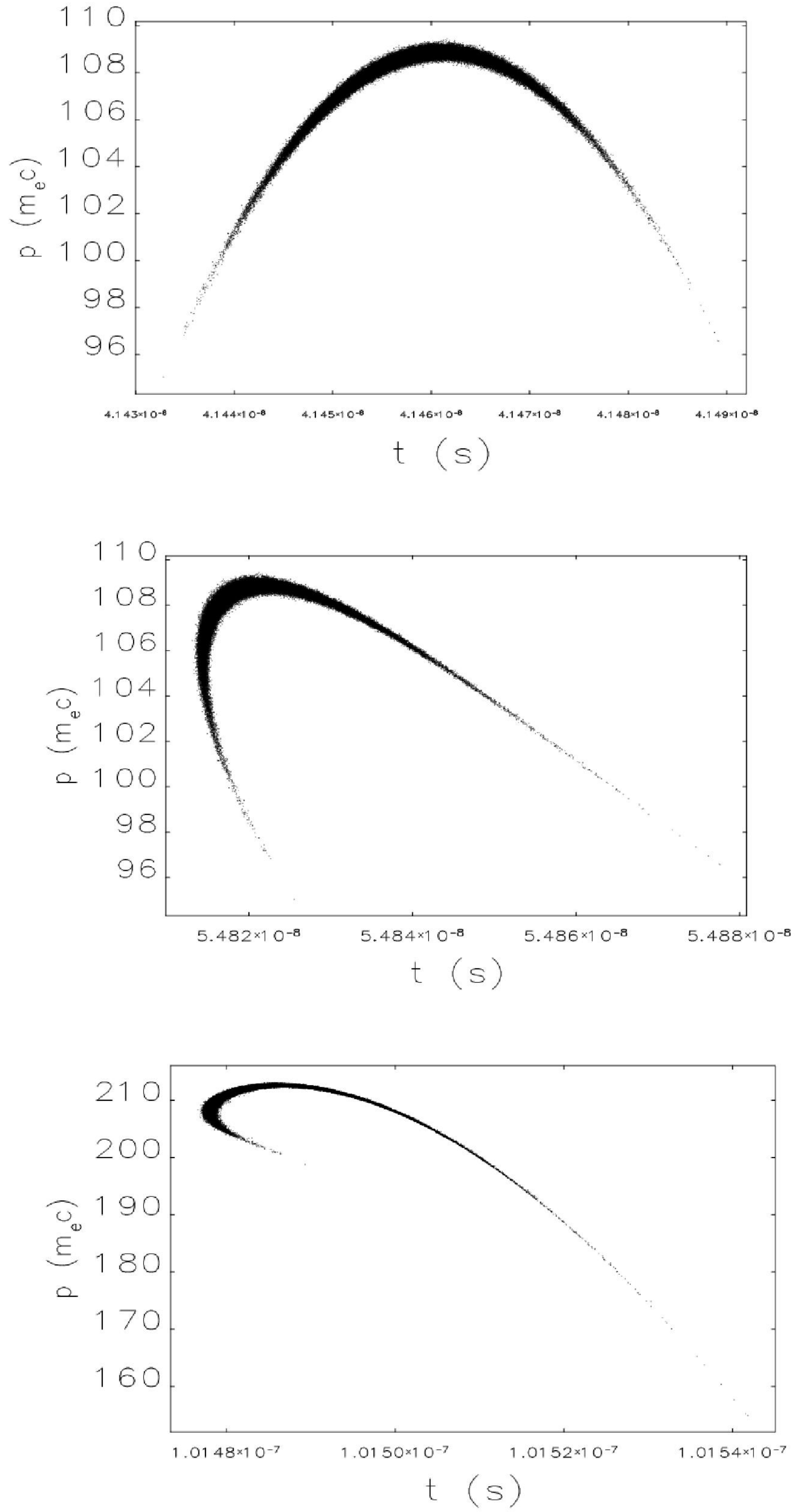

Fig. 5.5 Longitudinal dynamics of the bunch in 100 MeV standing wave linac

(a) before compression (b) after bunch compressor (c) at the end of linac 10

5.1.3 TRANSVERSE DYNAMICS

The beam envelopes in two transverse planes is shown in Fig. 5.6. The quadrupole focusing scheme ensures a focused beam at the output.

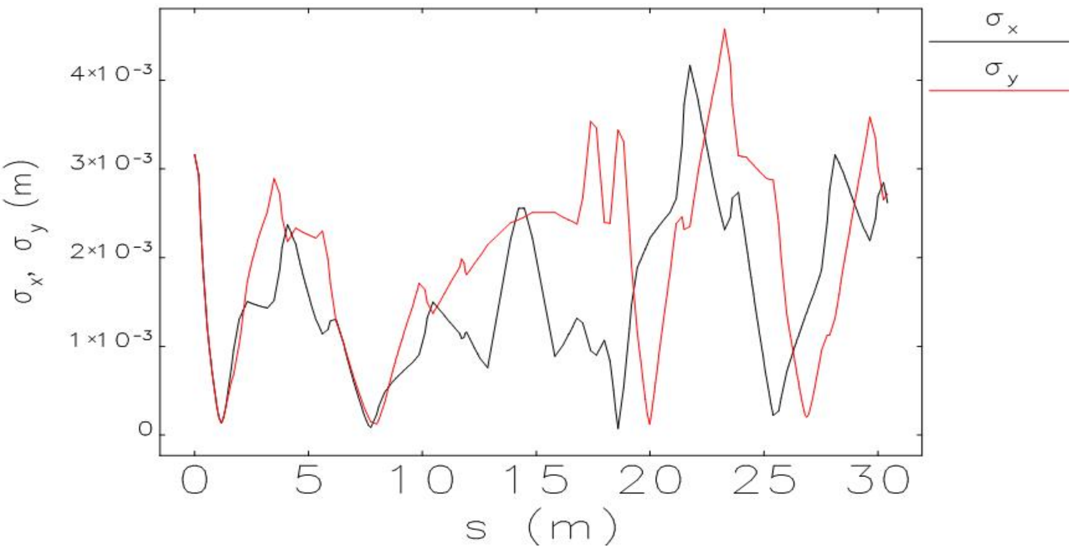

Fig. 5.6 Beam envelope in two transverse planes in 100 MeV standing wave linac

The transverse emittance growth in the two transverse planes is plotted in Fig. 5.7 along the linac. The growth of transverse emittance along the linac is minimized to ensure delivery of a high quality beam with low loss. The divergence decreases along the linac and beam converges to a smaller spot size of diameter 8 mm as shown in Fig. 5.8.

Fig. 5.9 shows the variation of Twiss parameter α along the linac. The value of $\alpha_{x,y} \sim 0$ indicates that the beam envelope is parallel to the axis at the centre of the quadrupole lens. The variation of Twiss parameter β is shown in Fig. 5.10. The value of $\beta_y < 40$ indicates that the envelope width is smaller in y-direction and the output beam is elliptical.

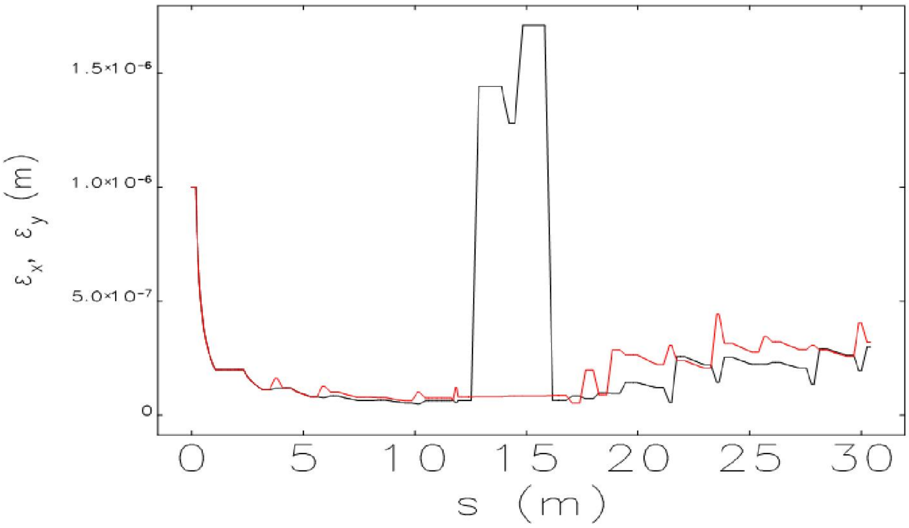

Fig. 5.7 Transverse emittance along the 100 MeV standing wave linac

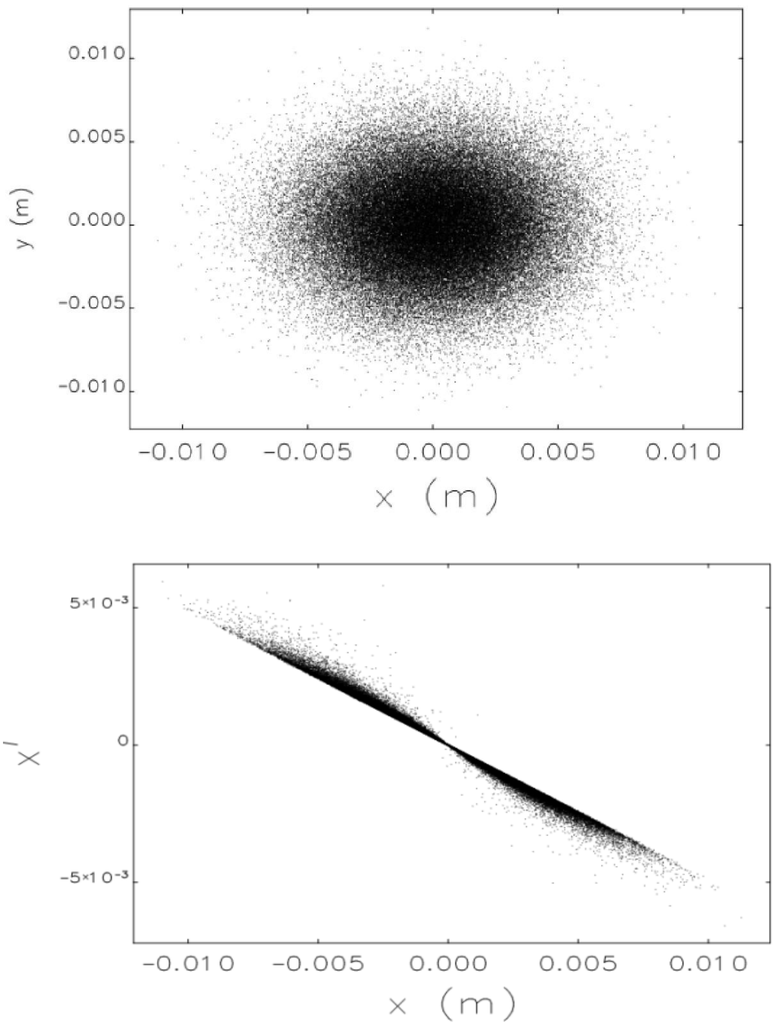

Fig. 5.8 (a) Beam size, and (b) Beam divergence at the end of the 100 MeV standing wave linac

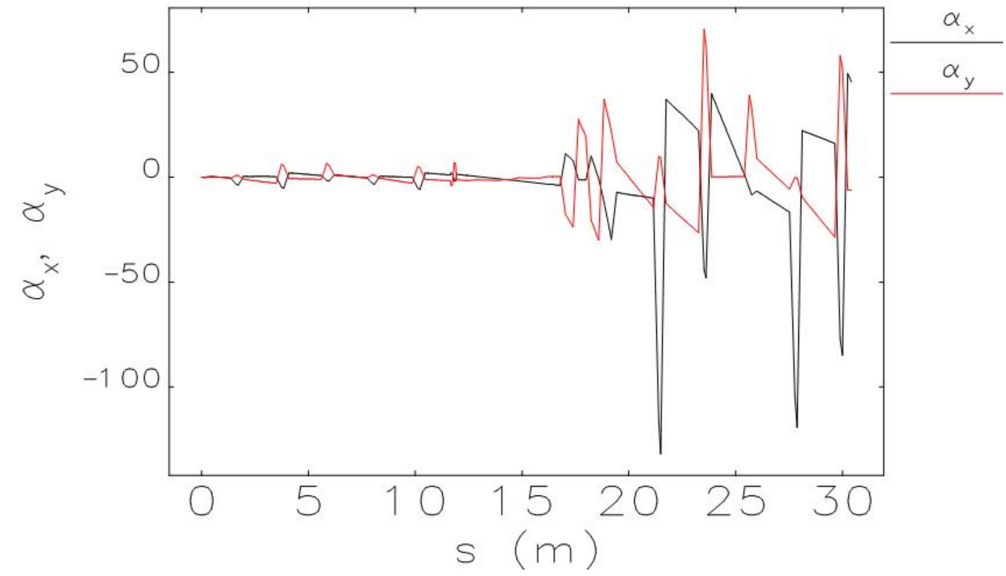

Fig. 5.9 Variation of Twiss parameter α along 100 MeV standing wave linac

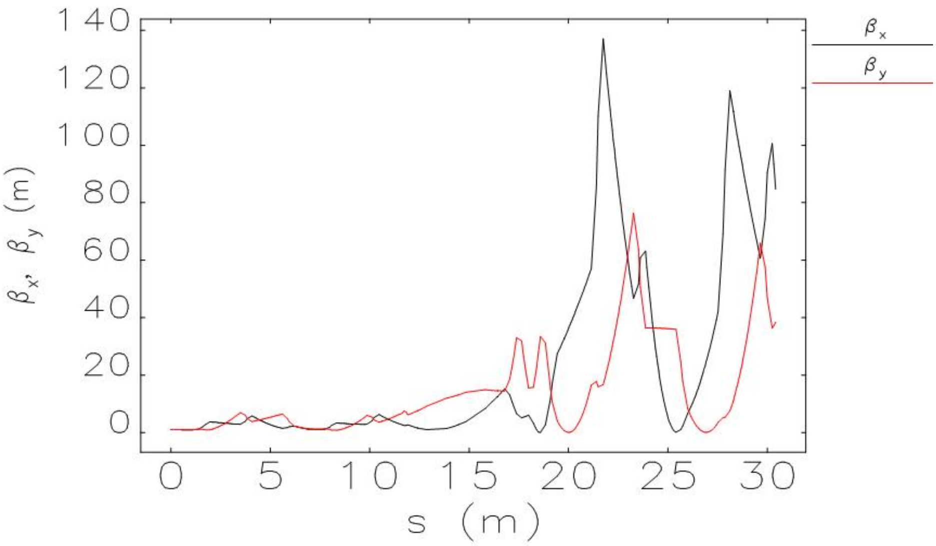

Fig. 5.10 Variation of Twiss parameter β along 100 MeV standing wave linac

The dispersion in the chicane magnet during bunch compression along with the twiss parameter β is shown in Fig. 5.11. The green coloured picture in this plot indicates the lattice profile over the entire length of the linac after injector section.

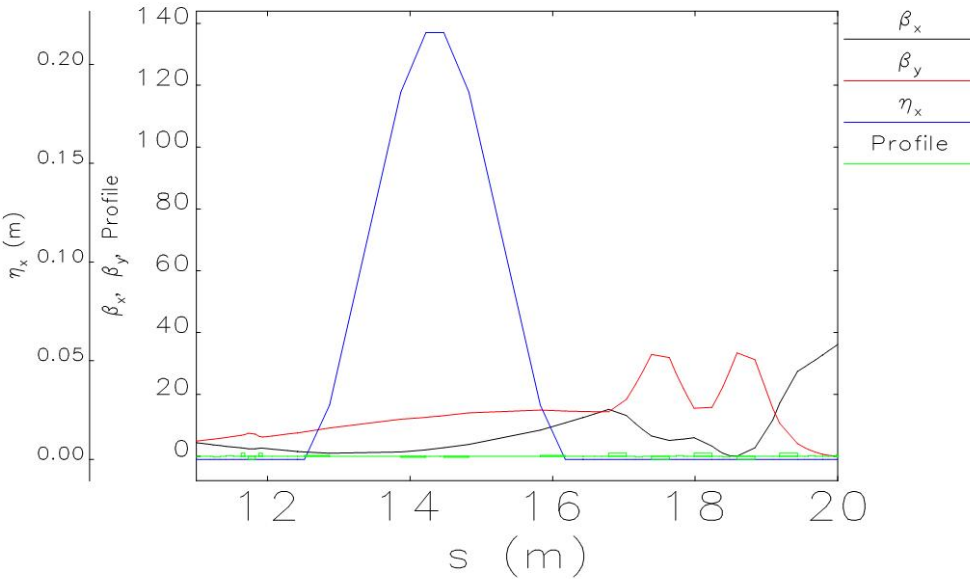

Fig. 5.11 Variation of Twiss parameter β and the dispersion in chicane for 100 MeV standing wave linac

5.2.BEAM DYNAMICS OF A 100 MEV TRAVELLING WAVE STRUCTURE

5.2.1 GENERAL LAYOUT OF THE LINAC

A schematic of the 100 MeV travelling wave structure is given in Fig. 5.12 and the main design parameters are specified in Table 5.4 and Table 5.5. It consists of an injector section, two accelerating sections and a bunch compressor chicane in between two accelerating sections. The injector section consists of a DC thermionic gun, followed by a pre buncher and buncher section, whose specifications are same as section 5.1.

The accelerating sections consist of 10 S-band linacs TWS1, TWS2, …, TWS10, each of which is composed of one SLAC type travelling wave cavity of length 1.26 m operating at a frequency of 2856 MHz. Each of these linacs requires proper lattice design in order to minimize the transverse emittance. The Linac TWS1 and TWS2 include horizontal corrector and a vertical corrector, beam position monitor and quadrupoles.

Table 5.4. Main specification of the 100 MeV travelling wave electron Linac

Parameters	Values Unit
RF Frequency	2856 MHz
Beam Energy	100 MeV
Beam Current (Max.)	500 mA
Energy Spread (1σ)	5 %
Emittance (1σ)	2×10^{-7} m-rad
Beam Pulse Width	4 μs
Accelerating Structure	10 units / 1.26 m
Klystron	6 units (30 MW)
RF Pulse Width	5 μs
RF Pulse Repetition rate (max.)	400 Hz

The TWS1,…, TWS5 linacs exist after the injector section and accelerate the bunched electron from the injector section from an energy of 2.5 MeV to an energy of 53 MeV with an off-crest angle 8.8^0 and thus provides the necessary energy-time correlation that is required by the bunch compressor to compress the bunch. The bunch compressor is a 4 dipole chicane magnet and it compresses the beam from the TWS5 linac from 60 ps to 20 ps. The TWS6,…,TWS10 linac exists between the bunch compressor and the beam transport line and these linacs accelerate the beam from 53 MeV to 100 MeV. The rms energy spread becomes 5% from 7%.

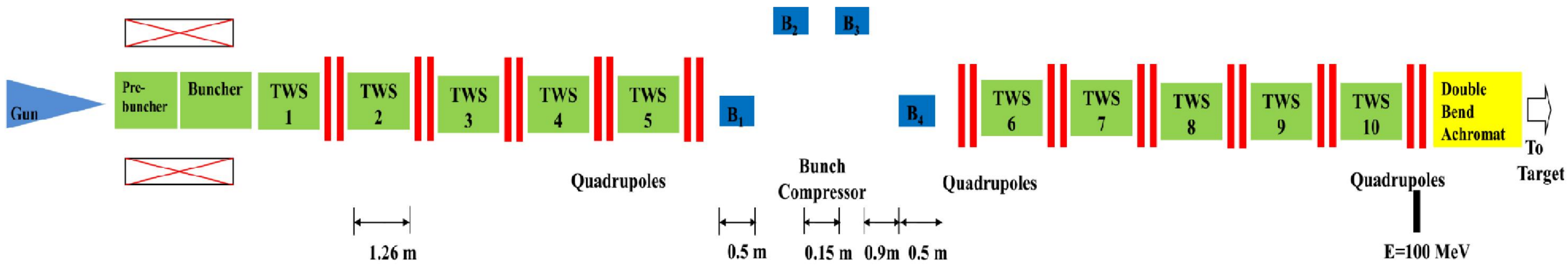

Fig. 5.12 Schematic diagram of 100 MeV travelling wave linac

Quadrupole doublets are placed in between each cavity sections along with drift spaces to focus the beam during acceleration. The length of quadrupole doublets are of 0.250 m each. The focusing strengths of doublets are 5.50 each. Further upstream the bunch compressor quadrupole triplet of length 0.05, 0.1 and 0.05 each having strength 6.5, -15, 25.0 respectively along with steering magnets are used to focus the beam before it enters the chicane magnet. Down stream the bunch compressor quadrupoles of length 0.25 and strength 5.2, -6.1, 10.6, -7.9, 5.2 are used to focus the beam before it enters the linac TWS6.

Table 5.5. Main specification of 100 MeV travelling wave accelerating structure

Parameters	Values Unit
Operation RF Frequency	2856 MHz
Operation Temperature	40 ± 0.2˚C
No. of cells	34 (regular cells) + 2 (coupler cells)
Section Length	34.989783 mm
Cell Length	1260 mm (36 cells)
Phase shift per cell	120˚ (2π/3)
Shunt Impedance	51.514 – 57.052 MΩ/m
Q Factor	13806 - 13753
Filing Time	215 ns

To study the beam dynamics the longitudinal electric field components on the symmetry axis (r=0) of the prebuncher and buncher section have been computed using CST Microwave Studio [54]. The electric field profiles are shown in Fig. 5.2. The solenoid field profile is computed with CST Particle studio [54] and is shown in Fig. 5.3. The beam dynamics simulation of injector section is carried out with ASTRA [14] and that of linacs including bunch compressor is carried out with ELEGANT.

Bunch Compressor

We adopted a 4 dipole chicane system which seems to be an economical and convenient approach for a relatively small-scale linac of 100 MeV. From the results of longitudinal beam dynamics simulations the parameters of the bunch compressor is chosen to reduce the bunch length to 20 ps. The bunch compressor of this accelerator facility provides a bunch compression in a factor of 3. The design parameters for bunch compressor are given in Table 5.6.

Table 5.6. Parameters of the bunch compressor for 100 MeV travelling wave Linac

Beam Energy	53 MeV
Initial bunch length	60 ps
Final bunch length	20 ps
Magnetic Field	0.05547 T or 554.7 gauss
R_{56}	-60.8 mm
Bending Angle	0.157 rad
Maximum Dispersion	220 mm
Length of Bending Magnet	50 cm

5.2.2 LONGITUDINAL BEAM DYNAMICS

The phase space plot of the electron bunch after the injector section is shown in Fig. 5.4. Fig. 5.13 describes the longitudinal dynamics of the electron bunch during acceleration and compression processs. The bunched beam after the TWS5 linac is shown in Fig. 5.13 (a).

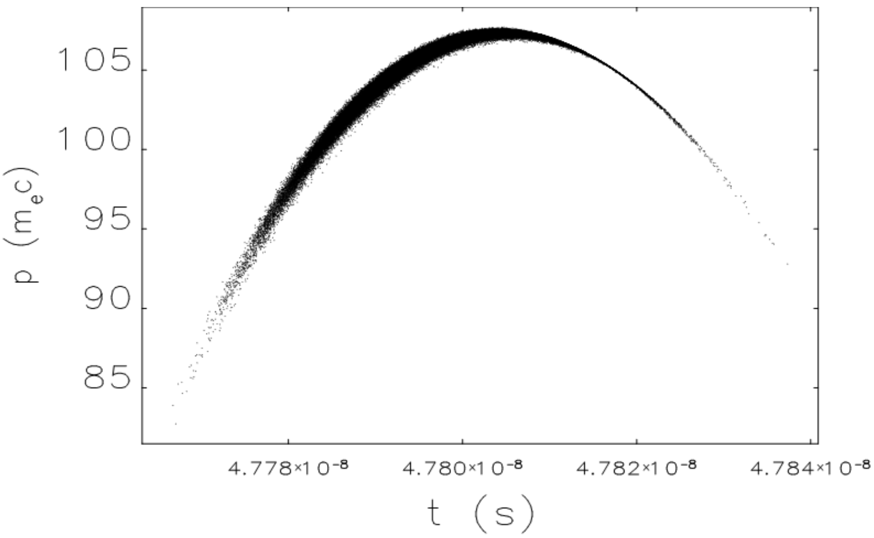

(a)

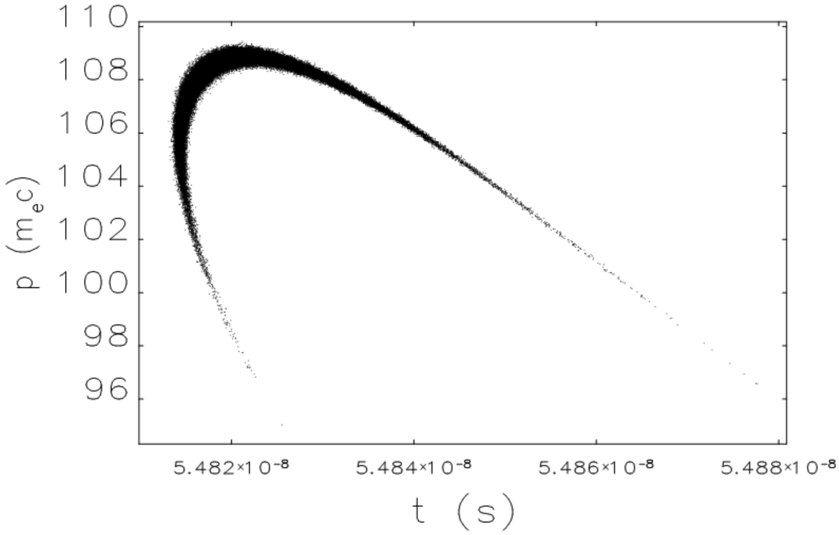

(b)

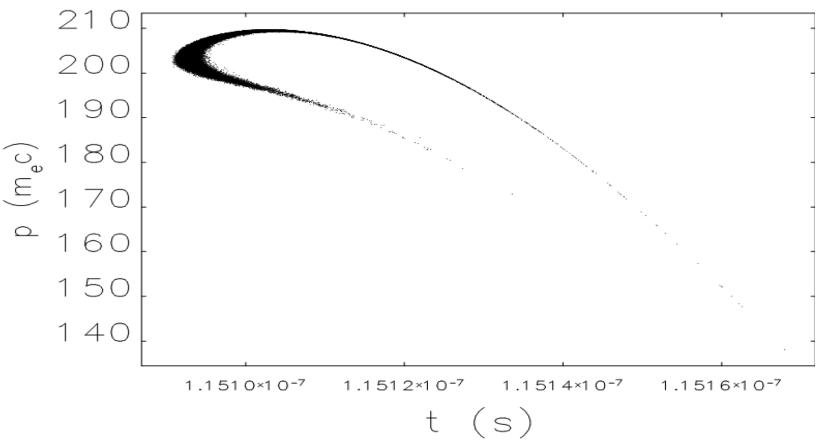

(c)

Fig. 5.13 Longitudinal dynamics of the bunch in 100 MeV travelling wave linac

(a) before compression (b) after bunch compressor (c) at the end of linac 10

Table 5.7. Beam parameters at injection and at the output of 100 MeV travelling wave linac

Beam Parameter	Input Value	Output Value
Energy	2.5 MeV	103.0 MeV
Energy Spread	3 %	5 %
Bunch Length	60 ps	20 ps
Beam size	4.0 mm	2.4 mm
Beam divergence	1.5 mrad	0.5 mrad

The 4-dipole chicane compress the bunch from 60 ps to 20 ps as shown in Fig. 5.13 (b). The final bunch at the linac TWS10 output as shown in Fig. 5.13 (c) indicates that that the energy gain of 100 MeV is achieved with ≈ 5 % energy spread. Table 5.7 shows the typical beam parameters at injection and at the output.

5.2.3 TRANSVERSE DYNAMICS

The beam envelopes in two transverse planes is shown in Fig. 5.14. With the quadrupole focusing scheme the beam is focused to a smaller spot size.

The transverse emittance growth in the two transverse planes is plotted in Fig. 5.15 along the linac. The minimized growth of emittance along the linac ensures delivery of a high quality beam with low loss.

The divergence decreases along the linac and beam converges to a smaller spot size of diameter 2.4 mm as shown in Fig. 5.16.

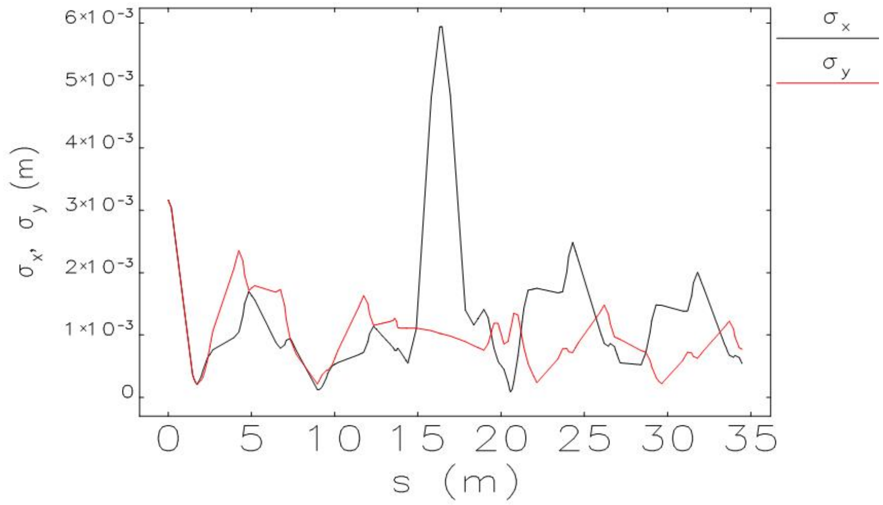

Fig. 5.14 Beam envelope in two transverse planes in 100 MeV travelling wave linac

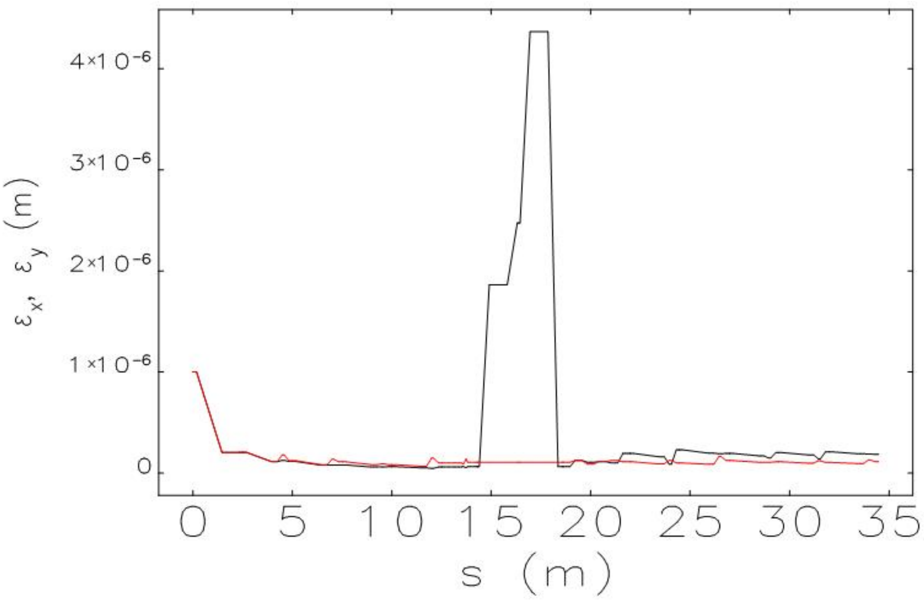

Fig. 5.15 Transverse emittance along the 100 MeV travelling wave linac

Fig. 5.17 describes the variation of Twiss parameter α along the linac. The variation of Twiss parameter β is shown in Fig. 5.18. The value of $\beta_{x,y} < 40$ indicates that the envelope width is smaller and $\alpha_{x,y} \sim 0$ indicates that the beam envelope is parallel to the axis at the centre of the quadrupole lens.

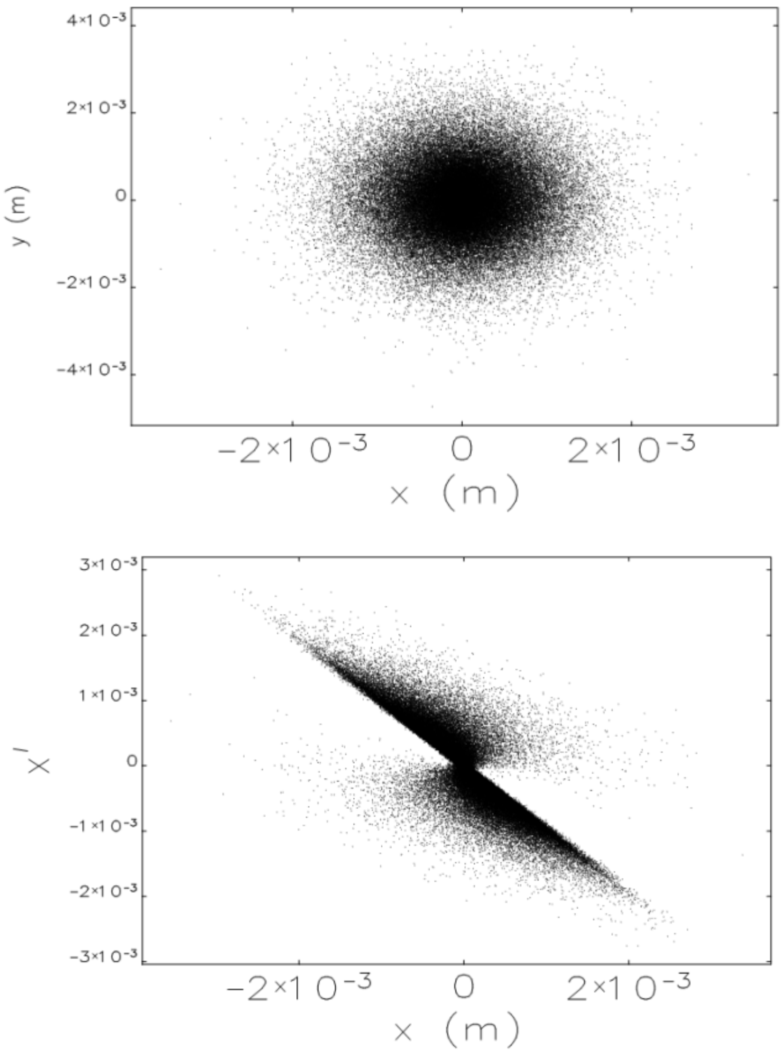

Fig. 5.16 (a) Beam size, and (b) Beam divergence at the end of the 100 MeV travelling wave linac

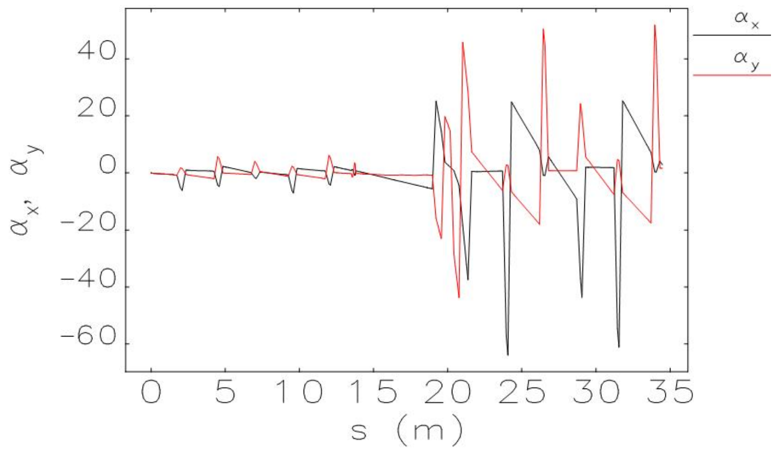

Fig. 5.17 Variation of Twiss parameter α along the 100 MeV travelling wave linac

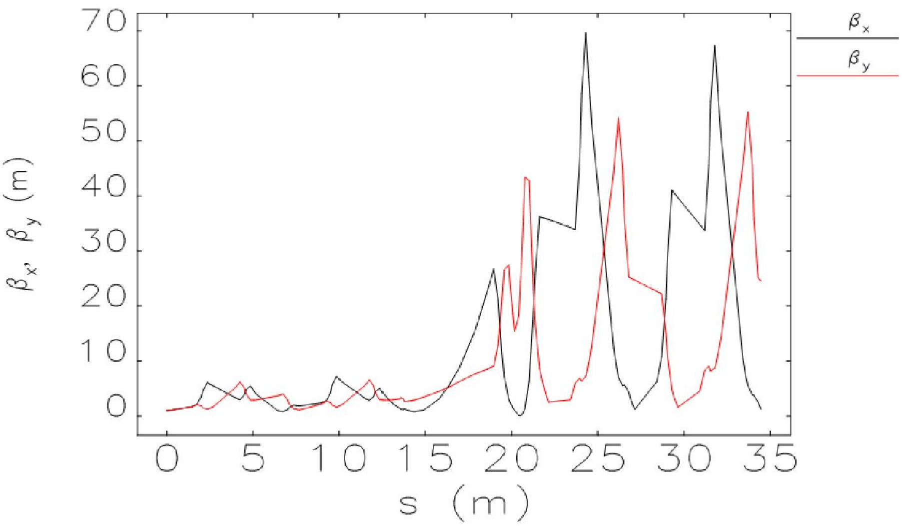

Fig. 5.18 Variation of Twiss parameter β along the 100 MeV travelling wave linac

The dispersion in the chicane magnet along with the twiss parameter β is shown in Fig. 5.19. The green coloured picture in this plot indicates the lattice profile over the entire length of the linac after injector section.

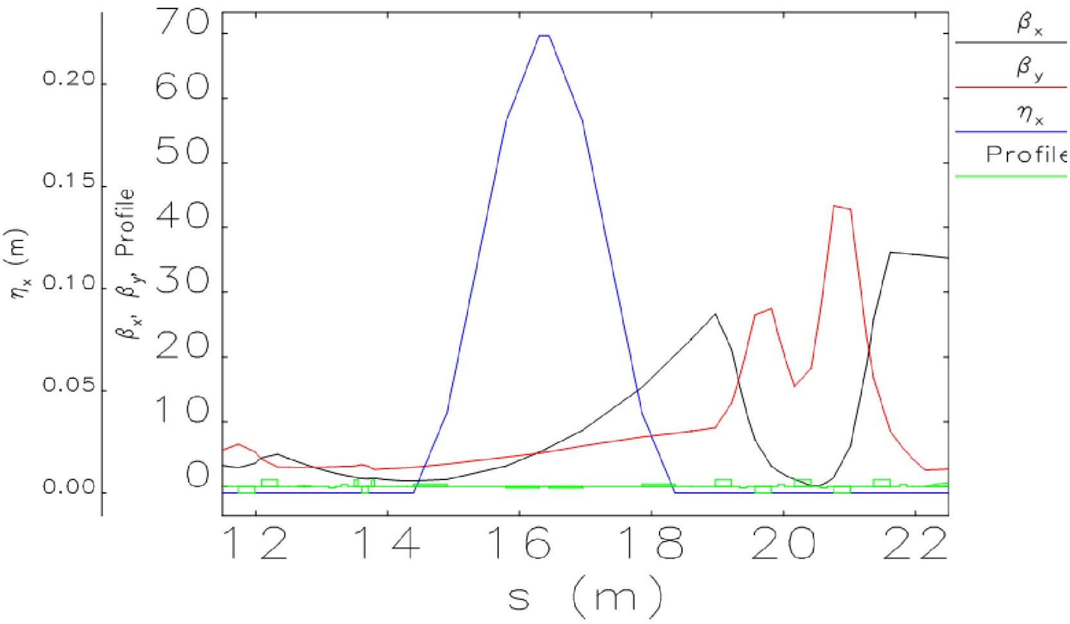

Fig. 5.19 Variation of Twiss parameter β and the dispersion in chicane magnet of 100 MeV travelling wave linac

5.4 CONCLUSION

A start to end simulation for beam dynamics of a 100 MeV, 100 kW linac has been carried out. The effects of the space charge and typical beam parameters like variation of beam size, divergence, emittance growth have been studied theoretically. We conclude from these beam dynamics studies that the desired 100 MeV energy gain is achieved with about 7% energy spread in the output bunched beam for a standing wave linac and the desired 100 MeV energy gain is achieved with about 5% energy spread in the output bunched beam for a travelling wave linac.

Further, the output beam in case of travelling wave linac is small in less diverged and spot size is small as compared to the standing wave linac. The corresponding growth of rms emittance along the linac are smaller. This ensures minimization of hitting of the beam against the cavity wall that may induce growth of radioactivity.

CHAPTER 6

EFFECT OF SPHERICAL ABERRATION ON THE EMITTANCE GROWTH OF A BEAM

In an RF gap of an accelerator, the off-axis particles experience radial electric and magnetic forces. When these particles cross the gap, these forces vary with the radial displacement of the particles and particles experience a net radial impulse due to the time dependent harmonic electric field [10].

Expansion of the radial electric field up to third order leads to a r^3 term whose coefficient gives rise to spherical aberration [24]. This term is responsible for growth of transverse emittance and hence increase the beam size. Taking uniform distribution of the beam, an expression has been derived for the growth of transverse RMS emittance of a bunch crossing an RF gap [70]. In [71] the transverse emittance growth due to spherical aberration has been discussed , but the correlation between the radial increment in momentum and phase spread is neglected. In our analysis we present a generalized expression for transverse emittance growth which incorporates the correlation between third order radial term and phase spread of the bunch.

Invariant envelope solution [72] of the reduced RMS envelope equation for a laminar beam is a minimum for a particle moving in the potential of a RF cavity [72, 73]. An analytical expression has been established for shift of this minimum in the presence of spherical aberration in section 6.2. The spherical aberration leads to a change in the frequency of oscillation of the beam envelope in an RF Cavity [74]. Using Lindstedt –Poincare method

[26], an analytical approach is used to find out the evolution of beam size and the frequency shift.

For most optical elements used for focusing, deflecting, or otherwise manipulating beams of charged particles, the dominant effect is linear and the quantities that characterize it are focal lengths, positions of foci, principal planes, and nodal planes. The perturbations are then the geometric aberrations [75] which measure any departure from linear behaviour and are characterized by the geometric aberration coefficients. The focusing effect of a lens or other optical element may well be changed by mechanical or other imperfections [76, 77]. Lenses are subjected to parasitic aberrations such as deviation of roundedness from perfect circular symmetry, inhomogenity in the magnetic material of pole pieces, and misalignment of a sequence of lenses.

In practice, the final spot size of a beam focused by a magnetic lens depends on typical beam parameters, such as the emittance, variations in beam current, energy, envelope, envelope slopes and nonlinearity of the lens. In ideal case, all particles leaving a point in the object plane arrive at the same point in the image plane. When aberrations are present, particles emerging from an object point with different initial angles arrive at different points in the image plane [78-82]. Spherical aberration is a geometrical phenomenon that arises from third order terms which are neglected under the paraxial approximation [24, 83]. Spherical aberration in a solenoid gives rise to blurring of image and more importantly leads to growth of RMS emittance. Also nonuniformity of space charge introduces spherical aberration in the beam [28]. In earlier works the spherical aberration coefficient has been calculated for uniformly distributed beam taking into account the magnetic field only [43]. In this thesis we include the effect of both magnetic field and self field effects and evaluate the transverse rms emittance growth [84-87] due to spherical aberration for Uniform, Gaussian, Waterbag and parabolic distribution functions.

In section 6.3 of this thesis we have studied the effect of nonlinear terms of the magnetic field in the radial direction that leads to spherical aberration which in turn gives rise to transverse emittance growth. Also we have included the aberration due to nonuniformity of space charge for different beam distributions. In section 6.3.3, we have calculated the transverse rms emittance growth taking into account the combined effect of magnetic field and space charge.

Chromatic aberration occurs [30, 88] when there is a spread in the momentum of the charged particle beam passing through a magnetic lens. Focusing power of a magnetic lens depends inversely on the kinetic energy. So if electrons are present with different kinetic energies, they will be focused at a different distances from a lens; for any image plane, there will be a chromatic disk of confusion rather than a point focus. The spread in kinetic energy can arise from several causes like the statistics of the electron-emission process, ripple in the accelerating voltage etc-. In section 6.4 we have analysed the effect of energy spread of the beam which results in phase space distortion and transverse emittance growth.

6.1. ANALYTICAL FORMULATION OF THE PROBLEM OF RF GAP

6.1.1 EXPRESSION FOR SPHERICAL ABERRATION DUE TO ELECTRIC FIELD

The standing wave electric field solution for E_z near the axis [10] is

$$E_z(r,z,t) = E_a(z)Cos(\omega t + \varphi) \tag{6.1}$$

Radial momentum increment near the axis is $\Delta P_r = q\int_{-\frac{L}{2}}^{+\frac{L}{2}}(E_r - \beta c B_\theta)\, {dz}/{\beta c}$ (6.2)

$$= q\int_{-\frac{L}{2}}^{\frac{L}{2}}\left(-\frac{r}{2}\frac{\partial E_z}{\partial z} - \frac{r^3}{6}\frac{\partial^3 E_z}{\partial z^3} - \beta c\frac{r}{2c^2}\frac{\partial E_z}{\partial t}\right) {dz}/{\beta c}$$

Where we have included the third order term in the expansion of radial electric field.We have considered L as the rf gap length, $\beta=v/c$ is the relativistic factor, B_θ is the azimuthal component of the magnetic field, q is the charge of the particle,

The rate of change of field experienced by a moving particle is the sum of the spatial and temporal variation of the field, so

$$\frac{\partial E_z}{\partial z} = \frac{dE_z}{dz} - \frac{1}{\beta c}\frac{\partial E_z}{\partial t} \tag{6.3}$$

The integral over the total derivative vanishes if the interval L extends to zero field at both ends, or if the field is periodic with period L. The substitution of equation (6.3) in (6.2) and subsequent integration leads to the expression for the radial impulse as

$$\Delta P_r = -\frac{qr}{\beta c}\int_{-\frac{L}{2}}^{+\frac{L}{2}}\left[\left(-\frac{1}{2\beta c}\frac{\partial E_z}{\partial t} + \frac{\beta}{2c}\frac{\partial E_z}{\partial t}\right) + \frac{r^2}{6}\frac{\partial^3 E_z}{\partial z^3}\right]dz \tag{6.4}$$

Using expression (6.1) in (6.4) for total radial impulse, we get $\Delta P_r = C_3 r + C_1 r^3$ (6.5)

where $C_3 = -\frac{q\omega}{2\beta^2 c^2\gamma^2}\int_{-\frac{L}{2}}^{+\frac{L}{2}} E_a(z) Sin(\omega t + \varphi)$ and $C_1 = \frac{q}{6\beta c}\int_{-\frac{L}{2}}^{+\frac{L}{2}}\frac{\partial^3 E_z}{\partial z^3}\, dz$

The r^3 term leads to spherical aberration and distortion of beam size. C_1 is the spherical aberration coefficient.

6.1.2 EFFECT OF ABERRATION ON TRANSVERSE EMITTANCE

In this part the growth of transverse emittance of a bunched beam due to the third order term of the radial electric field is discussed. Evaluation of equation (6.5) using equation (6.1) gives the radial impulse as

$$\Delta P_r = -\frac{qr\omega}{2\gamma^2\beta^2c^2}\int_{-\frac{L}{2}}^{+\frac{L}{2}} E_a(z)\,Sin(\omega t+\varphi)dz + \frac{q}{6\beta c}r^3\int_{-\frac{L}{2}}^{+\frac{L}{2}}\frac{\partial^3 E_z}{\partial z^3}dz$$

With origin at the electrical centre of the gap and $\omega t = kz$, at t=0 the radial momentum increment is

$$\Delta P_r(t=0) = -\frac{qr\omega}{2\gamma^2\beta^2c^2}Sin\varphi\int_{-\frac{L}{2}}^{+\frac{L}{2}} E_a(z)\,Coskz\,dz + \frac{q}{6\beta c}r^3\int_{-\frac{L}{2}}^{+\frac{L}{2}}\frac{\partial^3 E_z}{\partial z^3}dz$$

The above expression reduces to

$$\Delta P_r = k' r sin\varphi \; + C_1 r^3 \qquad (6.6)$$

Where

$$k' = -\frac{q\omega}{2\gamma^2\beta^2c^2}\int_{-\frac{L}{2}}^{+\frac{L}{2}} E_a(z)\,Coskz\,dz$$

As this transverse impulse depend on φ, and φ varies from one end of the bunch to the other, there is a net increase in emittance which will be discussed below:

RMS emittance is defined as $\epsilon^2 = <r^2><\Delta P_r{}^2> - <r\Delta P_r>^2$

Under thin lens approximation, particle position remains unchanged while its radial momentum changes while crossing an RF gap.

Assuming there is no correlation between r and φ , the rms emittance becomes

$$\epsilon^2 = k'^2 < r^2 >< r^2 >< Sin^2\varphi > +{C_1}^2 < r^2 >< r^6 > +2k'C_1 < r^2 >< r^4 >< Sin\varphi >$$
$$-k'^2 < r^2 >< r^2 >< Sin\varphi >< Sin\varphi > -k'C_1 < r^2 >< r^4 >< Sin\varphi > -k'C_1 < r^2 ><$$
$$r^4 >< Sin\varphi > -{C_1}^2 < r^4 >< r^4 > \qquad (6.7)$$

For an uniformly distributed beam, we can write

$< r^n >= {}^{2R^n}/_{n+2}$ where R is the hard edge radius of the beam.

Also, it is known that $< Sin\varphi >= Sin\varphi_s f(\Delta\varphi)$ and $< Sin^2\varphi >= g(\varphi_s, \Delta\varphi)$ and $\Delta\varphi$ is the half width of phase spread [70], φ_s is the synchronous phase.

Where

$$f(\Delta\varphi) = \frac{15}{(\Delta\varphi^2)}\left[\frac{3}{\Delta\varphi^2}\left(\frac{Sin\Delta\varphi}{\Delta\varphi} - Cos\Delta\varphi\right) - \frac{Sin\Delta\varphi}{\Delta\varphi}\right]$$

And $g(\varphi_s, \Delta\varphi) = \frac{1}{2}[1 + (Sin^2\varphi_s - Cos^2\varphi_s)f(2\Delta\varphi)]$

In the limit $\Delta\varphi \to 0, f(\Delta\varphi) \to 1, g(\varphi, \Delta\varphi) \to Sin^2\,\varphi_s$

Substituting these values in the above expression (6.7), we find an expression for the growth of RMS emittance as $\Delta\epsilon = \sqrt{\frac{7}{72}}C_1R^4$

6.2. ANALYSIS OF ENVELOPE EQUATION INCLUDING SPHERICAL ABERRATION DUE TO ELECTRIC FIELD

6.2.1 INVARIANT ENVELOPE SOLUTION

Beam envelope equation for evolution of an axisymmetric relativistic bunched beam of spot size $\sigma(z)$ under the effects of an external linear focusing channel of average strength k_r is [73]

$\sigma'' + \frac{\gamma'}{\beta^2\gamma}\sigma' + k_r\sigma - \frac{k_s}{\beta^3\gamma^3\sigma} - \frac{{\epsilon_n}^2}{\beta^2\gamma^2\sigma^3} = 0$ where

$k_r = \left(\frac{\gamma'}{\beta\gamma}\right)^2\left(\frac{CB_z}{Sin\varphi E_0}\right)^2$, B_z, $k_s = \frac{Ig(\xi)}{2I_0}$ are the external focusing strength , applied magnetic field and beam perveance respectively, I_0 is the Alfven current (17 kA for electrons), I is the peak current in the bunch, $g(\xi)$ is a geometrical factor that describes the field distribution of the bunch [89].

Taking $\widetilde{\sigma} = \sqrt{\beta\gamma}\,\sigma$, such that $\sigma'' + \frac{\gamma'}{\beta^2\gamma}\sigma' = \frac{1}{\sqrt{\beta\gamma}}\left(\widetilde{\sigma}'' - \frac{\sqrt{\beta\gamma''}}{\sqrt{\beta\gamma}}\,\widetilde{\sigma}\right)$,

the reduced envelope equation [72] becomes

$$\widetilde{\sigma}'' + \left(\frac{\gamma'}{\beta\gamma}\right)^2\left(\Omega^2 + \frac{1}{4}\right)\widetilde{\sigma} - \left(\frac{\gamma'}{\beta\gamma}\right)^2\frac{S}{\widetilde{\sigma}} - \frac{{\epsilon_n}^2}{\widetilde{\sigma}^3} = 0 \qquad (6.8)$$

where $\Omega^2 = \left(\frac{CB_z}{Sin\varphi E_0}\right)^2$, $S = \frac{k_s}{\gamma'^2}$

Dropping the emittance term in the laminar regime, an obvious special solution of equation (6.8) is given by

$$\widetilde{\sigma}' = \widetilde{\sigma}'' = 0$$

For laminar beam without aberration invariant envelope solution is

$$\widetilde{\sigma} = \sqrt{\frac{S}{\Omega^2 + {}^1/_4}} = \sigma_0 \qquad (6.8a)$$

The potential corresponding to the Hamiltonian of envelope equation (6.8) is

$$V_1 = \left(\frac{\gamma'}{\beta\gamma}\right)^2\left(\Omega^2 + \frac{1}{4}\right)\frac{\widetilde{\sigma}^2}{2} - \left(\frac{\gamma'}{\beta\gamma}\right)^2 S\, ln\frac{\widetilde{\sigma}}{\sigma_0} + \frac{{\epsilon_n}^2}{2\widetilde{\sigma}^2}$$

We find that $\left.\frac{\partial V_1}{\partial\sigma}\right|_{\sigma_0}$ =0 and $\left.\frac{d^2V_1}{d\sigma^2}\right|_{\sigma_0} = 2\left(\frac{\gamma'}{\beta\gamma}\right)^2\left(\Omega^2 + \frac{1}{4}\right) > 0$

Hence σ_0 is a minimum.

Taking aberration into account the reduced envelope equation becomes

$$\tilde{\sigma}'' + \left(\frac{\gamma'}{\beta\gamma}\right)^2 \left(\Omega^2 + \frac{1}{4}\right)\tilde{\sigma} - \left(\frac{\gamma'}{\beta\gamma}\right)^2 \frac{S}{\tilde{\sigma}} - \frac{{\epsilon_n}^2}{\tilde{\sigma}^3} + C_2\tilde{\sigma}^3 = 0 \tag{6.9}$$

We get the corresponding envelope Hamiltonian as $H = {}^1\!/_2\, {P_{\tilde{\sigma}}}^2 + V(\tilde{\sigma})$ with a time-dependent modified potential

$$V = \left(\frac{\gamma'}{\beta\gamma}\right)^2 \left(\Omega^2 + \frac{1}{4}\right)\frac{\tilde{\sigma}^2}{2} - \left(\frac{\gamma'}{\beta\gamma}\right)^2 S\, ln\frac{\tilde{\sigma}}{\sigma_0} + \frac{{\epsilon_n}^2}{2\tilde{\sigma}^2} + \frac{C_2\tilde{\sigma}^4}{4}$$

Where C_1 is the aberration coefficient and $C_2 = \frac{1}{\beta^2\gamma^2}\frac{dC_1}{dz}$.

For $\tilde{\sigma}' = \tilde{\sigma}'' = 0$, the invariant envelope solution of a laminar beam can be found out

$$\left(\frac{\gamma'}{\beta\gamma}\right)^2 \left(\Omega^2 + \frac{1}{4}\right)\tilde{\sigma}^2 - \left(\frac{\gamma'}{\beta\gamma}\right)^2 S + C_2\tilde{\sigma}^4 = 0$$

The solution of above equation gives

$$\sigma_{0new} = \sqrt{\frac{S}{\Omega^2+\frac{1}{4}} - \left(\frac{\beta\gamma}{\gamma'}\right)^2 \frac{S^2}{\left(\Omega^2+\frac{1}{4}\right)^3} C_2} \quad = \sigma_0\left[1 - \left(\frac{\beta\gamma}{\gamma'\left(\Omega^2+\frac{1}{4}\right)}\right)^2 C_2\right]^{\frac{1}{2}}$$

We find that

$$\left.\frac{d^2V}{d\tilde{\sigma}^2}\right|_{\sigma_{0new}} = 2\left(\frac{\gamma'}{\beta\gamma}\right)^2 \left(\Omega^2 + \frac{1}{4}\right) + \frac{C_2}{\left(\Omega^2 + \frac{1}{4}\right)} + 3\frac{C_2 S}{\left(\Omega^2 + \frac{1}{4}\right)} \quad > 0$$

Thus without aberration term from expression (6.8a) $\sigma_0{}'$ is zero. That is the envelope solution has an invariant beam size. When we take aberration term in to account, the beam deviates from this Brillouin flow characteristics.

6.2.2 SOLUTION OF ENVELOPE EQUATION AND FREQUENCY SHIFT BY LINDSTEDT POINCARE METHOD

Equation of motion of a particle in reduced envelope form in an RF Cavity is equivalent to equation of a simple harmonic oscillator [74] which is $\tilde{\sigma}'' + \left(\frac{\gamma'}{\beta\gamma}\right)^2 \left(\Omega^2 + \frac{1}{4}\right)\tilde{\sigma} = 0$ with its solution as $\tilde{\sigma}(z) = \sigma_0 Cos\omega z$ where $\omega = \sqrt{\left(\frac{\gamma'}{\beta\gamma}\right)^2 \left(\Omega^2 + \frac{1}{4}\right)}$.

But in the presence of spherical aberration the above equation takes the form

$$\tilde{\sigma}'' + \left(\frac{\gamma'}{\beta\gamma}\right)^2 \left(\Omega^2 + \frac{1}{4}\right)\tilde{\sigma} + C_2\tilde{\sigma}^3 = 0 \tag{6.10}$$

Which is the reduced envelope equation (6.9) without space charge and emittance . The nonlinear term C_2 is treated as a small perturbation to the linearized equation and from this we can find an expression for shift in frequency of oscillation of the beam inside an RF Cavity.

Equation (6.10) is equivalent to $\tilde{\sigma}'' + {\omega_0}^2\tilde{\sigma} + \varepsilon{\omega_0}^2\tilde{\sigma}^3 = 0$ with the initial conditions $\tilde{\sigma}(0) = \sigma_0$ and $\tilde{\sigma}'(0) \approx 0$ where $C_2 = \varepsilon{\omega_0}^2$.

In order to make the analysis simpler, we take the approximation that particle has a very negligible initial divergence.

Equation (6.10) can be solved with the help of Lindstedt-Poincare method [26, 90, 91].

Let us expand $\tilde{\sigma}$ in an asymptotic series

$$\tilde{\sigma}(z) = \sum_{n=0}^{\infty} \tilde{\sigma}_n(z)\,\varepsilon^n$$

Substituting Poincare type expansion for zeroth order

$\sigma_0'' + \omega_0{}^2\sigma_0 = 0$ and its first order correction

$\widetilde{\sigma}_1'' + \omega_0{}^2\widetilde{\sigma}_1 = -\omega_0{}^2\sigma_0{}^3$

zeroth order equation solution is $\sigma_0(z) = \sigma_0 Cos(\omega_0 z)$ (6.11)

Substituting (6.11) in first order equation and making use of the identity

$Cos^3\theta = \frac{3}{4}Cos\theta + \frac{1}{4}Cos3\theta$ the result becomes an equation for a driven harmonic oscillator

$$\widetilde{\sigma}_1'' + \omega_0{}^2\widetilde{\sigma}_1 = -\frac{\omega_0{}^2\sigma_0{}^3}{4}[3Cos(\omega_0 z) + Cos(3\omega_0 z)]$$

and its solution is

$$\widetilde{\sigma}_1(z) = -\frac{\sigma_0{}^3}{32}[Cos(\omega_0 z) - Cos(3\omega_0 z)] - \frac{3\sigma_0{}^3}{8}\omega_0 z Sin(\omega_0 z)$$

Hence up to first order perturbation theory, the solution of the equation (6.10) is

$\widetilde{\sigma}(z) = \sigma_0 Cos(\omega_0 z) - \sigma_0{}^3\left\{\frac{1}{32}[Cos(\omega_0 z) - Cos(3\omega_0 z)] - \frac{3}{8}\omega_0 z Sin(\omega_0 z)\right\}\varepsilon + o(\varepsilon^2)$

(6.12)

But the presence of a secular term $\frac{3}{8}\omega_0 z Sin(\omega_0 z)$ in equation (6.12), leads to a linearly growing behaviour of $\widetilde{\sigma}(z)$. In particular, $\widetilde{\sigma}(z)$ is unbounded for very large z since it grows more or less like $\omega_0 z$, which is unphysical.

Hence to remove this term from the expression, we can introduce a new variable $S = \omega z$ with $\omega = \omega_0 + \omega_1\varepsilon + o(\varepsilon^2)$ such that $\omega_0 z = \left(1 - \frac{\omega_1}{\omega_0}\varepsilon\right)S + o(\varepsilon^2)$ (6.13)

Substituting the expression for $\omega_0 z$ into Poincare type perturbation solution (6.11) and expanding in ε we arrive

$$\tilde{\sigma}(s) = \sigma_0 Coss + \sigma_0 \frac{\omega_1}{\omega_0} \varepsilon s Sins - \sigma_0{}^3 \left\{ \frac{1}{32} [Coss - Cos3s] - \frac{3}{8} sSins \right\} \varepsilon + O(\varepsilon^2) \tag{6.14}$$

The secular term is cancelled if $\omega_1 = \frac{3}{8} \sigma_0{}^2 \omega_0$.

Resubstituting $S = \omega z$, we have the uniform asymptotic expansion

$$\tilde{\sigma}(z) = \sigma_0 Cos\omega z - \sigma_0{}^3 \left\{ \frac{1}{32} [Cos\omega z - Cos3\omega z] \right\} \varepsilon + O(\varepsilon^2) \tag{6.15}$$

with new oscillation frequency $\omega = \omega_0 \left[1 + \frac{3}{8} \sigma_0{}^2 \varepsilon \right]$ (6.16)

Expression (6.15) presents the effect of spherical aberration on the evolution of beam size $\tilde{\sigma}(z)$ of a particle moving inside a RF cavity and expression (6.16) gives the shift in frequency of oscillation which arises due to aberration. The above result is consistent with [74], when aberration term is neglected. Thus with the help of Lindstedt-Poincare technique we can treat the third order perturbation term in an effective manner and find analytical expressions for beam size and oscillatory behaviour of an aberrated.

6.3. EFFECT OF SPHERICAL ABERRATION ON EMITTANCE GROWTH DUE TO MAGNETIC FIELD AND SPACE CHARGE

6.3.1 SPHERICAL ABERRATION INDUCED BY MAGNETIC FIELD

Magnetic field of the solenoid can be expanded up to second order in radial direction in terms of on -axis field components as

$$B_z(r,z) = B(z) - \frac{r^2}{4} B''(z) + \ \dots \tag{6.17}$$

$$B_r(r,z) = -\frac{r}{2} B'(z) + \frac{r^3}{16} B'''(z) + \ \dots \tag{6.18}$$

where $B(z) = B_z(0,z)$, z is the distance along the solenoid axis, r is the radial distance from the solenoid axis and the prime denotes a derivative with respect to z.

Thus equation of motion along the radial direction is

$$\gamma m\ddot{r} = \gamma m r\dot{\theta}^2 + qr\dot{\theta}B_z \tag{6.19}$$

where q is the charge and m is the mass of the charged particle. Dot (.) denotes derivatives with respect to time. β and γ are used as relativistic factors.

Motion along the azimuthal direction is described using Busch's theorem [28]

$$\gamma m r^2\dot{\theta} = q\psi \,/\, 2\pi \tag{6.20}$$

where ψ is the magnetic flux enclosed by a circle of radius r. It is assumed that initially $\dot{\theta}$ is zero and particle is in field-free region. In the paraxial approximation we take

$$\psi = \pi r^2 B(z) \tag{6.21}$$

If we substitute the value of $\dot{\theta}$ in equation (6.19) and consider terms up to third order in r, we get the following equation for evolution of the radial co-ordinate

$$\ddot{r} = -\frac{q^2}{4\gamma^2}\frac{B^2(z)}{m^2}\left[r - \frac{B''(z)}{2B(z)}r^3\right]$$ which reduces to

$$\beta^2 c^2 r'' = -\frac{q^2}{4\gamma^2}\frac{B^2(z)}{m^2}\left[r - \frac{B''(z)}{2B(z)}r^3\right] \tag{6.22}$$

To study the effect of third order term in the expansion of magnetic field on the optics of beam, we take an example of a focusing solenoid made up of iron core having length 270 mm, bore radius 75mm, pole gap 30 mm, no. of turns 136, as shown in Fig. 6.1. We have carried out simulation of this solenoid in the beam dynamics code ASTRA [14] for a Gaussian distribution electron beam for two magnetic field strengths of peak value 0.4 T and 0.6 T respectively. B_z component of this solenoid for a magnetic field of strength 0.4 T at $r = 0$ is shown in Fig. 6.2.

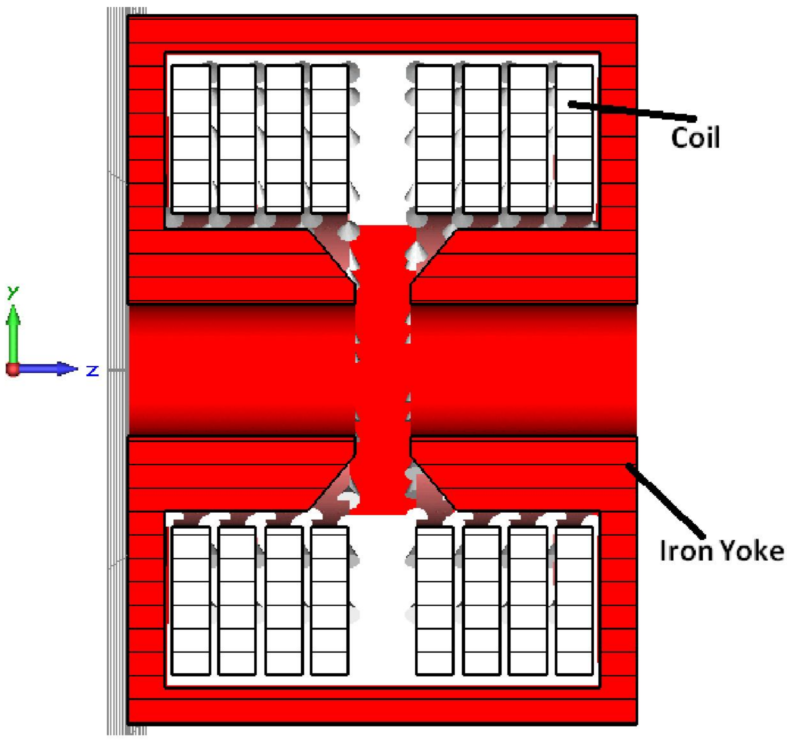

Fig. 6.1 Picture of iron core solenoid

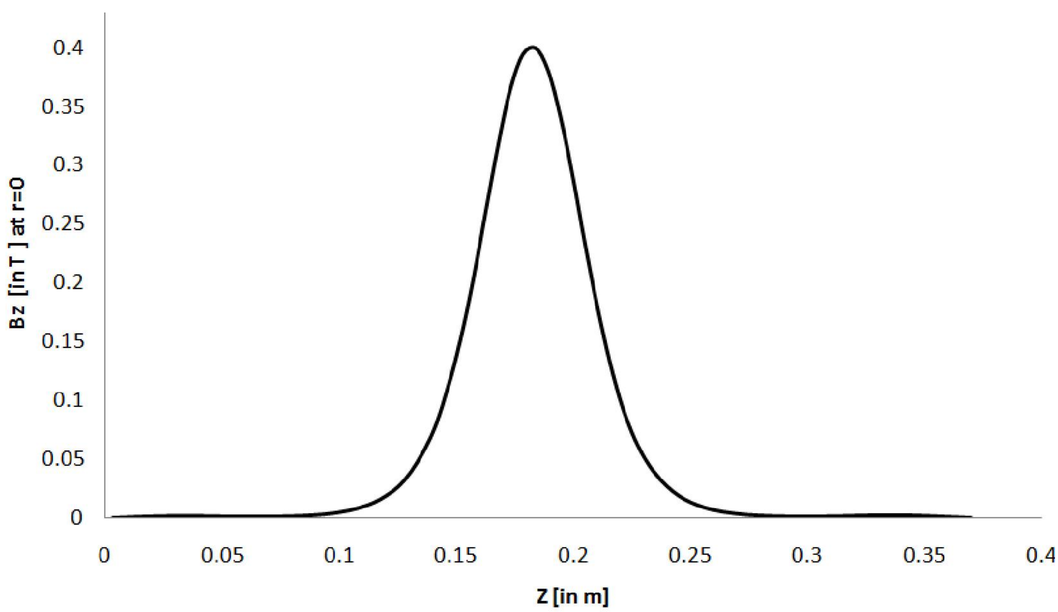

Fig. 6.2 Magnetic field profile on the axis of the solenoid

The third order term in the expression for magnetic field expansion introduces nonlinearity for higher r and B'' values. In order to study the effect of nonlinearity, we consider two different rms beam radii 2mm and 17mm as well as two different magnetic field of magnitude 0.4T and 0.6T respectively. To observe the effect of spherical aberration, at first we consider an input beam of rms radius 17 mm (which is no longer under paraxial approximation) and track it in a peak solenoidal magnetic field of 0.4 T for two cases: one without third order term and the other with third order term of the magnetic field expansion $\frac{B''(z)}{2B(z)}r^3$. The beam size at the waist increases from a diameter of 1.2 mm to a diameter of 14 mm due to the spherical aberration as shown in Fig. 6.3. As shown in Fig. 6.4 (a) and (b), the spherical aberration leads to the distortion of phase space and increase in effective emittance. Further, when the rms radius of a beam increases from 2 mm to 17 mm, the spherical aberration leads to the distortion of the phase space as is evident from Fig. 6.4 (c) and Fig. 6.4 (b).

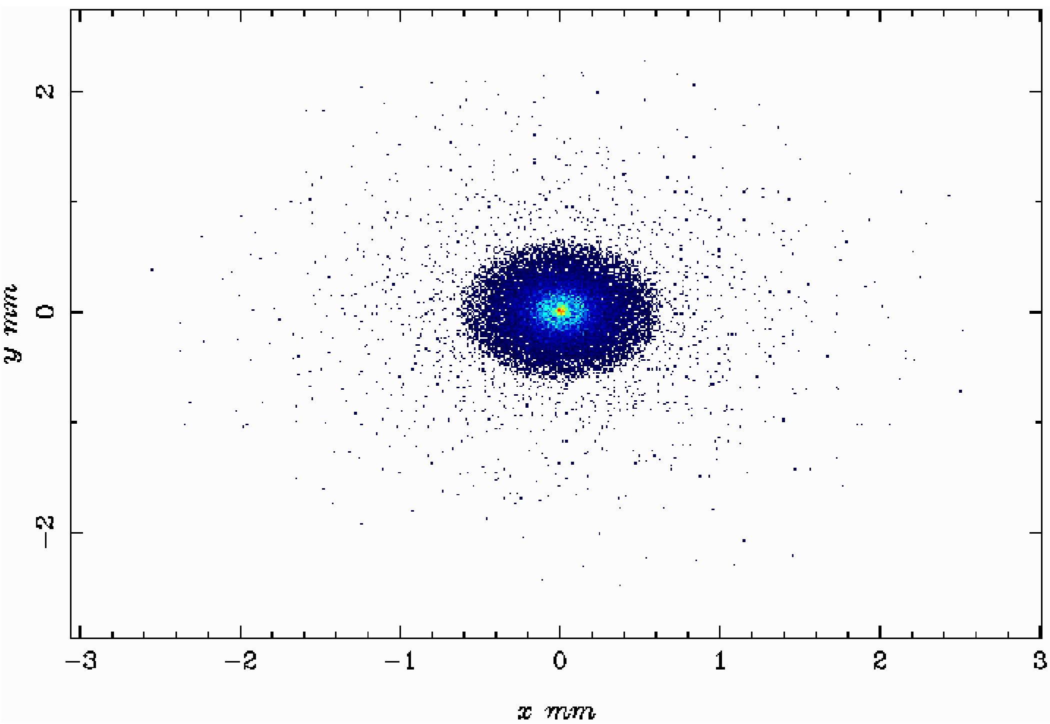

(a)

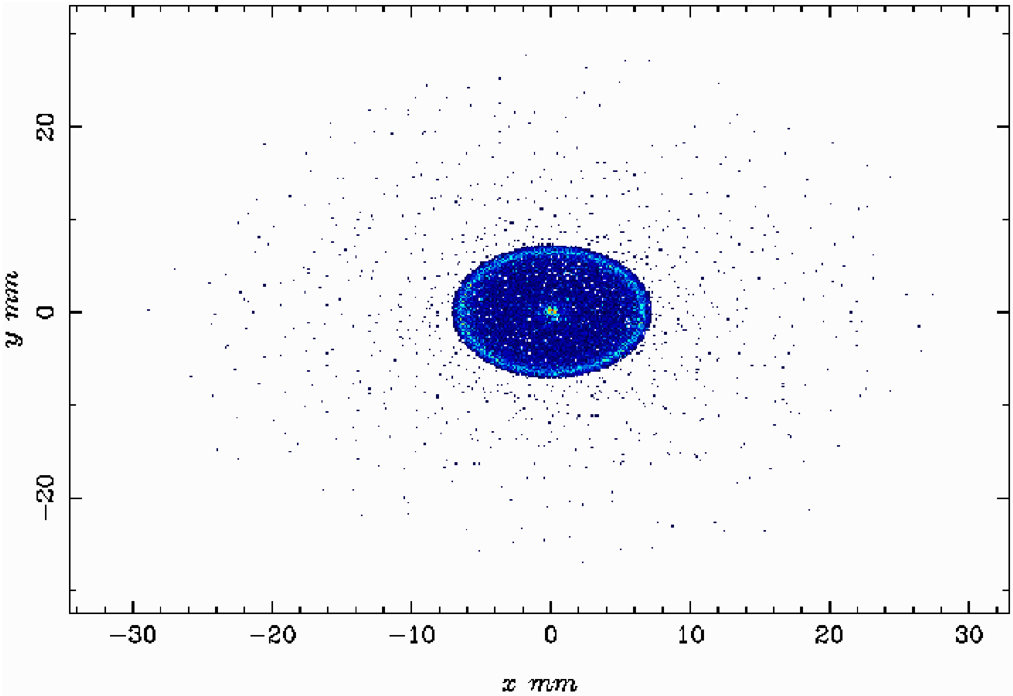

(b)

Fig. 6.3 Beam Size at the focal point for a beam of initial rms radius of 17 mm and peak B-field 0.4 T (a) without spherical aberration (b) with spherical aberration

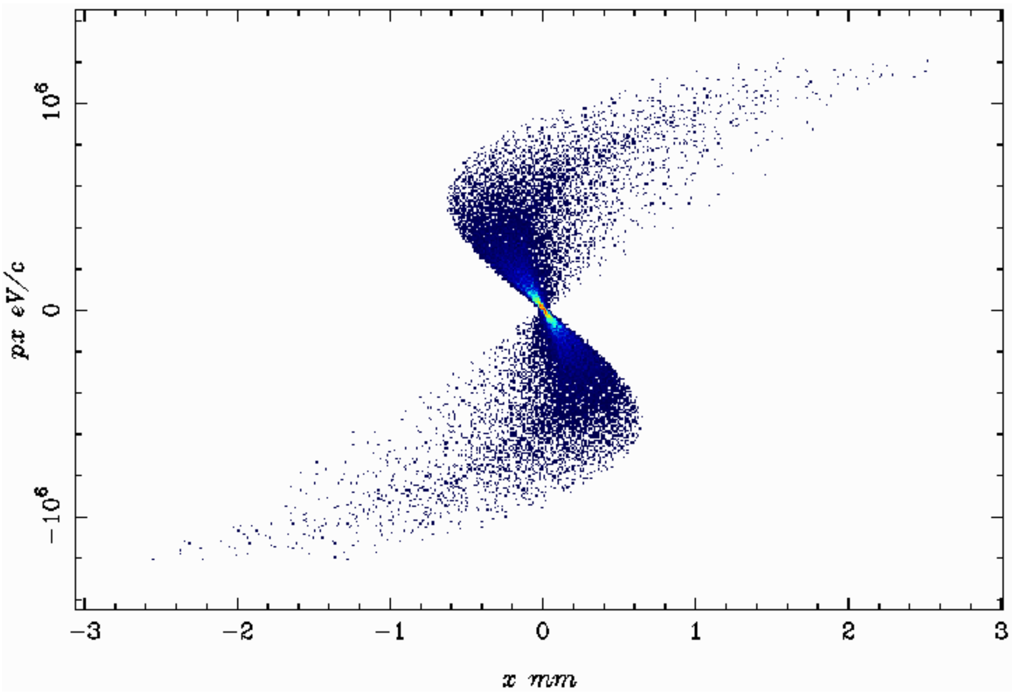

(a)

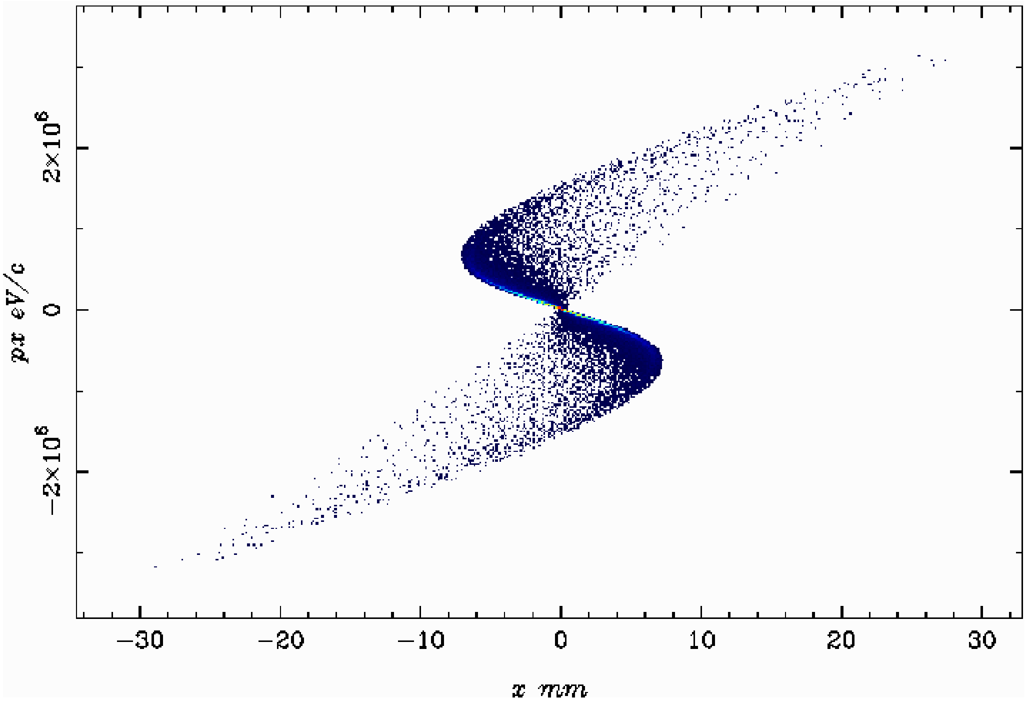
px eV/c
2×10^6
0
−2×10^6
−30
−20
−10
0
10
20
30
x mm

(b)

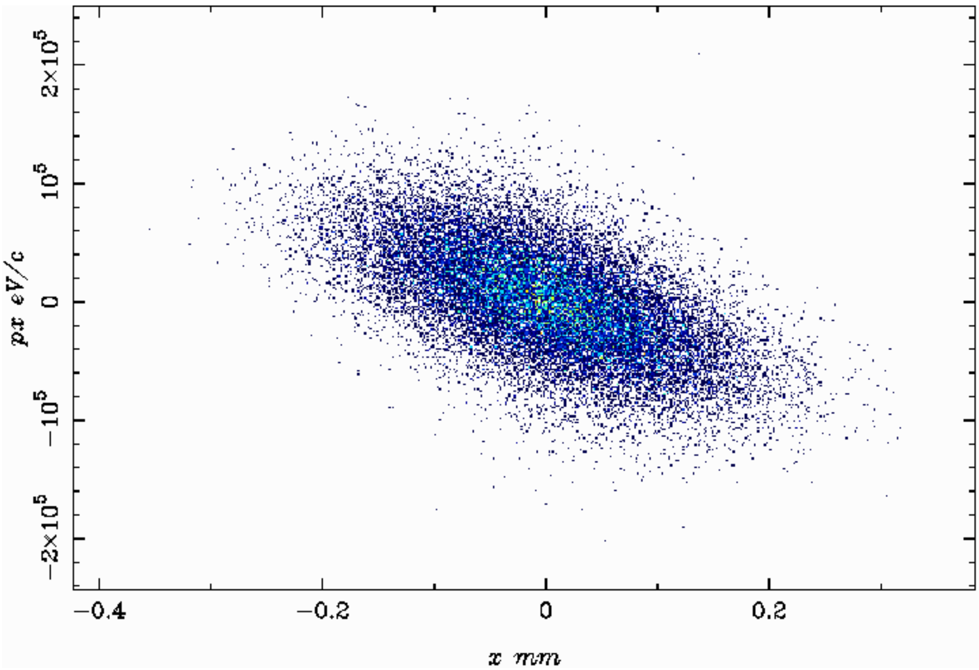
px eV/c
2×10^5
10^5
0
−10^5
−2×10^5
−0.4
−0.2
0
0.2
x mm

(c)

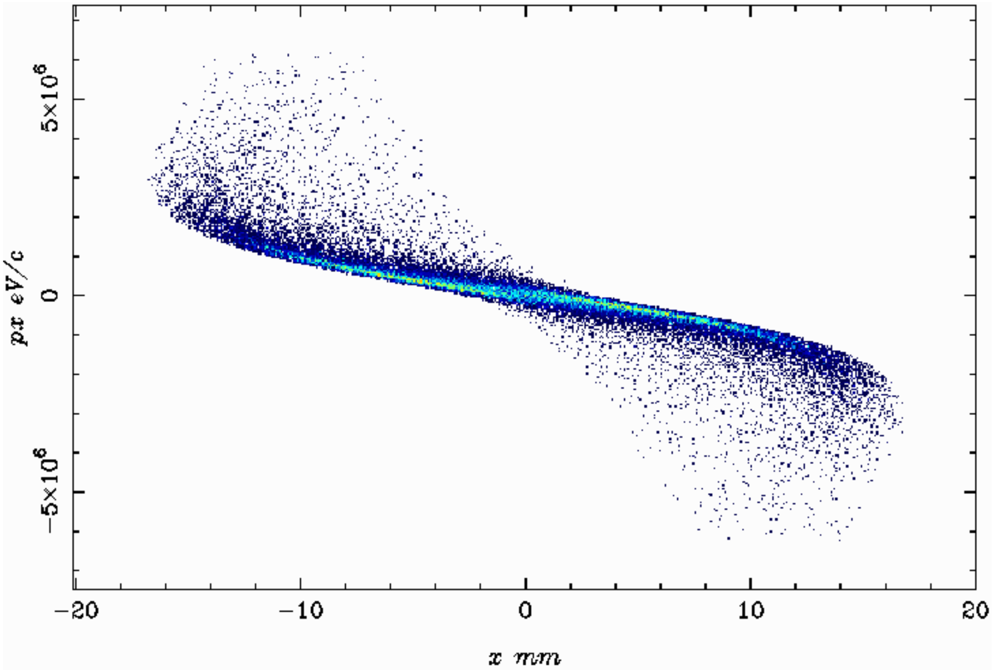

(d)

Fig. 6.4 Phase space plots of a beam at the waist (a) initial rms radius of 17 mm, peak B-field 0.4 T, without spherical aberration (b) initial rms radius of 17 mm, peak B-field 0.4 T with spherical aberration (c) initial rms radius of 2 mm, peak B-field 0.4 T with spherical aberration (d) initial rms radius of 17 mm and peak magnetic field 0.6 T with spherical aberration

To observe the effect of magnetic field, for a particular beam radius, particles are tracked in two magnetic fields. When the magnetic field changes from 0.4 T to 0.6 T for a beam of initial rms radius 17 mm, the spherical aberration distorts and rotate the phase space and increase the emittance as shown in Fig. 6.4 (b) and Fig. 6.4 (d).

Hence from the simulation results, we find that higher magnitude of rms beam radius and high magnetic field value introduce non-linearity in the beam optics.

Further we have studied the effect of variation of magnetic field on the spherical aberration and the subsequent emittance growth. We find that the effect of spherical aberration is minimum for a magnetic field of 0.4 T that corresponds to a beam diameter of 17 mm as shown in Fig.6.5.

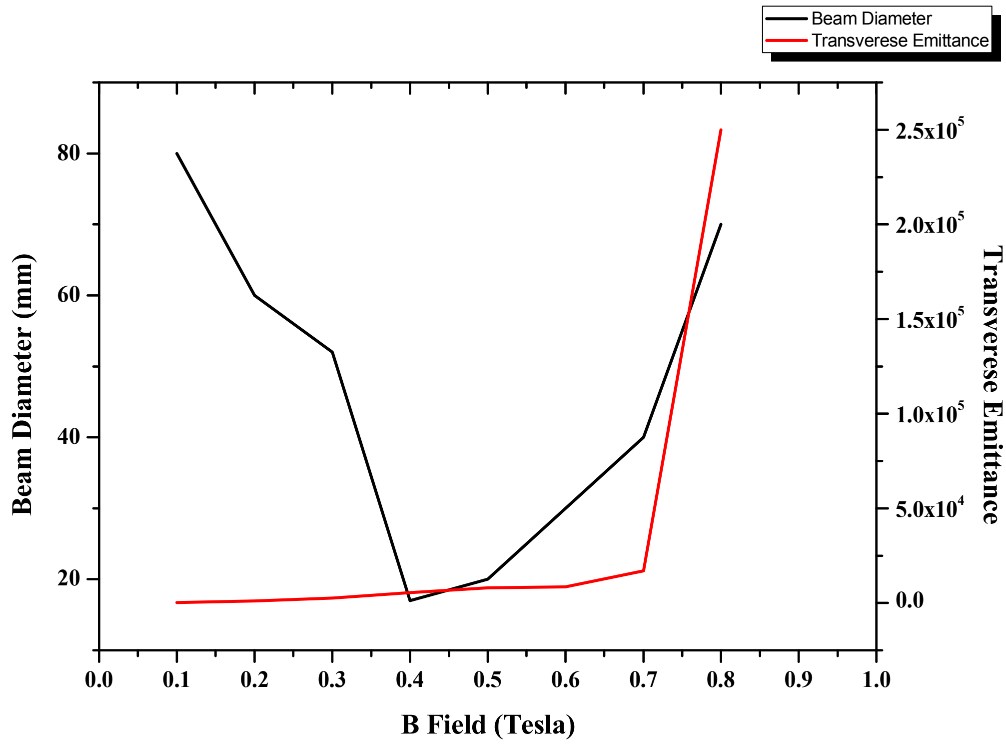

Fig. 6.5 Variation of beam size and transverse emittance with magnetic field

6.3.2 SPHERICAL ABERRATION INDUCED BY SPACE CHARGE

In an ideal beam with uniform charge density, the electric field and hence the defocusing force are proportional to radius r [92]. In practice, the charge density is not uniform and this nonuniformity causes spherical aberration. We consider a space charge dominated Gaussian beam profile of rms radius a in radial coordinate as

$$\rho(r) = \frac{I}{\pi a^2 \beta c} exp\left(-\frac{r^2}{2a^2}\right) \tag{6.23}$$

From Maxwell's equation $\nabla . \mathrm{E} = \rho/\epsilon_0$, radial electric field is

$$E_r(r) = \frac{I}{2\pi\epsilon_0 r\beta c}\left(1 - exp\left(-\frac{r^2}{2a^2}\right)\right) \tag{6.24}$$

where I is the beam current ϵ_0 is the permittivity of free space.

The nonlinear function in space charge field is expanded as

$$exp\left(-\frac{r^2}{2a^2}\right) \approx 1 - \frac{r^2}{2a^2} \tag{6.25}$$

From Ampere's law $\int \mathrm{B.dl} = \mu_0 \int \mathrm{J.ds}$, the azimuthal component of magnetic field is

$$B_\theta = \frac{\mu_0 Jr}{2} \text{ for } r \leq a \tag{6.26}$$

With $\rho(r) = {}^{J}/_{v}$ where J is the current density, v is the velocity of the beam and the equation of radial motion of a particle in this force field is

$$\frac{\mathrm{d}}{\mathrm{dt}}(\gamma m\dot{r}) = qE_r - q\beta cB_\theta \tag{6.27}$$

If we use the expressions for E_r and B_θ the equation of motion reduces to

$$r" = q\rho_0 \frac{r}{2m\epsilon_0\beta^2c^2\gamma^3}(1 - \frac{r^2}{2a^2}) \tag{6.28}$$

where $\rho_0 = \frac{I}{\pi a^2\beta c}$ and the dependence of ρ_0 on radial and longitudinal coordinate is neglected.

We include third order term for spherical aberration due to combined effect of the magnetic field and space charge such that the equation of motion becomes

$$r" = -\frac{q^2B^2(z)r}{4\gamma^2m^2\beta^2c^2} + \frac{q^2B(z)B''(z)}{8\gamma^2m^2\beta^2c^2}r^3 + \frac{q\rho_0}{2m\epsilon_0\beta^2c^2\gamma^3}r - \frac{q\rho_0}{4m\epsilon_0\beta^2c^2\gamma^3a^2}r^3 \tag{6.29}$$

Taking a thin lens approximation, we assume that the radial co-ordinate doesn't change significantly inside the solenoid, but the slope $r' = dr/dz$ gets a net impulse. Under this approximation, Integration of the equation (6.29) gives

$$\Delta r' = \frac{-q^2}{4\gamma^2 m^2 \beta^2 c^2}\left[\int B^2(z)\,dz - \int \frac{2m\rho_0}{q\gamma\epsilon_0}dz\right] r + \frac{q^2 r^3}{8\gamma^2 m^2 \beta^2 c^2}\int B(z)B''(z)dz - \int \frac{q\rho_0}{4m\epsilon_0 \beta^2 \gamma^3 c^2 a^2} r^3 dz \tag{6.20}$$

We rewrite equation (6.20) in a compact form as

$$\Delta r' = -\frac{r}{f_0}[1 + C_1 r^2] \tag{6.21}$$

where $\frac{1}{f_0} = \frac{q^2}{4\gamma^2 m^2 \beta^2 C^2}\int B_{eff}{}^2 dz$, (6.22)

$$C_1 = \frac{1}{\int B_{eff}{}^2 dz}\left[\left(-\frac{1}{2}\int B(z)B(z)'' + \frac{\rho_0}{\gamma q a^2 \epsilon_0} m\right) dz\right] \tag{6.23}$$

where C_1 is the spherical aberration term.

and $$B_{eff}{}^2 = B^2(z) - \frac{2m\rho_0}{q\gamma\epsilon_0} \tag{6.24}$$

The physical significance of C_1 is that the fractional reduction in focal length for an off-axis particle incident at a distance r from the solenoid axis, is given by $C_1 r^2$. A gaussian distributed electron beam of energy 6 MeV is tracked in a magnetic field of 0.4 T with different rms beam sizes. Equation (6.21) is numerically evaluated and plotted in Fig. 6.6. The effect of the spherical aberration on the beam can be clearly observed as it decreases the focal length of the beam with an increase in rms beam sizes.

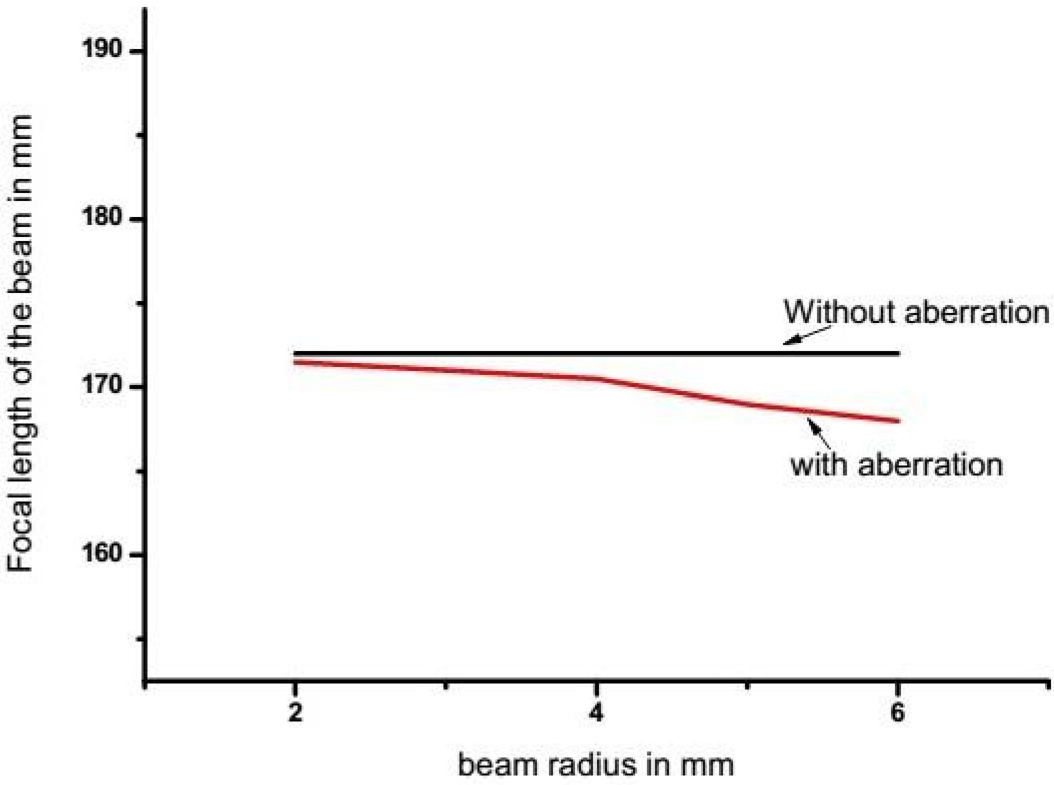

.

Fig. 6.6 Variation of focal length of a Gaussian beam profile with and without aberration

6.3.3 EXPRESSIONS FOR TRANSVERSE EMITTANCE GROWTH OF DIFFERENT BEAM DISTRIBUTIONS

The rms radial emittance of a beam ε_r is defined as

$$\varepsilon_r{}^2 = < r^2 >< r'^2 > - < rr' >^2 \tag{6.25}$$

The quantities in the braces $< >$ represent the average rms values. The spherical aberration coefficient C_1 changes with the beam distribution function. We can evaluate the transverse emittance growth due to aberration for Uniform, Gaussian, Waterbag and parabolic distribution functions [93] as discussed below.

6.3.3.1 UNIFORM DISTRIBUTION FUNCTION

First we consider uniform distribution of the beam. In this case it is assumed that before entering the solenoid, $r'_0 \approx 0$ for all particles and r is unchanged under the thin lens approximation.

For the calculation of emittance growth, as we assume initial $r'_0 \approx 0$, so $\Delta r' = r'$.

Substituting expression for r' from equation (6.21) in equation (6.25)

$$\varepsilon_r{}^2 = \frac{C_1}{f_0^2}[C_1 < r^2 >< r^6 > -C_1 < r^4 >^2] \tag{6.26}$$

For uniform distribution, we can write $< r^n >= 2\,a^n/(n+2)$, where a is the hard edge radius of the beam.

Evaluation of equation (6.26) gives the expression for emittance growth for an uniform beam distribution due to spherical aberration in a thin solenoid lens as

$\varepsilon_r = \sqrt{1/72}\ C_1 \frac{a^4}{f_0}$ where dependence of C_1 on r has been neglected assuming $B(z)$ is negligible variation over the radial direction as compared to beam size.

6.3.3.2 GAUSSIAN DISTRIBUTION FUNCTION

For a beam having Gaussian distribution, taking particle motions are uncoupled, the initial rms emittance is $\sigma_{r_0}\,\sigma_{r_{o'}}$, where σ_{r_0} and $\sigma_{r_{o'}}$ are initial rms values of the beam size and the divergence respectively. We assume that $\sigma_{r_{o'}}$ is very small.

Gaussian Distribution function is defined as

$$n(r, r') = \frac{1}{2\pi\sigma_{r_0}\sigma_{r'_0}} e^{-\frac{r^2}{2\sigma_{r_0}{}^2}} e^{-\frac{r'^2}{2\sigma_{r'_0}{}^2}} \tag{6.27}$$

The average rms values can be expressed as

$$< r^2 >= \frac{1}{2\pi\sigma_{r_0}\sigma_{r'_0}} \int r^2 \, e^{-\frac{r^2}{2\sigma_{r_0}{}^2}} dr \int e^{-\frac{r'^2}{2\sigma_{r'_0}{}^2}} \, dr' = 5\sigma_{r_0}{}^2 \tag{6.28}$$

$$< r'^2 > = \frac{1}{f_0{}^2} (5\sigma_{r_0}{}^2 + 40C_1\sigma_{r_0}{}^4 + 120C_1{}^2\sigma_{r_0}{}^6) \tag{6.29}$$

$$< rr' > = -\frac{1}{f_0} (5\sigma_{r_0}{}^2 + 20C_1\sigma_{r_0}{}^4) \tag{6.30}$$

Hence, the rms emittance becomes

$$\varepsilon_r = 10\sqrt{2}\frac{C_1}{f_0}\sigma_{r_0}{}^4 \tag{6.31}$$

6.3.3.3 WATERBAG DISTRIBUTION FUNCTION

Distribution function of a beam with waterbag distribution is

$$n(r) = \frac{2N}{\pi a^2}\left(1 - \frac{r^2}{a^2}\right) \tag{6.32}$$

where $N = \frac{I}{qv}$

We evaluate the rms values as

$$< r^2 > = \frac{1}{N}\int_{-a}^{a} r^2 \, n(r) dr = \frac{a^2}{3} \tag{6.33}$$

$$< r'^2 >= \frac{1}{f_0{}^2}\left(\frac{a^2}{3} + \frac{C_1 a^4}{3} + \frac{C_1{}^2 a^6}{10}\right) \tag{6.34}$$

$$< rr' >= -\frac{1}{f_0}\left(\frac{a^2}{3} + \frac{C_1 a^4}{6}\right) \tag{6.35}$$

So the expression for rms emittance growth is $\varepsilon_r = \frac{C_1 a^4}{6\sqrt{5} f_0}$ (6.36)

6.3.3.4 PARABOLIC DISTRIBUTION FUNCTION

Distribution function of a parabolic beam is [28]

$$n(r) = \frac{3N}{\pi a^2}\left(1 - \frac{r^2}{a^2}\right)^2 \tag{6.37}$$

The corresponding rms values can be written as

$$< r^2 > = \frac{1}{N}\int_{-a}^{a} r^2\, n(r)dr = \frac{a^2}{4} \tag{6.38}$$

$$< r'^2 > = \frac{1}{{f_0}^2}\left(\frac{a^2}{4} + \frac{C_1 a^4}{5} + \frac{{C_1}^2 a^6}{20}\right) \tag{6.39}$$

$$< rr' > = -\frac{1}{f_0}\left(\frac{a^2}{4} + \frac{C_1 a^4}{10}\right) \tag{6.40}$$

Hence, the rms emittance is found to be

$$\varepsilon_r = \frac{C_1 a^4}{20 f_0} \tag{6.41}$$

The above expressions for emittance growth can be used to estimate the upper limit of C_1 .

For example, for a 6 MeV rf Linac ,one post-focusing solenoid (which is used to focus the beam after it exits from the Linac cavity) of length 270 mm, field strength 0.4 T will be used to focus the beam. For 6 MeV beam, the focal length is 100 mm, rms beam size is 3.5 mm with the emittance from the RF cavity is 4π mm-mrad. It will be desirable that emittance doesn't increase by more than 5% of its value in the solenoid. Therefore, substituting the numbers in the formula, the maximum allowable value of C_1 for Gaussian beam distribution is 29.60/m^2. Using an approximate formula given in [94] $C_1 = {}^{1}/_{(3.24bl)}$ where b is the bore radius of the solenoid and l is the length of the solenoid, one obtains that value of C_1 is 41.2/m^2 where b =75 mm. Taking the above analysis, we calculate the transverse rms emittance growth for uniform, Gaussian, Waterbag and parabolic beam distributions to be 0.007 mm-mrad, 0.874 mm-mrad, 0.004 mm-mrad, 0.03 mm-mrad respectively.

6.4. EFFECT OF CHROMATIC ABERRATION ON EMITTANCE GROWTH

6.4.1 PHASE-SPACE DISTORTION DUE TO ENERGY SPREAD

To study the effect of energy spread on area of phase space, it is assumed that the initial beam emittance is ε. Here we consider the first order term of spread in momentum with initial divergence of the beam is $r_0^{'}$.

Let us estimate the emittance growth of the beam passing through the solenoid lens. We assume that the position of the particle is not changed while crossing the lens, and only slope of the particle trajectory is changed. Neglecting C_1 term in equation (6.21), we take transformation from initial particle variables before lens (r_0, r_0') to that after lens (r, r') as

$$r = r_0$$

$$r^{'} = r_0^{'} - \frac{r_0}{f_0}(1-\eta) \tag{6.42}$$

where $\eta = 2\Delta p/p$ and $p = p_0\left(1 + \frac{\Delta p}{p_0}\right)$

Suppose the initial phase space is bounded by the ellipse

$$\left(\frac{r_0^2}{a^2}\right) + \left(\frac{r_0^{'2}}{\varepsilon^2}\right)a^2 = 1$$

where $a =$ beam radius

To find the deformation of the beam phase space after passing through the lens, let us substitute inverse transformation

$$r_0 = r$$

$$r_0' = r' + \frac{r}{f_0}(1 - \eta)$$

The boundary of the new phase space volume occupied by the beam after passing through the lens at phase plane (r, r') is given by

$$\left(\frac{r^2}{a^2}\right)\varepsilon + \left[\left(r' + \frac{r}{f_0}\right) - \frac{r}{f_0}\eta\right]^2 \frac{a^2}{\varepsilon} = \varepsilon \qquad (6.43)$$

Let us introduce new variables (T, Θ) instead of (r, r') according to transformation

$$\frac{r}{a} = \sqrt{T} cos\Theta$$

$$\left(r' + \frac{r}{f_0}\right)\frac{a}{\varepsilon} = \sqrt{T} sin\Theta$$

In terms of new variable the shape of the beam emittance is

$$T + TV^2 cos^2\Theta - TV sin2\Theta = 1 \qquad (6.44)$$

where $V = \frac{\eta a^2}{f_0 \varepsilon}$

Without nonlinear perturbation $= 0$, equation (6.44) describes ellipse (circle) in phase space. If $V \neq 0$ then equation (6.44) describes distorted phase space ellipse.

In this case the transformation (6.42) conserves the phase space area as Jacobian of this transformation equals to unity, where the Jacobian

$$J = \begin{vmatrix} \frac{\partial r}{\partial r_0} & \frac{\partial r}{\partial r_0{}'} \\ \frac{\partial r'}{\partial r_0} & \frac{\partial r'}{\partial r_0{}'} \end{vmatrix} = 1 \qquad (6.45)$$

So in this case the phase space area occupied by the beam before and after the magnetic lens are same, the effective area occupied by the beam is increased and hence there is a growth of emittance of the beam.

6.4.2 EMITTANCE GROWTH DUE TO ENERGY SPREAD

Under thin lens approximation for solenoid lens, if we consider the first term of Taylor series expansion for the cosine and sine functions, the transformation matrix M, [3, 70, 95] from initial state (x_0, x_0') to final state(x, x') becomes

$$M = \begin{pmatrix} 1 & 0 \\ -k(\eta) & 1 \end{pmatrix} \tag{6.46}$$

where $k(\eta) = \left(\frac{eB}{2P}\right)^2 L = \frac{k(0)}{(1+\eta/2)^2}$ and $\eta = 2\Delta p/p$,

$k(0)$= Focusing strength of solenoid without momentum spread.

We write the expression for x and x' correct up to η^2 term as

$$x = x_0 \tag{6.47}$$

$$x' = x_0' - \frac{k(0)}{(1+\eta/2)^2} \cong x_0' - k(0)\left(1 - \eta + \frac{3}{4}\eta^2\right) \tag{6.48}$$

We can calculate the variation of second-order moments as follows:

$$\Delta < x^2 > = 0 \tag{6.49}$$

$$\Delta < x'^2 > = \frac{5}{2}[k(0)]^2 < \eta^2 >< {x_0}^2 > - \frac{3}{2}k(0) < \eta^2 >< x_0 x_0' > \tag{6.50}$$

$$\Delta < xx' >^2 = \frac{3}{2}[k(0)]^2 < \eta^2 >< {x_0}^2 >^2 - \frac{3}{2}k(0) < \eta^2 >< {x_0}^2 >< x_0 x_0' > \tag{6.51}$$

Hence, there is a growth of emittance and the corresponding variation $\Delta\varepsilon$ is proportional to $< \eta^2 >$. As $< \eta^2 >$ is a non zero quantity, it introduces a correlation between x and x' .

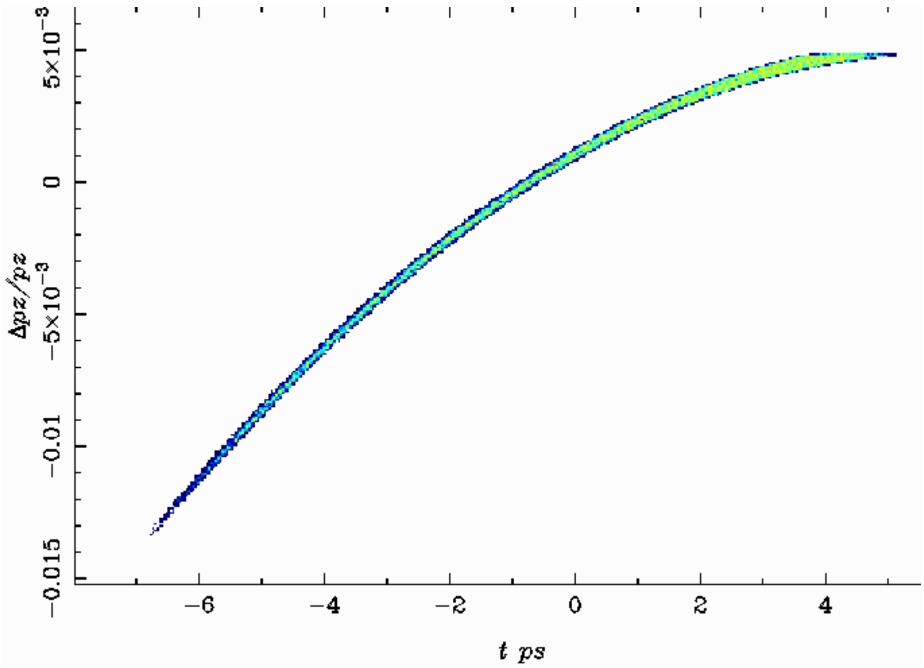

(a)

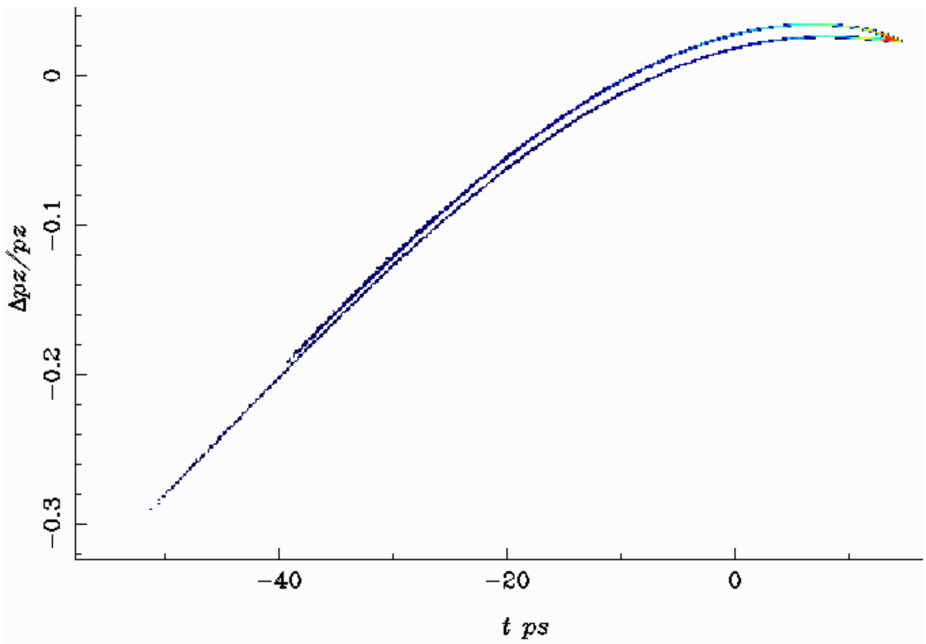

(b)

Fig. 6.7 Relative Energy spread at the linac output for injection of input bunch (a) bunch length 10 ps (b) bunch length 100 ps

To study the effect of energy spread that gives rise to chromatic aberration of the beam that in turn leads to distortion of transverse phase space, we take an example of a 6 MeV, 160 mA , 5 μs pulsed rf linac beam which is used for societal applications like cargo scanning and medical treatment. The accelerating cavity of the 6 MeV bi-periodic, coupled cavity linac consists of 3 bunching cells and 8 accelerating cells operating in π/2 mode at a frequency of 2856 MHz. The length of each accelerating cell is 52 mm, whereas the buncher cells are 45, 48 and 50 mm respectively. The bore radius is 5 mm for all the buncher cells and accelerating cells. The effective shunt impedance for the buncher cells is ~80 MΩ/m, while for the accelerating cells; it is ~ 90 MΩ /m.

To compare our analysis with simulation, we consider an example where two different electron bunches having bunch lengths 100 ps and 10 ps respectively are injected into the linac and track them through the accelerating cavities in the beam dynamics code ASTRA to gain an energy of 6 MeV. We find that the energy spread of the output beam of the linac is 1 % for an input bunch of length 10 ps where as for an input bunch of length 100 ps, the energy spread of the output beam is 10 % as shown in Fig. 6.7.

To study the effect of chromatic aberration on the transverse emittance growth, the beam coming out of the linac is focussed with the help of an iron core solenoid. The specification and field profile of this solenoid is as mentioned in Fig 6.1 and Fig. 6.2. The transverse phase space plots in both the cases are shown in Fig. 6.8. Fig. 6.8 (b) shows that the phase space is more distorted. Fig. 6.8 (a) corresponds to transverse emittance of 4.614 pi mm-mrad while the Fig. 6.8 (b) corresponds to a transverse emittance of 14.79 pi mm-mrad. Hence a bunch with more spread in energy gives rise to a significant growth in transverse emittance, which supports our theoretical analysis in section 6.4.

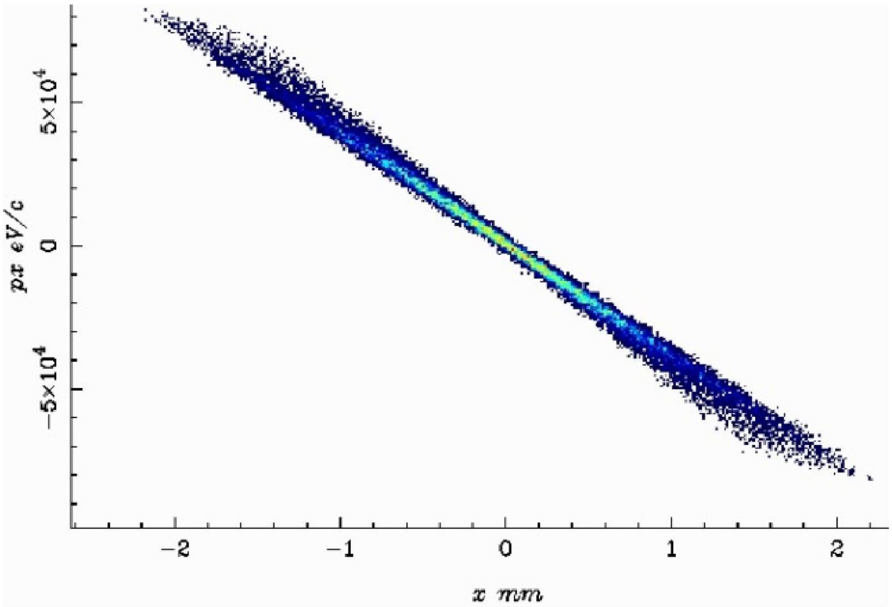

(a)

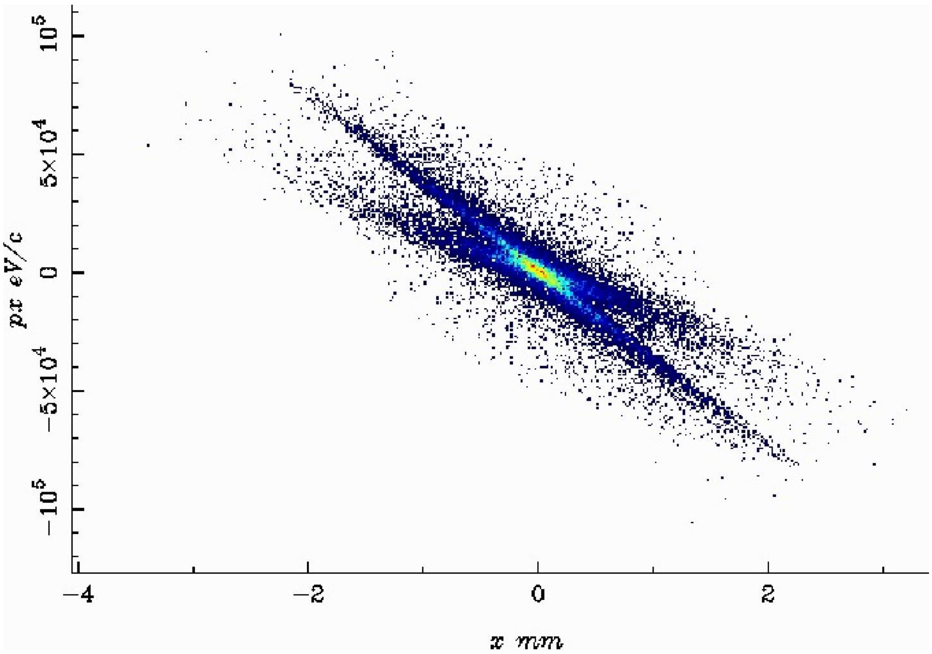

(b)

Fig. 6.8 Transverse phase space plots after solenoid that correspond to (a) bunch length 10 ps (b) bunch length 100 ps

This study tells that for requirements like cargo scanning and medical applications, where medium energy rf electron linacs are used and where beam quality (emittance) is the most important parameter, low energy spread of the bunch is a desirable criteria.

6.5. CONCLUSION

We have calculated the spherical aberration induced due to third order term in the radial co-ordinate of the electric field of a RF cavity. Growth of RMS emittance due to spherical aberration for uniform distribution beam has been analyzed. Using reduced envelope equation we have shown that the invariant envelope solution shifts from its original value due to spherical aberration induced term. A mathematical expression is established for solution of beam trajectory equation and change in frequency of oscillation of the beam using Lindstedt –Poincare expansion method.

Further, We have calculated the spherical aberration induced due to third order term in the radial co-ordinate of the magnetic field and space charge non-uniformity. The corresponding growth of rms emittance is evaluated for various types of beam distribution functions. This analysis can be used to estimate the limiting value of spherical aberration that can be tolerated for a given limiting value of acceptable emittance growth. We have derived an expression for spread in focal length due to the energy spread in the beam that experiences the external magnetic field and the self field forces together.

A mathematical expression is established for distortion in phase space due to the energy spread of the beam. Finally, Using matrix method we have found out that the energy spread makes a non-linear correlation between x and x' which gives rise to growth of rms emittance. Taking into account higher order terms of the radial magnetic field component, effect of other aberrations on rms emittance can be found in a similar approach.

.

CHAPTER 7

NUMERICAL EVALUATION OF APERTURE COUPLING IN RESONANT CAVITIES AND FREQUENCY PERTURBATION ANALYSIS

The coupling of electromagnetic energy through a small aperture in a common wall between two regions is an important problem in electromagnetic engineering. The examples of such type of problem occurs in the design of waveguide, directional couplers, coupled resonator filters, apertures in a conducting screen, waveguide-fed apertures, cavity-fed apertures, waveguide-to-waveguide coupling, waveguide-to-cavity coupling, and cavity to-cavity coupling systems. Bethe's theory [31] states that the coupling through a small circular aperture in a conducting plane wall of zero thickness. is equivalent to a combination of radiating electric and magnetic dipoles. Collins [32] modified Bethe's theory taking elliptical integral formulation for the electric and magnetic dipole moments of the ellipsoidal dielectric. The work of Bethe and Collin apply to small apertures in the walls of zero thickness. The electrolytic tank method by Cohn [96-98] and the network analysis method in [99-102] polynomial approximation method [103] and Rayleigh series method in [104] gives analysis on aperture coupling.

In section 7.1 of this chapter we present a new formulation to obtain the expression for electric and magnetic dipole moments of the elliptic apertures in cavities in terms of Carlson Symmetric integrals [34], specifically for small apertures of finite thickness. Unlike some of the earlier approaches referred to above, the present formulation [33, 105] is not restricted in its application to conducting walls of zero thickness, and its use is particularly suitable when numerical techniques are considered [106]. Carlson integral formulation consists of evaluation of elliptical integrals in terms of standard R functions instead of Legendre's integrals. In these integral equations the interval of the integration is not required to begin or end at a singular point of the integrand. Furthermore, the Carlson Integrals lead to the Legendre integral formulation of the earlier work [32] by imposing the condition that the thickness of the aperture tends to zero. We have given analytical expressions for Carlson integrals for the case of circular aperture.

In section 7.5 and section 7.6, we have analysed the effect of frequency change due to the opening of apertures on the cavity walls in a manner similar to [107] and the results presented by the former have been modified in terms of Carlson integrals.

In addition to the above we have proposed analytical formulae in terms of symmetric elliptic integral for various figures of merits of accelerating cavities such as quality factor (Q), shunt impedance, filling time, wake loss parameter, cell geometry etc-.

7.1 ANALYTICAL FORMULATION OF THE PROBLEM

We consider the problem of coupling between two identical cavities 1 and 2 by means of a small elliptical aperture in a common side wall as shown in the Fig. 7.1. Although the aperture shapes can be considered to be of various shapes like rectangular, diamond, rounded end slot, and ellipse, but the elliptical aperture problem can be solved exactly using elliptical integral techniques [103].

The aperture region is uniformly filled with a lossless material with electrical characteristics $\in$ and μ and the cavity regions are assumed air filled ($\in_0, \mu_0$). A plane wave is incident from cavity 1 onto the aperture.

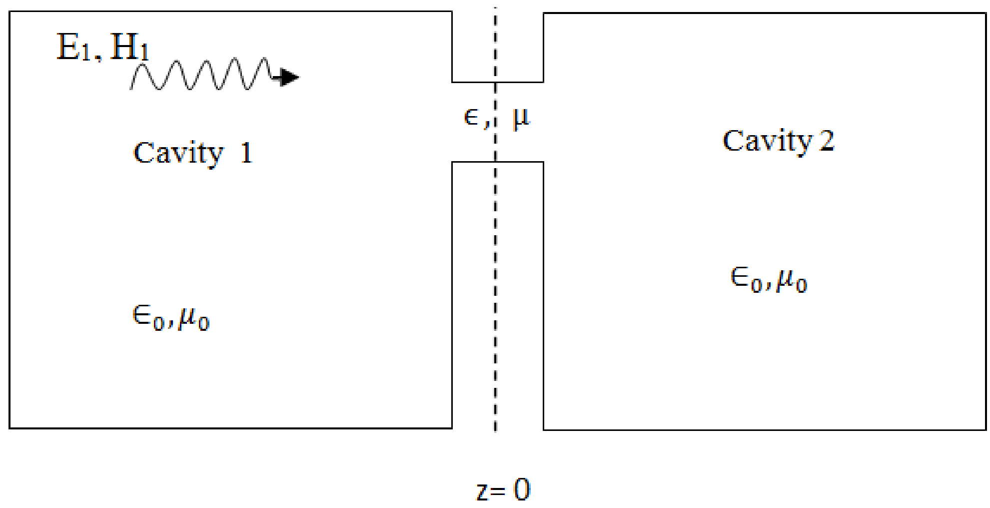

Fig. 7.1 Two Cavities coupled by a small aperture

If we let E_1, H_1 are the incident field and E_s, and H_s are the scattered field, with the aperture closed by a perfect magnetic wall, the following boundary conditions are satisfied on the magnetic wall in the aperture

$$\hat{n} \times (H_s + H_1) = 0 \tag{7.1}$$

$$\hat{n} \cdot (E_s + E_1) = 0 \tag{7.2}$$

The magnetic charge and the magnetic current distribution that exist on the aperture can be expressed as

$$\mu_0 \hat{n} \cdot H_s = \rho_m \tag{7.3}$$

$$-\hat{n} \times E_s = J_m \tag{7.4}$$

Since the two cavities are identical, a current J_m will radiate identical fields into the two cavities. The effective dipole moments associated with the aperture current J_m and charge $-\rho_m$ for radiation into the cavity 2 will be $-M/2$ and $-P/2$. The total field in the cavity 1 is the sum of the incident fields and the field radiated by the dipole of strength $M/2$ and $P/2$ and the other components cancel out.

A static field solution for the dipole moments of small elliptic and circular shaped apertures can be found quite readily [32]. In the practical applications of the theory, the static field solution gives results of small apertures [96].

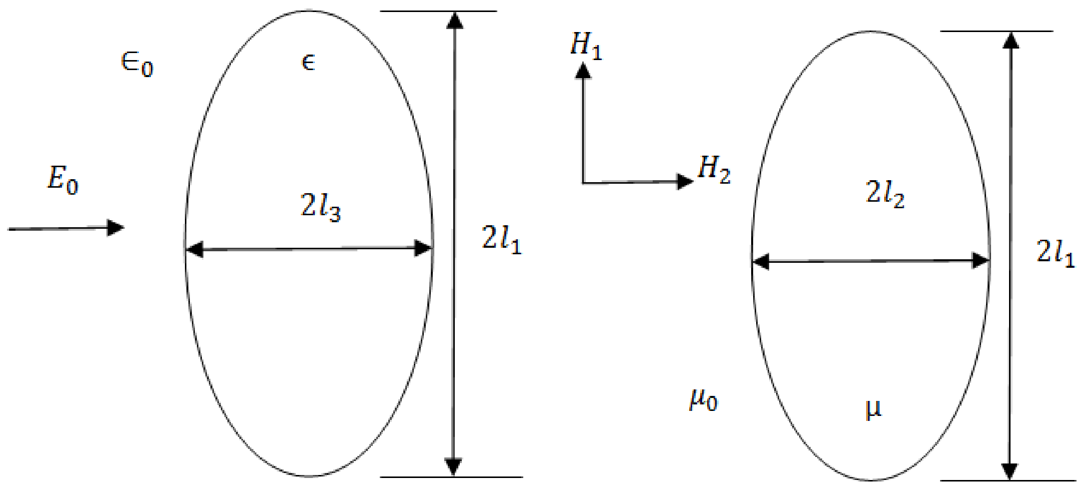

Fig. 7.2 (a) Dielectric ellipsoid (b) Permeable magnetic

The dipole moments of the elliptical aperture can be obtained from the static dipole moments of a dielectric ellipsoid with semi axes l_1, l_2, l_3 and placed in a uniform static electric field E_0 directed along the l_3 axis as shown in the Fig. 7.2. The three principal axes are orthogonal and can be easily analyzed with the symmetry that usually exists for a practical aperture shape. In an analogy with [108] the electric dipole moment P_3 of the ellipsoid with the field E_0 applied along l_3 axis is

$$P_3 = \frac{\in_0 E_0 V}{L_3 + \in_0 / (\in - \in_0)} \tag{7.5}$$

Where

$$L_3 = \frac{l_1 l_2 l_3}{2} \int_0^\infty \frac{ds}{(s + l_1^2)^{1/2} (s + l_2^2)^{1/2} (s + l_3^2)^{3/2}} \tag{7.6}$$

and $V = \frac{4\pi}{3} l_1 l_2 l_3$ is the volume of the ellipsoid.

We let $\in = 0$, such that the ellipsoid behaves like a perfect magnetic wall and its net internal displacement flux becomes zero. The electric field at the wall satisfies the boundary condition as polarization charge developed cancels out the normal component of the applied field on the surface of the ellipsoid.

The magnetic dipole moment M_1 due to the field H_1 along l_1 axis and M_2 due to field H_2 along axis l_2 are

$$M_1 = \frac{VH_1}{L_1 + \mu_0/(\mu - \mu_0)} \quad , \tag{7.7}$$

Where

$$L_1 = \frac{l_1 l_2 l_3}{2} \int_0^\infty \frac{ds}{(s + l_2^2)^{1/2} (s + l_3^2)^{1/2} (s + l_1^2)^{3/2}} \tag{7.8}$$

and

$$M_2 = \frac{VH_2}{L_2 + \mu_0/(\mu - \mu_0)} \tag{7.9}$$

Where

$$L_2 = \frac{l_1 l_2 l_3}{2} \int_0^\infty \frac{ds}{(s + l_3^2)^{1/2} (s + l_1^2)^{1/2} (s + l_2^2)^{3/2}} \tag{7.10}$$

If we let μ approach infinity , the internal magnetic field H_i vanishes since $\hat{n} \cdot \mu_0 H_e$ equals $\hat{n} \cdot \mu_0 H_i$ i.e the normal component of the the external field applied H_e is equal to the normal component of the internal field, hence the product μH_i is finite . So as μ approach infinity, H_i tend to zero.

7.2 DIPOLE MOMENTS IN TERMS OF CARLSON SYMMETRIC ELLIPTICAL INTEGRALS

The integrals L_1, L_2, L_3 may be evaluated in terms of Carlson Symmetric elliptic integrals of 2nd kind.

Earlier approach by [32] used to consider the elliptical integrals of the form for which Jahnke and Emde tabulated solutions [109]. The limit of such an approach is that the thickness of the aperture is to be set to zero in order to use the elliptic integrals of the first kind and second kind K and E respectively. Carlson integral can lead to the elliptical integrals of the form K and E choosing the thickness of the aperture l_3 tends to zero.

Therefore, the expression for the integral L_3 in terms of the Carlson Elliptical Integrals is

$$L_3 = \frac{l_1 l_2 l_3}{3} R_D\left(l_1^2, l_2^2, l_3^2\right) \tag{7.11}$$

Where

$$R_D\left(l_1^2, l_2^2, l_3^2\right) = \frac{3}{2}\int_0^\infty \frac{ds}{\left(s+l_1^2\right)^{1/2}\left(s+l_2^2\right)^{1/2}\left(s+l_3^2\right)^{3/2}} \tag{7.12}$$

Similarly, the integrals L_1 and L_2 can be written in terms of Carlson Integrals as

$$L_1 = \frac{l_1 l_2 l_3}{3} R_D\left(l_2^2, l_3^2, l_1^2\right) \tag{7.13}$$

and,

$$L_2 = \frac{l_1 l_2 l_3}{3} R_D\left(l_3^2, l_1^2, l_2^2\right) \tag{7.14}$$

The Carlson integrals can be written in a compact form as

$R_1 = R_D\left(l_2^2, l_3^2, l_1^2\right)$, $R_2 = R_D\left(l_3^2, l_1^2, l_2^2\right)$, $R_3 = R_D\left(l_1^2, l_2^2, l_3^2\right)$

The dipole moment of the aperture is one half of that of an ellipsoidal dielectric, since only one side of the ellipsoid is under consideration while the ellipsoid has two sides with polarization charges on both the sides. Again the radiating dipole moment in the aperture is one-half of the moment of an aperture closed by a magnetic wall. Hence the effective radiating dipole moment in the aperture is one –quarter of the moment of a complete ellipsoid [32].

Thus the dipole moments can be expressed as

$$P_3 = -\frac{\pi}{\left(R_1 + R_2\right)} \in_0 E_0 \tag{7.15}$$

$$M_1 = \frac{\pi}{R_1} H_1 \tag{7.16}$$

$$M_2 = \frac{\pi}{R_2} H_2 \tag{7.17}$$

According to Bethe's theory the dipole strengths of the scattered field are equal to the static dipole moments induced by the incident field, such that the electric dipole and magnetic dipole can be expressed as

$$P_0 = \in_0 \alpha_e \hat{\boldsymbol{n}}\hat{\boldsymbol{n}}.\boldsymbol{E}_1 \tag{7.18}$$

Where $\hat{n}$ is normal to the magnetic wall surface

$$M_0 = \overline{\boldsymbol{\alpha}_m}.\boldsymbol{H}_1 \tag{7.19}$$

Where the electric polarizability of the aperture is determined to be

$$\alpha_e = -\frac{\pi}{(R_1 + R_2)} \tag{7.20}$$

and the dyadic magnetic polarizability of the aperture is

$$\overline{\boldsymbol{\alpha}_m} = \boldsymbol{a}_u \boldsymbol{a}_u \frac{\pi}{R_1} + \boldsymbol{a}_v \boldsymbol{a}_v \frac{\pi}{R_2} \tag{7.21}$$

$r = \boldsymbol{a}_u u + \boldsymbol{a}_v v$ is the position vector in the localized rectangular coordinate system with the origin at the centre of the aperture.

When the aperture polarizabilities concept is applied to the coupling between two lossless, identical waveguides or cavities through a small aperture of finite thickness, the coupling coefficient between the two cavities can be expressed as

$$\beta = \overline{\boldsymbol{\alpha}_m} \frac{\boldsymbol{H_t} \cdot \boldsymbol{H_t}}{\iiint \boldsymbol{H} \cdot \boldsymbol{H} dv} + \alpha_e \frac{\boldsymbol{E_n} \cdot \boldsymbol{E_n}}{\iiint \boldsymbol{E} \cdot \boldsymbol{E} dv} \tag{7.22}$$

Where the subscript t and n denotes the tangential and normal components of the field values respectively.

7.3 FORMULATION OF THE PROBLEM FOR APERTURE OF ZERO THICKNESS

The complete elliptical integrals of first and second kinds can be expressed as [35]

$$K(\mathrm{e}) = \frac{\pi}{2}\left[1 + \left(\frac{1}{2}\right)^2 e^2 + \left(\frac{1.3}{2.4}\right)^2 e^4 + \left(\frac{1.3.5}{2.4.6}\right)^2 e^6 + \left(\frac{1.3.5.7}{2.4.6.8}\right)^2 e^8 + \ldots\ldots\ldots\ldots\right] \tag{7.23}$$

$$\mathrm{E(e)} = \frac{\pi}{2}\left[1 - \left(\frac{1}{2}\right)^2 e^2 - \left(\frac{1.3}{2.4}\right)^2 \frac{e^4}{3} - \left(\frac{1.3.5}{2.4.6}\right)^2 \frac{e^6}{5} - \left(\frac{1.3.5.7}{2.4.6.8}\right)^2 \frac{e^8}{7} - \ldots\ldots\ldots\ldots\right] \tag{7.24}$$

With

$$e = \left(1 - \frac{l_2^2}{l_1^2}\right)^{1/2} \tag{7.25}$$

If we choose the thickness of the aperture l_3 tends to zero Carlson symmetric integrals reduces to the complete elliptical integrals of first and second kinds using the following expressions [110]

$$K(\mathrm{e}) - \mathrm{E}(\mathrm{e}) = \frac{e^2}{3} R_D(0, 1-e^2, 1) \tag{7.26}$$

$$\mathrm{E}(\mathrm{e}) - (1-\mathrm{e}^2)K(\mathrm{e}) = \frac{e^2(1-\mathrm{e}^2)}{3} R_D(0, 1, 1-e^2) \tag{7.27}$$

$$\mathrm{E}(\mathrm{e}) = \frac{(1-\mathrm{e}^2)}{3}\left[R_D(0, 1-e^2, 1) + R_D(0, 1, 1-e^2)\right] \tag{7.28}$$

We have numerically evaluated equations (7.26), (7.27), (7.28) with the help of equations (7.23), (7.24), (7.25) and the plots shown in Fig. 7.3 give a comparison study of numerical evaluation of Carlson Symmetric integrals and complete elliptical integrals of first and second kind.

These plots in Fig. 7.3, shows that the approximation of complete elliptical integrals of first and second kinds up to few order term matches closely with the Carlson integral inequalities for aperture of zero thickness. Both the curves will perfectly match when higher order terms are considered in approximations of $\mathrm{K(e)}$ and $\mathrm{E(e)}$. In section 7.5 and 7.6, we have discussed the physical significance of the plots, where we apply the Carlson integral technique to solve the effect of frequency perturbation due to an aperture of finite thickness.

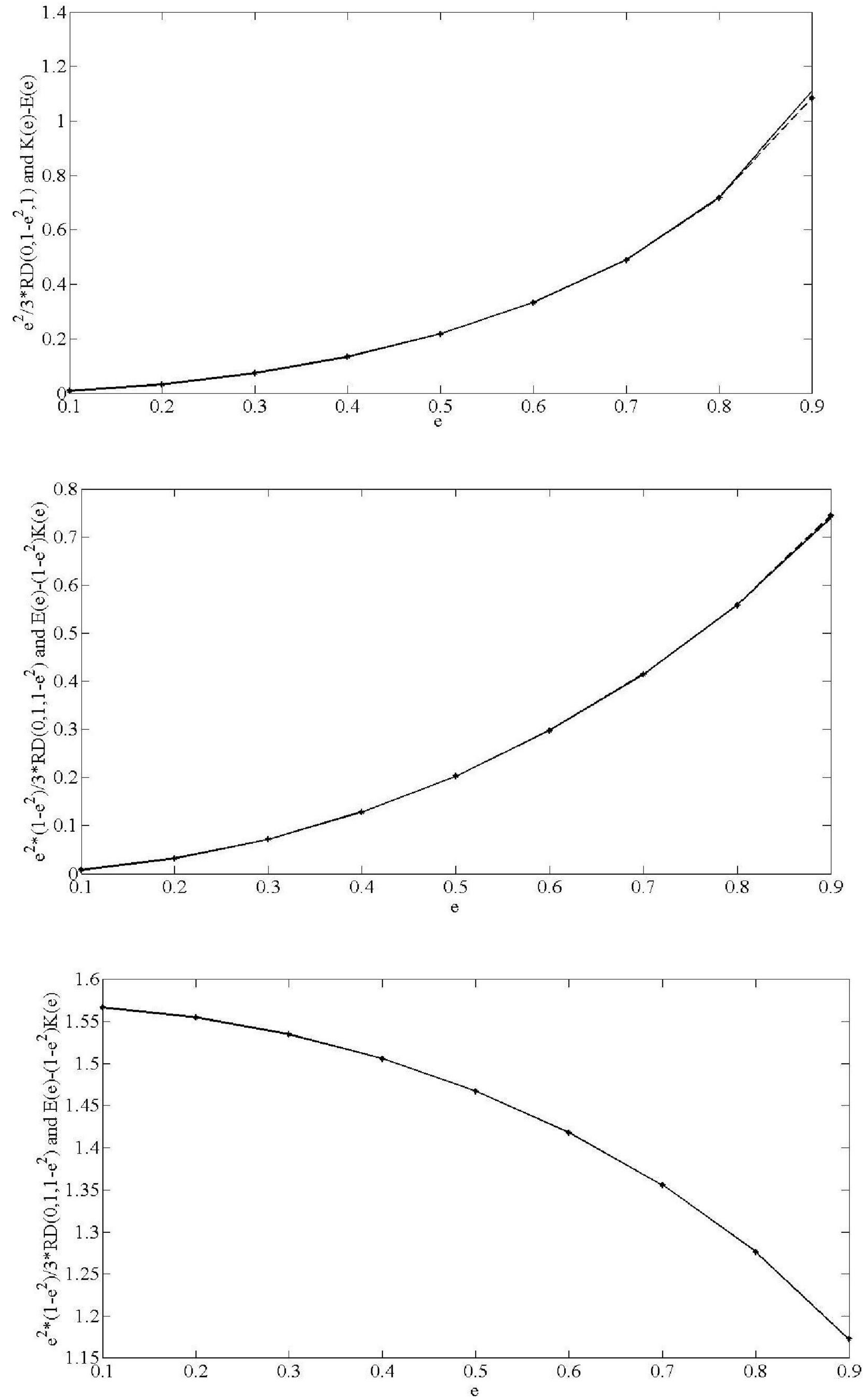

Fig. 7.3 Comparison of the plots for Carlson Symmetric integrals (Solid Line) and complete elliptical integrals of first and second kind (Dotted Line).

7.4 ANALYTICAL EXPRESSION OF CARLSON INTEGRALS FOR CIRCULAR APERTURE

Following the procedure discussed in [41] an approximate analysis of the Carlson integral can be presented which is accurate for aperture of circular cross-section. We introduce a form factor ξ defined as

$$\xi(g) = \frac{g}{2}\int_0^\infty \frac{dt}{(t+1)\left(t+g^2\right)^{3/2}} = \frac{1}{1-g^2}\begin{cases} 1-\dfrac{g}{\sqrt{1-g^2}}\cos^{-1} g & \mathit{for}\ g<1 \\ 1-\dfrac{g}{\sqrt{g^2-1}}\cosh^{-1} g & \mathit{for}\ g>1 \end{cases} \tag{7.29}$$

Where g is a dimensionless quantity.

Although ξ is defined by the integral expression, however, this integral may be expressed analytically in terms of elementary functions as described.

Using the form factor we can approximate the elliptic integrals as :

$$R_D\left(l_2^2, l_3^2, l_1^2\right) = \frac{3}{l_1 l_3}\frac{1}{l_1+l_2}\left[1-\xi\left(\frac{l_3}{\sqrt{l_1 l_2}}\right)\right] \tag{7.30}$$

$$R_D\left(l_3^2, l_1^2, l_2^2\right) = \frac{3}{l_2 l_3}\frac{1}{l_1+l_2}\left[1-\xi\left(\frac{l_3}{\sqrt{l_1 l_2}}\right)\right] \tag{7.31}$$

$$R_D\left(l_1^2, l_2^2, l_3^2\right) = \frac{3}{l_1 l_2 l_3}\frac{1}{l_1+l_2}\xi\left(\frac{l_3}{\sqrt{l_1 l_2}}\right) \tag{7.32}$$

The above approximations for the transverse plane elliptic integrals are only accurate up to order ε and approximations for longitudinal plane integrals are accurate up to order ε^2.

7.5 EFFECT OF FREQUENCY PERTURBATION ON COUPLING BETWEEN CAVITIES DUE TO OPENING OF APERTURES ON CAVITY WALLS

Slater's Pertubation formula [36, 51] describes the change in resonant frequency of a lossless resonant cavity when a small change in volume of ΔV is introduced in the cavity wall. If ω_0 is the resonant frequency before perturbation, ω is the resonant frequency after perturbation, U is the total energy stored in the cavity, E and H are the electric and magnetic fields in the small volume

$$\frac{\omega-\omega_0}{\omega_0}=\frac{\iiint\limits_{\Delta V}\left(\mu|H|^2-\in|E|^2\right)}{\iiint\limits_{\Delta V}\left(\mu|H|^2+\in|E|^2\right)} \tag{7.33}$$

The change in resonant frequency due to perturbation on the cavity walls can be written as

$$\frac{\omega-\omega_0}{\omega_0}=\frac{\Delta W_m-\Delta W_e}{U} \tag{7.34}$$

Where U is the total energy stored in the cavity.

Bethe's theory considers that the aperture on the cavity wall is equivalent to electric and magnetic dipoles with their moments given by [eqns(7.15), (7.16), (7.17)]. These dipoles interact with applied driving electromagnetic field. The magnitude of these driving fields are

$E'=\frac{E_0}{2}$, $\mathrm{H}_1'=\frac{\mathrm{H}_1}{2}$, $\mathrm{H}_2'=\frac{\mathrm{H}_2}{2}$, where E_0, H_1 , H_2 the field values at the centre of the aperture before being perturbed.

Taking the time average of the energy changes due to these electromagnetic dipoles, we have

$$\Delta U_e = -\frac{1}{2}\boldsymbol{P}\cdot\boldsymbol{E'} = \frac{\pi}{(R_1+R_2)} \in_0 \frac{E_0^{\ 2}}{4} = -\Delta W_e \tag{7.35}$$

$$\Delta U_m = \Delta U_{m,1} + \Delta U_{m,2} = -W_m \tag{7.36}$$

With

$$\Delta U_{m,1} = \frac{1}{2}\boldsymbol{M_1}\cdot\boldsymbol{H_1'} = \frac{\pi}{R_1}\frac{H_1^{\ 2}}{4} \tag{7.37}$$

$$\Delta U_{m,2} = \frac{1}{2}\boldsymbol{M}_2\cdot\boldsymbol{H}_2' = \frac{\pi}{R_2}\frac{H_2^{\ 2}}{4} \tag{7.38}$$

7.5.1 ELECTRIC COUPLING

Let us consider coupling between the two cavities through an aperture of finite thickness on the common wall. Assuming that the frequency of electromagnetic field oscillation in both the cavities are same, the energy change in the first cavity due to the electric dipole is

$$\Delta W_{e,1} = \frac{1}{2}\boldsymbol{P_1}\cdot\boldsymbol{E_1'} - \frac{1}{2}\boldsymbol{P_1}\cdot\boldsymbol{E}_2' \tag{7.39}$$

Where $\boldsymbol{P_1}$ is the dipole moment corresponding to the first cavity with the driving field $\boldsymbol{E_1'} = \frac{1}{2}\boldsymbol{E_1}$ and the driving field of the second cavity as seen by first cavity is $\boldsymbol{E}_2' = \frac{1}{2}e^{-2\alpha_1 l_3}\boldsymbol{E}_2$.

$\boldsymbol{E}_1$ and $\boldsymbol{E}_2$ are the electric fields at the centre of the aperture in the two cavities when the aperture is replaced by an ideal metallic boundary. $2l_3$ is the thickness of the common wall where the aperture is located.

The frequency change of the first cavity due to electric coupling is

$$\omega_1^2 = \omega_{0,1}^2 \left[1 - \frac{2}{U} \left\{ \frac{1}{2} \boldsymbol{P_1} \cdot \boldsymbol{E_1'} - \frac{1}{2} \boldsymbol{P_1} \cdot \boldsymbol{E_2'} \right\} \right] \tag{7.40}$$

Now

$$\frac{1}{2} \boldsymbol{P_1} \cdot \boldsymbol{E_1'} = -\frac{\pi}{(R_1 + R_2)} \in_0 \frac{E_1^2}{4} = -\frac{\pi}{(R_1 + R_2)} \in_0 \frac{(\boldsymbol{E_1} \cdot \boldsymbol{E_1})}{4} \tag{7.41}$$

$$\frac{1}{2} \boldsymbol{P_1} \cdot \boldsymbol{E_2'} = -\frac{\pi}{(R_1 + R_2)} \in_0 \frac{(\boldsymbol{E_1} \cdot \boldsymbol{E_2})}{4} e^{-2\alpha_1 l_3} = -\frac{\pi}{(R_1 + R_2)} \in_0 \frac{E_1 E_2}{4} \cos\theta e^{-2\alpha_1 l_3} \tag{7.42}$$

Where θ is the phase difference between $\boldsymbol{E}_1$ and $\boldsymbol{E}_2$.

Thus the frequency change of the first cavity becomes

$$\omega_1^2 = \omega_{0,1}^2 \left[1 + \frac{1}{2} \frac{\pi}{(R_1 + R_2)} \in_0 \left\{ \frac{E_1^2}{U} - \frac{E_1 E_2}{U} \cos\theta e^{-2\alpha_1 l_3} \right\} \right] \tag{7.43}$$

We can follow the same procedure to get the frequency change for second cavity.

7.5.2 MAGNETIC COUPLING

If the two cavities are magnetically coupled then the frequency change of the first cavity is

$$\omega_1^2 = \omega_{0,1}^2 \left(1 + 2 \frac{\Delta W_m}{U} \right) \tag{7.44}$$

The energy change in the first cavity due to the magnetic dipole is

$$\Delta W_{m,1} = \frac{1}{2} \boldsymbol{M_1} \cdot \boldsymbol{H_1'} - \frac{1}{2} \boldsymbol{M_1} \cdot \boldsymbol{H_2'} \tag{7.45}$$

So we have

$$\omega_1^2 = \omega_{0,1}^2 \left[1 - \frac{2}{U} \left\{ \frac{1}{2} \boldsymbol{M_1} \cdot \boldsymbol{H_1}' - \frac{1}{2} \boldsymbol{M_1} \cdot \boldsymbol{H_2}' \right\} \right] \tag{7.46}$$

Now

$$\frac{1}{2} \boldsymbol{M_1} \cdot \boldsymbol{H_1}' = \frac{\pi}{R_1} \frac{\boldsymbol{H_1} \cdot \boldsymbol{H_1}}{4} = \frac{\pi}{R_1} \frac{H_1^2}{4} \tag{7.47}$$

$$\frac{1}{2} \boldsymbol{M_1} \cdot \boldsymbol{H_2}' = \frac{\pi}{R_1} \frac{\boldsymbol{H_1} \cdot \boldsymbol{H_2}}{4} e^{-2\alpha_2 l_3} = \frac{\pi}{R_1} \frac{H_1 H_2}{4} \cos\theta e^{-2\alpha_2 l_3} \tag{7.48}$$

Thus the frequency change of the first cavity due to magnetic coupling is

$$\omega_1^2 = \omega_{0,1}^2 \left[1 - \frac{1}{2} \frac{\pi}{R_1} \left\{ \frac{H_1^2}{U} - \frac{H_1 H_2}{U} \cos\theta e^{-2\alpha_2 l_3} \right\} \right] \tag{7.49}$$

For the second cavity we can follow the same procedure accordingly.

If this coupling aperture is located where electric field and magnetic fields do not vanish, the total frequency change is the due to the combined effects of electric and magnetic and is given by

$$\omega_1^2 = \omega_{0,1}^2 \left[1 + \frac{1}{2} \frac{\pi}{(R_1 + R_2)} \in_0 \left(\frac{E_1^2}{U} - \frac{E_1 E_2}{U} \cos\theta e^{-2\alpha_1 l_3} \right) - \frac{1}{2} \frac{\pi}{R_1} \left(\frac{H_1^2}{U} - \frac{H_1 H_2}{U} \cos\theta e^{-2\alpha_2 l_3} \right) \right] \tag{7.50}$$

7.6 EFFECT OF FREQUENCY PERTURBATION ON THE GROUP VELOCITY OF ACCELERATING STRUCTURE

The earlier work [107] discusses the dispersion relation of accelerating structure for coupling aperture of zero thickness. We proceed in a manner analogous to [107] and modify the previous expressions considering the finite thickness of the aperture. We consider a periodic disc loaded accelerator structure as shown in the Fig. 7.4.

According to Floquet's theorem, cell to cell phase shift $\theta = \beta_0 D$ where β_0 is the fundamental wave number and D is the space periodicity of the periodic structure.

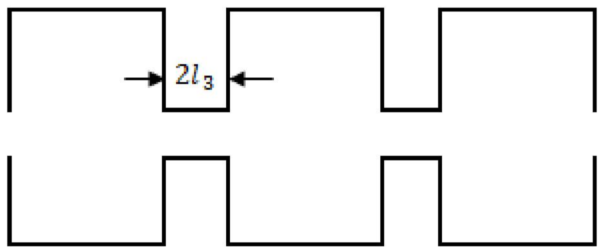

Fig. 7.4 Electrically Coupled Slow wave structure

7.6.1 GROUP VELOCITY OF ELECTRICALLY COUPLING STRUCTURE

First we consider the case of electrical coupling structure of Fig. 7.4.

According to equation (7.43), the resonant frequency after perturbation is

$$\omega^2 = \omega_0^2 \left[1 + \frac{N}{2} \frac{\pi}{(R_1 + R_2)} \in_0 \left\{ \frac{E_1^2}{U} - \frac{E_1 E_2}{U} \cos\theta e^{-2\alpha_1 l_3} \right\} \right] \tag{7.51}$$

Where N is the no of coupling apertures on the wall of each cavity (assuming that the physical condition for these N apertures are same).

If $\beta_0 D = \frac{\pi}{2}$ (for $\frac{\pi}{2}$ mode), then

$$\omega_{\pi/2}^2 = \omega_0^2 \left[1 + \frac{N}{2} \frac{\pi}{(R_1 + R_2)} \in_0 \frac{E_1^2}{U} \right] \tag{7.52}$$

So we can write equation (7.51) as

$$\omega^2 = \omega_{\pi/2}^2 - \frac{\left(\omega_0^2 - \omega_{\pi/2}^2\right)}{\omega_{\pi/2}^2}\omega_{\pi/2}^2 \frac{N}{2}\frac{\pi}{\left(R_1 + R_2\right)} \in_0 \frac{E_1 E_2 \cos\left(\beta_0 D\right)}{U} e^{-2\alpha_1 l_3}$$
$$- \omega_{\pi/2}^2 \frac{N}{2}\frac{\pi}{\left(R_1 + R_2\right)} \in_0 \frac{E_1 E_2 \cos\left(\beta_0 D\right)}{U} e^{-2\alpha_1 l_3}$$

Usually $\left|\left(\omega_0 - \omega_{\pi/2}\right)/\omega_{\pi/2}\right| << 1$, Hence

$$\omega^2 = \omega_{\pi/2}^2 \left[1 - \frac{N}{2}\frac{\pi}{\left(R_1 + R_2\right)} \in_0 \frac{E_1 E_2 \cos\left(\beta_0 D\right)}{U} e^{-2\alpha_1 l_3}\right] \tag{7.53}$$

It is very clear to observe that equation (7.53) is the dispersion relation of an electrically coupled slow wave structure.

By comparing that obtained from an equivalent circuit as shown in Fig. 7.5

$$\omega^2 = \omega_{\pi/2}^2 \left[1 - k\cos\left(\beta_0 D\right)\right] \tag{7.54}$$

Where $k = 2C/\left(C + C'\right)$.

So we can write the coupling constant k in the dispersion relation as

$$k = \frac{N}{2}\frac{\pi}{\left(R_1 + R_2\right)} \in_0 \frac{E_1 E_2}{U} e^{-2\alpha_1 l_3} \tag{7.55}$$

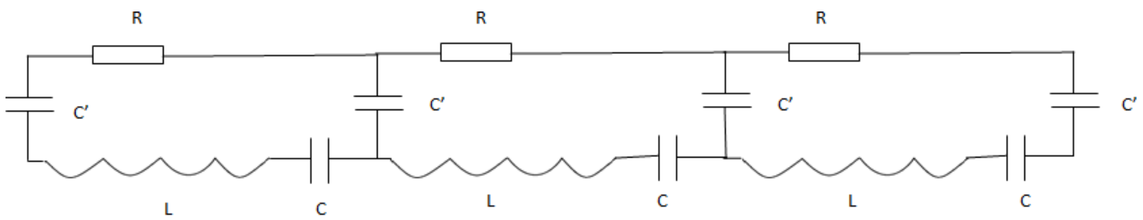

Fig. 7.5 Equivalent circuit of electrically coupled slow wave structure

We can write the resonant frequency as

$$\omega = \omega_{\pi/2}\left[1 - \frac{N}{4}\frac{\pi}{(R_1+R_2)}\in_0 \frac{E_1E_2\cos(\beta_0 D)}{U}e^{-2\alpha_1 l_3}\right] \tag{7.56}$$

The group velocity of this electrically coupled structure is

$$v_g = \frac{d\omega}{d\beta_0} = \omega_{\pi/2}\frac{N}{4}\frac{\pi}{(R_1+R_2)}\in_0 \frac{\alpha_e D E_1^2\sin(\beta_0 D)}{U}e^{-2\alpha_1 l_3} \tag{7.57}$$

Where $\alpha_e = \left|\frac{E_2}{E_1}\right|$, $1 \geq \alpha_e \geq 0$ and in the normal accelerating structure $\alpha_e = 1$

7.6.2 GROUP VELOCITY OF MAGNETICALLY COUPLING STRUCTURE

Next we shall take into account the magnetic coupling structure (Fig. 7.6). According to eqn (6.49), the resonant frequency after perturbation is

$$\omega^2 = \omega_0^2\left[1 - \frac{N}{2}\frac{\pi}{R_1}\left\{\frac{H_1^2}{U} - \frac{H_1H_2}{U}\cos(\beta_0 D)e^{-2\alpha_2 l_3}\right\}\right] \tag{7.58}$$

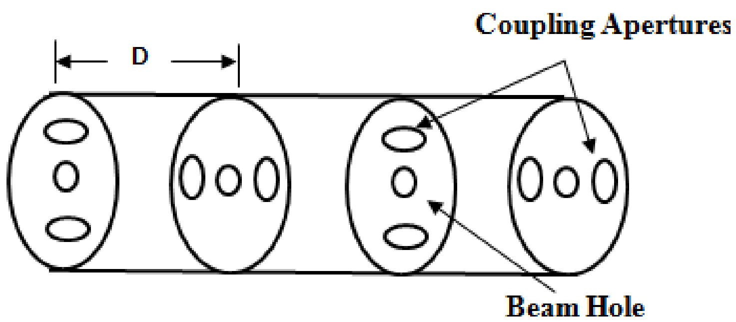

Fig. 7.6 Magnetically coupled slow wave structure

If $\beta_0 D = \frac{\pi}{2}$ (for $\frac{\pi}{2}$ mode), then

$$\omega_{\pi/2}^2 = \omega_0^2\left[1 - \frac{N}{2}\frac{\pi}{R_1}\frac{H_1^2}{U}\right] \tag{7.59}$$

So we can write

$$\omega^2 = \omega_{\pi/2}^2 \left[1 + \frac{N}{2} \frac{\pi}{R_1} \frac{H_1 H_2}{U} \cos(\beta_0 D) e^{-2\alpha_2 l_3} \right] \tag{7.60}$$

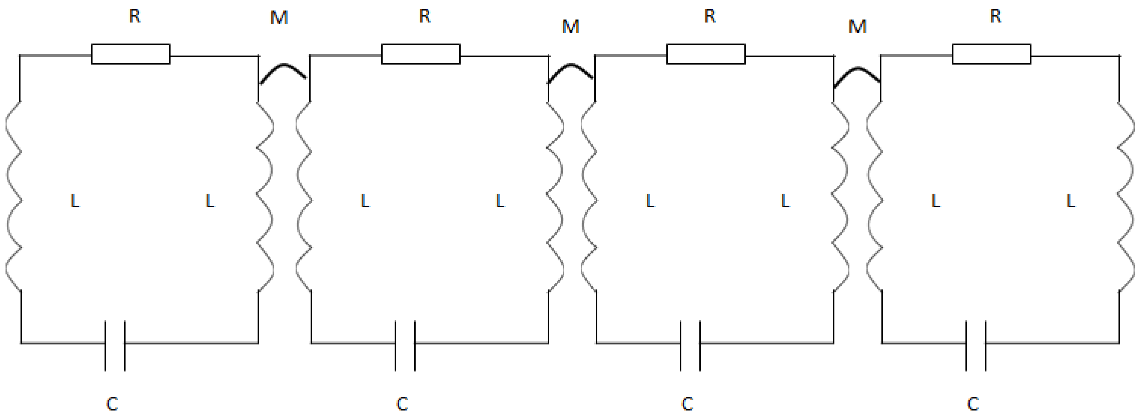

Fig. 7.7 Equivalent circuit of magnetically coupled slow wave structure

By comparing that obtained from an equivalent circuit (Fig. 7.7)

$$\omega^2 = \frac{\omega_{\pi/2}^2}{\left[1 - k\cos(\beta_0 D)\right]} \approx \omega_{\pi/2}^2 \left[1 + k\cos(\beta_0 D)\right] \tag{7.61}$$

Where $k = M/L$.

We can write the coupling constant for magnetically couple case as

$$k = \frac{N}{2} \frac{\pi}{R_1} \frac{H_1 H_2}{U} e^{-2\alpha_2 l_3} \tag{7.62}$$

We can write the resonant frequency as

$$\omega = \omega_{\pi/2} \left[1 + \frac{N}{4} \frac{\pi}{R_1} \frac{H_1 H_2}{U} \cos(\beta_0 D) e^{-2\alpha_2 l_3} \right] \tag{7.63}$$

The group velocity of this magnetically coupled structure is

$$v_g = \frac{d\omega}{d\beta_0} = -\frac{N}{4}\frac{\pi}{R_1}\frac{\alpha_m D H_1^2 \sin(\beta_0 D)}{U} e^{-2\alpha_2 l_3} \tag{7.64}$$

Where $\alpha_m = \left| H_2 / H_1 \right|$, $1 \geq \alpha_m \geq 0$ and in the normal accelerating structure $\alpha_m = 1$.

7.7 EFFECT OF FREQUENCY PERTURBATION ON THE FIGUREOF MERIT OF ACCELERATING CAVITIES

An important figure of merit of an rf accelerating cavity as a resonator [10] is the quality factor (Q_0). It is defined as the ratio of the energy stored in the cavity (U) to the energy lost due to rf power dissipated on the cavity walls (P_c) per radian of the rf cycle. The frequency dependence of the Q_0 is given by

$$Q_0 = \frac{\omega_0 U}{P_c}$$

For a magnetically aperture coupled cavity in $\frac{\pi}{2}$ mode, the modified Q_0 can be expressed as

$$Q_0 = \frac{\omega_{\pi/2,m}\left[U + \frac{N}{4}\frac{\pi}{R_1} H_1 H_2 \cos(\beta_0 D) e^{-2\alpha_2 l_3}\right]}{P_c}$$

For electrically aperture coupled cavity in Q_0 is

$$Q_0 = \frac{\omega_{\pi/2,e}\left[U - \frac{N}{4}\frac{\pi}{(R_1 + R_2)} \in_0 E_1 E_2 \cos(\beta_0 D) e^{-2\alpha_1 l_3}\right]}{P_c}$$

Where the $\omega_{\pi/2,m}$ and $\omega_{\pi/2,e}$ are given by eqns (6.54) and (6.61) respectively.

Another Figure of merit of the rf cavity is the ratio r_0 over Q_0 denoted by (r_0 / Q_0) and defined as $r_0 / Q_0 = \frac{E_0^2}{\omega_0 U}$, where r_0 is the effective shunt impedance of the cavity. But the energy stored in the cavity (U) is proportional to E_0^2 times the cross-sectional area of the cavity and the area varies as ω_0^{-2}.

Thus the $r_0 / Q_0 \propto \omega_0$.

When the cavity is perturbed by aperture r_0 / Q_0 is proportional to the perturbed frequency ω.

The diameter of the aperture of the accelerator structure through which the beam is transmitted is inversely proportional to ω_0. Hence after perturbation the aperture diameter varies as ω^{-1}.

The filling time of rf power in the accelerator cavities varies as $\omega_0^{-3/2}$, hence the filling time changes with perturbation in frequency due to apertures.

Another figure of merit , which is of interest for relativistic electron accelerator is the wake loss parameter k_L which is defined as [111]

$$k_L = \frac{\omega_0 r_0}{4Q_0}$$

As r_0 varies as $\omega_0^{1/2}$ and Q_0 varies as $\omega_0^{-1/2}$, hence after the aperture perturbation k_L is proportional to the square of the perturbed frequency i.e. ω^2.

7.8 CONCLUSION

A general method for the electromagnetic coupling through small elliptic aperture has been developed. Explicit formulas for an elliptical aperture in a conducting plane excited by an incident plane wave have been derived. The method is based on Carlson symmetric integral equations and the satisfaction of boundary conditions at the aperture. Previous techniques using Legendre integral is unable to consider the finite thickness of the aperture. We have shown that the new method, on the other hand, extends the concept of aperture polarizability to include apertures in walls of finite thickness that also explains the well-established zero wall thickness case. The numerical evaluation of elliptic integrals [33, 105] gives a faster and efficient method for aperture coupling problems. We have found expressions for the frequency changes due to small aperture perturbation of appropriate thickness on the cavity wall, which may be useful for practical cavities and coupling structures.

CHAPTER 8

SUMMARY AND CONCLUSION

In this dissertation, the beam dynamics of a 100 MeV 100 kW electron accelerator has been carried out. The topic is of fundamental importance to future high energy machines for neutron generation purposes. Further the beam dynamics studies of a 30 MeV standing wave rf electron linac and a 10 MeV standing wave rf electron linac for industrial purposes have been done. Also, analytical calculations have been carried out for transverse emittance growth due to spherical aberration that arises due to the third order terms in the electric and magnetic field expansion respectively. Further numerical investigation of the aperture coupling in resonant cavities and the frequency perturbation analysis has been done.

Based on the above studies the following conclusions have been made.

a) It is found that space charge effect plays a pivotal role in the injector section and 1st cavity of the 30 MeV linac. A solenoid of length 15 cm and 15000 ampere turns over the injector section is necessary to compensate the space charge effect. With an output beam of size ~ 4.5 mm in the bore of aperture diameter 10 mm, and an energy spread of ~ 2.5% the beam loss on the cavity wall is minimized and the heavy irradiation of accelerator components is prevented.

b) For a 10 MeV linac, space charge effect is minimized with a solenoid of 15000 ampere turns and the beam satisfies the industrial norms to generate X rays.

c) The 100 MeV linac beam dynamics study explores that although both standing wave linac and travelling wave linac are highly efficient for high energy beam, the travelling wave linac may be preferred because of its large aperture and versatility to deal with high current and high power beam.

d) Spherical aberration that is induced due to third order term in the radial co-ordinate of the electric field of a RF cavity results in a growth of transverse emittance for a uniform beam distribution and shifts the invariant envelope solution from its original value. Change in frequency of oscillation of the beam is found using Lindstedt –Poincare expansion method.

e) Spherical aberration induced due to third order term in the radial co-ordinate of the magnetic field and space charge non-uniformity results in growth of transverse rms emittance for uniform, Gaussian, parabolic and waterbag beam distributions. Also, distortion in phase space due to the energy spread of the beam gives rise to growth of rms emittance.

f) It is found that numerical evaluation of elliptic integrals for electromagnetic coupling through small elliptic aperture gives a faster and efficient method for aperture coupling problems. Further, this method extends the concept of aperture polarizability to include apertures in walls of finite thickness and explains the well-established zero wall thickness case.

This study can be expanded in several directions to expand the application of the beam dynamics simulation for future high energy accelerators and to gain further insights of the high energy accelerators so to benefit its operation and reduce beam losses.

Finally some future scope of work has been outlined.

a) Study of photo neutron generation using various target materials is to be carried out.

b) Thermodynamical studies are to be carried out for heating of the accelerator components during high power beam generation and transport.

REFERENCES

[1] A. Sessler, and E. Wilson, *Engines of Discovery: A Century of Particle Accelerators*: World Scientific Publishing Company Pvt Limited, 2013.

[2] S. Hanna, *RF Linear Accelerators for Medical and Industrial Applications*: Artech House, 2012.

[3] E. D. Courant, and H. S. Snyder, “Theory of the Alternating-Gradient Synchrotron,” *Annals of Physics* vol. 3, no. 1, 1958.

[4] J. Buon, “Beam phase space and emittance,” *CAS - CERN Accelerator School : 5th General Accelerator Physics Course, Jyväskylä, Finland*, pp. 89-116, 7 - 18 Sep 1992.

[5] K. Floettmann, “Some basic features of the beam emittance,” *Physical Review Special Topics - Accelerators and Beams,* vol. 6, no. 3, pp. 034202, 2003.

[6] K. Floettmann, *Private communications*.

[7] R. W. Hamm, and M. E. Hamm, *Industrial Accelerators and Their Applications*: World Scientific, 2012.

[8] C. J. Karzmark, C. S. Nunan, and E. Tanabe, *Medical Electron Accelerators*: McGraw-Hill, Incorporated, Health Professions Division, 1993.

[9] H. Nifenecker, O. Meplan, and S. David, *Accelerator Driven Subcritical Reactors*: CRC Press, 2003.

[10] T. P. Wangler, *RF Linear Accelerators*, 2nd ed.: Wiley-VCH Verlag GmbH & Co. KGaA, 2010.

[11] K. Floettmann, “rf-induced beam dynamics in rf guns and accelerating cavities,” *Physical Review Special Topics - Accelerators and Beams,* vol. 18, no. 6, pp. 064801, 2015.

[12] R. Dash, B. Nayak, A. Sharma, and K. C. Mittal, “Study of beam dynamics of a 100 MeV electron linac,” *XXVI International Symposium on Discharges and Electrical Insulation in Vacuum (ISDEIV), 2014* pp. 573-575, Sept. 28 2014-Oct. 3 2014, 2014.

[13] R. Dash, B. Nayak, A. Sharma, and K. C. Mittal, “Beam dynamics study of a 100 MeV RF electron linac,” *2015 International Conference on Microwave, Optical and Communication Engineering (ICMOCE)*, pp. 303-306, 18-20 Dec. 2015, 2015.

[14] K. Floettmann, "ASTRA, A Space charge Tracking Algorithm," *<http://www.desy.de/~mpyflo/Astra_dokumentation>*.

[15] M. Borland, “elegant: A Flexible SDDS-Compliant Code for Accelerator Simulation,” *Advanced Photon Source LS-287*, September 2000.

[16] R. Dash, J. Mondal, A. Sharma, and K. C. Mittal, “Beam dynamics studies and parametric characterization of a standing wave electron linac,” *Journal of Instrumentation,* vol. 8, no. 07, pp. T07002, 2013.

[17] R. Dash, J. Mondal, A. Sharma, and K. C. Mittal, “Beam Dynamics Studies of a 30 MeV Standing Wave Electron Linac,” *Proceedings of PAC 2013, Pasadena, CA USA*, pp. 451-453, 29 Sept-04 Oct, 2013.

[18] R. Dash, J. Mondal, A. Sharma, and K. C. Mittal, “Study of beam dynamics of a 30 MeV standing wave electron linac,” *Proceedings of the Indian Particle Accelerator Conference*, pp. 320-322, 19-22 Nov 2013.

[19] K. C. Mittal, “High power electron accelerators for radiation processing and its safety aspects,” *Indian Journal of Pure & Applied Physics,* vol. 50, no. 11, pp. 772-775, 2012.

[20] R. Dash, A. Sharma, and K. C. Mittal, “Beam dynamics studies of a 10 MeV standing wave electron linac,” *XXVI International Symposium on Discharges and Electrical Insulation in Vacuum (ISDEIV), 2014* pp. 609-612, Sept. 28-Oct. 3, 2014.

[21] R. C. Sethi, V. T. Nimje, and etal, “Design and Development of 10 MeV RF Electron Linac for Applied Research and Industrial Applications,” *Proceedings of the Ist Asian Particle Acc. Conf. KEK, Japan*, October 1998.

[22] V. T. Nimje, and etal, “Beam Energy Measurement of 10 MeV, 10kW Industrial RF Electron Linac,” *Proceedings of the Indian Particle Accelerator Conference, India*, 2006.

[23] K. C. Mittal, and etal, “Operating Experience of 10 MeV Industrial Linac,” *Proceedings of the Indian Particle Accelerator Conference, India*, 2011.

[24] P. R. Sarma, S. K. Pattanayak, and R. K. Bhandari, “Improvement of field quality of Glaser magnets used for focusing ion beams,” *Nuclear Instruments and Methods in Physics Research Section A: Accelerators, Spectrometers, Detectors and Associated Equipment,* vol. 426, no. 2–3, pp. 243-248, 1999.

[25] B. Nayak, R. Dash, and K. C. Mittal, “Effect of spherical aberration on the emittance growth and frequency of oscillation of a beam crossing an RF gap,” *Nuclear Instruments and Methods in Physics Research Section A: Accelerators, Spectrometers, Detectors and Associated Equipment,* vol. 746, pp. 1-3, 2014.

[26] A. H. Nayfeh, *Perturbation Methods*: Wiley-VCH Verlag GmbH, 2007.

[27] R. Dash, B. Nayak, A. Sharma, and K. C. Mittal, "Analysis of transverse RMS emittance growth of a beam induced by spherical and chromatic aberration in a solenoidal field," *Nuclear Instruments and Methods in Physics Research Section A: Accelerators, Spectrometers, Detectors and Associated Equipment,* vol. 807, pp. 94-100, 2016.

[28] M. Reiser, *Theory and Design of Charged Particle Beams*, 2nd ed.: Wiley-VCH Verlag GmbH & Co. KGaA, 2008.

[29] J. Ximen, and Z. Liu, "Analytical analysis and numerical calculation of first- and third-order chromatic aberrations in Glaser's bell-shaped magnetic lens," *Optik,* vol. 109, no. 2, 1998.

[30] Z. Liu, and J. Ximen, "Numerical computation of higher-order chromatic aberrations for rotationally symmetric electrostatic lenses," *Journal of Applied Physics,* vol. 72, no. 1, pp. 28-32, 1992.

[31] H. A. Bethe, "Theory of Diffraction by Small Holes," *Physical Review,* vol. 66, no. 7-8, pp. 163-182, 1944.

[32] R. E. Collin, *Field Theory of Guided Waves*, 2nd ed., New York: IEEE Press, 1991.

[33] R. Dash, B. Nayak, A. Sharma, and K. C. Mittal, "Numerical evaluation of aperture coupling in resonant cavities and frequency perturbation analysis," *Journal of Instrumentation,* vol. 9, no. 01, pp. P01012, 2014.

[34] B. C. Carlson, "A table of elliptic integrals of the second kind," *Math. Comp.,* vol. 49, pp. 595-606, 1987.

[35] D. Zwillinger, *CRC Standard Mathematical Tables and Formulae, 31st Edition*: CRC Press, 2002.

[36] J. C. Slater, "Microwave Electronics," *Reviews of Modern Physics,* vol. 18, no. 4, pp. 441-512, 1946.

[37] R. B. Miller, *Electronic Irradiation of Foods*: Springer US, 2005.

[38] D. E. Nagle, E. A. Knapp, and B. C. Knapp, "Coupled Resonator Model for Standing Wave Accelerator Tanks," *Review of Scientific Instruments,* vol. 38, no. 11, pp. 1583-1587, 1967.

[39] W. D. Kilpatrick, "Criterion for Vacuum Sparking Designed to Include Both rf and dc," *Review of Scientific Instruments,* vol. 28, no. 10, pp. 824-826, 1957.

[40] J. T. J. Boyd, "Kilpatrick's criterion," *Los Alamos Group AT-1 report AT-1:82-28* 1982.

[41] C. K. Allen, and N. Pattengale, “Theory and technique of beam envelope simulation,” *Los Alamos National Laboratory Internal Report LA-UR-02-4979*, 2002.

[42] S. Humphries, *Charged particle beams*: Wiley, 1990.

[43] J. D. Lawson, *The Physics of Charged-particle Beams*, 2nd ed.: Clarendon Press, 1988.

[44] R. W. Hockney, and J. W. Eastwood, *Computer Simulation Using Particles*: CRC Press, 1988.

[45] P. M. Lapostolle, “Possible Emittance Increase through Filamentation Due to Space Charge in Continuous Beams,” *Nuclear Science, IEEE Transactions on,* vol. 18, no. 3, pp. 1101-1104, 1971.

[46] F. J. Sacherer, “RMS Envelope Equations with Space Charge,” *Nuclear Science, IEEE Transactions on,* vol. 18, no. 3, pp. 1105-1107, 1971.

[47] W. T.P., “High-Brightness Injectors for Hadron Colliders, November 7–14,Hilton Head, SC.,” *1990 Joint US-CERN School on Particle Accelerators*, 1990

[48] J. Rossbach, and P. Schmüser, “Basic course on accelerator optics,” *in Proc. CERN Accelerator School, University of Jyv¨askyl¨a, Finland*, 1994.

[49] H. Wiedemann, *Particle Accelerator Physics I Basic Principles and Linear Beam Dynamics*, 2nd ed.: Springer Berlin Heidelberg, 1999.

[50] D. A. Edwards, and M. J. Syphers, *An Introduction to the Physics of High Energy Accelerators*: Wiley, 2008.

[51] J. C. Slater, *Microwave electronics*: Van Nostrand, 1950.

[52] S. C. Hartman, and J. B. Rosenzweig, “Ponderomotive focusing in axisymmetric rf linacs,” *Physical Review E,* vol. 47, no. 3, pp. 2031-2037, 1993.

[53] M. Ferrario, J. E. Clendenin, J. B. Rosenzweig, D. T. Palmer, and L. Serafini, “HOMODYN study for the LCLS rf photo-injector,” *LCLS Technical Notes,* vol. lcls-tn-00-4, 2000.

[54] "CST Studio Suite 2008 ", <http://www.cst.com>

[55] T. P. Wangler, “Space-Charge Limits in Linear Accelerator,” *Los Alamos Scientific Laboratory Report LA-8388*, July, 1980.

[56] T. P. Wangler, K. R. Crandall, R. S. Mills, and M. Reiser, “Relation between Field Energy and RMS Emittance in Intense Particle Beams,” *Nuclear Science, IEEE Transactions on,* vol. 32, no. 5, pp. 2196-2200, 1985.

[57] T. P. Wangler, P. Lapostolle, and A. Lombardi, "Space-charge-induced emittance growth in an elliptical charged particle beam with a parabolic density distribution." pp. 3606-3608 vol.5.

[58] C. K. Allen, and T. P. Wangler, "Parameters for quantifying beam halo." pp. 1732-1734 vol.3.

[59] J.-M. Lagniel, "On halo formation from space-charge dominated beams," *Nuclear Instruments and Methods in Physics Research Section A: Accelerators, Spectrometers, Detectors and Associated Equipment,* vol. 345, no. 1, pp. 46-53, 1994.

[60] K. C. Mittal, "Status of industrial electron linac development programme at BARC, India," *Bulletin of the Indian Vacuum Society,* vol. 13, no. 2, pp. 9-13, June 2010.

[61] K. C. Mittal, and etal, "Design and Development of 10 MeV Industrial RF Electron Linac at Electron Beam Centre, Kharghar for Radiation Processing Applications," *BARC Newsletter*, no. 322, pp. 193-197, October 2011.

[62] D. Bhattacharjee, and etal, "The UHV system of the 10 MeV RF electron linac," *Journal of Physics: Conference Series,* vol. 114, no. 1, pp. 012026, 2008.

[63] M. Reiser, C. R. Chang, D. Kehne, K. Low, T. Shea, H. Rudd, and I. Haber, "Emittance Growth and Image Formation in a Nonuniform Space-Charge-Dominated Electron Beam," *Physical Review Letters,* vol. 61, no. 26, pp. 2933-2936, 1988.

[64] J. A. Nation, and M. Read, "Limiting currents in unneutralized relativistic electron beams," *Applied Physics Letters,* vol. 23, no. 8, pp. 426-428, 1973.

[65] N. Chaudhary, S. Acharya, and etal, "Monte Carlo Simulation & Dosimetric Measurement for a 10MeV RF Electron Linear Accelerator " *Proceedings of the Indian Particle Accelerator Conference, India*, 2011.

[66] N. Chaudhary, S. Acharya, and etal, "Measurement of Beam Spot Size for a 10 MeV RF Industrial Electron Linear Accelerator " *Conference on accelerator radiation safety (CARS 2011)*, 2011.

[67] S. Y. Lee, *Accelerator Physics*, 3rd ed.: World Scientific, 2012.

[68] E. Prebys, "Accelerator Physics " *US Particle Accelerator School, Knoxville*, January 20-31, 2014.

[69] M. G. Minty, and F. Zimmermann, *Measurement and Control of Charged Particle Beams*: Springer Berlin Heidelberg, 2013.

[70] K. R. Crandall, and D. P. Rusthoi, *TRACE 3-D Documentation*, 3rd Edition, Los Alamos National Laboratory report, LA-UR-97-886, 1997.

[71] L. Serafini, "Beam dynamics in rf guns and emittance correction techniques," *Nuclear Instruments and Methods in Physics Research Section A: Accelerators, Spectrometers, Detectors and Associated Equipment,* vol. 340, no. 1, pp. 40-51, 1994.

[72] C.-x. Wang, "Comment on the invariant-envelope solution in rf photoinjectors," *Nuclear Instruments and Methods in Physics Research Section A: Accelerators, Spectrometers, Detectors and Associated Equipment,* vol. 557, no. 1, pp. 94-97, 2006.

[73] C.-x. Wang, "Hamiltonian analysis of transverse beam dynamics in high-brightness photoinjectors," *Physical Review E,* vol. 74, no. 4, pp. 046502, 2006.

[74] S. G. Anderson, and J. B. Rosenzweig, "Nonequilibrium transverse motion and emittance growth in ultrarelativistic space-charge dominated beams," *Physical Review Special Topics - Accelerators and Beams,* vol. 3, no. 9, pp. 094201, 2000.

[75] P. W. Hawkes, "Some approximate magnetic lens aberration formula: a commentary," *Optik,* vol. 56, no. 3, pp. 293–320, 1980b.

[76] G. D. Archard, "Magnetic electron lens aberrations due to mechanical defects," *Journal of Scientific Instruments,* vol. 30, no. 10, pp. 352, 1953.

[77] P. A. Sturrock, "The Aberrations of Magnetic Electron Lenses due to Asymmetries," *Philosophical Transactions of the Royal Society of London. Series A,* vol. 243, no. 868, pp. 387-429, 1951b.

[78] W. Glaser, "Uber ein von sphärischer Aberration freies Magnetfeld," *Z. Physik,* vol. 116, pp. 19-33, 1940.

[79] W. Glaser, "Exact Calculation of Magnetic Lenses with the Field Distribution $H = H_0 /[1 + (z/a)^2]$," *Z. Physik,* vol. 117, pp. 285-315, 1941.

[80] O. Scherzer, "Über einige Fehler von Elektronenlinsen," *Z. Physik,* vol. 101, pp. 593-603, 1936.

[81] A. B. El-Kareh, and J. C. J. El-Kareh, *Electron Beams, Lenses, and Optics, Vol. 2*, 2nd ed.: Academic Press, 1970.

[82] P. Grivet, *Electron Optics*, 2nd ed.: Pergamon, 1972.

[83] V. Kumar, "A Simple Formula for Emittance Growth due to Spherical Aberration in a Solenoid Lens," *Proceedings of the Indian Particle Accelerator Conference*, pp. 580-582, 15-18 Feb 2011, 2011.

[84] B. E. Carlsten, "Emittance growth due to radial density variations of an emittance-dominated electron beam in a channel with continuous acceleration and focusing," *Physics of Plasmas,* vol. 5, no. 4, pp. 1148-1161, 1998.

[85] V. Kumar, "Understanding the focusing of charged particle beams in a solenoid magnetic field," *American Journal of Physics,* vol. 77, no. 8, pp. 737-741, 2009.

[86] G. Franchetti, "Linear beam optics in solenoidal channels," *Physical Review Special Topics - Accelerators and Beams,* vol. 4, no. 7, pp. 074001, 07/20/, 2001.

[87] M. Eshraqi, G. Franchetti, and A. M. Lombardi, "Emittance control in rf cavities and solenoids," *Physical Review Special Topics - Accelerators and Beams,* vol. 12, no. 2, pp. 024201, 2009.

[88] P. W. Hawkes, "The paraxial chromatic aberrations of quadrupole systems," *Proceedings of the Third European Regional Conference on Electron Microscopy, Prague,* vol. A, pp. 5-6, 1964.

[89] L. Serafini, and J. B. Rosenzweig, "Envelope analysis of intense relativistic quasilaminar beams in rf photoinjectors:mA theory of emittance compensation," *Physical Review E,* vol. 55, no. 6, pp. 7565-7590, 1997.

[90] A. Aceves, N.Ercolani, and C. J. etal, " Lecture notes Summer school held in Cork,Ireland , 1994-1997."

[91] A. H. Nayfeh, and D. T. Mook, *Nonlinear Oscillations*: Wiley-VCH Verlag GmbH, 2007.

[92] C. Chen, R. Pakter, and R. C. Davidson, "Phase space structure for matched intense charged-particle beams in periodic focusing transport systems," *Physics of Plasmas,* vol. 6, no. 9, pp. 3647-3657, 1999.

[93] C. Prior, "Dynamics of Nonlinear Beams with Space Charge," *CERN Accelerator School, ESS Bilbao, Spain*, 2011.

[94] A. Burov, "Antiproton and Electron Optics for Electron Cooling," *FERMILAB-TM-2117* 2000.

[95] A. D. Dymnikov, "Matrix methods in periodic focusing systems," *Nuclear Instruments and Methods in Physics Research Section A: Accelerators, Spectrometers, Detectors and Associated Equipment,* vol. 427, no. 1–2, pp. 6-11, 1999.

[96] S. B. Cohn, "Determination of Aperture Parameters by Electrolytic-Tank Measurements," *Proceedings of the IRE,* vol. 39, no. 11, pp. 1416 - 1421, 1951.

[97] S. B. Cohn, "The Electric Polarizability of Apertures of Arbitrary Shape," *Proceedings of the IRE,* vol. 40, no. 9, pp. 1069-1071, 1952.

[98] S. B. Cohn, "Microwave Coupling by Large Apertures," *Proceedings of the IRE,* vol. 40, no. 6, pp. 696-699, 1952.

[99] R. F. Harrington, and J. R. Mautz, "A generalized network formulation for aperture problems," *IEEE Transactions on Antennas and Propagation,* vol. 24, no. 6, pp. 870-873, 1976.

[100] H. A. Wheeler, "Coupling Holes Between Resonant Cavities or Wave-Guides Evaluated in Terms of Volume Ratios," *IEEE Transactions on Microwave Theory and Techniques,* vol. 12, no. 2, pp. 231-244, 1964.

[101] J. Van Bladel, "Small-hole coupling of resonant cavities and waveguides," *Proceedings of the Institution of Electrical Engineers,* vol. 117, no. 6, pp. 1098-1104, 1970.

[102] J. Van Bladel, "Small holes in a waveguide wall," *Proceedings of the Institution of Electrical Engineers,* vol. 118, no. 1, pp. 43-50, 1971.

[103] N. A. McDonald, "Polynomial Approximations for the Electric Polarizabilities of Some Small Apertures," *IEEE Transactions on Microwave Theory and Techniques,* vol. 33, no. 11, pp. 1146-1149, 1985.

[104] Y. Rahmat-Samii, and R. Mittra, "Electromagnetic coupling through small apertures in a conducting screen," *IEEE Transactions on Antennas and Propagation,* vol. 25, no. 2, pp. 180-187, 1977.

[105] R. Dash, B. Nayak, A. Sharma, and K. C. Mittal, "Numerical evaluation of aperture coupling in resonant waveguides and frequency perturbation analysis," *XXVI International Symposium on Discharges and Electrical Insulation in Vacuum (ISDEIV)*, pp. 117-120, Sept. 28-Oct. 3, 2014.

[106] W. H. Press, S. A. Teukolsky, W. T. Vetterling, and B. P. Flannery, *Numerical Recipes: The Art of Scientific Computing*, 3rd ed.: Cambridge University Press, 2007.

[107] J. Gao, "Analytical formulas for the resonant frequency changes due to opening apertures on cavity walls," *Nuclear Instruments and Methods in Physics Research Section A: Accelerators, Spectrometers, Detectors and Associated Equipment,* vol. 311, no. 3, pp. 437-443, 1992.

[108] J. A. Stratton, *Electromagnetic Theory*, New York: McGraw-Hill, 1941.

[109] E. Jahnke, and F. Emde, *Tables of Functions*, 4th ed., New York: Dover, 1945.

[110] B. C. Carlson, "Numerical computation of real or complex elliptic integrals," *Numerical Algorithms,* vol. 10, no. 1, pp. 13-26, 1995.

[111] K. Halbach, and R. F. Holsinger, "Poison Superfish Manual Documentation," *Los Alamos National Laboratory*, 1987.